REPORT DOCUMENTATION PAGE

AFRL-SR-AR-TR-04-

O2Lf(f

1. AGENCY USE ONLY *(Leave blank)*

2. REPORT DATE

3. REPORT TYPE AND DATES COVERED
15 Jan 2004 to 14 Jul 2004 FINAL

4. TITLE AND SUBTITLE
Symposium W, "Engineered Porosity for Microphotonics and Plasmonics," 2003 MRS Fall Meeting in Boston, Massachusetts, during December 1-5. 2003

5. FUNDING NUMBERS
61102F
2305/DX

6. AUTHOR(S)
DR PACHAVIS

7. PERFORMING ORGANIZATION NAME(S) AND ADDRESS(ES)
MATERIALS RESEARCH SOCIETY
MRS
506 KEYSTONE DRIVE
WARRENDALE PA 15086-7537

8. PERFORMING ORGANIZATION REPORT NUMBER

9. SPONSORING/MONITORING AGENCY NAME(S) AND ADDRESS(ES)
AFOSR/NE
4015 WILSON BLVD
SUITE 713
ARLINGTON VA 22203

10. SPONSORING/MONITORING AGENCY REPORT NUMBER
FA9550-04-1-0039

11. SUPPLEMENTARY NOTES

20040520 061

12a. DISTRIBUTION AVAILABILITY STATEMENT
DISTRIBUTION STATEMENT A: Unlimited

12b. DISTRIBUTION CODE

13. ABSTRACT *(Maximum 200 words)*

Symposium W, "Engineered Porosity for Microphotonics and Plasmonics," held December 2-A at the 2003 MRS Fall Meeting in Boston, Massachusetts, combined the areas of optical nanoparticles, microphotonics, photonics crystals and the emerging field of plasmonics. The program started with a review and recent advances in the understandings of porous silicon. the famous light-emitting silicon sponge which caused a real hype in the beginning of the YOs. New results and first devices in the area of photonic crystals have been presented and caused very stimulating discussions. The understanding of the photonic crystal properties also resulted in new insight in the classical area of ridge waveguides, and new designs were proposed. Finally, the emerging field of plasmonics caused a lot of attraction and will possibly lead in the future to further exciting and well-attended workshops.

This volume represents 50% of the presentations and gives a very good overview of the symposium. Financial support by the AFOSR is gratefully acknowledged. The editors would also like to thank all of the invited speakers for their excellent presentations, the participants for their contributions and questions, and the referees for their work.

14. SUBJECT TERMS
MICROPHOTONICS AND PLASMONICS

15. NUMBER OF PAGES

16. PRICE CODE

17. SECURITY CLASSIFICATION OF REPORT
Unclassified

18. SECURITY CLASSIFICATION OF THIS PAGE
Unclassified

19. SECURITY CLASSIFICATION OF ABSTRACT
Unclassified

20. LIMITATION OF ABSTRACT
UL

Standard Form 298 (Rev. 2-89) (EG)
Prescribed by ANSI Std. 239.18

Engineered Porosity for
Microphotonics and Plasmonics

THIS DOCUMENT CONTAINED
BLANK PAGES THAT HAVE
BEEN DELETED

Engineered Porosity for Microphotonics and Plasmonics

Symposium held December 2–4, 2003, Boston, Massachusetts, U.S.A.

EDITORS:

Ralf Wehrspohn
Paderborn University
Paderborn, Germany

Francisco Garcia-Vidal
Universidad Autonoma de Madrid
Madrid, Spain

Masaya Notomi
NTT Basic Research Laboratories
Atsugi, Japan

Axel Scherer
California Institute of Technology
Pasadena, California, U.S.A.

Single article reprints from this publication are available through
University Microfilms Inc., 300 North Zeeb Road, Ann Arbor, Michigan 48106

CODEN: MRSPDH

This book has been registered with Copyright Clearance Center, Inc. For further information, please contact the Copyright Clearance Center, Salem, Massachusetts.

Manufactured in the United States of America

CONTENTS

POROUS SILICON

PHOTONIC CRYSTALS

*Invited Paper

*Invited Paper

PREFACE

Symposium W, "Engineered Porosity for Microphotonics and Plasmonics," held December 2–4 at the 2003 MRS Fall Meeting in Boston, Massachusetts, combined the areas of optical nanoparticles, microphotonics, photonics crystals and the emerging field of plasmonics. We started with a review and recent advances in the understandings of porous silicon, the famous light-emitting silicon sponge which caused a real hype in the beginning of the 90s. New results and first devices in the area of photonic crystals have been presented and caused very stimulating discussions. The understanding of the photonic crystal properties also resulted in new insight in the classical area of ridge waveguides, and new designs were proposed. Finally, the emerging field of plasmonics caused a lot of attraction and will possibly lead in the future to further exciting and well-attended workshops.

This volume represents 50% of the presentations and gives a very good overview of the symposium. Financial support by the AFOSR is gratefully acknowledged. The editors would also like to thank all of the invited speakers for their excellent presentations, the participants for their contributions and questions, and the referees for their work.

Ralf Wehrspohn
Francisco Garcia-Vidal
Masaya Notomi
Axel Scherer

February 2004

MATERIALS RESEARCH SOCIETY SYMPOSIUM PROCEEDINGS

MATERIALS RESEARCH SOCIETY SYMPOSIUM PROCEEDINGS

Prior Materials Research Society Symposium Proceedings available by contacting Materials Research Society

Porous Silicon

Fabrication of Flexible One-Dimensional Porous Silicon Photonic Band-Gap Structures

Natalya Tokranova, Bai Xu, James Castracane
School of NanoSciences and NanoEngineering, University at Albany (SUNY)

Photonic crystals are periodic dielectric structures that have a photonic band gap to control the propagation of light in a certain wavelength range. This property offers a means to manipulate photons in the same way as electrons can be controlled in an atomic lattice. Porous silicon is an ideal candidate for the fabrication of photonic crystals because of the availability of a variety of silicon micromachining techniques. One-dimensional photonic crystals with customized parameters can be economically fabricated using porous silicon multilayer structures with periodically modulated porosity. Despite the structural non-homogeneities, porous silicon fabricated on a p-type Si substrate has optical properties similar to a dielectric material with a single effective refractive index. The exact value of the refractive index for each layer depends on its porosity. An engineered porosity can be obtained by changing the etching currents during the anodization process. This results in a modulation of the refractive index. A stack of alternating layers with high and low porosity produces a distributed Bragg reflector (DBR). Various designs incorporating multilayer porous silicon structures with an optical Fabry-Perot resonator and coupled microcavities are under development and can serve as an optical filter. Prototypes of such free-standing structures with 21-200 stacked layers to be used as DBRs, Fabry-Perot resonators or coupled microcavities are being fabricated. These structures are coated with polystyrenesulfonate on their backsides to increase mechanical strength and at the same time maintain flexibility. In this work, reflectance spectra of these porous silicon multilayers with and without polymer on the backside were measured. Simulations of the multilayer one-dimensional photonic crystals were performed to predict the reflectance spectrum and optimize their structures before the fabrication and to compare to experimental data.

Introduction

Photonic crystals are structures with a periodically varying index of refraction. This allows the control of the light propagation, similar to electrons in a semiconductor crystal. Although many new ideas based on using two- and three-dimensional photonic crystals were proposed recently [1,2], one-dimensional (1D) Photonic Band Gap (PBG) structures still remain one of the most practical ways of applying the photonic-crystal concepts to the solution of many problems of optical communications, laser physics, etc. Dielectric mirrors (Bragg reflectors) and interference filters (Fabry-Perot resonators) were actually the first (1D) photonic crystals. However, they usually are not referred to as crystals because the name crystal is normally reserved for 2D or 3D structures. Typically, these 1D photonic crystals are prepared by layer-by-layer deposition of alternating materials. A stop gap in a desired spectral range can be achieved by appropriately adjusting the dielectric constant and the thickness ratios of the alternating layers [3]. One-dimensional PBG structures have been employed in tunable optical delay lines [4], optical switches [5] and frequency converters allowing for phase and group-velocity matching through nonlinear optical interactions [6]. Multilayer reflectors are one of the most rapidly growing areas of modern optical technologies, where the remarkable properties of 1D PBG structures are widely employed. Multilayer mirrors ensure high reflectivity within broad spectral

ranges and allow for the control of the parameters of short light pulses as passive optical components. The use of porous silicon is limited by its chemical and mechanical stability, in particular, if the fabricated structure is freestanding.

Experimental Details

Electrochemical etching techniques provide continuous control over the porosity and thickness of the silicon layer as a function of etching conditions. The porosity is a linear function of the current density for a specific hydrofluoric acid (HF) concentration. An engineered porosity can be obtained by changing the etching currents during the anodization process. The layer thickness depends on the etch time. Changing the current density does not affect the porous silicon layers previously formed because silicon dissolution occurs at the silicon electrolyte interface [7].

The reflectance spectrum of porous silicon multilayer structures can be precisely controlled by varying the parameters of the anodization process. A stack of alternating layers with high and low porosity produces a distributed Bragg reflector (DBR).). To form an optical interference filter or Fabry-Perot resonator the central active medium called a microcavity is embedded between two DBRs. Both top and bottom reflectors are quarter wave stacks of low- and high-porosity layers. The cavity layer can be the same porosity as a low- or high- porosity layers of the mirrors. The Fabry-Perot resonator has a very narrow pass-band region. The wavelength of the resonance is given by $\lambda_c = m n_c d_c$, where m is the order, n_c the refractive index of the cavity and d its thickness. [8] The mirrors can be created by using porous silicon multilayers where the refractive indices are chosen to give $\lambda/4$ stacks. The etched microcavities consist of a cavity layer of optical thickness $\lambda_c/2$ (λ_c corresponds to the maximum of the reflectance spectrum) between two Bragg mirrors. By choosing appropriate layer thicknesses, the center of the photonic band gap could be tuned to the desired wavelength.

The porous silicon multilayer stacks were prepared by periodic anodic etching of p-type (100)-oriented silicon wafers with resistivity 0.01 Ohm·cm in 15% solution of HF with ethanol. The process took place with a constant current applied between a silicon wafer and a platinum electrode. For all samples, the low and high porosities were fabricated at the current density 4 mA/cm^2 and 36 mA/cm^2, respectively. An SEM micrograph of a DBR structure fabricated using the conditions mentioned above is shown in Fig.1. The porosity was determined by gravimetric measurements [9] to be 36% for the lower current density and 59% for the higher current density. The thicknesses of porous layers were measured by Scanning Electron Microscopy analysis. Under these conditions, the size of the pores varies from 1 nm to 20 nm in diameter.
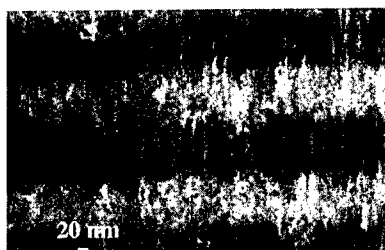
Fig.1. Cross-sectional SEM image of alternating layers with low (36%) and high (59%) porosities.

Computer simulations of the structure reflectivity were performed before its fabrication to obtain the desired spectra depending on the stack parameters. Figure 2 shows a computer simulation and experimental data of Fabry-Perot resonator containing two ten period DBRs and

microcavity. The porosities and thicknesses of the DBR layers are 36%, 105 nm and 59%, 130 nm, for the low and high porosity layers, respectively. The 210 nm thick microcavity has a 36% porosity. The small difference between the calculated and measured spectra can be explained by a drift in layer thickness and porosity.

A coupled microcavity structure is another interesting object for investigations because it introduces an additional possibility for the tailoring of spatially confined light-matter coupling [10]. The coupled porous silicon microcavity structures are formed by two cavities which are coupled through a DBR and have equal thickness and porosity (Fig.3). Optical coupling between the various cavities yields a splitting in the cavity modes with the appearance of multiple resonances within the stop band [11]. The reflectance spectrum of the coupled microcavity structure has a different transmittance for the two modes although the two cavities are equal (Fig.4). The residual absorption into the DBR between the cavities may cause this slight difference.
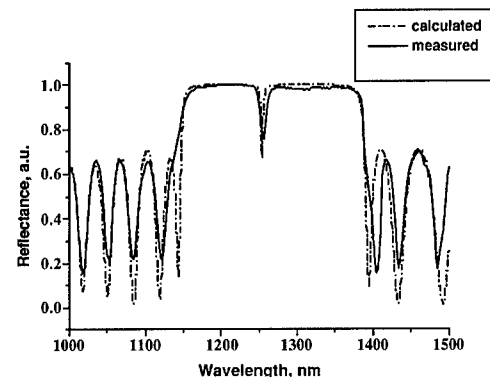
Fig.2. Calculated and experimental reflectance spectra of a Fabry-Perot Resonator structure. Each DBR contains ten period porous silicon multilayers with 36% and 59% porosities. The 210 nm thick microcavity has 36% porosity.
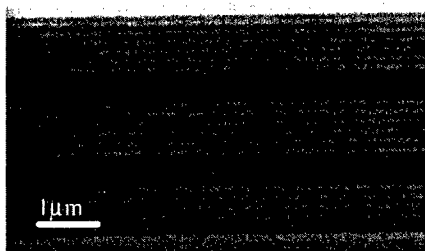
Fig.3. Cross-sectional SEM image of a coupled microcavity structure. Both 370 nm thick cavities have 36% porosity. The central DBR has 11 layers.
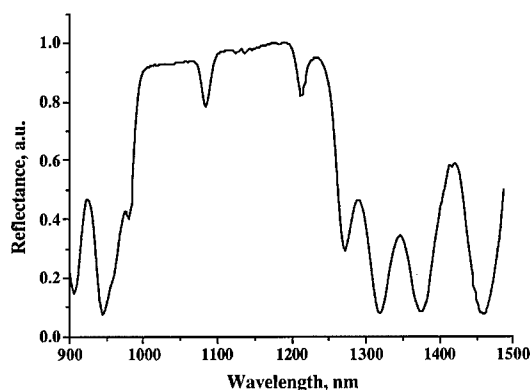
Fig.4. The experimental reflectance spectrum of the coupled microcavity structure containing two 370 nm thick cavities with 36% porosity and central DBR with 11 layers.

Aging effects in porous silicon structures are related to the changes of layer refractive indices due to oxidation. The porous silicon microcavity structure is highly sensitive to any changes in the optical properties of the active media and alternate layers modifying the reflectance spectrum, causing a spectral shift in the interference peaks. To stabilize the porous silicon multilayer structure after anodization, the samples were oxidized using an anodic reaction into a solution:

$$Si+2H_2O \rightarrow SiO_2+4H^++4e^-$$

The oxidation resulted in a shift towards shorter wavelengths (blue shift) in the reflectance spectrum (Fig.5) due to a change in the refractive index of the layers after oxidation. During the oxidation process, some porous silicon is transformed into silicon dioxide and the effective refractive index of a porous silicon layer is reduced because the refractive index of silicon dioxide, about 1.46, is much lower than that of silicon. The oxidation process is more efficient for higher-porosity

Fig.5. The reflectance spectra of Fabry-Perot Resonator structure before and after oxidation.

layers because of the larger internal surface and the lower content of silicon (Fig.6). As a consequence, the relative variation of refractive index is larger for the higher porosity layers. After oxidation, the porous silicon multilayer structure exhibits chemical stability and does not change its reflectance spectrum. Our measurements showed no changes four months following oxidation. The reflectance spectra of nonoxidized structures showed a slight blue shift with time due to the aging of the samples.

To produce a freestanding structure, the resulting porous silicon multilayer stack was

Fig.6. AES depth profile of oxidized porous silicon structure with alternating high and low- porosity layers.

removed from the substrate by applying an electropolishing current density 250 mA/cm^2 for 60 sec in the same solution of HF with ethanol. The films obtained by this process were very fragile. To increase the mechanical strength of the films, a polymer such as the polystyrenesulfonate was coated on the backside of the films. The reflectance spectra of the freestanding microcavity structures with various quantities of back DBR layers were measured to estimate the minimum layer quantity to achieve near 100% reflectivity. It is well known that the reflectivity of the multilayer mirror increases as the number of layers increases. The reflectance spectra of free-standing Fabry-Perot resonators are defined by dual DBR/cavity architecture. The spectral position of the dip in the reflectance curve is strongly dependent on the microporous structure and fill. After electrochemical etching of the silicon, the samples have a hydrophobic surface and the penetration of the water-soluble polymer (the polystyrenesulfonate) into the pores is hampered. The penetration of material (including polymer) into micropores can be measured in several ways. The SEM measurements did not show polymer penetration into the pores (Fig.7). The reflectance spectra of the fabricated porous silicon multilayers with and without the polymer were measured. The existence of the polymer layer did not change the reflectance spectra if the number of back DBR layers exceeds 20. The structures with a 10 layer back DBR reflects about 87% of the incident light and the presence of polymer reduces this value to 84%.
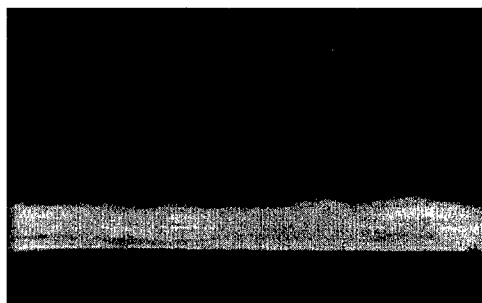
Fig.7. Cross-sectional SEM image of alternating porous silicon layer structure coated with polymer.

It should be pointed out that the reflectance spectrum of the free-standing sample depends on layer size changes during a deformation process. However, our measurements showed an insignificant spectrum shift (2 nm) under 45 degrees of bending when the incident light was normal to the plane of the film surface. A more important factor for changes in the reflectance spectrum of a porous silicon multilayer structure is the angle of incident light.

Conclusions

Multilayer porous silicon structures are an efficient and low cost method to fabricate optical components. The chemical properties of porous silicon multilayer structures can be stabilized by an oxidation process. The effective refractive indices of porous layers are reduced by the oxidation process and the stop band is shifted towards shorter wavelengths.

The application of a polymer support increases the mechanical strength of the free-standing multilayer structure without a deterioration of the optical properties, resulting in flexible, high-quality optical component.

The good agreement between the computer modeling and experimental data shows that the growth parameters can be well controlled during the anodization process.

References

1. S. Y. Lin, J. G. Fleming, D. L. Hetherington, B. K. Smith, R. Biswas, K. M. Ho, M. M. Sigalas, W. Zubrzycki, S. R. Kurtz and Jim Bur "A three-dimensional photonic crystal operating at infrared wavelengths" Nature, **394**, 251-253, 1998

2. A.Blanco, E.Chomski, S.Grabtchak, M.Ibisate, S.John, S.W.Leonard, C.Lopez, F.Meseguer, H.Miguez, J.P.Mondia, G.A.Ozin, O.Toader, and H.M.Van Driel "Large-scale synthesis of a silicon photonic crystal with a complete three-dimensional bandgap near 1.5 micrometers" Nature, **405**, 437-440, 2000

3. A.Birner, R.B.Wehrspohn, U.M.Gosele, K.Busch "Silicon-based Photonic Crystals" Adv.Mater., 13, 377-388 (2001)

4. M. Scalora, R. J. Flynn, S. B. Reinhardt, R. L. Fork, M. J. Bloemer, M. D. Tocci, C. M. Bowden, H. S. Ledbetter, J. M. Bendickson, J. P. Dowling, R. P. Leavitt "Ultrashort pulse propagation at the photonic band edge: Large tunable group delay with minimal distortion and loss" Phys.Rev.E 54, 1078-1081 (1996)

5. P.K. Kashkarov, L.A. Golovan, A.B. Fedotov, A.I. Efimova, L.P. Kuznetsova, V.Y. Timoshenko, D.A. Sidorov-Biryukov, A.M. Zheltikov, J.W. Haus "Photonic bandgap materials and birefringent layers based on anisotropically nanostructured silicon" J.Opt.Soc.Amer.B 19, 2273-2281 (2002)

6. M. Centini, C. Sibilia, M. Scalora, G. D'Aguanno, M. Bertolotti, M. J. Bloemer, C. M. Bowden, and I. Nefedov "Dispersive properties of finite, one-dimensional photonic band gap structures: Applications to nonlinear quadratic interactions" Phys.Rev. E 60, 4891-4898 (1999)

7. Lugo J.E., Lopez H.A., Chan S. and Fauchet P.M. "Porous multilayer structures: A photonic band gap analysis" J.Appl.Phys. , vol.91, ? 8, p.4966-4972 (2002)

8. Pavesi L., Mulloni V. "All porous silicon microcavities: growth and physics" Journal of Luminescence 80 (1999) pp.43-52

9. Halimaoui A., in "Properties of Porous Silicon", edited by L.V.Canham (INSPEC, London, 1997), Vol. 18, p.18

10. L.Pavesi, G.Panzarini, L.C.Andreani "All-porous silicon-coupled micricavities: Experiment versus theory" Phys. Rev. B **56**, p.15 794-15 800 (1998)

11. M.Ghulinyan, C.J.Oton, G.Bonetti, Z.Gaburro, and L.Pavesi "Free-standing porous silicon single and multiple optical cavities" J.Appl.Phys.,**93**, p.9724-9729 (2003)

Laterally Graded Rugate Filters in Porous Silicon

Sean E. Foss and Terje G. Finstad
Department of Physics, University of Oslo,
POBox 1048 Blindern, 0316 Oslo, Norway

ABSTRACT

Rugate optical reflectance filters with position dependent reflectance peaks in the visible to near infrared spectrum were realized in porous silicon (PS). Filters with strong reflection peaks, near 100%, no detectable higher order harmonics and suppressed sidebands compared to discrete layer filters were obtained by varying the current density continuously and periodically during etching. An in-plane voltage up to 1.5 V was used to obtain refractive index and periodicity change along the filter surface resulting in reflectance peak shifts of up to 100 nm/mm in the direction of the voltage drop. The effect of the lateral change in optical parameters on the filter characteristics is studied by varying the gradient and comparing measurements at different positions with measurements on a non-graded filter. We have observed extra features in the reflectance spectrum of these graded filters compared with reflectance from a non-graded filter which is likely caused by the gradient.

INTRODUCTION

The process of discretely varying the current density during etching of porous silicon (PS) to obtain thin layers with different refractive indexes was first reported by Vincent [1] and Berger *et al.* [2] in 1994. With this method Bragg reflectors and Fabry-Perot filters are now routinely made. By applying an in-plane voltage across the sample during etching, Hunkel *et al.* have shown that it is possible to produce PS discrete filters with laterally dependent filter characteristics [3,4]. In addition to the discrete layer filters (i.e. Bragg and Fabry-Perot) one may also realize structures in PS that are uniquely simple to this system. By varying the current density continuously and periodically, the refractive index into the PS layer will vary accordingly [5]. The refractive index may be calculated from the porosity by the effective medium approximation. With this approach one obtains reflecting rugate filters which may have narrow reflection peaks, no higher order harmonics and suppressed sidebands. For an overview of rugate filter theory, see Bovard [6]. Here we report on rugate filters with laterally varying characteristics which have been made for the visible to near infrared optical spectrum.

EXPERIMENTAL DETAILS

The Si substrate used was 0.018 Ω·cm B-doped, p-type Czochralski-grown single crystal with <100> orientation polished on both sides. The HF-based solution used for etching consisted of 1:2 HF(40 %):ethanol. The etching current was controlled by a computer, in this case with a time step of 1 second which sufficiently reproduced the refractive index sinusoid. The used current profile is shown in Fig. 1. The etching occurs mostly at the pore tips which is why porosity may be modulated by the current. There will also be a small chemical etching which is

dependent on time. This is corrected for by etching the deeper part of the layer with a slightly higher current.

The starting point for the design was a 1 cm diameter, circular, non-graded rugate filter with a reflectance peak-wavelength at 738 nm measured with light incident at 24 deg. The filter was made relatively thin with 23 periods of the porosity sinusoid over 5 μm. Etching was done with current density varying between 9.4 mA·cm^{-2} and 19.7 mA·cm^{-2}, which corresponds to refractive indexes at the peak wavelength of 1.78 and 1.48 respectively. Index matching for the air-PS interface and the PS-substrate interface was employed to reduce sidebands. This may be observed in the beginning and end of the current profile of Fig. 1 where there are large slopes.

A schematic of the etching setup is shown in Fig. 2. A lateral gradient in porosities and etch rates was obtained by applying a constant in-plane voltage up to 1.5 V between two contacts on the sample back side while etching with the same current profile as for the starting point design. By doing this the local current density varies. Ohmic contacts were made from evaporating Al on the samples followed by a short heat treatment. The resistance between the contacts varied between 0.6 and 0.7 Ω for the different samples. Contact resistance is a substantial fraction of this, so good, reproducible contacts were important to achieve control of the potential drop within the sample.

Reflectance measurements were conducted with a 0.275 m focal-length monochromator with a Si-detector. The focused probe beam had a diameter of less than 1 mm and was directed at the filter at an angle of about 24 deg. Both the size of the beam and the angle contribute to a widening of the reflectance peak to some extent compared to the peak from the non-graded filter. The effect depends on the gradient of the filter. Reflectance spectra are only plotted from 600 nm to 1100 nm because of the combination of the detector and diffraction grating used in the monochromator.

For the optical images a microscope with a mounted digital camera was used. Several images were stitched together to get a better overview. To show the striation effects on the filter
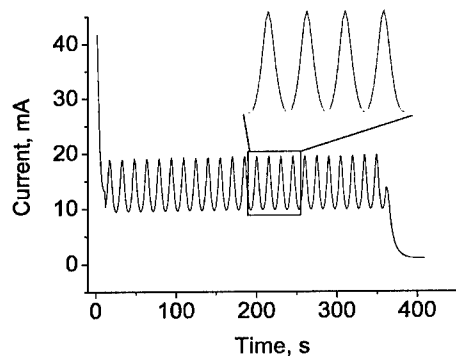
Figure 1. Applied current during etching of all filters. The slopes at the beginning and end are for index matching.
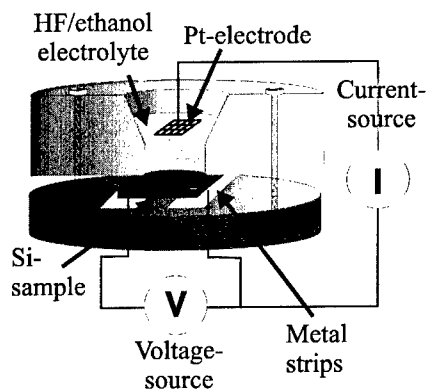
Figure 2. Sketch of the etch setup. The Si sample with Al back contacts is pressed on to two Cu-plates on the back side so an in-plane constant voltage can be set up. The current-source is connected to a computer.

reflectance clearly in these images, the RGB colors were split into separate images and only the green was used for analysis as this had the largest contrast between striation minimum and maximum.

A white light interferometer, WYKO NT-2000 by Veeco, was used to measure surface topography profiles of the samples after the PS was stripped away with a concentrated NaOH etch. This instrument has a large dynamical range and can measure μm and nm height differences in the same measurement. Even with the gradient in the samples present, measurements showing the ridges caused by striations, in the order of 100 nm high, were possible.

RESULTS AND DISCUSSION

The reflectance spectrum of the non-graded starting point filter is shown in Fig. 3. Often when designing rugate filters one employs apodization to further reduce sideband reflection [6]. This was not done on the presently reported filters. Observed sidebands show a periodicity dependent on the average optical thickness, $n \cdot d$, of the PS film at the measured position which may be used to calculate the average refractive index. Because of the refractive index dispersion in Si the sidebands in the reflectance plot will decrease in frequency with increasing wavelength.

Reflectance spectra at four different positions along a line through the center of a filter made with an in-plane voltage of 1.0 V are shown in Fig. 4. Comparing these peaks with the one from the non-graded filter in Fig. 3 it is clear that the grading affects the shape, width and height. The position of the maximum reflected wavelength shifts along the filter as expected. The amplitude of the maximum reflectance decreases towards shorter wavelengths. This is most likely due to increased absorption [3]. There is also a broadening of the peaks away from the mid position towards shorter wavelengths caused by the fact that the refractive index does not have a linear
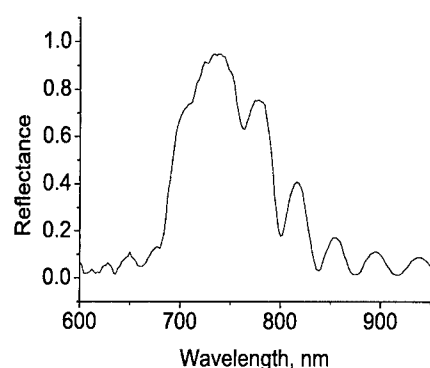
Figure 3. Reflectance spectrum of a non-graded rugate filter used as a starting point for graded filters. Measurements are taken at 24 deg. incident angle. FWHM is 100 nm.
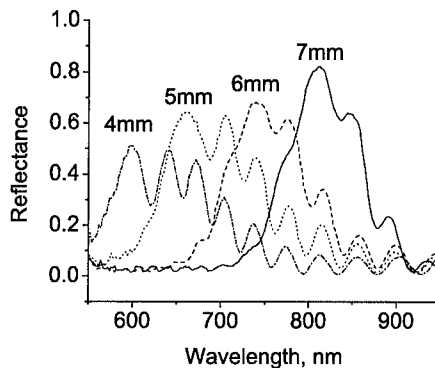
Figure 4. Plot of reflectance spectra from a filter made with an in-plane voltage of 1.0 V. Marked positions are along a centerline across the circular filter in the direction of the gradient. Note the spreading of the peak as it moves towards lower wavelengths.

dependence on current density [3]. Therefore the amplitude and period in the refractive index sinusoid will only be optimal at one point along the filter surface. All the graded filters show similar behavior. A decrease of amplitude between samples with increasing grading is also observed. This is most likely caused by the finite spot size of the probe beam. When this covers a too large area compared to the gradient at that point, the resulting measurement will be an average of spectra and hence the filter window will be smeared out.

Figure 5 shows the peak wavelengths at different positions for a series of filters with changing in-plane voltage. As expected, the shift increases with the voltage caused by the increase in the porosity and etch rate gradient. The horizontal line across the plot shows the peak wavelength of the non-graded filter. The reflectance peak is clearly not at 738 nm for the mid position for any of the graded filters. Thus the current density does not vary linearly with position. This is as expected considering the geometry of the etch setup.

Although the shift in peak wavelength seems close to linear, depth profiles of the PS layer made by white light interferometry after stripping, shown in Fig. 6, show tendencies towards non-linearity. This is also supported by [7] where Bohn and Marso describe an equivalent circuit model for the etch situation. A non-linear current density distribution will result in a varying position of the crossing point between the peak shift curves and the non-graded peak wavelength. One would, however, expect that at some point the filter would have the characteristics of the non-graded filter as the total current is the integral of the local current density at all positions on the filter area. This is true for the filters of Fig. 5 except for the 0.1 V case. A slight difference in process parameters is most likely the cause. In Fig. 7 the change in peak shift with applied in-plane voltage is shown. The line corresponds to a linear fit which seems appropriate for this range of voltages. A non-linearity might be expected for higher voltages as the necessary current
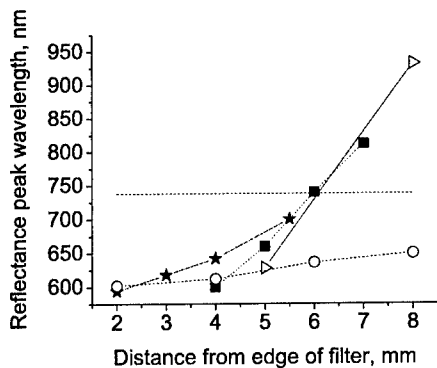
Figure 5. The wavelength of reflection peaks measured at different positions on samples with different gradients, (o) for an in-plane voltage of 0.1 V, (★) for 0.5 V, (■) for 1.0 V and (▷) for 1.5 V. The shift of the peaks increases with increasing in-plane voltage.
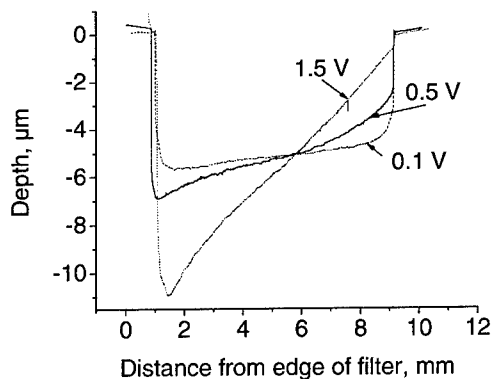
Figure 6. Depth profiles of the PS-substrate interface measured with white light interferometry after removal of the PS layer. One clearly sees the increasing gradient with in-plane voltage. Curves are composed of several single measurements stitched together which cause drift in measured height, therefore only tendencies are discussed.

reaches amperes, hence heating will probably affect the process. The geometry of the filter has an effect on the local current density, as may be observed visually. Perpendicular to the gradient direction reflection colors shift somewhat away from the center line, indicating a non-constant current density towards the edges.

Visible stripes of slightly different colors are present in all the filters made. These seem circular and centered around the center of the 4" wafers used for samples. After stripping away the PS with an NaOH etch these stripes are still present as ridges. Figure 8 shows a compilation of a light microscope image representing the intensity of the green component from a color image (to increase contrast) and the subsequent intensity plot of the 2-dimensional height profile from white light interferometry measurements at the same position after stripping of PS. Peak to peak height of the ridges are about 100 nm. These ridges indicate locally different etch rates. Similar results have been reported earlier by Lérondel et al. [8] as likely being caused by striations, i.e. radially symmetric resistivity inhomogeneities in the substrate due to an inhomogeneous dopant distribution. One way of smoothing the PS-substrate interface is suggested by Setzu et al. [9] where etching is done at low temperatures down to -35 °C.
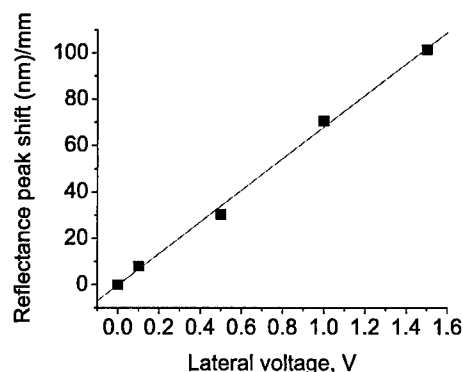
Figure 7. Plot showing the rate of change of the shift of the reflection maximum along the grading of the filters as a function of applied voltage.
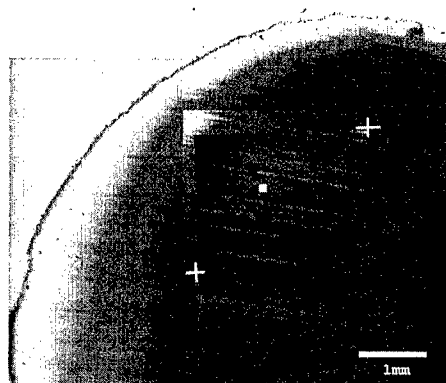
Figure 8. Image of the 0.1V filter with an overlay (between the two white crosses) of an intensity plot of the corresponding surface topography profile of the PS-substrate interface measured by white light interferometry. The white square in the intensity plot is missing data.

CONCLUSION

We have shown it is possible to make a laterally graded rugate filter with good reflectance. The filter may be improved by optimizing the parameters used, especially by using a smaller difference between minimum and maximum refractive index and more periods, hence a thicker PS film. Apodization may also be used to optimize the reflectance characteristics. Striations causing locally differing etch rates have been shown.

REFERENCES

1. G. Vincent, *Appl. Phys. Lett.* **64**, 2367 (1994).
2. M. G. Berger, C. Dieker, M. Thönissen, L. Vescan, H. Lüth, H. Münder, W. Theiss, M. Wernke and P. Grosse, *J. Phys. D: Appl. Phys.* **27**, 1333 (1994).
3. D. Hunkel, R. Butz, R. Arens-Fischer, M. Marso and H. Lüth, *J. Lumin.* **80**, 133 (1999).
4. D. Hunkel, M. Marso, R. Butz, R. Arens-Fischer and H. Lüth, *Mater. Sci. Eng. B* **69-70**, 100 (2000).
5. M. G. Berger, R. Arens-Fischer, M. Thönissen, M. Krüger, S. Billat, H. Lüth, S. Hilbrich, W. Theiss and P. Grosse, *Thin Solid Films* **297**, 237 (1997).
6. B. G. Bovard, *Applied Optics* **32**, 5427 (1993).
7. H. G. Bohn and M. Marso, (unpublished report).
8. G. Lérondel, R. Romestain and S. Barret, *J. Appl. Phys.* **81**, 6171 (1997).
9. S. Setzu, G. Lérondel and R. Romestain, *J. Appl. Phys.* **84**, 3129 (1998).

Strong light confinement in microporous photonic silicon structures

G. Lérondel, P. Reece[1], A. Bruyant and M. Gal[1]
Laboratoire de Nanotechnologie et d'Instrumentation Optique Université de Technologie de Troyes - CNRS (FRE 2671) 12 rue Marie Curie BP 2060 10010 Troyes cedex - France
[1] School of Physics University of New South Wales, Sydney 2052 NSW Australia

ABSTRACT

We have recently reported the fabrication of Si based subnanometer linewidth microcavities and omnidirectionnal mirrors. The structures were made of microporous silicon by electrochemical anodization. The structure high quality and the observation of omnidirectionnal stop bands have been made possible by the optimisation of the starting material, the etching conditions, and the structure design. In this paper we discuss more specifically the choice of these parameters considering the material intrinsic limitations.

INTRODUCTION

Following the initial works of Vincent [1] and Berger and al. [2], microporous silicon based refractive index multilayers have received, since 1994, more and more attention leading to the fabrication of numerous structures and devices as, for example, to name only a few, tuneable emitting diodes [3] and more recently polarization dependant mirrors [4]. Structures are simply obtained by modulating the current density during an electrochemical anodization of a crystalline silicon wafers. Leading to smoother interfaces [5] and a larger refractive index difference ($\Delta n \sim 0.9$) [2], mesoporous Si obtained via the anodisation of highly doped p-type wafers has been usually preferred. For resonant structures centred in the visible-NIR, Q factors defined as the full width half maximum divided by the resonance wavelength lie in the 50-300 range. Considering the Δn, these relatively low Q factors suggest that in mesoporous silicon optical losses strongly limit the structure quality. This last point was confirmed by the fabrication of low doped p-type porous silicon (nanoporous) microcavities exhibiting similar finesse but with a smaller refractive index modulation (0.5) [6]. This was made possible by the use of low temperature anodisation in order to decrease the wavelength-scale layer thickness fluctuations (roughness) which were found to limit the structure quality. In the case of mesoporous silicon layer thickness fluctuations mainly occur at a large waviness was expected. Following our recent papers on the fabrication of mesoporous silicon subnanometer linewidth microcavities [7] and omnidirectionnal mirrors [8] we aimed here to address a few specific points on the structure quality limitations and optimization like, the effect of lateral thickness fluctuations (waviness) on the cavity mode width probed by spatially resolved reflectivity, the uniformity of the periodic structures probed by scanning electron microscopy and absorption losses. Finally we show how the structure design can be used to optimize ominidrectionnal stop bands.

EXPERIMENTAL DETAILS

Samples were prepared from highly doped (0.008 ohm.cm) p-type <100> oriented silicon wafers. Room temperature (RT) microcavities were made using the now standard 1:1:2 HF:water:ethanol solution and low/high current densities of 10/220 mA/cm^2, high and

low current densities corresponding respectively to low, n_L (high porosity) and high, n_H (low porosity) refractive indexes. Microcavities made at low temperature around -20°C were anodised using a 3.5:3.5:3 HF:Ethanol:water solution and current densities varying between 10mA/cm^2 and 86mA/cm^2. Quarter-wave layers of low and high porosity are respectively formed in about 6s and 0.5s. To prevent any porosity gradient in the dissolution direction, etch breaks have been added after each layer. Break durations is in the order of the anodisation time for the low porosity layer and ten times longer for the high porosity layer were found empirically to both enable the regeneration of the HF concentration at the dissolution front and to minimize the chemical dissolution. The typical dissolution time for one period becomes of 20s. Porosity values given in this paper were deduced from reflectivity simulations using the Looyenga model to account for the refractive index dispersion. Refractive index profile was chosen to obtain the highest refractive index contrast at each interface.

Samples have been characterized by electron Microscopy using a Hitachi S9000 scanning electron microscope and by reflectivity using a standard measurement setup and spatially resolved setup where the core of a multimode fibre was imaged on the sample surface leading to a spot size of around 70 μm and a collecting angle of less than 1°.

RESULTS AND DISCUSSION

Waviness and low temperature anodisation

Figure 1 shows spatially resolved reflectivity spectra around the cavity mode of a room temperature anodized microcavity. Spectra have been measured at two different places separated by 100μm. The two modes exhibit similar features, a 2nm FHWM and a minimum of reflectivity less than 20%. These features have to be compared with the 3.5nm line width and 70% of minimum of reflectivity measured on the same sample using usual reflectivity setup.

In order to assess the origin of these spatial fluctuations, we measured several spectra covering on area of 500x500 μm^2. The results are shown on the bottom of figure 2. We found that the fluctuation amplitude is maximum in the radial direction referring to the wafer geometry and almost null in a direction perpendicular to the previous one. The mode position variation is about 5 nm on a typical length of half of a millimetre.

Figure 1: Spatially resolved reflectivity spectra of a microcavity anodized at RT. The structure is composed of a top DBR of 5.5 periods a $\lambda/2$ spacer and a bottom DBR of 7 periods.

The average of the different peaks leads to a FWHM of 3.5nm in agreement with the line width measured using the standard reflectivity setup. The typical length of these fluctuations and the preferential radial direction are in keeping with the large scale fluctuations (waviness) observed in the porous silicon dissolution front due to radial resistivity fluctuations [5].

Considering previous study [6], we applied the low temperature anodisation to highly doped substrate and reproduce on the sample surface the same spatially resolved set of measurements than for the room temperature sample. Results are shown on the top of the figure 2. The fluctuation of the cavity mode position has been reduced and the amplitude is around 1nm on half of a millimetre scale.
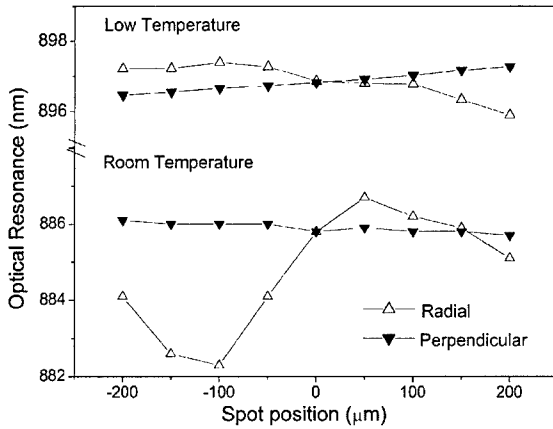
Figure 2: Spatial distribution on the millimetre scale of the cavity mode for low and room temperature microcavities. Radial refers to the silicon wafer geometry.

As it was already shown, the use of low temperature anodisation, for similar current density modulation, increases the porosity difference and hence the refractive index contrast [6]. This is due to the higher viscosity of the solution at low temperature. We observed here a similar effect. In order to lower the minimum porosity achievable and hence increase the porosity modulation, we increase the HF concentration. Low temperature and 35% concentrated HF were found to lead to optimized conditions.

Subnanometer line-width cavities in the visible-NIR have been achieved using these conditions [7].
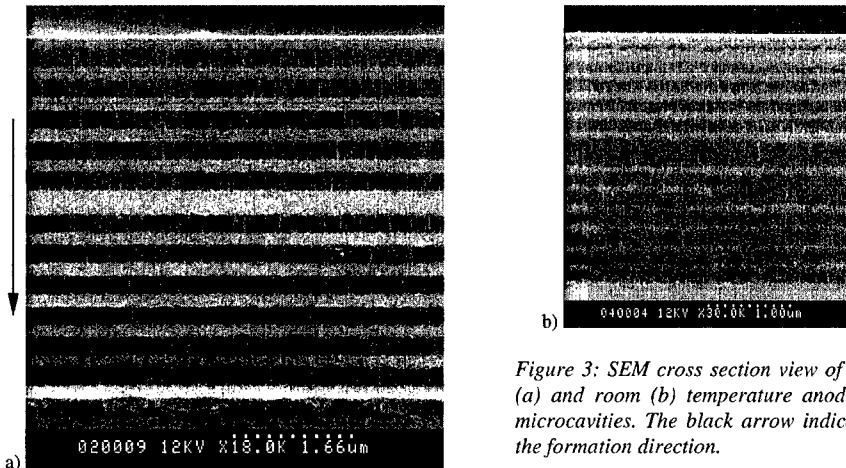
Figure 3: SEM cross section view of low (a) and room (b) temperature anodized microcavities. The black arrow indicates the formation direction.

The figure 3 compares the SEM pictures of an optimized porosity modulated structure and a typical structure made at RT. The porosity and layer thickness ($\lambda/4$) modulations appear

clearly on both images. Oscillations in the low porosity layers (in bright), have almost disappeared on the left image. Comparing the two images a difference in the porosity contrast can also be observed. This difference was confirmed by high resolution SEM pictures shown on the figure 4. The zoom of the central part of the cavity shown on the figure (a), highlights the porous structure difference between the low and high porosity regions for the optimized structure. The low porosity region which appears almost uniform at this magnification is sustained by very thin vertical (~10nm) silicon walls (many of them are broken probably due the cleavage). Surprisingly, the top interfaces of the low porosity layers exhibit a saw-teeth pattern whose typical length is believed to be correlated to the voids dimension. This was confirmed by the figure (b) showing the spacer region of a moderate porosity modulated structure also obtained at low temperature. In the high porosity region, the voids between the typical tree-like silicon structures are smaller. As a consequence at the scale of the layer thickness, the interface appears smoother.
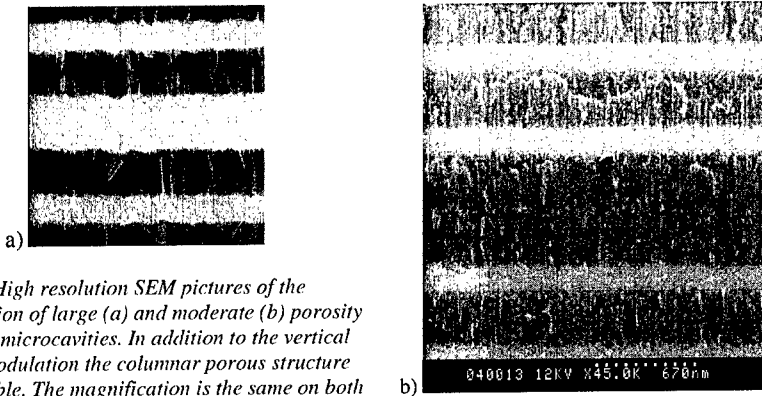
Figure 4: High resolution SEM pictures of the spacer region of large (a) and moderate (b) porosity modulated microcavities. In addition to the vertical porosity modulation the columnar porous structure is also visible. The magnification is the same on both images.

Optimised NIR microcavity
To investigate further the losses in our structure we intended to fabricate microcavity centred over the Si bandgap in a region where the absorption of porous Si is expected to be minimal. The figure 5 shows the reflectivity spectrum of a microcavity fabricated at low temperature centred around 1.53 µm. Experimental spectrum is truncated due to the cut-off of the detector. But an idea of the bandwidth of the plateau (~500nm) is given by the simulated spectrum. Refractive indexes have been determined from the simulation of a structure whose plateau was slightly shifted towards smallest wavelength to avoid the detector cut-off. On a large wavelength range the mode couldn't be experimentally either numerically resolved. The higher resolution spectrum (right side) obtained using the spatially resolved reflectivity setup shows the cavity mode position at 1,5355 µm with a width of 0.21 nm. Such characteristics lead to a Q factor of 7310. We compared the experimental resonance with simulated reflectivity spectra around the cavity mode obtained without any losses, with roughness losses and finally absorption losses. As shown on the figure, absorption losses taken into account only for the low porosity layers give the best agreement with the experimental spectrum. The value of 30 cm^{-1} was taken from the literature for samples of comparable porosity [8]. Although ones will need to know the exact absorption in our material this

comparison shows that in order to increase further the Q factor absorption losses need to be minimized.
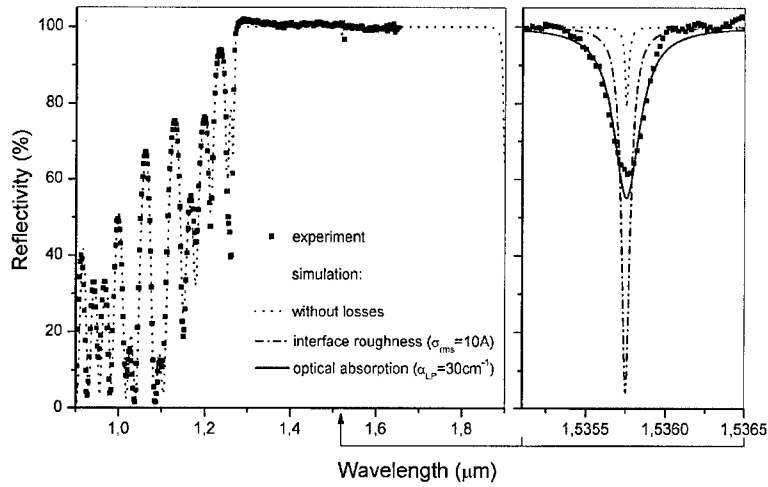
Figure 5: Low temperature NIR microcavity reflectivity. The structure is composed of a top DBR of 7.5 periods a λ/2 spacer and a bottom DBR of 10 periods.

Optimised photonic structures: band gap engineering

It has been recently shown that dielectric mirrors with a high refractive index difference give
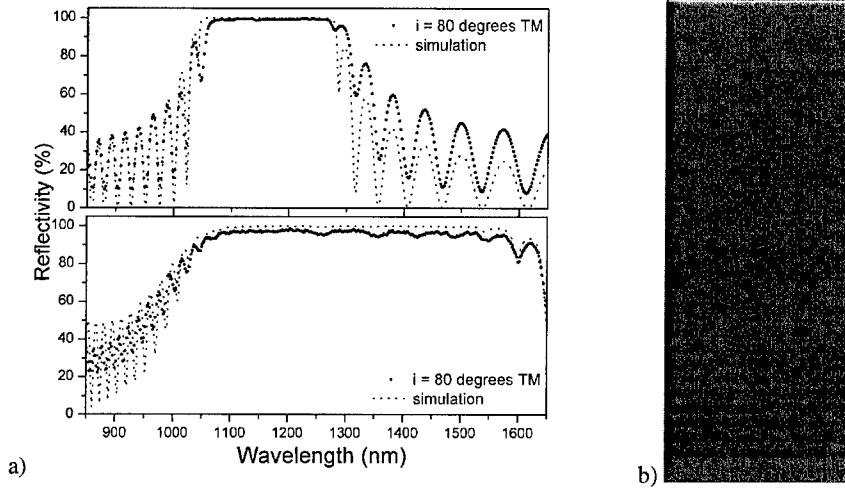
Figure 6: Bang gap engineering via optical thickness tuning. a) (top) reflectivity spectrum of a 25 periods low refractive index optimized mirror and (bottom) reflectivity spectrum of a 35 periods chirped omnidirectional mirror. Both structures were anodized at RT. b) SEM picture of the 55% chirped structure.

rise to an omnidirectionnal stop band [10] for a low refractive index incident medium, n_{lo} like air. One of the conditions to observe omnidirectionnality is that a plateau could still be observed for very large angle of incidence (i) and TM incident light. In addition, it has been shown that omnidirectionnality is optimal when the low refractive index, $n_L \sim 1.5 n_{lo}$. The figure 6 shows the reflectivity spectra of two different types of porous silicon mirrors obtained at grazing angle (i=80). For the structure whose spectra is shown on the top of the figure 6.a), starting from standard RT anodisation conditions, we increased the high current density to 330 mA/cm^2 to get a greater porosity (76%) corresponding to the optimal low refractive index, n_L of 1.5. For the structure whose spectrum is shown on the bottom of figure 6a), standard current densities were used but as shown by the SEM picture on figure 6.b), the periodicity of the structure has been chirped such that the thickness of the last bi-layer is 55% larger than the first bi-layer. For the last structure the stop band is more than twice larger. For both structures an omnidirectional stop band was observed. The gap-to-midgap ratio is of 8.2% and 35% for the unchirped and chirped structure respectively [9].

CONCLUSION

Microporous silicon microcavity quality was found to be limited by large scale layer thickness fluctuations induced by radial intrinsic resistivity variations in the Si wafer. It was demonstrated that using low temperature anodisation, the structure quality, regarding both interface smoothness and refractive index difference, can be drastically improved leading to an amplification factor as high as 7000 in the NIR. Such factor is in the order of magnitude of optical absorption losses. Besides resonant structures, the fabrication of tuneable omnidirectionnal mirrors has been experimentally and theoretically demonstrated. These results in addition to already reported devices and structures, confirm the versatility of the porous silicon approach towards Si based integrated photonic devices.

REFERENCES

[1] G. Vincent, Appl.Phys.Lett. **64**, 2367 (1994) M. G. Berger, S. Frohnhoff, W. Theiss, U. Rossow, H. Muender, *Porous silicon science and technology*, ISBN 3-540-58936-8, Springer p. 345 (1994)
[2] S. Chan and P. M. Fauchet *Appl. Phys. Lett.* Vol 75(2) pp. 274-276 (1999).
[3] J. Diener, N. Künzner, D. Kovalev, E. Gross, V. Yu. Timoshenko, G. Polisski, and F. Koch *Appl. Phys. Lett.* Vol 78(24) pp. 3887-3889 (2001)
[5] G. Lérondel, R. Romestain, S. Barret, *J. Appl. Phys.* **81** (9), p6171 (1997)
[6] S. Setzu, G. Lérondel, R. Romestain, *J. Appl. Phys.* **84,** p3129 (1998)
[7] P. J. Reece, G. Lérondel W. H. Zheng and M. Gal, *Appl. Phys. Lett.* **81**, 4895 (2002).
[8] A. Bruyant, G. Lérondel, P. J. Reece and M. Gal, *Appl. Phys. Lett.* **82**, 4895 (2003)
[9] M.C. Chan, S. K. So, K. W. Cheah *J. Appl. Phys.*79, p3273 (1996).
[10] Y. Fink, J. N. Winn, S. Fan, C. Chen, J. Michel, J. D. Joannopoulos, and E. L. Thomas, *Science* **282**, 1679 (1998).

Optical devices based on anisotropically nanostructured silicon

J. Diener, N. Künzner, E. Gross and D. Kovalev
Technische Universitäat München, Physik-Department E16, D-85747 Garching, Germany

M. Fujii
Department of Electrical and Electronics Engineering, Faculty of Engineering, Kobe University,
Rokkodai, Nada, Kobe 657-8501, Japan

Abstract

Anisotropic nanostructuring of bulk silicon (Si) leads to a significant optical anisotropy of single porous silicon (PSi) layers. A variation of the etching current in time allows a controlled modification of the porosity along the growth direction and therefore a three-dimensional variation of the refractive index (in plane an in depth). This technique can be important for photonic applications since it is the basis of a development of a variety of novel, polarization sensitive, silicon-based optical devices: retarders, dichroic Bragg Reflectors, dichroic microcavities and Si based polarizers.

Introduction

Silicon (Si) is the basis for the majority of integrated electronic devices. However, a key limitation of its application for active and passive optical devices stems from its indirect band gap and highly isotropic cubic lattice structure. However, recently it has been realized that nanostructuring of semiconductors is an alternative approach to create artificial materials exhibiting specific properties, particularly optical ones.

To obtain a Si-based material which is sensitive to the polarization state of light it is necessary to reduce the cubic symmetry of bulk Si. This can be achieved by the concept of anisotropic dielectric nanostructuring. The simplest approach based on "drilling" holes in semiconductors is proved to be an effective strategy for a variety of applications. Important novel structures based on this concept have already been realized [1]. For instance periodic arrays of "holes" result in two-dimensional photonic crystal properties of the structure. However, not all photonic applications require a strictly ordered distribution of holes.
A quasiuniform distribution will be sufficient for optical applications if the dimensions of both holes and skeleton fragments are much smaller than the wavelength of the propagating light. These conditions are fullfilled for PSi layers and light propagates in the optically homogeneous medium without significant internal scattering. The random spatial distribution of holes implies simply a reduced refractive index of the layers. Its value is defined by the fraction of the empty space inside of the layers and well described by treating PSi as an effective dielectric medium. A preferential alignment of holes and Si fragments results in a strong polarization anisotropy of the refractive index.
The simplest approach leading to dielectric nanostructuring of Si is electrochemical etching of bulk silicon substrates. Anodic etching of bulk Si in hydrofluoric acid results in a sponge-like network of interconnected Si nanowires having sizes dependent on the doping level of the Si

substrate, the etching current density and the concentration of the etching solution used. Within a bulk Si crystal the etching rate and therefore the alignment of pores and remnant silicon fragments depends on the crystallographic direction. Transmission electron microscopy (TEM) studies show that during the etching process pores propagate preferentially in equivalent <100> crystallographic directions independent on the substrate orientation [2].

The Si fragments remaining after the etching process are aligned along the same crystallographic directions. For (100) oriented substrates this results in a preferential direction of the pores and remnant Si perpendicular to the wafer surface.

This results in a dielectric constant which is largest for light polarized along this direction. However, for most of practical applications an in-plane birefringence is required. The fundamental idea to achieve in-plane birefringence is to employ the crystallographic selectivity of the etching process for the nanostructuring of (110) Si wafers. For (110) oriented Si substrates the pore propagation along the [010] and [100] crystallographic direction results in an alignment of the remnant silicon fragments tilted with respect to the (110) surface plane (schematically depicted on the left side of Fig.1).
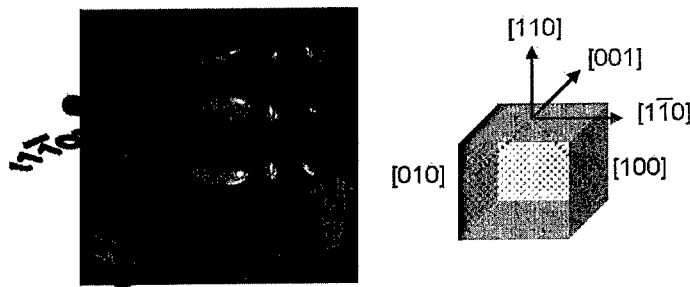
Fig. 1: Right side: crystallographic frame used for PSi produced from [110] oriented Si substrate (for convenience called (110) PSi)
Left side: scheme of the orientation of the remnant Si fragments in (110) PSi (top view)

This reduces the symmetry of the system from isotropic cubic to in-plane uniaxial. For this anisotropic nanostructure the dielectric constant and consequently the refractive index depend on the polarization of an applied electric field due to different internal screening by induced polarization charges. As a result the refractive indices differ for the components polarized along the two main axes in the (110) surface plane [3] ($n_{[1\bar{1}0]} \neq n_{[001]}$, subscripts indicate the polarization direction of the incident light, the coordinate frame used is shown on the right side of Fig.1).

Experimental details

For studying the optical properties of (110) porous Si layers/multilayers a set of different porous Si layers has been prepared according to a standard procedure [2]. We used B-doped wafers with resistivities of 1 m $\cdot$cm, 50 m $\cdot$cm and 5 $\cdot$cm [4]. The etching solution was a 1:1 by volume mixture of HF (49 wt. %) and ethanol. To vary the porosity of the layers (and therefore their mean refractive indices) the etching current density has been chosen between 20 and 75 mA/cm^2. The multilayer structures (Bragg reflectors, microcavities and polarizers) have been produced by electrochemical etching (in the dark) of (110) oriented p$^+$ (Boron doped) 1.5 m $\cdot$cm Si wafers. The etching solution was a 1:1 (by volume) mixture of C$_2$H$_5$OH and concentrated aqueous HF (50%). Under preparation of stacks two current densities were used: 22 mA/cm^2 (=J$_1$) and 70 mA/cm^2 (=J$_2$). To characterize the optical parameters of layers the separate layers etched with J$_1$ and J$_2$ have been produced. Multilayer structures were processed by alternating high and low current density (10 repetitions of a J$_1$-J$_2$ cycle). White light of a 100 W halogen lamp was dispersed with a monochromator, polarized with a Glann-Thompson prism and directed onto the sample. The reflected light was detected at small angle ~1^0 with respect to normal to the surface with a Si- or Ge photodiode. For transmittance measurements normal incidence has been used. Spectra are normalized to the reflectivity of bulk Si.

Results and Discussion

The left side of Fig. 2 shows a high resolution (HR) TEM image of the anisotropic morphology of a porous Si layer prepared from a 1 m $\cdot$cm (110) Si wafer. The magnification factor is 10^5. The macroscopical alignment of the pores (bright field) and Si nanowires (dark field) along the $[1\bar{1}0]$ crystallographic direction is evident. HRTEM images with higher resolution show the alignment of single wires along $[1\bar{1}0]$ direction and their regular diamond lattice structure. This assures the preferential alignment of the Si wire-like structure along the $[1\bar{1}0]$ crystallographic direction as schematically shown in Fig.1. Consequently the value of the refractive index depends on the angle between the crystallographic axes and the polarization direction of normally incident light. From the right side of Fig. 2 the uniaxial symmetry of the refractive index is evident, the largest value is for the light polarized in the $[1\bar{1}0]$ crystallographic direction (direction of wires alignment). Thus the layer is a negative uniaxial crystal. The measured level of in-plane birefringence ($\Delta n = n_{[1\bar{1}0]} - n_{[001]}$ is 0.22) what is larger than that one found in natural crystals (Calcite and Rutile). We note that one of the unique properties of birefringent PSi layers is an almost unlimited spectral range of optical action. Indeed, because bulk Si is not polar material and interaction of light with phonons is inefficient, contrary to other birefringent crystals these layers are transparent over entire optical range from visible to far-infrared. Therefore our layers can act as an efficient controllers of the polarization state of transmitted light for the entire spectral range from near- to far-infrared.

Optical retarders

To demonstrate the capability of our layers to be efficient controllers of the polarisation state of light the thickness of layers was intentionally chosen to achieve desired retardation values (λ/4 and λ/2 conditions) in the transparency range of optical communication lines [5]. Fig. 3 (left side)

shows how linearly polarized incident light having wavelength 1.53 μm transforms into circularly polarized light. Respectively the right side shows how a λ/2 retardation condition can be achieved at λ=1.3 μm. The analysis of the angular polarization pattern of the transmitted light shows a high retardation accuracy: the deviation from the ideal circularly or linearly polarized light is on the order of 0.1 % for λ/4 and λ/2 plates conditions what is in fact an experimental accuracy (see Fig. 3). This accuracy is comparable or even better than that of standard retardation plates produced from crystalline quartz.
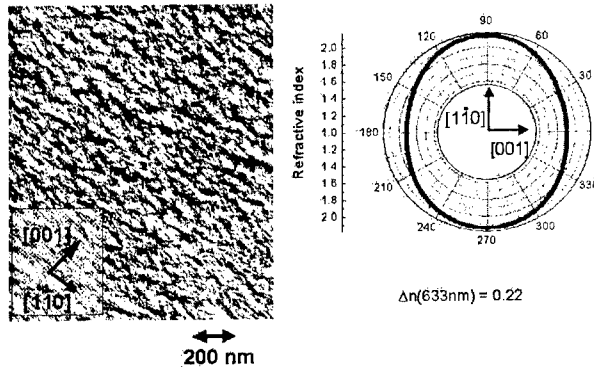
Fig.2: Left side: HR TEM image of the surface of a highly doped (110) porous Si layer
Right side: Polar plot of the refractive index value versus the polarization direction of the incident light. λ_{light}=633 nm.
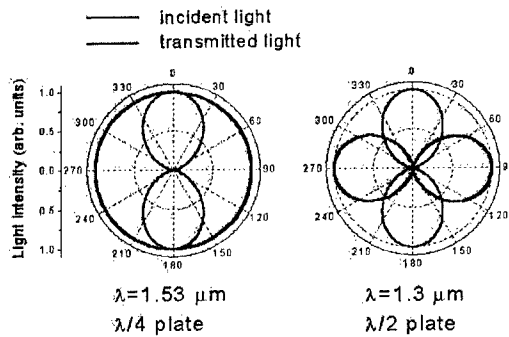
Fig. 3: Polar plots of the intensity of incident (dashed lines) and transmitted (solid lines) light as a function of the angle of the analyzing polarizer. Measurements are performed at λ/4 (left side) and λ/2 (right side) retardation values.

As mentioned before, alternative PSi layers having certain refractive indices exhibit additionally in-depth variation of their refractive index. Each layer additionally has in-plane optical anisotropy and, therefore, a stack of layers, acting as a distributed Bragg-reflector/microcavity, should have two spectrally distinct reflection/transmission bands, depending on the polarization direction of the incident linearly polarized light. This effect is governed by a 3-dimensional (in-plane and in-depth) variation of the refractive index. These structures can yield optical effects which are difficult to achieve with conventional Bragg reflectors/microcavities.

Dichroic Bragg reflectors/microcavities

A distributed Bragg reflector (DBR) is characterized by a high reflectivity band with the Bragg wavelength λ_{Bragg} approximately in its center. λ_{Bragg} depends on the thickness of the layers (d_1, d_2) and the corresponding refractive indices (n_1, n_2). The m order of the Bragg peak is given by: $m\lambda_{Bragg} = 2 (d_1 n_1 + d_2 n_2)$. The left side of Fig. 4 shows the reflectivity of a polarization sensitive DBR at almost normal incidence. Contrary to standard porous silicon DBRs the spectral position of λ_{Bragg} depends on the polarization direction of the incident light [6]. For E parallel to [001] (dashed line) the first order λ_{Bragg} appears around 1060nm but is significantly shifted towards longer wavelength (~ 1170 nm) for E parallel to $[1\bar{1}0]$ crystallographic direction (solid line). In a similar manner dichroic polarization-sensitive optical microcavities have been produced [7]. A microcavity consists of a $\lambda/2$ layer placed between two distributed Bragg reflectors made from pairs of alternating $\lambda/4$ layers of high and low refractive indices. The interference of the reflected waves of the two DBR`s leads to a transmission maximum within a spectral region of high reflection (stop band). Fig. 4 shows on the right side the transmission of a freestanding microcavity based on (110) PSi layers. For both polarization directions a sharp cavity mode approximately in the center of the stop band can be observed.
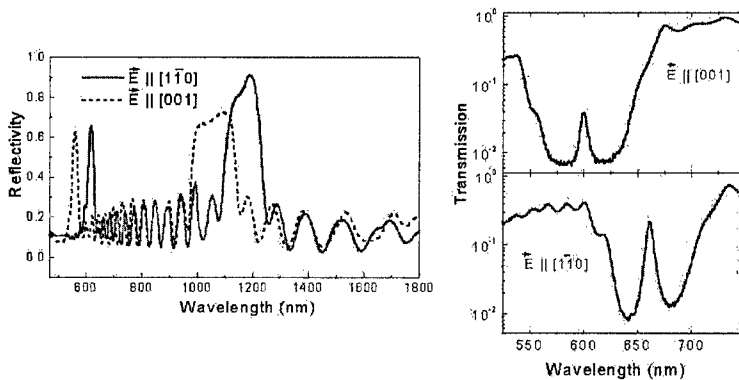
Fig. 4: Left side: Spectrally and polarization-resolved reflection of a (110) distributed
       Bragg reflector.
       Right side: Polarization-resolved optical transmission spectra of a freestanding
       (110) porous silicon microcavity.

25

Planar silicon-based light polarizers

By combining in one structure a dichroic reflector with a second one or a microcavity having different spectral responses planar polarizers can be realized [8].
The left part of Fig.5 sketches the operation principle of this device. An additional dichroic Bragg reflector having a polarized reflection band shown by the upper line in the sketch of Fig. 2 has been added on top of a dichroic microcavity. Its reflection band for light polarized along the [001] direction has been tuned to cover the spectral range of the transmittance band of the microcavity for light polarized along the perpendicular direction. For this specific spectral range light polarized along the [001] direction is reflected by the reflector. Light polarized along the [1$\bar{1}$0] direction passes the whole structure at the spectral position of the cavity mode. Therefore this dielectric stack acts as a narrow spectral band polarizer.
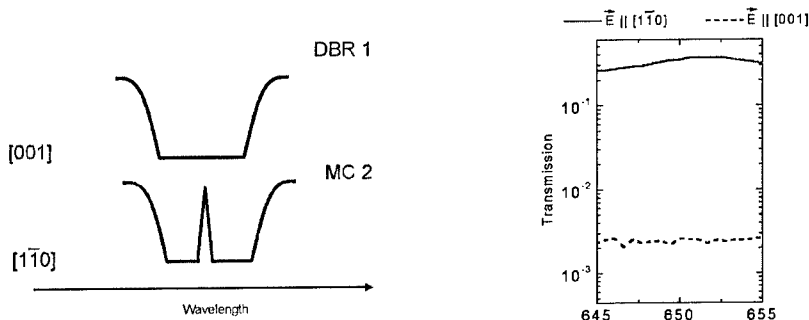
Fig. 5: Left side: Sketch of the operation principle of a Si-based polarizer
(combination of reflector and microcavity).
Right Side: Polarization-resolved transmission spectra of the device

Conclusions

The presented silicon-based optical devices are fabricated following the concept of anisotropic dielectric nanostructuring of bulk silicon. They are all based on artificially created highly birefringent porous silicon layers produced by anodic etching of (110) oriented Si wafers. The major advantage of this silicon based system is that the formation process is simple and well controlled. Therefore it opens new and cheap design freedom for various types of optical devices.

Referenzes

[1] J. Schilling, F. Müller, S. Matthias, R.B. Wehrspohn, U. Gösele, and K. Busch, Appl. Phys. Lett. **78**, 1180 (2001)
[2] A. G. Cullis, L. T. Canham and P. D. J. Calcott, J. Appl. Phys. **82**, 909 (1997)
[3] N. Künzner, D. Kovalev, J. Diener, E. Gross, V. Yu. Timoshenko, G. Polisski, F. Koch and M. Fujii
   Optics Letters **26**, 1265 (2001)
[4] D. Kovalev, G. Polisski, J. Diener, H. Heckler, N. Künzner, V. Yu. Timoshenko, F. Koch, Appl. Phys. Lett. **78**, 916 (2001)
[5] D. Kovalev, G. Polisski, J. Diener, H. Heckler, N. Künzner, F. Koch Phys. Stat. Sol.(a) **180**, r8-r11 (2000)
[6] J. Diener, N. Künzner, D. Kovalev, E. Gross, V. Yu. Timoshenko, G. Polisski and F. Koch,
   Appl. Phys. Lett. 78, 3887 (2001)
[7] J. Diener, N. Künzner, D. Kovalev, E. Gross, F. Koch, J. of Appl. Phys. **91**, 6704 (2002)
[8] J. Diener, N. Künzner, E. Gross, D. Kovalev, M. Fujii, Optics Letters accepted for publication

W1.9

Silicon Micro-Photonic Structure for Ultra-Sensitive Biosensing

Bradley Schmidt, Vilson Almeida, Christina Manolatou, Stefan Preble, Michal Lipson
School of Electrical and Computer Engineering, Cornell University
Ithaca, NY 14853, USA

ABSTRACT

We demonstrate a micron-size planar silicon photonic device that is able to detect low concentrations of metal nano-particles approaching single particle detection. This sensitivity is achieved by using strong light confining structures that enhance the extinction cross-section of metal nano-particles by orders of magnitude. Structures were fabricated and measurements of the transmission spectra of the devices demonstrate the detection of 10 nm diameter gold particles resting on the device with a density of fewer than 2 particles per 10^4 nm^2 (the area of the sensing region surface). Using such a device, in a fluidic platform, one could detect the presence of a single metal nano-particle specifically bound to various analytes, enabling ultra-sensitive detection of analytes including DNA, RNA, proteins, and antigens.

INTRODUCTION

There is a growing need for the development of environmental, health safety, and clinical microfabricated biosensors for many analytes such as DNA, RNA, proteins, antigens, and other bio-molecules, which allow for lower cost, smaller sample volumes, massive parallelism and ultra high sensitivity [1],[2],[3]. Many current systems for ultra sensitive bio-detection [4], [5], [6] are either complex, large, or lack the desired level of sensitivity. The challenge of improving the sensitivity of integrated systems is due to the low cross-sections (emission or absorption) of the label molecules to which the analyte is often bound.

Photonic structures are able to control the confinement of light into specific locations so that the fields inside the structures are many orders of magnitude greater than the incident field launched into the structure. The spectral and transmission properties of these structures can be extremely dependent on any variation in index of refraction of the propagation medium. This strong dependence, in conjunction with the techniques of specific binding of biological molecules, makes photonics a very attractive approach for biosensing [7].

In this paper we report results demonstrating a high degree of sensitivity approaching single detection of nano-particles. This sensitivity is achieved by using strong light confining structures on a planar photonic chip that enhance the extinction cross-section by orders of magnitude of metal nano-particles used as analyte labels.

DEVICE STRUCTURE

We detect metal nano-particles by enhancing the extinction cross-section of the particles using a micro-cavity structure. The structure strongly confines light in a micro-cavity; precisely where the particle is located. Light in the cavity interacts with the nano-particle and enhances the extinction cross-section of the nano-particle by orders of magnitude. As a result,

the presence of a metal nano-particle with a diameter as small as 5 nm can be detected by measuring the decrease in transmission of light propagating through the photonic structure.

The structure is a modified cavity embedded in a one-dimensional photonic crystal. The one-dimensional photonic crystal [10] consists of a high index contrast silicon waveguide (450 nm wide, 250 nm in height) with holes filled with a lower index material (silicon dioxide with n=1.46) in the waveguide to create Bragg Reflectors on either side of the cavity. A schematic of the device is shown in Figure 1. Light propagating at the resonance wavelength of the cavity is highly confined within the structure, and the length of the cavity (880 nm) is chosen to allow a local maximum of the field at the center of the cavity.

In order to further increase the degree of light confinement in the cavity, another SiO_2 pillar (filled hole) is added to the cavity, much smaller than the other holes with a diameter of only 100 nm. The addition of this defect at the center of the cavity creates a local discontinuity in the field, increasing the strength of the field in the center of the cavity [11].
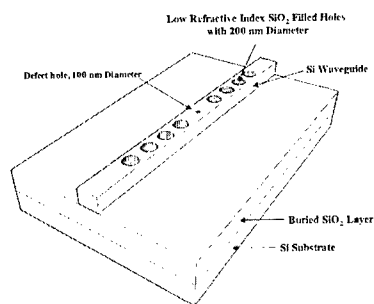
Figure 1: Schematic of photonic device. The length of the cavity from center of hole to hole is 880 nm. The period of the DBR holes center to center is 360 nm.

SIMULATION RESULTS

2-D Finite Difference Time Domain (FDTD) simulations of the structure were performed. The simulations demonstrate a strong field intensity (TE-like mode) at the center of the cavity as shown in Figure 2a. With the addition of the small low refractive index pillar in the center of the cavity, a local increase in the field is achieved, shown in Figure 2b. The peak intensity at the center of the cavity with the additional pillar is two times higher than in the same structure without the pillar. Not only is the magnitude of the field increased due to the presence of the hole, but also the quality factor Q of the device is higher (170.1 for the device with a low index pillar in the cavity vs. 111.5 for the device without the pillar).
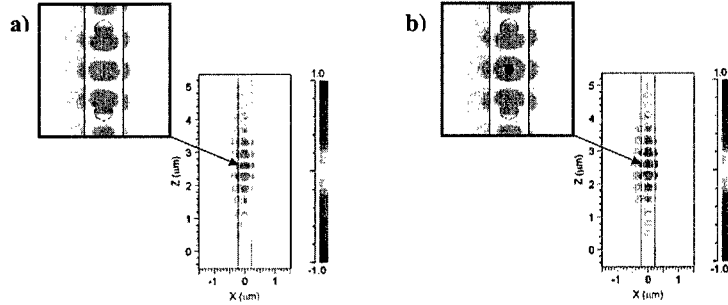
Figure 2: TE-like mode field profile of the field inside the micro-cavities a) without a defect at resonance wavelength = 1.5946 microns, b) with 100 nm diameter defect (n=1.46) at resonance wavelength = 1.5678 microns.

The "sensing region" is considered to be the area on top of the small central oxide pillar that is level with the top surface of the waveguide, as shown in Figure 3. In order to analyze the structure as a sensor we consider the presence of gold nano-particles assuming that they are bound to the sensing region. The top of the structure is assumed to be unclad and covered by water (n = 1.33, k=1.48x10^{-4}, at 25°C and a wavelength of 1550 nm).
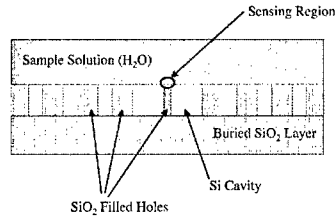
Figure 3: Cross-section of device showing the location of the sensing region at the top of the small central oxide pillar that rests within the cavity.

Gold particles are considered as a sensing probe due to their large extinction coefficient in the wavelength range of interest (1450-1600 nm) and their mature use as labels in biosensing systems [12]. We calculated the field distribution for several sizes of particles varying from 25 nm in diameter down to 2 nm in diameter. In all cases the absorption of the metal nano-particles is enhanced by the confinement of the field in the cavity. Using a waveguide with four period DBR's and 10 nm diameter gold particles placed at the center of the sensing region, a decrease in transmission intensity of 7-9 % per additional particle is observed. Similar results were achieved when the particles were randomly placed within the sensing region instead of just at the center, resulting in less than a 2% change in absorption losses. Since the difference in losses due to the random placement of the particle within the sensing region is much smaller than the loss due to the presence of the particle, it should be possible to resolve the number of particles bound to the sensing region despite their exact location within the region.

EXPERIMENTAL RESULTS

Fabrication

Sample devices were fabricated using Silicon on Insulator (SOI) wafers with 250 nm of crystalline silicon on top of a three microns thick buried oxide layer. The structure was defined using electron-beam lithography and etched by chlorine based reactive ion etching (RIE). A scanning electron microscope image of the unclad device is shown in figure 4. The holes were filled and the structure clad with SiO_2 using plasma enhanced chemical vapor deposition (PECVD).
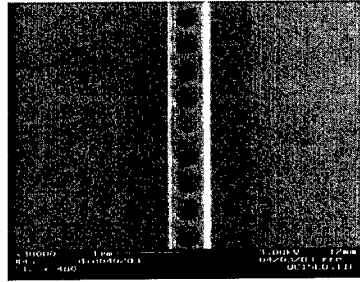
Figure 4: Scanning electron microscope image of fabricated device prior to PECVD deposition of silicon dioxide cladding.

Characterization of the Structure

The strong presence of the field inside the sensing region is demonstrated by measuring the spectral response of several devices, which all have the same dimensions except for varying sizes of the central oxide pillar. Figure 5 shows the measured spectral resonances of the micro-cavities.
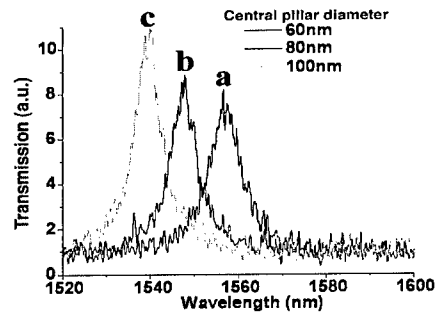
Figure 5: Spectral resonances of micro-cavities containing a central pillar in the cavity with diameters of a) 60 nm, b) 80 nm, and c) 100 nm.

These results show the strong dependence of the spectra due to the variation in size of the pillar in the micro-cavity, indicating that indeed the field is strongly confined within the low index pillar. The resonance shift and the spectral width variation due to the varying pillar diameters correspond to those predicted by FDTD calculations for a four period micro-cavity.

Nano-Particles Absorption

We measured the transmission losses due to the presence of gold metal nano-particles, using the same devices with a 100 nm diameter low index pillar in the cavity. The upper oxide cladding above the entire cavity was removed by patterning large holes using photolithography and etched using CHF_3 based RIE and HF wet chemistry. Once the cavities were exposed, the transmission through the devices was measured with water on top of the structures and various depositions of colloidal gold particles on top of the cavities. These depositions were achieved by placing small amounts of water-based solutions of 10 nm gold particles (1.9×10^{13} particles per ml) on top of the devices and allowing them to dry by evaporation. Each deposition step deposited approximately 1.2×10^2 particles per micron^2 on the entire structure, corresponding to approximately 2 ± 1 particles in the optical volume of the sensing region per additional deposition step. A clear decrease in transmission and shift in the resonance was observed with increasing number of particles, as shown in Figure 6. This demonstrates that the cavity senses an extremely small change in the number of particles in the sensing region.
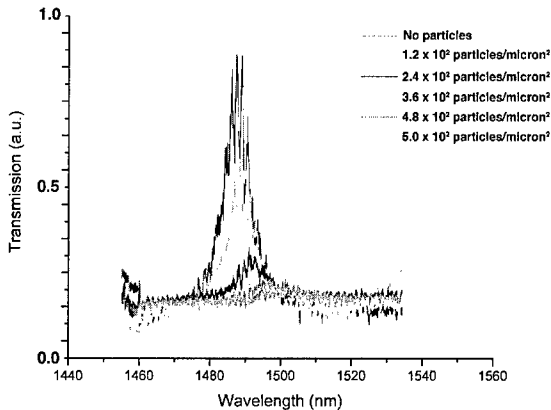
Figure 6: Transmission Spectra of TE mode from devices with 100 nm diameter low index pillar in cavity with various amounts of gold particles deposited on surface.

CONCLUSION

We have demonstrated a planar integrated micron-size photonic device that enables sensing of a discrete number of metal nano-particles. Using such a device, in a fluidic platform, one could detect the presence of a single metal nano-particle specifically bound to various analytes, enabling ultra sensitive detection of analytes including DNA, RNA, proteins, and antigens.

REFERENCES

1. Lotien Richard Huang, Jonas O. Tegenfeldt, Jessica J. Kraeft, James C. Sturm, Robert H. Austin, Edward C. Cox, "A DNA prism for high-speed continuous fractionation of large DNA molecules", *Nature Biotechnology*, **20**, 1048-1051 (2002).
2. Jason R. Epstein, Amy P. K. Leung, Kyong-Hoon Lee and David R. Walt, "High-density, microsphere-based fiber optic DNA microarrays", *Biosensors and Bioelectronics*, **18**, 541-546 (2003).
3. Guanghua Wu, Ram H. Datar, Karolyn M. Hansen, Thomas Thundat, Richard J. Cote, Arun Majumdar, "Bioassay of prostate-specific antigen (PSA) using microcantilevers", *Nature Biotechnology*, **19**, 856-860 (2001).
4. A. J. Haes, R. P. Van Duyne, "A Nanoscale Optical Biosensor: Sensitivity and Selectivity of an Approach Based on the Localized Surface Plasmon Resonance Spectroscopy of Triangular Silver Nanoparticles", *J. Am. Chem. Soc.*, **124**, 10596-10604 (2002).
5. S. Nie, R. Emory, "Probing Single Molecules and Single Nanoparticles by Surface-Enhanced Raman Scattering", *Science*, **275**, 1102-1106 (1997).
6. V. S.-Y. Lin, K. Moteshari, K.-P. S. Dancil, M. J. Sailor, M. R. Ghadiri, "A Porous Silicon-based Optical Interferometric Biosensor", *Science*, **278**, 840-843 (1997).
7. A. Brecht, G. Gauglitz, "Optical probes and transducers", *Biosensors and Bioelectronics*, **10**, 923-936 (1995).
8. J. Vörös, J.J. Ramsden, G. Csúcs, I. Szendro, S.M. De Paul, M. Textor, N. D. Spencer, "Optical grating coupler biosensors", *Biomaterials*, **23**, 3699-3710 (2002).
9. R. W. Boyd, J. E. Heebner, "Sensitive disk resonator photonic biosensor", *Applied Optics*, **40**, 5742-5747 (2001).
10. J. S. Foresi, P. R. Villeneuve, J. Ferrera, E. R. Thoen, G. Steinmeyer, S. Fan, J. D., Joannopoulos, L. C. Kimerling, H. I. Smith, E. P. Ippen, "Photonic-bandgap microcavities in optical waveguides", *Nature*, **390**, 143-145 (1997).
11. Vilson Almeida, Qianfan Xu, Roberto Panepucci, Carlos Barrios, Michal Lipson, "Light Guiding in Low Index Materials using High-Index-Contrast Waveguides", MRS Fall Meeting 2003 Proceedings.
12. I. Alexandre, S. Hamels, S. Dufour, J. Collet, N. Zammatteo, F. De Longueville, J.L. Gala, J. Remacle, "Colorimetric silver detection of DNA microarrays", Analytical Biochemistry, **295**, 1-8 (2001).

Second- and third-harmonic generation spectroscopy of coupled microcavities formed from all-silicon photonic crystals

D.G. Gusev, I.V. Soboleva, M.G. Martemyanov, T.V. Dolgova, A.A. Fedyanin, O.A. Aktsipetrov
Department of Physics, Moscow State University, 119992 Moscow, Russia

ABSTRACT

The enhancement of second- and third-harmonic generation (SHG and THG) in all-silicon coupled microcavities (CMC) formed from mesoporous silicon photonic crystals are observed at the resonance of the fundamental radiation with the CMC eigenmodes. Angular splitting of the peaks in intensity spectra of SHG and THG shows monotonous dependence on magnitude of coupling between two identical microcavity spacers controlled by the reflectivity of the intermediate Bragg reflector.

INTRODUCTION

Nonlinear optics of photonic band gap (PBG) materials: photonic crystals and photonic-crystal microcavities stands out as one of the prospective areas of modern optics both from fundamental and applied viewpoints. Coupled photonic-crystal microcavities [1] (CMC) are formed from photonic crystal with several spacers. One-dimensional photonic crystal with two identical spacers is the simplest structure of CMC [2]. Such coupled microcavities have two eigenmodes, which are symmetric and antisymmetric ones. Their transmission or reflection spectra have two resonant features in PBG, which are split spectrally because of the electromagnetic coupling between spacers. The coupling is defined by transmittance of intermediate photonic crystal. Inside the spacers, the amplitude of the optical wave resonant to one of the CMC modes is increased strongly that should leads to the resonant enhancement of the nonlinear-optical response, such as second- and third-harmonic generation (SHG and THG). The strong spatial localization of the resonant optical field inside coupled microcavities results in narrowing and tuning of photoluminescence [3] in CMC fabricated from porous silicon. However, SHG has not been observed in CMC up to now, while strong manifestation of the optical coupling between spacers is expected in the SHG response.
Mesoporous silicon is a promising material for fabrication of PBG structures. The possibility of controllable variation of the pore size in the interval from approximately 10 nm till 50 nm and the well-defined arrangement of the pores open the wide prospects for fabrication of all-silicon-based nano- and microstructures. Examples are photonic band gap materials such as photonic crystals, quasi-crystals and microcavities. Photonic crystals formed from mesoporous silicon are grown by the electrochemical etching of silicon by means of periodic variation of chemical reaction parameters during the etching process [4]. The strong spatial localization of the resonant optical field inside porous silicon microcavities, directly probed by near-field optical scanning microscopy [5], results in the manifold enhancement of Raman scattering [6], and giant second [5, 7] and third-harmonic [8] generation. Very recently, the fabrication of high-quality-factor CMC composed from multiple-spacers has been reported [9, 10]. In this paper, the enhancement of SHG and THG in one-dimensional coupled photonic-crystal microcavities formed from

mesoporous silicon is studied. The peaks in the angular spectra of the second-harmonic (SH) and third-harmonic (TH) intensities are correlated with angular positions of the split CMC modes and caused by the combination of the resonant enhancement of the fundamental radiation and constructive interference of the second-harmonic fields induced in the microcavity spacers. The shape of the SHG resonances and THG peaks is shown to be dependent on the variation of the electromagnetic coupling between the microcavity spacers, which is controlled by the reflectivity of the intermediate distributed Bragg reflector.

EXPERIMENTAL

The set of one-dimensional CMC is fabricated using technique described in Ref.[4] by the electrochemical etching of the p-type Si(100) wafers with resistivity of 0.005Ohm·cm in electrolyte containing 15% of fluoric acid, 27% of water and 58% of ethanol. After removing the native oxide, the silicon wafer fits in the electrochemical cell and its backside is tightly clamped to a flat copper cathode. The platinum spiral anode is immersed into electrolyte. The density of current, flowing through the wafer, defines the porosity of the etching porous silicon layer. The layer thickness is controlled by etching time. Since the silicon etching process is self-limited and the porous silicon layer once etched is excluded from the subsequent etching [4], the profile "current density - time" transforms into the profile "porosity (refractive index) - thickness". Schematic view of all-silicon CMC is shown in Figure 1.
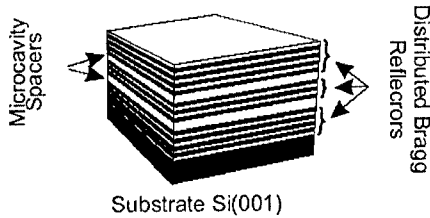
Figure 1. Schematic of the porous silicon coupled microcavities.

The CMC samples consist of three one-dimensional photonic crystals, separated by two identical $\lambda_0/2$-thick spacers with corresponding wavelength of $\lambda_0 = 1200$ nm. External Bragg reflectors are formed from four pairs of $\lambda_0/4$-thick layers of porous silicon. The number of layers in the intermediate Bragg reflector (IBR), N, is changed in series from three to nine. Porous silicon layers with high refractive index are etched with the current density of 25mA/cm^2 during 7.2 sec, the layers with low refractive index are formed during the 3.6 sec-etching with the current density of 83mA/cm^2. Refractive indices of the porous silicon layers are found from the calibration reflection spectra of the single porous silicon layers. Porosities of layers are calculated using effective medium approximation. Layers with high refractive index have $n_H = 1.78$ and porosity of $f_H = 0.64$, and layers with low refractive index have $n_L = 1.42$ and $f_L = 0.77$. Refractive index of spacers is n_L. The wave vector domain SHG spectroscopy is performed by tuning the angle of incidence, θ, of the 1064 nm s-polarized output of 10 ns-YAG:Nd^{3+} laser with energy of approximately 10mJ per pulse and spot diameter of 1 mm. The goniometer provides the rotation of the sample and the detection system in the range of angles of incidence from 15° to 80°. The radiation reflected from the CMC sample passes through color and interference filters

extracting the SH radiation and a Glan prism separating the p-polarized SH wave. The SHG signal is detected by a photomultiplier tube and a gated electronics. The angular spectrum of the linear reflection coefficient is measured in the identical alignment.

RESULTS AND DISCUSSION

The linear reflection spectrum of the porous silicon CMC is shown in Figure 2. The spectrum has a plateau with high reflectivity, corresponding to the PBG, and two resonant dips at approximately 730 and 780 nm, corresponding to the split CMC modes.
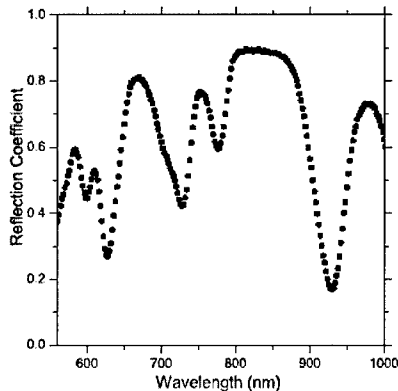
Figure 2. The reflection spectrum of the porous silicon CMC sample with $\lambda_0 = 800$ nm and $N = 5$ measured for 45° angle of incidence of s-polarized wave.

Figure 3 shows the angular spectra of linear reflection, SH intensity and TH intensity measured at the series of porous silicon CMC with different reflectivity of the intermediate Bragg reflector. The linear spectra have two dips, where reflection coefficient value decreases up to 0.2, corresponding to the resonance of the fundamental radiation with the CMC modes. In the other parts of spectra, reflection coefficient reaches the values up to 0.85 that corresponds to the PBG. For all CMC samples, the right dip in the spectra related to the long-wavelengthmode of CMC is smaller than the left one that can be attributed to the monotonous decrease of optical thickness of porous silicon layers with the depth. Angular spectra of the SH and TH intensities have resonant features in the range of θ from 20° to 70°. Angular positions of the SHG and THG peaks correlate with the CMC mode positions defined from the reflection spectra of fundamental radiation. However, they are slightly shifted from positions of dips of linear reflection coefficient and located mostly on their external slopes. The increase of the SH intensity is up to two orders of magnitude in comparison with the SHG signal in the PBG. The enhancement of the TH intensity is larger and reaches values up to three orders of magnitude in comparison with the THG signal in the PBG. For all CMC samples, the amplitude of the SHG peak at the long-wavelength mode exceed the SHG enhancement in the peak at the short-wavelength mode of CMC. The values of full width at half maximum (FWHM) of the long-wavelength SHG peaks strongly increase with the R decrease from approximately 9° for CMC with $N = 9$ to 16° for the sample with $N = 3$. Additional arise of the SH intensity at approximately 65° is observed in the SHG spectra of the CMC samples with $N = 7$ and $N = 9$. The angular splitting of dips in

reflection spectra and SHG peaks decreases gradually with the increase of the IBR reflectivity that characterizes the reduction of the coupling between microcavities. The observed enhancement of SHG and THG is caused by the increase of the amplitude of the resonant fundamental field inside CMC. The spatial distributions of the field strength along the periodicity direction calculated for CMC using transfer matrices show that for used parameters of CMC the fundamental field amplitude inside the spacers is approximately threefold enhanced in comparison with that of the incident wave. Since fundamental field localization inside the microcavity spacers is maximal at the resonance with the CMC modes, the angular positions of the SHG and THG peaks are located nearby the dips of the linear reflection spectra. The fundamental field is enhanced both in spacers and in surrounding layers of Bragg reflectors, and the nonlinear sources contributed to SHG and THG are extended over the micron-size distance. Thus the magnitude and shape of the SHG and THG peaks are influent significantly by interference of the partial contributions to the total outgoing SH and TH fields from various layers of CMC. The phases of these partial SH and TH fields, calculated within the nonlinear transfer-matrix formalism [11, 12], depend essentially on the spectral position of CMC modes governed by refractive indices and thicknesses of porous silicon layers. It is shown that destructive interference of the SHG partial contributions results in the splitting of the SHG peaks at the long-wavelength mode for the sample with $N = 7$ and $N = 9$ and in the changes of their amplitudes. Interference effects define also the spectral shift of the SHG resonances from the dip minima of the linear reflection spectra.

Angle of Incidence (deg.)
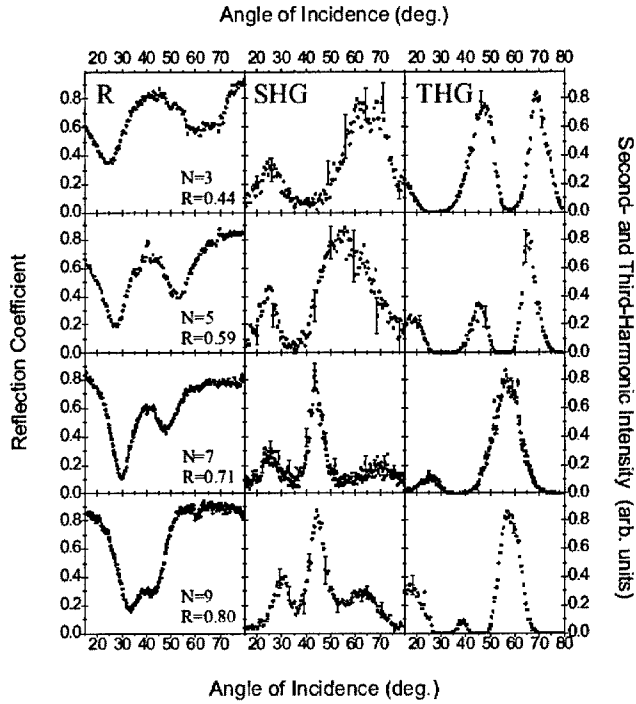
Figure 3. Angular spectra of TH intensity (right panels), SH intensity (middle panels) and linear reflection coefficient (left panels) of porous silicon CMC with λ_0 =1200 nm and different reflection coefficient of IBR, R.

CONCLUSIONS

In conclusion, the enhancement of second- and third-harmonic generation from the coupled microcavities based on the all-silicon photonic crystals is studied. The enhancement of SH and TH intensities is observed in the vicinity of the resonance of the fundamental radiation with the CMC eigenmodes. Angular splitting of the peaks in SHG and THG spectra shows monotonous dependence on magnitude of coupling between two identical microcavity spacers controlled by the reflectivity of the intermediate Bragg reflector. The basic mechanism of the enhancement is localization of the fundamental field inside the spacers, which leads to the increase of the amplitudes of the SH and TH fields induced inside them.

ACKNOWLEDGEMENTS

REFERENCES

1. M. Bayindir, C. Kural, and E. Ozbay, *J. Opt. A* **3**, pp. S184–S189, 2001.
2. R. Stanley, R. Houdre, U. Oesterle, M. Ilegems, and C. Weisbuch, *Appl. Phys. Lett.* **65**, pp. 2093–2095, 1994.
3. L. Pavesi, G. Panzarini, and L. C. Andreani, *Phys. Rev. B* **58**, pp. 15794–15800, 1998.
4. O. Bisi, S. Ossicini, and L. Pavesi, *Surf. Sci. Rep.* **38**, pp. 1–126, 2000.
5. T. V. Dolgova, A .I. Maidykovski,M. G. Martemyanov, A . A . Fedyanin, O. A .Aktsipetrov, G. Marowsky, V.A.Yakovlev, and G. Mattei, *Appl. Phys. Lett.* **81**, pp. 2725–2727, 2002.
6. L. A. Kuzik, V. Yakovlev, and G. Mattei, *Appl. Phys. Lett.* **75**, pp. 1830–1832, 1999.
7. T. V. Dolgova, A. I. Maidikovsky, M. G. Martemyanov, G. Marowsky, G. Mattei, D. Schuhmacher, V. A. Yakovlev, A . A . F edyanin, and O. A . A k tsipetrov, *JETP Lett.* **73**, pp. 6–9, 2001.
8. T. V. Dolgova, A. I. Maidikovsky, M. G. Martemyanov, A. A. Fedyanin, and O. A. Aktsipetrov, *JETP Lett.* **75**, pp. 15–19, 2002.
9. M. Ghulinyan, C. J. Oton, Z. Gaburro, P. Bettotti, and L. Pavesi, *Appl. Phys. Lett.* **82**, pp. 1550–1552, 2003.
10. M. Ghulinyan, C. J. Oton, G. Bonetti, Z. Gaburro, and L. Pavesi, *J. Appl. Phys.* **93**, pp. 9724–9729, 2003.
11. D. S. Bethune, *J. Opt. Soc. Am. B* **6**, pp. 910–916, 1989.
12. T.V.Dolgova, A . I. Maidykovski,M. G.Martemyanov, A . A . Fedyanin,O. A . A ktsipetrov,D. Schuhmacher, G. Marowsky, V.A.Yakovlev, G. Mattei, N. Ohta, and S. Nakabayashi, *J. Opt. Soc. Am. B* **19**, pp. 2129–2140, 2002.

Photonic Quasiperiodic Multilayers of Porous Silicon

R. Nava, J. A. del Río[1], J.C. Alonso, and C. Wang
Instituto de Investigaciones en Materiales, UNAM, A.P. 70-360, 04510, México D.F., MEXICO
[1]Centro de Investigación en Energía, UNAM, A.P. 34, 62580 Temixco, Mor., MEXICO

ABSTRACT

Porous silicon is an efficient photo- and electro-luminescence material and represents a promising candidate for opto-electronic applications. In the last years, porous silicon multilayers with a high enough refractive index contrast have been obtained. In this work, we study the light transmission in Fibonacci multilayers made of porous silicon. The theoretical reflectance spectra are compared with experimental data, observing a good agreement, even though they are extremely fragile when the number of quasiperiodic layers increases. The photoluminescence spectra show evidences of the quasiperiodic structure and in particular, the observed enhancement in comparison with that of single porous silicon layer could be due to the quasiperiodicity.

INTRODUCTION

Photonic crystals have the ability to control propagation of light by means of multiple scattering of photons leading to a band structure [1]. In particular, quasiperiodic multilayers possess a self-similar photonic band structure arisen from its peculiar long-range order [2, 3]. One of the most studied quasiperiodic structure is the Fibonacci sequence (F_j), which can be constructed by defining F_1=A, F_2=AB, and the addition rule, F_j=F_{j-1}⊕F_{j-2}, understood as the joining of sequences. Therefore, we have F_3=ABA, F_4=ABAAB, and so on. On the other hand, porous silicon (PS) is an interesting opto-electronic material, which can be tuned to give a large luminescence emission and high index contrast required by photonic applications, such as light-emitting diodes, optical filters, Bragg reflector, microcavities, etc. [4]. Recently, photonic quasiperiodic multilayers have been built with PS, observing mode beating and strong pulse stretching in the light transport through these systems, and a strongly suppressed group velocity for frequencies close to a Fibonacci band gap [5]. In this paper, we report the synthesis of PS luminescent multilayers and their reflectance data are compared with the theoretical calculations.

EXPERIMENTAL PROCEDURE

Two kinds of Fibonacci PS multilayers were built. The first samples has a high refractive index contrast without emission of light, and the second ones show photoluminescence. The PS layers are obtained by an anodic electrochemical dissolution of a crystalline silicon (c-Si) wafer in an aqueous HF/ethanol/glycerol electrolyte. Layers of different refractive index (porosity) are formed by alternating the density of electrical current between the wafer and the electrolyte. For the first kind of samples a p-type c-Si substrate with a resistivity of 0.001-0.005 Ω-cm is etched in the electrolyte with a ratio of 3:7:1 [6]. The electrical current density applied are J_A=3.7mA/cm² and J_B=37 mA/cm², producing refractive indices of 2.3 for layers A and 1.4 for layers B. The layer thickness is controlled by the etching time, being t_A=28 s and t_B=8 s,

corresponding approximately to 81 nm and 130 nm, respectively. These samples were thermally oxidized in an oxygen atmosphere at 300°C during 10 minutes. As the multilayer structure is formed on a c-Si substrate and then we measured its reflectance instead of the transmittance. For the luminescent multilayers, a p-type c-Si substrate with a resistivity of 10 Ω-cm is etched in an electrolyte with a ratio of 7:7:1. A current of 3.7 mA/cm^2 is applied to produce the high refractive index and 51.8 mA/cm^2 for the low refractive index layers. The etching time in this case are t_A=39 s and t_B= 3 s. These samples were dried with pentane in order to avoid fracture [7].

THEORETICAL CALCULATIONS

Based on the transfer matrix theory [8], the light propagation through the entire multilayer can be described by a transfer matrix (M). This matrix is the product of the matrices $T_{n-1|n}$ and T_n, representing respectively the transmission across the interfaces of layers n-1 and n,

$$T_{n-1|n} = \begin{pmatrix} 1 & 0 \\ 0 & \dfrac{\eta_n \cos\theta_n}{\eta_{n-1}\cos\theta_{n-1}} \end{pmatrix} \qquad (1)$$

and that inside each layer

$$T_n = \begin{pmatrix} \cos\delta_n & -\sin\delta_n \\ \sin\delta_n & \cos\delta_n \end{pmatrix}, \qquad (2)$$

where $\delta_n = k\eta_n d_n/\cos\theta_n$, being θ_n the incidence angle, k the wave vector in vacuum, d_n and η_n the thickness and the refractive index of layer n, respectively.

The general expression of the reflectance (R) can be written as

$$R = \frac{|M| - 2\det(M)}{|M| + 2\det(M)} \qquad (3)$$

where $|M| = m_{11}^2 + m_{12}^2 + m_{21}^2 + m_{22}^2$, $\det(M) = m_{11}m_{22} - m_{12}m_{21}$, and m_{ij} are elements of the transfer matrix M. In the calculations we have assumed that the optical path length in each layer is a quarter wavelength, that is $\eta_A d_A = \eta_B d_B = \lambda_0/4$.

RESULTS

In figure 1, a scanning electron microscope (SEM) image of a first-kind Fibonacci multilayer of generation 10 with 89 layers is shown, where layers A and B correspond to light gray and dark zones, respectively. As can be observed, the thickness of the layers is almost uniform and the interface quality is good for the visible light wavelength. The measured reflectance (solid line) of this multilayer as a function of the wavelength is shown in figure 2 and it is compared with the calculated one (dashed line). A good agreement between experimental and theoretical spectra is observed in the large wavelength region, except a small shift. Notice that in general the experimental peaks are predicted by the model, despite of the relative intensities difference. These spectra are highly sensitive to small variations in the optical path length of the layers and in their refractive index [9]. In figure 2, quarter optical path length and constant refractive index are used for calculation.

Figure 1. Cross-sectional SEM image of a Fibonacci PS multilayer of generation 10 with 89 layers on a c-Si substrate.

Figure 2. Measured (solid line) and calculated (dashed line) reflectance spectra of the multilayer shown in figure 1.

In figure 3 we show the reflectance of a luminescent Fibonacci PS multilayer of generation 6 with 13 layers, where solid and dashed lines correspond respectively to measured and calculated spectra. It is noted that for long wavelengths (>1300 nm) the minima of spectrum do not reach zero since the light wavelength is larger than the sample thickness (~1363 nm). Furthermore, the theory predicts correctly the position of peaks. However, for short wavelength region (<600 nm) the theoretical peak intensities are systematically larger than the experimental ones. This fact could be due to the non consideration of refractive index wavelength dependence of porous silicon [10] in the calculations, *i.e.*, constant η_A=2.2 and η_B=1.8 were used. Finally, figure 4 shows the photo luminescence spectrum (solid line) of the same sample as in figure 3, where it is excited by using an UV light of 350 nm. Dashed line corresponds to a PS monolayer of

approximately 12 μm prepared under the same conditions of layer B in figure 3. It is worth mentioning that these spectra were taken from samples covered with a mask to avoid light emission from the inhomogeneous borders. Notice that the photoluminescence spectrum of Fibonacci multilayer is proportionally larger than expected one in comparison with that of the PS monolayer, since the latter is almost nine times ticker than the former. Also, a clear signature of the Fibonacci sequence can be observed in figure 4, *i.e.*, the position of the maximums are found close to those of the corresponding reflectance spectrum (see figure 3).
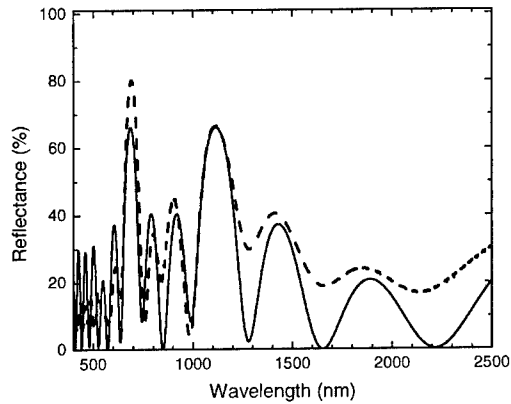
Figure 3. Measured (solid line) and calculated (dashed line) reflectance spectrum of a Fibonacci PS multilayer of generation 6 with 13 layers on a c-Si substrate.
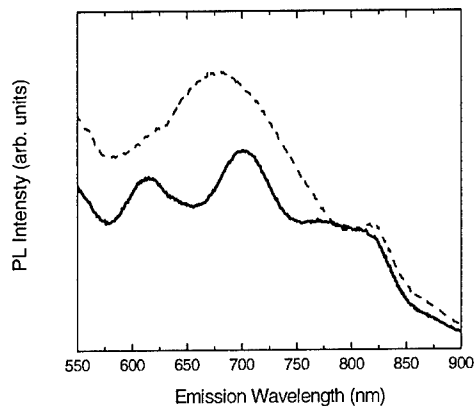
Figure 4. Photoluminescence spectrum of the same sample as in figure 3 (solid line) compared with a PS monolayer (dashed line), both excited by an UV light with wavelength of λ=350 nm.

CONCLUSIONS

In summary, we have prepared samples of luminescence PS multilayer following the Fibonacci sequence, despite the fragility of the high porosity layers. The measured reflectance spectra are compared with theoretical ones, where good agreements are observed. The preliminary photoluminescence spectra show signs of the quasiperiodic structure and the observed enhancement in the luminescence intensity could be interpreted as a consequence of the quasiperiodicity. However, a closer comparison with a theoretical model is required and it is currently under developing. Finally, this work could be extended to analyze other non-linear optics of these quasiperiodic multilayers, since efficient emissions of second and third harmonics are observed in ferroelectric Fibonacci multilayers [11].

ACKNOWLEDGMETS

REFERENCES

[1] J. Joannopoulos, *Photonic Crystals* (Princeton University Press, 1995).
[2] M. Kohmoto, B. Sutherland, and K. Iguchi, *Phys. Rev. Lett.* **58**, 2436 (1987).
[3] W. Gellermann, M. Kohmoto, B. Sutherland, and P. Taylor. *Phys. Rev. Lett.* **72**, 633 (1994).
[4] O. Bisi, *Surf. Sci. Rep.* **38**, 1 (2000).
[5] L. dal Negro, *et al.*, *Phys. Rev. Lett.* **90**, 055501 (2003).
[6] V. Agarwal and J.A. del Río, *Appl. Phys. Lett.* **82**, 1512 (2003).
[7] D. Bellet and L. Canham , *Adv. Mater.* **10**, 487 (1998)
[8] M. Born and E. Wolf, *Principles of Optics*, 3rd. edition (Pergamon Press, 1965).
[9] R. Nava, V. Agarwal, J. A. del Río and C. Wang, *J. non Crystalline Solids* **329**, 140 (2003).
[10] N. Koshida, *et. al*, *Appl. Phys. Lett.* **63**, 2774 (1993).
[11] S. Zhu, Y. Zhu, and N. Ming, *Science* **278**, 843 (1997).

Anodization Time Dependent Photoluminescence Intensity of Porous Silicon

Md. N. Islam[1] and Satyendra Kumar

Department of Physics, Indian Institute of Technology, Kanpur – 208 016, INDIA
[1]QAED/SRG, Space Applications Centre (ISRO), Ahmedabad – 380015, INDIA

ABSTRACT

The photoluminescence (PL) intensity first increases with anodization time (t_a) and then decreases at very large t_a. The increase in PL intensity with t_a may be understood if the PL intensity is taken to be proportional to the effective volume of porous silicon (PS) layer under the probe laser beam. The effective volume of PS layer will be proportional to its thickness and reciprocal to the porosity. For a fixed anodization condition, the thickness and porosity both increase with t_a. The increase in thickness increases the effective PS volume, while the increase in porosity causes the effective volume to decrease. Therefore, the intensity variation is governed by these two parameters: thickness and porosity. The observed results suggest that the thickness dominates the PL intensity initially and then the porosity becomes more important for very long t_a. The PS layers prepared under ambient light illumination also exhibited the similar behaviour. The intensity variation with t_a was explained as the interplay of thickness and porosity variations with t_a.

INTRODUCTION

Visible photoluminescence (PL) at room temperature from electrochemically etched porous silicon (PS) has been a strong motivating factor to study nanocrystalline silicon for their possible applications in optoelectronic integration[1]. PL intensity is normally increases with anodization time (t_a) for shorter t_a. However, PL intensity was found to decrease after reaching a maximum for a longer t_a in stain etching[2]. It is due to the fact that after a certain t_a, the loss of PS layer by chemical dissolution becomes more than the gain in PS layer thickness. In this article, we present the effect of longer t_a on PL from PS formed by electrochemical anodization.

EXPERIMETAL DETAILS

The thick PS layers fabricated by electrochemical anodization of p-Si (100) wafers of 6-10 Ω.cm resistivity in a Teflon cell using HF (48%) and C_2H_5OH (99.9%) (1:1 by volume) as electrolyte and a platinum disc as the counter electrode. For a uniform current distribution over the exposed area, an Ohmic back contact of Al film was provided. The wafers were anodized at a current density of about 10 mA.cm^{-2} for a wide range of t_a (few min to several hours) under ambient light as well as external white light illumination. After PS layer formation, samples were rinsed in deionized water and then in methanol and soaked in propanol for few minutes to minimize the structural damage during drying.

The gravimetric porosity of PS layers was measured by a sophisticated electronic weighing machine having resolution of 10 µg. The concentrated aqueous KOH solution was used to etch out the PS layer completely from the substrate Si. In order to remove the moisture and electrolyte residues, PS layers and substrate Si were vacuum dried at an elevated temperature just before weighing. Unpolarized PL spectra were recorded in back scattering configuration at room

temperature in a Spex Micro-Raman setup fitted with triplet monochromator. PL was excited with a 514.5nm line from Ar$^+$ laser source. The PL intensity as a function of emitted photon energy was measured using a photo multiplier tube, which was kept at low temperature (-30°C) for the best response.

RESULTS AND DISCUSSION

The study of microstructure reveals wide cracks, voids and island formation in PS layers. Micro-PL and -Raman facilitate the study of individual islands and cracks. It was found that the PL spectra from island and wide crack/channel were different, in terms of both PL intensity and peak position, suggesting structure dependency. The change in PL peak position may be due to the crystallite size variation and/or strains variations and is therefore complex. We shall not discuss the variation in PL peak position in this article. It was also found that PL spectra vary for different islands (or channels) on the same PS sample. But the variations are comparatively small (the maximum variations so far obtained are ±30% for PL intensity). In order to compare PL spectra from different PS layers, we used PL spectra from similar regions on PS layers.

Figure 1 shows PL peak intensity plotted along with the integrated (total) intensity against the anodization time (t_a). The PS layers were anodized under white illumination. The PL intensity increases with t_a and then decreases for further increase in t_a. The maximum variations between the sampling slots were taken as the error bars (not shown for clarity). Both the intensities go to a maximum and then decrease. The PS layers prepared under ambient light (without external white light illumination) also exhibited the same behaviour except that the maximum occurred at higher value of t_a. The increase in PL intensity with t_a may be understood
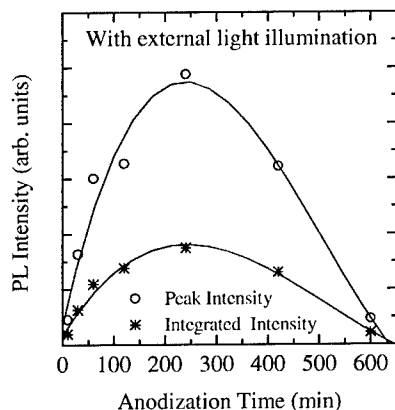
Figure 1. PL intensity (peak and integrated) variation with anodization time.

if we take the PL intensity to be proportional to the effective volume of PS layer under the probe laser beam. The effective volume of PS layer will be proportional to its thickness and the solidness (i.e., 1 − porosity). For a fixed anodization condition, we found that the thickness of PS layer increases monotonically with t_a as shown in Figure 2 (open-circles). The increase in thickness should increase the effective PS volume, and hence increase the PL intensity with t_a. Accordingly, the PL intensity would have increased to saturation when the penetration depth of probe laser beam into PS layer becomes less than the PS layer thickness under the probe beam. But the observed decrease in PL intensity beyond a certain t_a value implies decrease in effective volume of luminescent PS layer with increasing t_a. The decrease in effective luminescent PS value may be caused by increase in porosity of the PS layer with t_a.

The porosity as a function of t_a is also plotted in Figure 2 (solid-circles), which shows that like thickness, the porosity also increases monotonically with increasing t_a. However, unlike thickness, the increase in porosity is slow initially and becomes faster at longer t_a. Over the period of 10 h, change in porosity is about 30 - 40% under different anodization conditions (with and without external light illumination). Our results of increasing porosity with t_a confirm the report of Halimaoui[3] who observed the higher porosity for 10 μm thick than that for 1 μm thick PS layers obtained by anodizing p-type Si under the same conditions except t_a. Thus for a fixed anodization condition, the thickness and porosity both increase with t_a. The increase in thickness increases the effective PS volume, while the increase in porosity causes the effective volume to decrease. Therefore, the intensity variation is governed by these two parameters: thickness and porosity. The observed results suggest that the thickness dominates the PL intensity initially and then the porosity becomes more important for very long t_a.
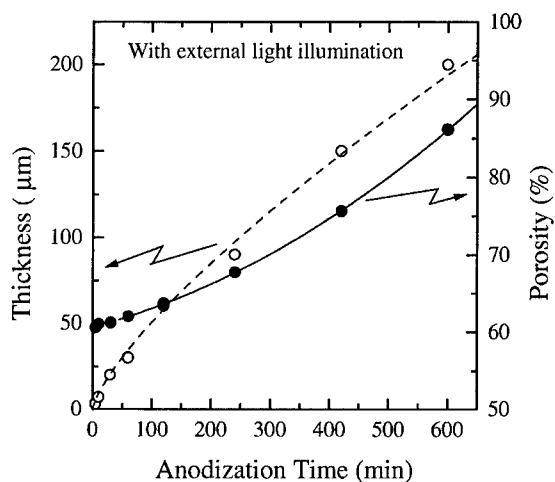
Figure 2. Variations of PS layer thickness (○) and porosity (●) with anodization time

If p is porosity and ρ is the density of c-Si skeleton in PS layer, the overall density of the PS layer becomes $\rho(1-p)$. Since the PL is proportional to the light absorbing volume, the PL intensity will be proportional to the product of penetration depth of incident light and the volume density, i.e., $I \propto h.\rho.(1-p)$, where h is the PS layer thickness (d) when d is smaller than the penetration depth (λ) and h represent the penetration depth when d is longer the penetration depth. Therefore, it is easily understandable that PL intensity will decrease with increasing porosity (i.e., anodization time) for very thick PS layers where $d>\lambda$. However, when $d<\lambda$, the PL intensity becomes a complex function of t_a as both d and p depend on t_a. The detail study will be published elsewhere.

CONCLUSION

We prepared various porous silicon layers by electrochemically etching of p-Si (100) wafers for a wide range of anodization time varying from minutes to several hours under both ambient light and external white light illumination. The porosity and thickness of PS layer both increase monotonically with t_a. The PL intensity increases with t_a, goes to a maximum, and then decreases with increasing t_a for very longer anodization. The intensity variation with t_a is the interplay of thickness and porosity variations with t_a. Therefore, depending upon the anodization conditions, an optimum value of t_a is required to achieve highest PL intensity from a PS layer

ACKNOWLEDGEMENTS

REFERENCES

[1] R. Collins, P.M. Fauchet and M.A. Tischler, Phys. Today **50,** 24 (1997)
[2] M. J. Winton, S. D. Russell, J. Wolk, and R. Gronsky, Appl. Phys. Lett. **69** 4026 (1996)
[3] A. Halimaoui, in *Porous Silicon Science and Technology*, edited by J. C. Vial and J. Barrien (Springer, 1994), pp. 33.

Photonic Crystals

Interaction of Periodically Arranged Point Defects in a Two Dimensional Photonic Crystal - The Photonic Analogue to a Doped Semiconductor

S. Richter[1], S. L. Schweizer[2], R. Hillebrand[1], C. Jamois[1], R. B. Wehrspohn[2], M. Zacharias[1] and U. Goesele[1]

[1]Max-Planck-Institut für Mikrostrukturphysik, Weinberg 2, D-06120 Halle, Germany
[2]Universtät Paderborn, Warburgerstr. 100, D-33098 Paderborn

ABSTRACT

We present and characterize hexagonal point defects in a two dimensional photonic crystal based on macroporous silicon. These point defects are prepatterned periodically, forming a superstructure within the photonic crystal after electrochemical etching. Spatially resolved, optical investigations related to morphological properties, like defect concentration and pore radius, are compared to bandstructure calculations. The confined defect states are identified and their interaction is evaluated quantitatively.

INTRODUCTION

The concepts of photonic bandgap materials and photonic crystals have been extensively studied over the recent years. By applying theoretical methods of solid state physics to periodic dielectric structures, the prediction of their properties and behavior is possible. So the dispersion relation of a photonic crystal is a bandstructure similar to semiconductors.[1]

Structures disturbing the periodicity of the photonic crystal are of special interest, because of their acting as guiding or confining elements for light within the crystal. If, e.g., a point defect is introduced, defect levels within the photonic bandgap will arise. Their behavior can be donor like or acceptor like, regarding on the type of the defect.[2]

A first theoretical approach of interacting resonators was proposed by Yariv et.al.[3] The coupled-resonator optical waveguide (CROW) relies on evanescent field coupling of resonator modes of adjacent resonators. Similar structures were realized by a linear arrangement of point defects in photonic crystals. [4, 5] A formation of bands within the photonic bandgap was observed. The linear arrangement of the point defects causes a breaking of the translational symmetry within the crystal. Therefore, only a projection of the bandstructure along the direction of the waveguides is possible.

A periodic arrangement of point defects in low concentration, where interaction with each other can be neglected, would correspond to doping of a semiconductor. A successive increase of the defect concentration allows the investigation of the point defect interaction. An approach for experimental and theoretical realisation of periodic point defects is presented in this work.

EXPERIMENTAL

Macroporous silicon is a very suitable model system for photonic crystals. The high refractive index contrast allows the fabrication of structures with complete photonic bandgaps. Two dimensional (2D) photonic crystals in the near infrared have been already established. [6, 7, 8] The 2D photonic crystals consist of ordered macropores prepared by an electrochemical etching
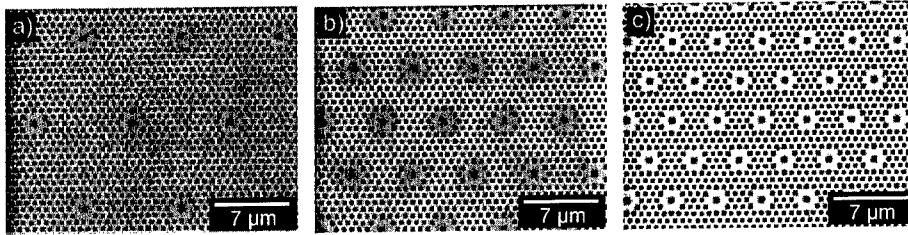
Figure 1: Variation of the defect concentration by setting different distances in Γ-K direction; a) $1.86 \cdot 10^4 cm^{-2}$, distance 13 lattice constants; b) $4.91 \cdot 10^4 cm^{-2}$, distance 8 lattice constants; c) $8.73 \cdot 10^4 cm^{-2}$, distance 6 lattice constants.

process. [9, 10] The pores are etched in hydrofluoric acid applying a photoelectrochemical dissolution process. Using lithographic prestructuring the nucleation spots of the pores can be defined at the surface of the n-type silicon wafer. This allows to control pore pattern and lattice constant. During the etching process the backside of the wafer must be illuminated to generate electronic holes in the silicon which are consumed by the dissolution of silicon. Due to electrochemical passivation of the pore walls very high aspect rations (length/diameter) of 100-500 are obtained. Therefore, macroporous silicon represents an excellent system to study 2D photonic crystal properties.

The lithographic prestructuring before the etching process allows setting and also leaving out single pores in the hexagonal lattice of the photonic crystal as well as the creation of periodic structures. The investigated structure is a hexagonal cavity similar to H2 cavities, reported by Olivier et.al.[5] A H2 cavity is a point defect in a hexagonal 2D photonic crystal and consists of seven missing pores. In contrast to the H2 structure, a central pore is introduced to create a hexagonal ring, shown in Fig. 1a. The lattice constant of the host crystal is 700 nm.

This point defect geometry causes two types of disturbances. The six missing holes in the hexagonal ring introduce more dielectric material into the crystal. Furthermore, the pores around the defect as well as the center pore show slightly larger diameters than all the other pores of the crystal. This is caused by the so called proximity effect. During the etching process, a missing pore offers additional electronic holes which are consumed by surrounding pores, leading to larger pore diameter.

The defects studied here, are arranged in a hexagonal lattice according to the symmetry of the photonic crystal. A variation of the defect concentration is achievable by setting different distances between the hexagonal rings. As shown in Fig. 2a-c, the distance between the defects varies from 13 to 6 lattice constants in Γ-K direction. In principle, any integer value larger 3 of the lattice constant can be chosen. The corresponding defect concentrations are $1.86 \cdot 10^4 cm^{-2}, 4.91 \cdot 10^4 cm^{-2}$ and $8.73 \cdot 10^4 cm^{-2}$.

To investigate the optical properties of the photonic crystal structures, FTIR (Fourier Transform Infrared) reflection measurements were made by coupling light perpendicular into the cleaved facet of the pores of the 2D photonic crystal and detecting the reflected light using an IR microscope coupled to the FTIR spectrometer.
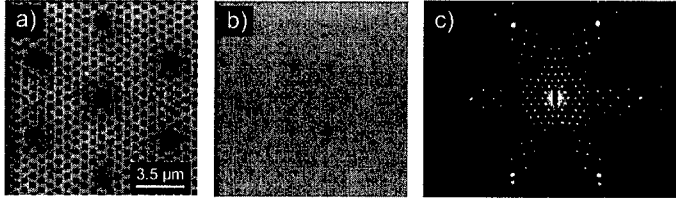
Figure 2: a) Scanning electron micrograph of point defects within the photonic crystal, b) Fourier transformation of an SEM image of the photonic crystal with periodic point defects, c) Laser surface diffraction pattern with point defect spots between the host reflections.
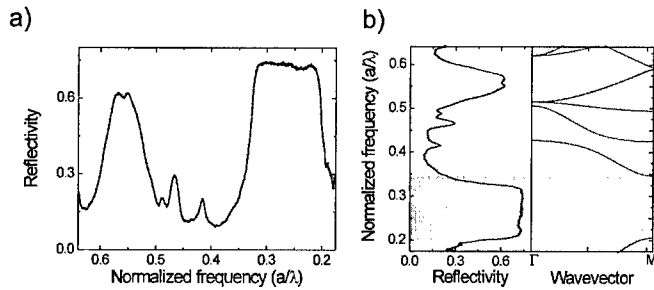
Figure 3: a) Reflection measurement of a 2D photonic crystal (lattice constant 700 nm, Γ-M direction, TE polarization), b) Comparison of a reflection measurement to the corresponding bandstructure (r/a= 0.36).

RESULTS and DISCUSSION

The periodic arrangement of the point defects can be verified by comparing a Fourier transformation of scanning electron microscope (SEM) images, as shown in Fig. 2b, and a laser surface diffraction pattern (Fig. 2c). A laser hits the surface of the crystal parallel to the pores, the directly reflected intensity is detected on a flat screen and imaged by a digital camera. This causes a diffraction pattern, because the wavelength of the laser (488 nm) is smaller than the lattice constant of 700 nm. This pattern of the hexagonal surface lattice is similar to the Fourier transformation of the SEM images (Fig. 2b). In between the six spots of the perfect photonic crystal (distance a^*) a hexagonal pattern appears with distances a^*/d, where $d \cdot a$ is the distance between two defects in real space. The distances of the additional pattern correspond to a hexagonal lattice with a lattice constant 8 times larger for this example than the lattice constant of the host crystal.

For the unperturbed crystal the reflection spectrum features a broad frequency interval (from 0.22 to 0.34 norm. frequency) of high reflectivity (Fig. 3a). Comparing this spectrum to the corresponding bandstructure a matching of high reflectivity and fundamental bandgap is found, Fig. 3b. Light frequencies within the bandgap cannot enter the crystal and will be reflected by interference total reflection.
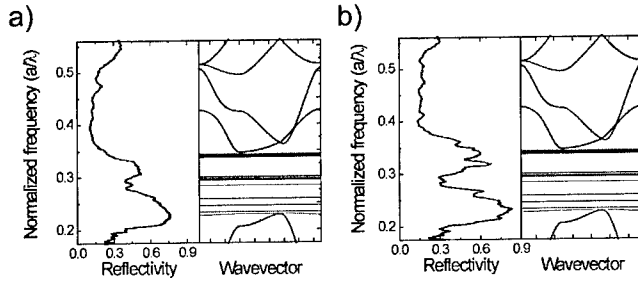
Figure 4: a) Reflection measurement of a PC including point defects (defect concentration $1.86 \cdot 10^4 \text{cm}^{-2}$, distance 13 lattice constants) compared to a bandstructure calculation; b) same as a) but for a defect concentration of $4.91 \cdot 10^4 \text{cm}^{-2}$, distance 8 lattice constants.

A reflection spectrum for a crystal including point defects (defect concentration $1.86 \cdot 10^4 \text{cm}^{-2}$) is shown in Fig. 4a. The plateau of high reflectivity shows several notches of lower reflectivity. A comparison of the reflection measurement to the corresponding bandstructure calculation clearly identifies these notches as defect states within the photonic bandgap. Light that enters the crystal couples to resonators close to the surface of the cleaved pores and will not be reflected. The bandstructure shows 19 states within the first photonic bandgap for TE polarization (Fig. 4a). These states are energetically separated and form discrete levels within the bandgap. This is a clear indication for separated point defects within the crystal. Due to their distance of 13 lattice constants they are not interacting.

The large number of defect levels can be explained by the complex defect geometry. Two types of defect states are expected, dielectric defects due to the six missing pores and air defects caused by larger pores during the etching process [proximity effect]. Dielectric defects are similar to donor levels in semiconductors. Introducing some more dielectric material to a crystal site, additional states are pulled from the air band into the bandgap. Vice versa for the so called air defects, they correspond to acceptor levels in semiconductors. Defect states from the dielectric band are created within the bandgap.

Increasing the defect concentration to $4.91 \cdot 10^4 \text{cm}^{-2}$ (corresponding to a defect distance of 8 lattice constants) causes broader and deeper notches in the high reflectivity region (Fig. 4b). Light, entering the crystal, couples to more resonators close to the surface of the cleaved pores. After a further increase of the defect concentration ($1.26 \cdot 10^5 \text{cm}^{-2}$, distance of 5 lattice constants) only several peaks of high reflectivity remain in the spectrum (Fig. 5a). The reason for these peaks is the overlapping of defect modes. This is shown via the corresponding bandstructure (Fig. 4b), discrete levels begin to form bands within the bandgap. A bending of levels towards air and dielectric band, respectively, takes place. Only small gaps remain in between bands of defect levels (Fig. 5a).

To extrapolate this behavior, a bandstructure for a defect density of $1.96 \cdot 10^5 \text{cm}^{-2}$ (defect distance of 4 lattice constants) is calculated (Fig. 5b). Within the host bandgap several groups of bands are forming. Smaller gaps remain in between them. The host bandgap splits up in 2 smaller
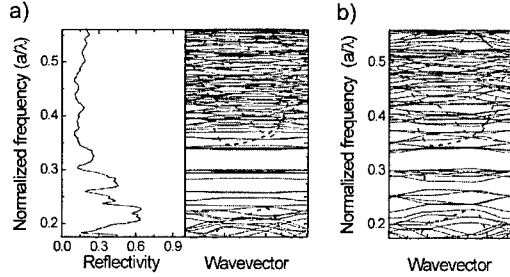
Figure 5: a) Reflection measurement of a PC including point defects ($1.26 \cdot 10^5 \mathrm{cm}^{-2}$, distance 5 lattice constants) compared to a bandstructure calculation; b) bandstructure for a defect concentration of $1.96 \cdot 10^5 \mathrm{cm}^{-2}$, distance 4 lattice constants.

gaps.

To characterize the interaction of the resonators quantitatively, the bandwidth Δ of the defect states within the original bandgap of the pure photonic crystal was calculated. To compare different concentrations the bandwidths of all defect states were averaged. An increase of more than one order of magnitude in the investigated range of defect distances was observed and is displayed in Fig. 6.

An single exponential decay fit, $\Delta_{\mathrm{avg}} = A + B e^{-\frac{D}{\gamma}}$ (decay constant $\gamma = 0.81 a$), shows an excellent agreement with the averaged bandwidth Δ_{avg}. This can be explained by an increasing coupling of the resonator modes with decreasing distance of the resonators. Localized fields of resonator modes can be treated similar to electron wavefunctions in a tight-binding model. [3, 11, 12] If the distance between two resonators decreases, the localized fields begin to overlap and to split. The tight-binding model predicts such an exponential decay of the interaction with increasing distance.

CONCLUSION

A periodic arrangement of point defects in a photonic crystal is fabricated and analyzed. The point defect concentration ranges from small perturbations of the crystal to strong modifications of its original periodicity. The periodicity of the point defects is verified by laser surface diffraction, an optical technique similar to diffraction experiments in solid state physics. The optical properties are investigated by a comparison of reflection measurements and bandstructure calculations. At low point defect concentrations, discrete levels inside the photonic bandgap appear. These levels are the resonator modes of the point defects. They can be clearly identified by reflection measurements.

An increase of the defect concentration causes a broadening of the discrete levels to bands and results in narrow gaps in between the bands. A quantitative evaluation of the defect bands shows an exponential decay of their bandwidth with increasing distance between them. This is a measure for interaction of periodic point defects.
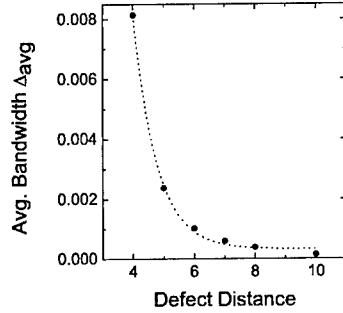
Figure 6: Averaged bandwidth Δ of defect levels as function of the defect distance

ACKNOWLEDGEMENT

[1] S. John. *Phys. Rev. Lett.*, 58:2486–2489, 1987.

[2] J.D. Joannopoulos, R.D. Meade, and J.N. Winn. *Photonic crystals: Molding the flow of light.* Princeton University Press, 1995.

[3] A. Yariv, Y. Xu, R. K. Lee, and A. Scherer. *Opt. Lett.*, 24:711–713, 1999.

[4] M. Bayindir, B. Temelkuran, and E. Ozbay. *Phys. Rev. B*, 61:11855, 2000.

[5] S. Olivier, C. Smith, M. Rattier, H. Benisty, C. Weisbuch, T. Krauss, R. Houdre, and U. Oesterle. *Opt. Lett.*, 26:1019–1021, 2001.

[6] U. Gruening, V. Lehmann, S. Ottow, and K. Busch. *Appl. Phys. Lett.*, 68:747, 1996.

[7] A. Birner, U. Gruening, S. Ottow, A. Schneider, F. Mueller, V. Lehmann, H. Foell, and U. Goesele. *Phys. Stat. Sol. (a)*, 165:111, 1998.

[8] J. Schilling, A. Birner, F. Mueller, R. B. Wehrspohn, R. Hillebrand, U. Goesele, K. Busch, S. John, S. W. Leonard, and H. M. van Driel. *Opt. Mater.*, 17:7–10, 2001.

[9] V. Lehmann and H. Foell. *J. Electrochem. Soc.*, 137:653, 1990.

[10] V. Lehmann. *J. Electrochem. Soc.*, 140:2836, 1993.

[11] M. Bayindir, B. Temelkuran, and E. Ozbay. *Phys. Rev. B*, 84:2140, 2000.

[12] E. Lidorikis, M. M. Sigalas, E. N. Economou, and C. M. Soukoulis. *Phys. Rev. Lett.*, 81:1405, 1998.

JAHN-TELLER EFFECT IN PHOTONIC CRYSTALS

Natalia Malkova, Venkatraman Gopalan
Materials Research Institute, the Pennsylvania State University, University Park, 16802 PA

ABSTRACT

The Jahn-Teller effect in photonic crystals as a prototype of photon-phonon interactions is studied. We are interested in removing the degeneracy of a defect state due to coupling with vibronic mode. Two-dimensional square photonic lattice of the dielectric rods in vacuum doped by the defect rod, giving the doubly degenerate E state in the first TM band gap is studied. We show that coming from the Jahn-Teller theorem, the lattice vibration with the symmetry of B_1 and B_2 modes should result in splitting the degeneracy of the E photon state, the lattice vibration being frozen. The stable configuration in the presence of the Jahn-Teller effect is determined from the dependence of the energy as a function of the rod displacement. Using the value of the vibronic constants, obtained from the suppercell plane wave calculations and the Finite Difference Time Domain simulations, we find the stable configuration of the lattice. We discuss the conditions to observe the effect.

Photonic crystals are of importance for numerous applications involving light modulation [1]. Interest in the construction of *active tunable* photonic elements has led to the idea of introducing interactions into the photonic crystal. Following the analogy with the solids, the interaction effects in the photonic crystals may be realized in two ways. The first is the Coulombic interaction, which in the case of the photonic crystal implies nonlinear optical behavior [2]. Another possible interaction is photon-phonon interaction, which should appear in a photonic crystal subject to mechanical vibrations [3].

In this paper we study the Jahn-Teller effect as a prototype of photon-phonon interactions in photonic crystals [4]. The Jahn-Teller effect has been studied in solids for hundred years [5]. This is a structural phase transition caused by coupling between the degenerate electronic state and lattice vibrations. We show that the Jahn-Teller effect is possible in two-dimensional photonic crystals. This means that if a proper vibronic mode is excited into the system, then it can be frozen and the crystal will show a structural phase transition. When dealing with the Jahn-Teller effect [5], we are interested in removing the degeneracy of a defect state due to coupling with vibronic mode. This motivates the aim of this paper, that is to study the splitting of the degenerate state due to interaction with allowed lattice vibrations and to find the stable configuration of the system in the case of presence of the Jahn-Teller effect.

The first step is to present Maxwell's equations for a photonic crystal subject to vibrations with a driven frequency ω in a Schrodinger-like form $i\dfrac{\partial \Psi(\vec{r},t)}{\partial t} = H\Psi(\vec{r},t)$, where we define a wave function and Hamiltonian as

$$\Psi = \begin{pmatrix} \vec{D} \\ \vec{H} \end{pmatrix}, \quad H = \begin{pmatrix} 0 & i\nabla\times \\ i\nabla\times\dfrac{1}{\varepsilon(\vec{r}+\vec{R}(t))} & 0 \end{pmatrix} = H^\circ + V . \tag{1}$$

Here we consider the magnetic neutral medium with $\mu = 1$, $\vec{D}$ is the electric displacement field, $\vec{H}$ is the magnetic field, $\vec{R}(t)$ is the harmonic function that describes the vibrations of the dielectric rods. In the first approximation of the perturbation theory we assume that amplitude of the vibrations is much less than the lattice constant. Then we can present the Hamiltonian H as a sum of the unperturbed Hamiltonian H° and perturbation potential $V \propto \nabla \times \dfrac{\delta \varepsilon}{\varepsilon(r)^2}$, where

$\delta \varepsilon = \dfrac{\partial \varepsilon}{\partial \vec{r}}\Big|_o \vec{R}$ (the index 0 shows that the derivative is taken at zeroth displacement). In the framework of time dependent perturbation theory for non-Hermitian perturbation potential V, we are looking for a solution of the Schrodinger equation as an extension over unperturbed states $\psi_i^{(o)}$ describing the degenerate state with the frequency ω_o, $\psi = \sum_i a_i(t)\psi_i^{(o)}$, where $a_i(t)$ are time-dependent coefficients. We arrive at

$$i\frac{\partial a_j(t)}{\partial t} = \sum_i a_i(t) V_{ij} e^{i\omega t} , \qquad (2)$$

where $V_{ij} = \left\langle \psi_i^{(o)} \left| V \right| \psi_j^{(o)} \right\rangle = -\omega_o \int \dfrac{\delta \varepsilon}{\varepsilon} \vec{H}_i^{(o)*} \bullet \vec{H}_j^{(o)} d\vec{r}$. Since all $\psi_i^{(o)}$ wave functions represent just the same energy state, the resonance condition will be in the case when the driven frequency of the rod vibrations $\omega = 0$. This corresponds to a frozen vibronic mode. But this effect will be realized if and only if the matrix elements V_{ij} do not equal to zero. This gives the main statement of the Jahn-Teller theorem [4].

First, we consider two-dimensional square photonic lattice doped by the defect rod. The point group symmetry of the square lattice is C_{4v}. If the defect rod is localized in the site of the lattice, then by symmetry it may be described both by one-dimensional $A_{1,2}$, $B_{1,2}$ and two-dimensional E irreducible representations of the group C_{4v} [6]. One-dimensional irreducible representations result in non-degenerate photon state. The two-dimensional representation results in doubly degenerate state represented by the two 1 x 2 column basis vectors having the shape of the p_x and p_y orbitals. That is the state under our consideration here.

All vibrations of the lattice can be presented in terms of the normal coordinates as a sum of the normal irreducible vibrations α. The vibronic perturbation can then be extended over normal vibrations $\delta \varepsilon(\vec{r}) = \sum \vec{R}_\alpha \bullet \dfrac{\partial \varepsilon}{\partial \vec{r}}\Big|_o$ [5]. Each normal vibration α is determined by the symmetrized displacements $\vec{R}_\alpha$ and so-called deformation potential $\dfrac{\partial \varepsilon}{\partial \vec{r}}\Big|_o$. In this case, there are allowed $2A_1$, B_1, $2B_2$ and 2E normal irreducible vibrations of the lattice. The $2A_1$ normal vibrations are total symmetrical one, while the B_1 and $2B_2$ modes are nonsymmetrical normal vibrations described by the one-dimensional irreducible representations [5]. The E mode of the normal vibrations are characterized by the two dimensional irreducible representation with the 1 x 2 basis vector, composed of components with the symmetry of the $\left| p_x \right\rangle$ and $\left| p_y \right\rangle$ states.

To satisfy the Jahn-Teller theorem [5], we have to find now such a vibronic mode α that gives $V_{ij}^\alpha \neq 0$. From the symmetry analysis, this matrix element is nonzero if and only if

$E \times E = \alpha$. Since, $E^2 = A_1 + A_2 + B_1 + B_2$, the non-trivial perturbations that can shift the degeneracy of the E defect state, are B_1 and B_2 vibrations. For the B_1 mode, $V_{xx}^{B1} = -V_{yy}^{B1} = V^{B1}$ and $V_{xy}^{B1} = 0$. While for the B_2 mode, $V_{xx}^{B2} = V_{yy}^{B2} = 0$ and $V_{xy}^{B2} = V_{yx}^{B2} = V^{B2}$. The degeneracy of the E-photonic mode is removed, resulting in two levels $\omega^{B1,2} = \omega_o \pm V^{B1,2}$, characterized by the $|p_x\rangle$ and $|p_y\rangle$ eigenvectors for the B_1 mode and by the $|p_x \pm p_y\rangle$ eigenvectors for the B_2 mode.

Next let us consider two-dimensional hexagonal photonic lattice doped by the defect rod. The point group symmetry of the hexagonal lattice is C_{6v}. If the defect rod is localized in the site of the lattice then by symmetry it may be described both by one-dimensional $A_{1,2}$, $B_{1,2}$ and two-dimensional $E_{1,2}$ irreducible representations of the group C_{6v} [6]. Again we are interested in splitting doubly degenerate states $E_{1,2}$. In this case, there are allowed $2A_1$, $2B_1$, B_2, $2E_1$ and $3E_2$ normal irreducible vibrations of the lattice. The A_1 normal vibration is total symmetrical one, while the $B_{1,2}$ modes are nonsymmetrical normal vibrations described by the one-dimensional irreducible representations [5]. The $E_{1,2}$ modes of the normal vibrations are characterized by the two dimensional irreducible representation with the 1 x 2 basis vector, composed of the $|p_x\rangle$ and $|p_y\rangle$ states for the E_1 mode and of the $|d_{xy}\rangle$ and $|d_{x^2-y^2}\rangle$ states for the E_2 mode. Since, $E_{1,2}^2 = A_1 + A_2 + E_2$, only the perturbation with the symmetry of the E_2 vibration can shift the degeneracy of the $E_{1,2}$ defect states. The degenerate state splits into

$$\omega_{1,2}^{E1,2} = \omega_o + (V_{xx}^{E1,2} + V_{yy}^{E1,2})/2 \pm \sqrt{(V_{xx}^{E1,2} - V_{yy}^{E1,2})^2/4 + V_{xy}^{E1,2}V_{yx}^{E1,2}},$$ with the eigenvectors as a linear combination of the $|p_x\rangle$ and $|p_y\rangle$ states for the E_1 mode and as a linear combination of the $|d_{xy}\rangle$ and $|d_{x^2-y^2}\rangle$ states for the E_2 mode.

Next we present supercell plane wave and Finite Difference Time Domain (FDTD) calculations of the two-dimensional defect crystal. As a model crystal, we consider a square photonic crystal of the dielectric rods, embedded in the air, with the lattice constant a, the radius of the rods $r = 0.2a$ and the dielectric constant $\varepsilon_r = 11.9$. Here, only modes with odd (TM-like) symmetry are considered, since that is the symmetry of the bands exhibiting a gap for the square lattice. We study the defect state created by the defect rod with radius $r_d = 0.3a$ and the same dielectric constant $\varepsilon_d = 11.9$ as the other rods. We are interested in the doubly degenerate defect state that, in this case, lies inside the first band gap. We consider distortions of the lattice in the limits $\Delta r = 0:0.3a$, keeping in mind that only small distortions ($\Delta r \ll a$) allow for the applicability of the linear approximation of the vibronic potential.

The supercell plane wave calculations of the defect state have been performed with the number of plane waves N=1225 for the supercell including 8, and 16 rods to test our data. Our computational domain for the FDTD simulation contained 7 x 7 unit cells, with the defect localized at the center. Each unit cell was divided into 20 x 20 discretization grid cells. The computational domain was surrounded by Perfect Matched Layers, with the thickness corresponding to 10 layers of the discretization grid. The total number of the time steps was 80,000 with each time step $\Delta t = \Delta x/(2c)$. The analysis of the convergency of our data obtained

in the framework of the supercell plane-wave technique and the FDTD simulations, showed that the error in our calculations was less than 1%.

Figure 1a shows the dependence of the frequency splitting of the defect state on the relative amplitude of the distortion for the B_1 and B_2 modes. The data were obtained by the supercell plane wave technique (dashed line) and by the FDTD calculations (solid line). The distributions of the Poynting's vector for the two split defect states: in the cases of coupling with the B_1 mode and the B_2 mode are shown in Fig.1b,c and Fig.1d,f, respectively. First, we note that the data calculated by both the techniques are in reasonable agreement. Secondly, the magnitude of the splitting of the defect level shows a fairly linear scaling with the amplitude of the distortion for both the perturbations, with the tangent of the slope angle giving the vibronic constant. We note that the relative slope of the curve for the B_1 mode is two and half times greater than for the B_2 mode. The reason for this is that the diagonal matrix element V_{xx}^{B1}, that determines the splitting by the B_1 mode, should be larger than the non-diagonal matrix element V_{xy}^{B2}, determining split by the B_2 mode. Third, the symmetries of the split states support our theoretical prediction.
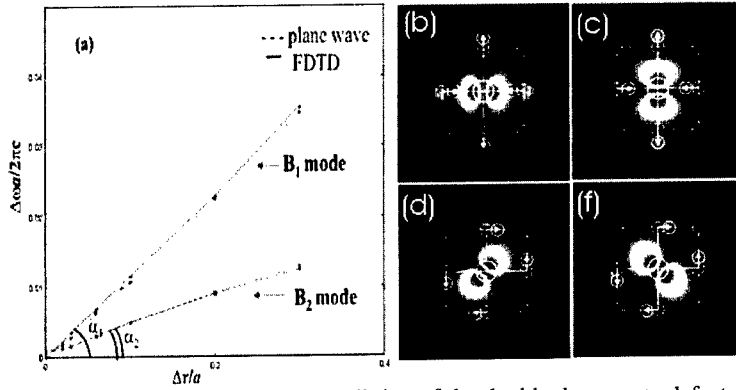
Figure 1. (a) Dependence of the frequency splitting of the double degenerate defect state on the relative amplitude of the distortion for the case of coupling the defect state with the $B_{1,2}$ modes. The data obtained from the supercell plane wave and FDTD calculations are shown by dashed and solid lines, respectively. The distribution of the Poynting's vector for two split defect states: in the cases of coupling with the B_1 mode (b,c) and with the B_2 mode (d,f). The Jahn-Teller cell with the corresponding displacements of the nearest neighbours to the central defect is shown.

These results are a consequence of the Jahn-Teller theorem, where the lattice vibration with the symmetry of B_1 and B_2 modes should result in splitting the degeneracy of the E photon state. Now we can answer a question: what is the stable configuration for the cell in the presence of the Jahn-Teller effect? To answer this question the energy as a function of the rod displacement in the Jahn-Teller cell $\omega(R)$, that is an adiabatic potential, must be determined. For

the degenerate E photon state interacting linearly with the B_1 and B_2 vibronic modes, the adiabatic potential can be found as a solution of the secular equation:

$$\begin{vmatrix} \omega_o + \upsilon_o(R_{B1}^2 + R_{B2}^2) - \upsilon_{B1}R_{B1} - \omega(R) & \upsilon_{B2}R_{B2} \\ \upsilon_{B2}R_{B2} & \omega_o + \upsilon_o(R_{B1}^2 + R_{B2}^2) + \upsilon_{B1}R_{B1} - \omega(R) \end{vmatrix} = 0. \quad (3)$$

The first order vibronic constants $\upsilon_{B1} = \left\langle p_i \left| \dfrac{\partial V^{B1}(r)}{\partial r} \right| p_i \right\rangle$ and $\upsilon_{B2} = \left\langle p_x \left| \dfrac{\partial V^{B2}(r)}{\partial r} \right| p_y \right\rangle$, as well as

the second order vibronic constant $\upsilon_o = \left\langle p_i \left| \dfrac{\partial^2 V(r)}{\partial r^2} \right| p_i \right\rangle$ can be evaluated from the supercell

plane-wave and the FDTD calculations shown in Fig.1a [4]. We present in Fig. 2a the solution of Eq. (3) for $\omega(R) - \omega_o$ constructed in the space of the $\Delta r^{B1,2} \equiv R_{B1,2}$ coordinates. The coordinates of the two minima give the stable configuration of the system when both of the modes are excited, while the depths of the walls determine the so-called the Jahn-Teller stabilization energy. In the case of the photonic crystal, we can excite in the system only one type of the vibronic modes. The adiabatic potentials for the E degenerate photon state interacting either with the B_1 or with the B_2 vibronic modes are shown in Fig.2b by the solid and dashed lines, respectively. The points of minima of the curves $\Delta_o^{B1,2} = \pm \upsilon_{B1,2}/(2\upsilon_o)$ determine the stable displacement of the Jahn-Teller cell. The Jahn-Teller stabilization energy, equal to $\omega_{JT}^{B1,2} = -\upsilon_{B1,2}^2/(4\upsilon_o)$, defines the gained energy because of the Jahn-Teller effect.
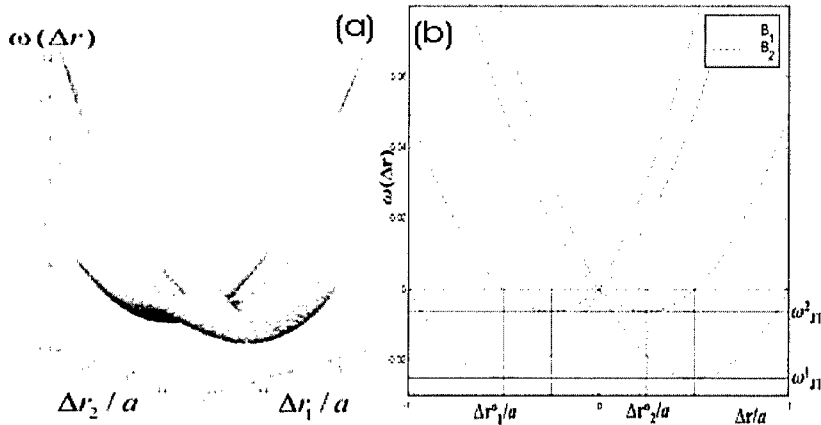
Figure 2. The adiabatic potential for the E degenerate photon state interacting linearly with the B_1 and B_2 vibronic modes in the space of the $\Delta r^{B1,2}$ coordinates (a). The adiabatic potentials for the E state interacting either with the B_1 (solid line) or B_2 (dashed line) vibronic modes. (b)

We conclude, that the adiabatic potential has a characteristic shape for the Jahn-Teller effect, when for the most symmetric configuration of the cell at the point $\Delta r = 0$, two branches of the adiabatic potential coincide resulting in degenerate photon state [5]. The Jahn-Teller theorem states that at the point of degeneracy the adiabatic potential has no minimum, and hence at this point the system is unstable. The system goes spontaneously to the minimum of the adiabatic potential, situated at the points $\Delta r = \pm \Delta r_o^{B1,2}$, being characterized by a lower energy and lower symmetry.

Now we can argue that if the proper α vibronic mode is excited in the photonic crystal then it may be condensed. The condition to observe the effect is that $\hbar \omega_{JT}^{\alpha} > K$, where K is the kinetic energy of the vibrations determined by the amplitude of the vibrations and the mass of the rods. This requires that the velocity of the vibrations should satisfy inequality $v^2 < 2\hbar \omega_{JT}^{\alpha} / m$ (where v is the velocity of the vibrations and m is the mass of the rods). In the case of the photonic crystal with nanometer scale of the lattice, this gives that the vibronic mode can be frozen if $v < 10^4 m/s$ and the frequency of the vibration $f < 10^6 1/s$. In reconfigurable artificial crystals, these experimental parameters may be tuned to satisfy the above inequality.

In conclusion, we have shown that the Jahn-Teller structure phase transition can be observed in artificial photonic crystals. The condition to observe the effect limits the frequency of the lattice vibrations. We emphasize that besides the basic interest in the Jahn-Teller phase transition firstly studied in Ref. [4], the symmetrical analysis presented gives an effective tool for control of the magnitude and symmetry of the degenerate state. The straightforward way to implement the Jahn-Teller effect is to construct a photonic crystal on the piezoelectric substrate giving a needed distortion of the lattice near the defect [7]. This distortion could, for example, be used for optical switch, or at the corners of sharp bends in optical waveguides to improve guiding efficiency [8]. More sophisticated designs can include coupling of elastic and electromagnetic waves in a lattice periodic in both dielectric and acoustic constants.

REFERENCES

1. Photonic Crystals and Light Localization in the 21st Centery, edited by C.M.Soukoulis, NATO Science Series, v.563 (Klumer Academic Publishers, 2001).
2. M. Scalora, M. J. Bloemer, A. S. Manka, J. P. Dowling, C. M. Bownden, R. Viswanathan and J. W. Haus, Phys. Rev. A **56**, p. 3166 (1997); M. D. Tocci, M. Scalora, M. J. Bloemer, J. P. Dowling and C. M. Bowden, Phys. Rev. A **53** p. 2799 (1996).
3. J. N. Winn, S. Fan, J. D. Joannopoulos, Phys.Rev.B **59**, 1551 (1999).
4. N. Malkova, S. Kim, V. Gopalan, Phys. Rev. B **68**, 045105 (2003); N. Malkova, S. Kim, V. Gopalan, J. Phys.: Condensed Matter **15** 4535 (2003).
5. I. B. Bersuker The Jahn-Teller Effect and Vibronic Interactions in Modern Chemistry, Plenum Press, New York and London, 1983.
6. K. Sakoda, H. Shiroma, Phys. Rev. B **56**, 4830 (1997).
7. S. Kim, V. Gopalan, Appl. Phys. Letters **78**, 3015 (2001).
8. N. Malkova, S. Kim, V. Gopalan, Appl. Phys. Letters **83**, 1509 (2003); N. Malkova, V. Gopalan, Phys. Rev. B to be published (2003).

Low loss Photonic Crystal Cladding Waveguide with Large Photonic Band Gap

Yasha Yi, Peter Bermel, Shoji Akiyama, Jessica G. Sandland, Xiaoman Duan,
and Lionel. C. Kimerling
Massachusetts Institute of Technology, 77 Massachusetts Avenue, Cambridge,
MA 02139

ABSTRACT

Light propagation in a low index core (e.g. SiO_2) is realized by a Photonic Band Gap (PBG) cladding waveguide structure with large dielectric index contrast layers (Si/Si_3N_4). The waveguide is fabricated with a CMOS compatible process. The measured loss for the asymmetric PBG cladding waveguide is about 0.5dB/cm for both polarizations at a wavelength of 1550nm. Potential applications include optical amplification when the SiO_2 core is doped with optical active materials (e.g. Er).

Microphotonics is an attempt to use current microelectronics process technology to create the next generation of optical computing devices. Electronic signal processing has inherent speed limitations due to RC delays [1,2]. Optical signals, which do not have this problem, should then become the next information carriers for various technologies [3,4]. Traditionally, silica optical fibers have been the *de facto* standard for the transportation of light. The guiding principle, based on total internal reflection (TIR), requires a high refractive index core and a lower refractive index cladding. This mechanism is also applied in many high index contrast waveguide for sharp turn on chip scale. However, many important future devices will require light guiding to take place in low index materials or even in hollow cores. Examples include fluorescent molecule detectors, light amplifiers, and scintillators. As a result, flexibility to choose suitable core materials is becoming more important.

In this work, we develop a new silicon-based waveguide with low refractive index materials (SiO_2 or air) as core, and stratified high index contrast dielectric layers (Si/SiO_2 or Si/Si_3N_4) as cladding. The guiding mechanism is based on the principle of a 1D Photonic Band Gap (PBG) [5-11]. The index contrast for the latter system is high enough to create an omnidirectional photonic bandgap, i.e., a range of wavelengths in which light is reflected from all incident angles and polarizations [12-14]. An omnidirectional bandgap is not strictly necessary to guide light in the low index core, but its presence enhances the confinement of the light in the low index core and allows for the creation of sharp, low loss bends (superior to those in an index-guided waveguide). The high index contrast between Si/SiO_2 (n=2.0) and Si/Si_3N_4 (n=1.5) is very important for many properties we discuss in this paper.

The silicon-based PBG cladding waveguide can be designed as a slab waveguide, a ridge waveguide, or a channel waveguide. In this work, an asymmetric PBG cladding waveguide is fabricated, with SiO_2 as the low index core layer and Si/Si_3N_4 as the high index contrast cladding pair – each layer having a quarter optical wavelength thickness. The asymmetric PBG waveguide configuration is illustrated in Fig.1. The SiO_2 guiding layer (with refractive index n_g) is between the air ($n_a=1$) and high index contrast Si_3N_4 (n_1) and Si (n_2) cladding pairs, which are deposited on the silicon substrate. For conventional dielectric optical waveguides, it is not possible to guide light in low index SiO_2 core materials. In the following, the photonic bandgap principle will be utilized to show that guided modes exist in a low index core under two conditions: first, that the wavelength is within the photonic bandgap range of the one dimensional Si/Si_3N_4 photonic crystal, and second, that the guiding layer has an optical thickness of at least half a wavelength. Simulation shows that the guided modes are robust across a large range of frequencies. This can be predicted from the large index contrast of the Si/Si_3N_4 pairs, which gives rise to a large photonic stop band for both TE and TM modes at almost all incident angles in the projected bandstructure.
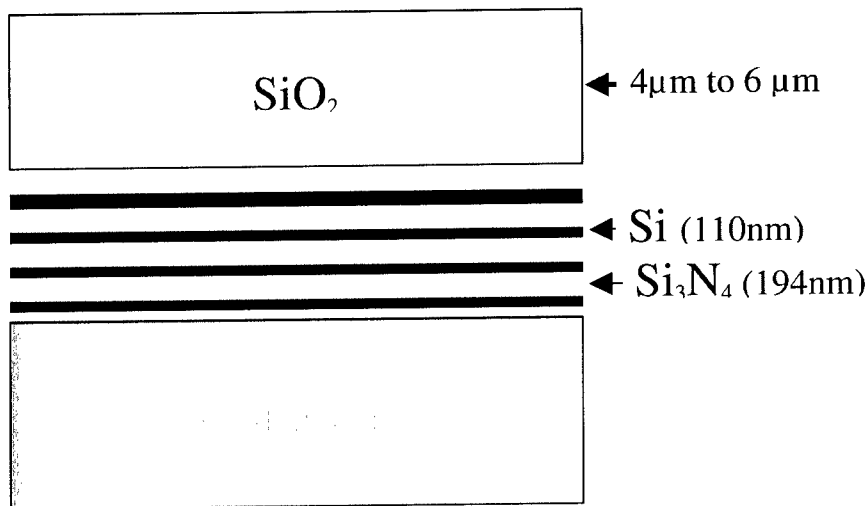
Figure 1. Illustration of an asymmetric PBG cladding waveguide.

The PBG cladding waveguide is fabricated using a CMOS compatible process. Starting from 6-inch Si wafers, the 194nm Si_3N_4 layer is deposited at 775C by Low Pressure

Chemical Vapor Deposition (LPCVD), at a deposition rate of 23A/min; the 110nm Poly-Si layer is deposited at 625C by LPCVD, at a deposition rate of 100A/min. Accurate thickness control of the Si and Si_3N_4 layers is achieved. The interface between each high index dielectric layer is very smooth, which helps reduce the scattering loss by roughness. The oxide core is deposited by LTO (Low temperature oxide), followed by 850C thermal annealing to form stochiometric and solidified oxide. Different oxide thickness at 4um, 5um and 6um are deposited by LTO plus thermal anneal. For better performance, Chemical Mechanical Polishing is used to smooth the oxide core.

We used Si/Si_3N_4 layers as PBG cladding pairs, as the refractive index contrast between Si (3.5) and Si_3N_4 (2.0) pairs is high (Δn=1.5), a large photonic band gap and omnidirectional band gap are expected in this system. Experimentally, just a few layers are enough to achieve more than 99% absolute reflectivity. This is crucial for the performance of waveguides based on the PBG guiding mechanism, as in principle, guided modes only exist with when an infinite number of layers give rise to 100% absolute reflectivity. In practice, all the modes of a finite system are leaky modes with complex propagation constant. High index contrast systems are superior because only a few layers are necessary to achieve a good approximation to perfect reflectivity, which means more practical devices can be achieved within fabrication process tolerance, and that each device will be smaller.

The loss of the asymmetric slab waveguide at λ=1550nm is measured: for the TE mode, it is 0.42dB/cm; for the TM mode, it is 0.47dB/cm (Fig. 2). Therefore, light guiding in a low index core can be achieved for both TE and TM modes, due to the large photonic band gap for both modes induced by high index contrast between Si and Si_3N_4 layers. Furthermore, the omnidirectional band gap in the Si and Si_3N_4 system is very helpful in confining the light to the low index core for both modes within a large range of wavelengths, compared to alternatives such as the ARROW waveguide and the low index contrast Bragg waveguide (results not shown). The superiority of high index-contrast PBG slab waveguides is therefore clearly demonstrated.

TE Mode

Loss= 0.42 dB/cm
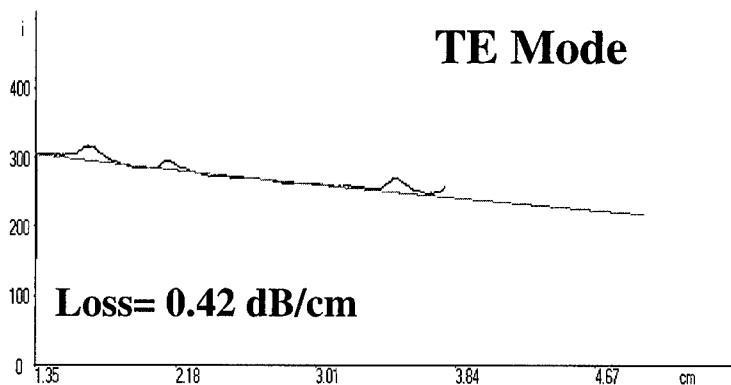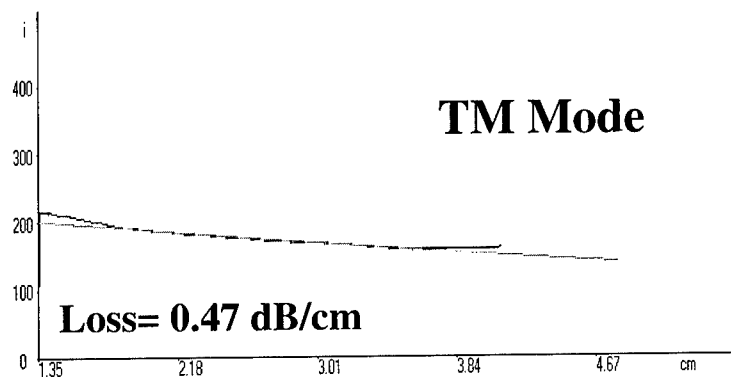
Figure 2. The waveguide loss measurement at 1550nm: intensity of signal vs. distance along waveguide.

In conclusion, a photonic crystal cladding waveguide with large index contrast dielectric layers is designed and fabricated. Light guiding in the low index core is achieved with low loss for both TE and TM modes, within a large range of operating wavelengths. A relatively thin PBG cladding, which works due to the large index contrast between the Si and Si_3N_4 layers, indicates the advantage of this technique over a benchmark index-guided silica waveguide.

References
1. L. C. Kimerling, "Silicon Microphotonics", *Applied Surface Science*, **159**, 8 (2000).
2. E. A. Fitzgerald and L. C. Kimerling, *MRS Bull.*, **23**, 39 (1998)
3. H. Pin Kao and J. S. Schoeniger, *Appl. Opt.*, **36**, 8199 (1997)
4. Y. Matsuura and J. A. Harrington, *J. Opt. Soc. Am. A*, **14**, 1255 (1997).

5. E. Yablonovitch , *Phys. Rev. Lett.* **58**, 2059 (1987); S. John , *Phys. Rev. Lett.* **58**, 2486 (1987).

6. J. D. Joannopoulos, R. D. Meade, and J. N. Winn, *Photonic Crystals: Molding the Flow of Light* (Princeton, 1995).

7. See *Photonic Band Gap Materials*, C. M. Soukoulis, ed., **B308** of NATO ASI Series (Kluwer Academic, Dordrecht, The Netherlands, 1996).

8. J. S. Foresi, P. R. Villeneuve, J. Ferrera, E. R. Thoen, G. Steinmeyer, S, Fan, J. D. Joannopoulos, L. C. Kimerling, H. I. Smith, and E. P. Ippen, *Nature*, **390**, 143 (1997).

9. J. C. Knight and P. St. J. Russell, *Science*, **296**, 276 (2002).

10. R. F. Cregan, B. J. Mangan, J. C. Knight, T. A. Birks, P. St. J. Russell, P. J. Roberts, and D. C. Allan, *Science*, **285**, 1537 (1999).

11. J. C. Knight, J. Broeng, T. A. Birks, and P. St. J. Russell, *Science*, **282**, 1476 (1998).

12. J. N. Winn, Y. Fink, S. Fan, and J. D. Joannopoulos, Opt. Lett., **23**, 1573 (1998).

13. Y. Fink, J. N. Winn, S. Fan, C. Chen, J. Michel, J. D. Joannopoulos, and E. L. Thomas, *Science* **282**, 1679 (1998).

14. D. N. Chigrin, A. V. Lavrinenko, D. A. Yarotsky, and S. V. Gaponenko, *Appl. Phys. A*, **68**, 25 (1999).

Three-Dimensional Lithography for Rutile TiO$_2$ Single Crystals using Swift Heavy Ions

Koichi Awazu[*1], Makoto Fujimaki,[2] Yoshimichi Ohki,[2] and Tetsuro Komatsubara[3]
[1]CAN-FOR, National Institute of Advanced Industrial Science and Technology, Tsukuba Central 4 305-8562 Japan
[2]Department of Electrical Engineering and Bioscience, Waseda University, 3-4-1 Ohkubo, Shinjuku-ku, Tokyo 169-8555, Japan
[3]UTTAC, Tsukuba University, Tennodai, Tsukuba 305-8577, Japan
*Corresponding author: k.awazu@aist.go.jp, voice +81-29-861-5650, fax +81-29-861-2919

ABSTRACT

We have developed a nano-micro structure fabrication method in rutile TiO$_2$ single crystal by use of swift heavy-ion irradiation. The area where ions heavier than Cl ion accelerated with MeV-order high energy were irradiated was well etched by hydrofluoric acid, by comparison etching was not observed in the pristine TiO$_2$ single crystal. Noticed that the irradiated area could be etched to a depth at which the electronic stopping power of the ion decayed to a value of 6.2keV/nm. We also found that the value of the electronic stopping power was increased, eventually decreased against depth in TiO$_2$ single crystal with, e.g. 84.5MeV Ca ion. Using such a beam, inside of TiO$_2$ single crystal was selectively etched with 20% hydrofluoric acid, while the top surface of TiO$_2$ single crystal subjected to irradiation was not etched. Roughness of the new surface created in the single crystal was within 7nm with the atomic forth microscopy measurement.

INTRODUCTION

Photonic crystal structures for controlling electromagnetic waves in two or three dimensions are applied for outstanding optical devices. One of the most conventional methods to obtain micro-structures must be the reactive ion etching (RIE), however, roughness and ripple pattern on the side wall of micro-structures, RIE-lag, and etch stop have been frequently observed. Besides the "main stream" of photonic crystals' researches based on semiconductors, photonic crystals based on TiO$_2$ have also been reported.[1] Micro fabrication techniques for the material have not been established indeed, but this material offers many advantages. Reflection loss due to connection between photonic crystals and silica based optical waveguides would be reduced because refractive index values of (2.4($\perp$c axis) and 2.7(//)) in a rutile TiO$_2$ single crystal are close to in silica, rather than in semiconductors. Furthermore, optical transmission loss of TiO$_2$ is ten times lower than in silicon in the vicinity of 1.5µm as mentioned previously.[2] Since TiO$_2$ remains high list as a material for the photonic crystals, it is desired to fabricate a nano-structure with nano-order flatness and precision. In the present work, we examined to fabricate the micro-structure with nano-flatness on both bottoms and side walls in rutile single crystal by swift heavy ions. Furthermore, as an unexpected phenomenon, three dimensional structure was created in rutile TiO$_2$ single crystal.

EXPERIMENTAL

The samples used in the present experiment are (100) rutile TiO_2 single crystal (purity > 99.99%, density: $4.25g/cm^3$) synthesized by the Verneuil flame-fusion method. Ion irradiation using the 12MV tandem accelerator at Tandem Accelerator Center, University of Tsukuba (UTTAC) was performed at room temperature. [3]   Structural change induced by ion irradiation was investigated by X-ray diffraction (XRD) measurements with a Rigaku FR-MDG apparatus.   A scanning electron microscope (SEM, Hitachi S-2500CX) and a high-resolution electron microscope (HREM, Hitachi H-9000NAR) were also employed to observe sample surfaces.   Chemical etching was performed with 20% hydrofluoric acid, hereafter 20% HF, at room temperature.

RESULTS

Figure 1 shows an SEM image of rutile TiO_2 (100) single crystal surface subjected to 45MeV Cu ion irradiation at an accumulated dose of $3.0\times10^{13}cm^{-2}$ through a $1\mu m$ thick gold stencil mask with a $1\mu m$ diameter dot pattern.   The irradiated rutile (100) single crystal was then immersed in 20% HF for 40min. Cylindrical patters with diameter of $1\mu m$ with $2\mu m$ height were created on TiO_2 single crystal. Figure 2 shows XRD spectra of the (100) rutile irradiated by the 84.5-MeV Cu ions.   The spectrum (i) is for the non-irradiated sample. Two peaks at $39.2°$ and $84.3°$, to be assigned to the (200) and (400) planes, are seen.   Curves (ii), (iii), (iv), and (v) are the spectra obtained in the samples after irradiation to respective doses of 1.0×10^{12}, 3.0×10^{12}, 7.0×10^{12}, and 5.0×10^{13} cm^{-2}.   The two XRD peaks become smaller by the ion irradiation.   Besides them, new peaks appear at $38.3°$ and $82.5°$ in spectrum (iii).   They become smaller and move to smaller angles as the irradiation dose increases, and finally disappear in spectrum (v).

Figure 3 shows electronic stopping power S_e calculated by SRIM 98 code as a function of the depth from the sample surface. Values of etched depth were plotted with closed circles in Fig. 3.   The point at $S_e = 0$ was close to the depth where the ion was stopped.   At first glance, the etched depth was shallower than the depth at $S_e = 0$.   For instance, the etched depth and the depth at $S_e = 0$ for 120MeV I ion were $6.5\mu m$ and $11\mu m$, respectively. The first order feature was that the values of S_e at the etched depth presented with closed circles were always located around the solid line of 6.2keV/nm irrespective of incident ions or acceleration energies.   In other words, a threshold electronic stopping power of 6.2keV/nm was apparently necessary to commence etching.
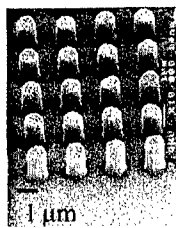
Figure 1. A SEM image of the TiO_2 surface etched by 20 % hydrofluoric acid for 40min. The sample was irradiated with 45MeV Cu ion irradiation to a dose of 3.0×10^{13} cm^{-2} through a $1\mu m$ thick gold mask with pattern of $1\mu m$ diameter.
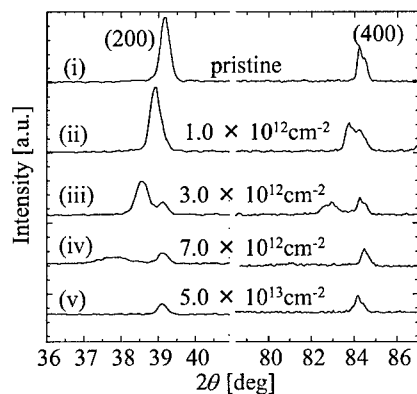
Figure 2. XRD spectra of the as-received sample (i), after the 84.5MeV Cu ion irradiation to a dose of $1.0 \times 10^{12} \text{cm}^{-2}$ (ii), $3.0 \times 10^{12} \text{cm}^{-2}$ (iii), $7.0 \times 10^{12} \text{cm}^{-2}$ (iv), and $5.0 \times 10^{13} \text{cm}^{-2}$ (v). The peaks at $39.2°$and $84.3°$ are due to the (200) and (400) planes of the rutile phase, respectively.

Furthermore, another surprising result was obtained. Namely, after the crystals were irradiated by the Ca ions with various energies to a dose of $8.0 \times 10^{13} \text{ cm}^{-2}$, they were cut perpendicularly to the surface and immersed in the HF solution. Figures 4 show typical cross-sectional SEM images taken for the sample irradiated by the 72.3, 82.0 and 84.5MeV ions. The position of the irradiated top surface and the direction of ions are indicated by arrows. The top surface was not etched, while an inside gap or a vacant hollow was created by etching about 4 μm below the surface in case of 72.3MeV Ca ions. Similar inside gaps
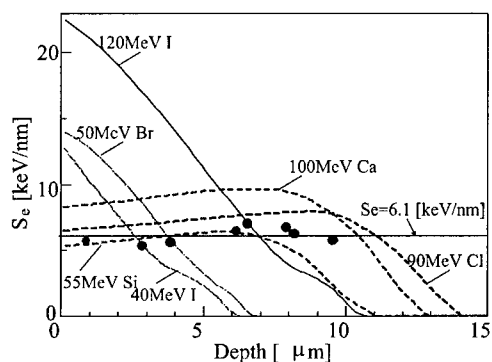
Figure 3. The electronic stopping power against depth calculated by SRIM98. Closed circles were experimental results of etched depth.

71
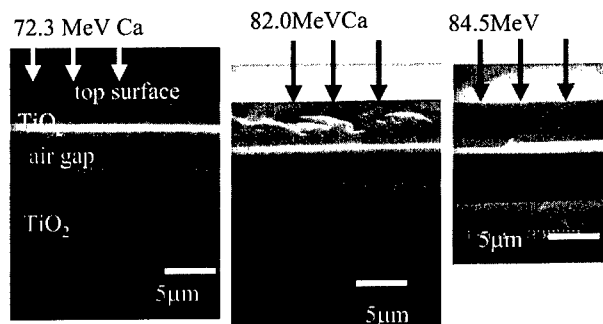
Figures 4. SEM images of the cross section of the sample etched following the (a) 72.3, (b) 82.0, and (c) 84.5MeV Ca ion irradiation to a dose of 3.0×10^{14} cm^{-2}. The ions were irradiated from the top of the image.

were always observed if the energy of Ca ions was higher than 72.3 MeV, and the position of the gap became deeper as the energy increased. For example, when the energy was 82.0 MeV, the gap was seen at depths between 5.4 to 7.7 µm from the top surface. Figure 3 shows the electronic stopping power S_e as a function of the depth. The dotted portion of each curve shows the depths where the hollow etching was made. Similar hollow etching was also observed in rutile irradiated by Cl ions with energies of 77.0 MeV and higher to a dose of 1.0×10^{15} cm^{-2}. It was also successful to demonstrate "micro-tunnel" in the middle of TiO$_2$ single crystal (Figure 5). An AFM observation of the bottom of the air gap depicted in Fig. 4 was shown in Figure 6. Roughness was estimated within 2.5 nm.

DISCUSSION

In XRD spectra shown in Fig.2, the 84.5-MeV Cu ion irradiation decreased the intensities of the peaks assigned to the original rutile crystal structure and induced the two peaks at the lower angular side. According to the Bragg law, a peak shift toward the lower
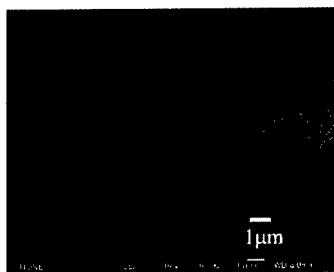
Figure 5. "Micro-tunnel" created by 84.5MeV Ca ion irradiation followed by etching.
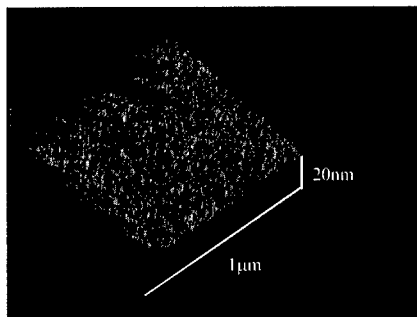
Figure 6. An AFM image of a TiO_2 surface subjected to 72.3MeV Ca ion irradiation at an accumulated dose of 8×10^{13} cm^{-2} through 1μm thick gold mask. Then, chemical etching with 20% hydrofluoric acid was performed for the irradiated sample.

angular side indicated the increase in a lattice constant. Actually, the expansion was observed as the upheaval by ion irradiation. Since TiO_2 crystal in rutile phase has the largest density among TiO_2 polymorphs, it seems that the expansion is due to a structural change induced by the ion irradiation. Decrease in intensities of both peaks at 39.2° and 84.3° means the degradation of a crystal structure, i.e. the formation of amorphous phase. From these considerations, it was found that the ion irradiation induces the amorphous phase and the expansion of lattice in a rutile TiO_2 single crystal. The original peak intensity decreased when the ions were irradiated to a dose of 4.0×10^{12} cm^{-2} (ii), but the intensity hardly changed with further irradiation (see in (iii) and (iv)). It does not imply the remaining of the crystal structure that the original peaks were still existed after irradiation, because x-ray intensity from Cu K_α was reduced by half through 50μm TiO_2 which is deeper than the ion penetration depth. In other words, the undamaged layer below the damaged layer could be detected by XRD measurement.

CONCLUSION

We have investigated the structural change in rutile TiO_2 single crystal induced by swift heavy-ion irradiation. It has been clarified that a rutile TiO_2 single crystal is not etched by hydrofluoric acid, however, the amorphous region and the stressed lattice region generated by the irradiation of swift heavy ions can be etched by hydrofluoric acid. When the ion whose value of electronic stopping power was decreased with depth of rutile TiO_2 single crystal and the depth that could be etched was limited to the point where the values of electronic stopping power was decayed to 6.2 keV/nm. It was also found that when the ion whose the maximum value of electronic stopping power was located at inside of TiO_2, inside could be selectively etched keeping the surface rutile phase and we can obtain the hollow structure. Energy deposited around the path of the ion showed that there was a threshold whether surface etching can be observed or not. Since the surface and aspect shape of rutile TiO_2 single crystals after etching was very flat in the order of nanometer, it was successful to fabricate 3-dimensional nano-structure by use of this etching technique.

This methods also makes it possible to fabricate rutile TiO$_2$ plates thinner than a few micron with nano order flatness, which has been difficult by the conventional methods. Our method will be available for the processing of solar cells, photonic catalysts, or photonic crystals, which require nano-fabrication technique.

ACKNOWLEDGEMENT

REFERENCES

1. M. Lanata, M. Cherchi, A. Zappettini, S. M. Pietralunga, and M. Martinelli, Opt. Mat. **17**, 11 (2001).
2. S.Yamazaki, N.Hata, T.Yoshida, H.Oheda, A.Matsuda, H.Okushi, K.Tanaka, J.Physique, **42**, C4-297 (1981).
3. K. Awazu, S. Ishii, K. Shima, S. Roorda, and J. L. Brebner, Phys. Rev. B **62**, 3689 (2000).

W3.9

Optical and Crystallographic Properties of Inverse Opal Photonic Crystals Grown by Atomic Layer Deposition

Jeffrey S. King, Curtis W. Neff, Dawn L. Heineman, Elton D. Graugnard, and Christopher J. Summers
School of Materials Science and Engineering, Georgia Institute of Technology,
Atlanta, GA 30332-0245

ABSTRACT

We report a technique for the formation of infiltrated and inverse opal structures that produces high quality, low porosity conformal material structures. ZnS:Mn and TiO_2 were deposited within the void space of an opal lattice by atomic layer deposition. The resulting structures were etched with HF to remove the silica opal template. Infiltrated and inverse opals were characterized by SEM, XRD, and transmission/reflection spectroscopy. The reflectance spectra exhibited features corresponding to strong low and high order photonic band gaps in the (111) direction (Γ-L). In addition, deliberate partial infiltrations and multi-layered inverse opals have been formed. The effectiveness of a post-deposition heat treatment for converting TiO_2 films to rutile was also studied.

INTRODUCTION

The work of John [1] and Yablonovitch [2] began an extensive research interest in the modeling, fabrication, and testing of a new class of materials, "photonic crystals". These materials exhibit a gap in the electromagnetic density of states within a given frequency range. Two & three-dimensional photonic crystal (PC) structures have the potential for controlling the emission wavelength, luminosity, efficiency, time response and threshold properties of phosphor materials, and are therefore attractive for luminescent structures. Many different PC structures have been proposed and studied [3-6] and a complete photonic band gap has been demonstrated at millimeter [3] and infrared [4,6] wavelengths. PC's based on the infiltration of synthetic opals have been established as promising structures for obtaining the required periodicity [6-11]. For an inverse opal with sufficient refractive index contrast (> 2.8), a complete PBG forms between high order photonic bands [12]. Recently, we have reported successful infiltrations of optically transparent, luminescent material using Atomic Layer Deposition (ALD) of ZnS:Mn[10,13]. When doped, ZnS is highly luminescent with a wide range of emission wavelengths. However, its refractive index is not high enough (~2.5) for the formation of a full photonic band gap, but is sufficient to produce a pseudo-photonic band gap. TiO_2 has a higher refractive index than ZnS, approaching 3.0 in the blue region [14].

In this study, we report results of the formation of ZnS:Mn and TiO_2 infiltrated and inverse opal films fabricated using ALD. In addition we report initial work on formation of luminescent, layered ZnS/TiO2 inverse opals similar to the semiconductor-based infrared photonic crystal structures recently demonstrated by García-Santamaría, et.al. [15]. The feasibility of obtaining the tetragonal TiO_2 rutile phase by heat treatment was also investigated. This phase exhibits the highest refractive index of TiO_2 crystallographic phases. For the rutile phase, the averaged refractive index (of the two polarization dependent indices) is 3.08 at 425 nm, and 2.67 at 750

nm [14]. TiO_2's increased refractive index at near ultraviolet wavelengths makes it a candidate for photonic crystal structures used at these wavelengths.

EXPERIMENTAL DETAILS

Face centered cubic (FCC) (111)-oriented silica opal structures were grown on silicon substrates in a manner similar to that of Park, *et al* [16], as described elsewhere [10]. The resulting opal films were 10 µm thick and polycrystalline (~100 µm grain size). The interstitial volume of the opal was next filled with ZnS:Mn or TiO_2 by ALD. $ZnCl_2$, H_2S, and $MnCl_2$ precursors were used for ZnS:Mn growth, and $TiCl_4$ and H_2O were used for TiO_2. For ZnS infiltrations, etching the infiltrated films in a 2% HF solution resulted in the removal of the silica spheres, and the formation of inverse opals. In the case of TiO_2 inverse opals, the top surface of the opal was first removed using an ion mill prior to etching with HF.

The films were characterized using specular reflectivity and Scanning Electron Microscopy (SEM) both after infiltration and after etching. In addition, X-ray diffraction was used for phase analysis. Energy band diagrams for the sintered, infiltrated and inverse opals were calculated using the plane wave expansion method [17].

RESULTS

The specular reflectance from deliberate partial infiltrations of 2.5, 5, 10 and 20 nm thick ZnS:Mn layers are shown in figure 1, for 15° from normal incidence. In the as-sintered condition, the peak at ~710 nm corresponds to the (111) Bragg diffraction peak, which arises due to a pseudo photonic band gap in the Γ-L direction. From calculations of the photonic band behavior of a stepwise infiltrated opal, we have found that as the shell layer thickness increases, the band gap should first shift to longer wavelength, then disappear at a set infiltration percentage, and reappear again, at an even longer wavelength, as shown in figure 2. This behavior was also predicted and observed by Blanco, et. al. [18]. The results in figure 1. confirm this progression, as the Γ-L peak was shown to increase after a projected 2.5 nm coating (0.7% of diameter), and disappear after a 5.0 nm coating (1.43% of diameter). The peak reappeared at a longer wavelength after a 10 nm coating (2.8% of diameter), shifting further and growing more pronounced after a 20 nm coating (5.7% of diameter). Figure 2. shows the experimental results compared with the calculated data. Each group has two lines, with the photonic band gap being clearly defined by the area between these lines. The experimental data is displaced from the calculated data, due in part to the 15° measurement angle, and part to thicker realized coatings than projected. The coating thicknesses are based on planar ZnS growth studies, and therefore are likely to differ when the deposition is in an opal. However, the crossover point where the (111) peak disappears is at 800 nm for both experimental and calculated data, indicating good agreement with theory. These results indicate that ALD infiltrations are highly controllable. The data also indicates that as the infiltration thickness increases, a higher energy pseudo photonic band gap forms around 400 nm.
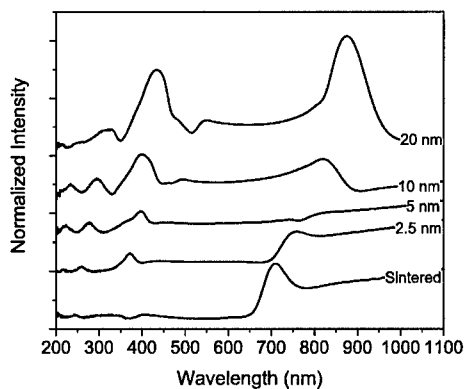
Figure 1. Specular reflectance measurements for 326 nm opal, before infiltration, and after 2.5, 5, 10 and 20 nm infiltrations.
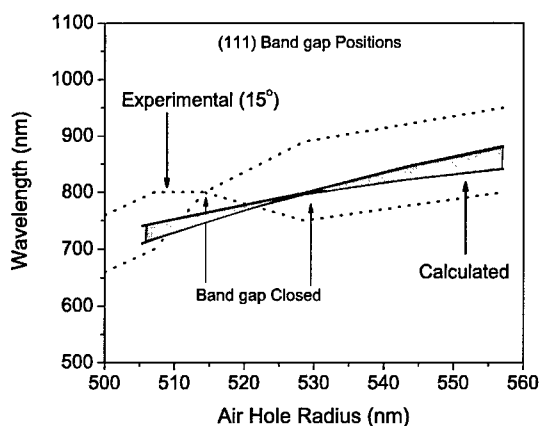
Figure 2. Calculated and experimental data illustrating Γ-L pseudo-band gap as a function of infiltration coating thickness. Lines represent boundaries of band gap.

Silica opals ranging from 150 to 460 nm in sphere diameter were successfully infiltrated with TiO_2 at both 100 and 500 ° C. Aarik, et.al. have demonstrated in planar TiO_2 growth studies that ALD produces amorphous films at low temperature ($<150°$ C), the anatase phase between 165° and 350° C, and the rutile phase above 350° C [19]. The motivation for growing amorphous films is that Aarik, et.al., also reported that amorphous films exhibited very smooth surfaces which are expected to be better suited for the conformal infiltration of opals.

Specular reflectance measurements of a 330 nm TiO_2 infiltrated opal are shown in figure 3. This data shows a shift of the Γ-L pseudo photonic band gap to longer wavelength after infiltration, as well as a shift back to a shorter wavelength for the inverse opal. In addition, after

infiltration, peaks appear at higher energy, indicative of higher order pseudo photonic band gaps. For the TiO_2 opal, the reflectivity spectra contain many more peaks than the ZnS opal [20], as a result of the increased refractive index contrast. After formation of the inverse opal, two peaks remain, the broad Γ-L peak, and the higher order peak.
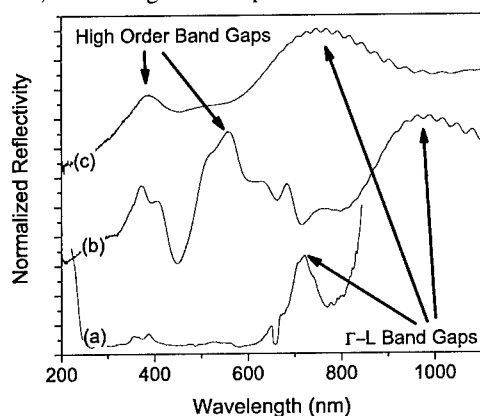
Figure 3. Specular reflectance for a 350 nm (a) sintered opal, (b) TiO_2 infiltrated opal, and (c) TiO_2 inverse opal. (a) was collected at 0°, (b) and (c) were at 15° from normal incidence.

After successfully forming inverse opals of ZnS:Mn and TiO_2, multi-layered infiltrations were performed where a layer of TiO_2 was first deposited, followed by a layer of ZnS:Mn. The TiO_2 layer was deposited at 100° C, and the ZnS:Mn layer at 500° C. A small part of the top layer of the resulting structure was milled off, in order to expose the underlying SiO_2 spheres, and the structure was then etched in 2% HF for 45 minutes. The resulting multi-layered opal is shown in figure 4, both before (inset) and after etching.
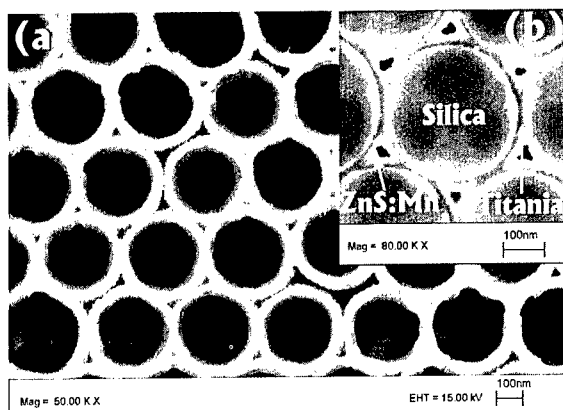
Figure 4. SEM of ZnS/TiO_2 (a) inverse opal and (b) infiltrated opal

The SEM image clearly shows the highly conformal coating achieved for both materials. This, in particular, is demonstrated by the well-defined spaces remaining at the FCC interstitial sites, which has been predicted to enhance the width of the photonic band gap [21]. Reflectivity measurements performed after each step also confirmed the stepwise nature of the infiltrations (results similar to figure 1), as well as the successful removal of the spheres.

In order to achieve highly conformal as well as high index infiltrations, the feasibility of converting infiltrated TiO_2 to rutile by heat treatments was also studied. The as-deposited opal was infiltrated at 500° C, but was primarily anatase. Figure 5 shows the development of the rutile phase in an infiltrated opal during heat treatments at different temperatures. A final rutile:anatase ratio of 1.35 was reached after a series of firings up to 1000° C. No degradation of the opal structure was found after the first 10 hours at 1000 ° C, but after 30 hours, the SiO_2 showed signs of dissolving in the TiO_2. However, it is anticipated that with a short firing time at even higher temperatures, a higher percentage of the rutile phase can be obtained with minimal effect on the opal.
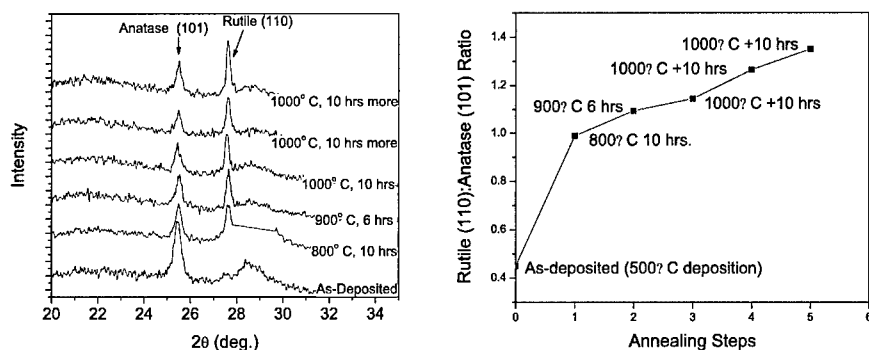
Figure 5. XRD data from TiO_2 opal. At left, increase in rutile phase due to annealing treatments. At right, ratio of (110) rutile peak to (101) anatase peak after annealing steps.

CONCLUSIONS

The potential for luminescence wavelength control, efficiency enhancement, threshold reduction, and improvement of other fundamental phosphor properties make photonic crystals an exciting new research area. The conformal nature, flexibility, and monolayer control of ALD makes it an important fabrication method for the formation of advanced photonic crystal structures. The work described has successfully demonstrated that ALD can be used for the formation of ZnS and TiO_2 opals that are robust enough to survive etching to form the inverse opal. In addition, the potential for making very complex luminescent photonic crystals has been demonstrated by the successful formation of multi-layered ZnS/TiO_2 inverse opals.

ACKNOWLEDGEMENTS

REFERENCES

1.   S.John, Phys. Rev. Lett. **58**, 2486 (1987).
2.   E. Yablonovitch, Phys. Rev. Lett. **58**, 2059 (1987).
3.   E. Yablonovitch, Phys. Rev. Lett. **67**, 2295 (1991).
4.   E. Özbay, E. Michel, G. Tuttle, R. Biswas, M. Sigalas, K.-M. Ho, Appl. Phys. Lett. **64**, 2059 (1994).
5.   S.Y.Lin, J.G. Fleming, D.L. Hetherington, B.K. Smith, R.Biswas, K.M. Ho, M.M. Sigalas, W.Zubrzycki, S.R. Kurtz, J. Bur, Nature **394**, 251 (1998).
6.   A.Blanco, E. Chomski, S. Grabtchak, M. Ibisate, S. John, S.W. Leonard, C. Lopez, F. Meseguer, H. Miguez, J.P. Mondia, G. A. Ozin, O. Toader, and H.M. Driel, Nature **405**, 437 (2000).
7.   Y. A. Vlasov, X-Z Bo, J. C. Sturm, and D. J. Norris, Nature **414**, 289 (2001).
8.   H. M. Yates, W. R. Flavell, M. E. Pemble, N. P. Johnson, S. G. Romanov, and CM Sotomayor Torres, J. Cryst. Growth **170,** 611 (1997).
9.   S. G. Romanov, R.M. De La Rue, H.M. Yates, and M. E. Pemble, J. Phys.: Cond. Matt. **12**, 339 (2000).
10.   J.S. King, C.W. Neff, W. Park, S. Blomquist, E. Forsythe, D. Morton, and C.J. Summers, Appl. Phys. Lett. **83**, 2566 (2003).
11.   W.Park, J.S.King, C.W. Neff, C. Liddell and C.J. Summers, Phys. Stat. Sol. (b) **229**, 949 (2002).
12.   H. S Sözüer, J. W. Haus, R. Inguva, Phys. Rev. B **45**, 13962, (1992).
13.   J.S. King, C. W. Neff, W. Park, D. Morton, E. Forsythe, S. Blomquist, and C .J. Summers. Presented at 2002 MRS Fall Meeting, Boston, MA December 1 – 5, (2002) (unpublished).
14.   E. D. Palik, *Handbook of Optical Constants of Solids*, San Diego: Academic Press (1998).
15.   F. García-Santamaría, M Ibisate, I. Rodríguez, F. Meseguer, C. Lopez, Adv. Mater., **15**, 788 (2003).
16.   S. H. Park, D. Qin, Y. Xia, Adv. Mater. **10,** 1028 (1998).
17.   S.G. Johnson and J.D. Joannopoulos, Opt. Express **8**, 173 (2001).
18.   A.Blanco, H. Míguez, F. Meseguer C. López, F. López-Tejeira, J. Sánchez-Dehesa, Appl. Phys.Lett. **78**, 3181 (2001).
19.   J. Aarik, A. Aidla, T. Uustare, V. Sammelselg, J. Crys. Growth **148**, 268 (1995).
20.   J. S. King, C. W. Neff, S. Blomquist, E. Forsthe, D. Morton, and C. J. Summers, *Physica Status Solidi, in press.*
21.   S. John, K. Busch *Journal of Lightwave Technology,* **17**, 1931 (1999).

Room temperature 1.3-1.55 µm laser-like emission from Ge/Si self-assembled islands in Si-based photonic crystals

J-M. Lourtioz, S. David, M. El Kurdi, C. Kammerer, X. Li, S. Sauvage, A.Chelnokov, V. Le Thanh, D. Bouchier, P. Boucaud,
Institut d'Electronique Fondamentale, UMR 8622 du CNRS, Université Paris-Sud,
Bâtiment 220 - 91405 Orsay - France

ABSTRACT

Experimental results are reported on various guided optic configurations that combine silicon-based photonic crystals (PC) and Ge/Si quantum island emitters. The feasibility of low-refractive-index-contrast PC waveguides by inductively-coupled-plasma (ICP) etching of buried SiGe/Si waveguides is briefly recalled from a previous work. The main body of the paper is focused on experiments that were carried out on the high-refractive-index-contrast silicon-on-insulator (SOI) system. Self-assembled Ge/Si quantum island layers were deposited on a SOI substrate that was further processed to get two-dimensional PC microcavities and waveguides. The room temperature 1.3-1.55 µm emission from Ge/Si islands is shown to be significantly enhanced in PC microcavities, the strongest enhancement being obtained with the smallest (micropillar-like) cavities surrounded by wide pores. In this latter case, the room-temperature photoluminescence amplitude is more than two-orders of magnitude larger than that of Ge/Si islands grown in unprocessed samples. A superlinear (laser-like) dependence with the optical pumping is observed in the same time. This behavior and other experimental trends would incriminate both a high carrier concentration of the photo-created electron-hole plasma and a good vertical coupling efficiency of the micro-structured silicon. A first attempt to characterize linear PC waveguides is also reported using the wideband luminescence of Ge/Si islands embedded in the guides.

INTRODUCTION

The last decade evolution of photonic crystals (PC) has open new solutions for the possible integration of compact optical devices in large scale photonic circuits. This evolution parallels the revolution accomplished in the domain of micro-electronics with the development of nano-transistors and memory quantum dots. Moreover, the combination of high-density photonics and electronics in future hybrid circuits may be an interesting issue of photonic crystals. From this viewpoint, silicon and silicon-based materials appear to be as choice materials. Indeed, impressive results have already been obtained in terms of fabrication, when, for instance, deeply etched photonic structures with short lattice period were needed for exploration studies of low-refractive-index-contrast PC waveguides [1,2]. Low loss performances have also been reported in recent experiments on high-refractive-index-contrast PC waveguides on Silicon-on-Insulator (SOI) [3,4].

However, the major drawback of silicon and other group IV materials for photonic applications is obviously their poor optical efficiency associated with their indirect gap characteristics. This is not only a penalty for active optical systems, but also a difficulty for the test of passive optical systems on chip such as those involved in future optical interconnects. Getting light efficiently out of silicon has always been a long standing goal for many researchers. Among the various existing solutions including rare-earth atom doping and

silicon nanocrystals [5], the use of electronic confinement in Si/SiGe heterostructures and nanostructures is particularly attractive since SiGe compounds are already recognized as standard materials for microelectronics. Moreover, room-temperature electro- (and photo-) luminescence of Ge/Si islands has been reported as early as in 2000 [6].

In this paper, we report on various guided optic configurations that combine Ge/Si self-assembled islands with silicon-based photonic crystals. Recent results obtained in the fabrication of low-refractive-index-contrast PC waveguides by inductively-coupled-plasma (ICP) etching of buried SiGe/Si waveguides are briefly recalled. The main body of the paper is focused on experiments that were carried out on the high-refractive-index-contrast SOI system. The room temperature 1.3-1.55 μm photoluminescence from Ge/Si islands is shown to be significantly enhanced in PC microcavities fabricated on SOI. A superlinear evolution of the signal with pump power is observed for the smallest (micropillar-like) cavities surrounded by wide pores, the signal amplitude at maximum being more than two-order of magnitude larger than that of Ge/Si islands grown on unprocessed samples. The luminescence results are also compared to those obtained around 1.5 μm from a single InGaAs quantum well optically pumped in the same conditions. The wideband luminescence of Ge/Si islands is also used in a first experimental attempt to characterize linear PC waveguides on SOI.

SILICON-BASED PHOTONIC CRYSTAL FABRICATION

There are basically two main options for two-dimensional (2-D) PC waveguides applicable to integrated optics : one uses a weak or moderate optical confinement in the third vertical direction like in conventional buried waveguides while the other is based on a strong confinement and is typical of membrane or semiconductor/oxide systems. The scientific community has now a clearer vision about the limits of these two alternatives, that merit to be studied simultaneously. Weakly confining PC waveguides are generally lossy waveguides, but with a relative insensitivity to perturbations such as bends, technological roughness...etc. In contrast, highly confining waveguides can theoretically provide lossless guiding but with a stronger dependence on structural perturbations.

For the silicon system as for other material systems, deep etching is the major fabrication challenge of weakly confining PC waveguides, since the minimization of their out-of-plane losses crucially relies on a sufficiently deep structuring of the guide cladding layers [7]. Two techniques are known to provide periodic lattices of holes with a high aspect ratio in silicon : macroporous silicon and ICP etching. Though macroporous silicon remains the model system with the highest aspect ratios (~100) [2,8], its compatibility with active opto-electronic devices is difficult due to the use of exact n-type doping for silicon. In contrast, ICP etching is applicable to a wide range of chemical compositions of the etched materials. Combined with electron lithography, ICP can thus be used for the fabrication of deeply etched PC structures. An illustration is given in fig. 1, which shows a profile of a PC etched in a buried Si-$Si_{0.95}Ge_{0.05}$-Si slab waveguide [1]. Actually, the SiGe guide core consists of a multilayer structure of Ge quantum islands, whose total thickness is around 1 μm. As seen, the pores are etched over a 10 μm depth and the pore walls remain vertical whatever the Ge concentration is. The lattice period is presently ~ 1.6 μm while the hole diameter is ~ 0.8 μm. Reduced sizes more adapted to the range of telecommunication wavelengths were achieved in recent experiments.
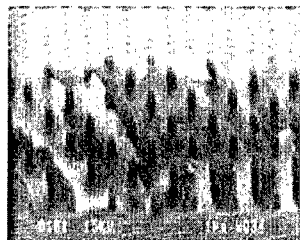
Figure 1. Triangular 2-D PC etched through a Si-Si$_{0.95}$Ge$_{0.05}$-Si slab waveguide. The profile of the holes does not change with the Ge concentration.

Unlike classical Si substrates, SOI substrates are ideally adapted to the fabrication of highly-confining PC waveguides. The holes of the 2-D PC lattice have just to be drilled in the Si top layer of typically ~0.3 μm thickness, much as in the membrane-type systems. Reactive-Ion-Etching (RIE) can be used for this purpose. Figure 2 shows a typical PC microcavity fabricated in the course of the present experiments
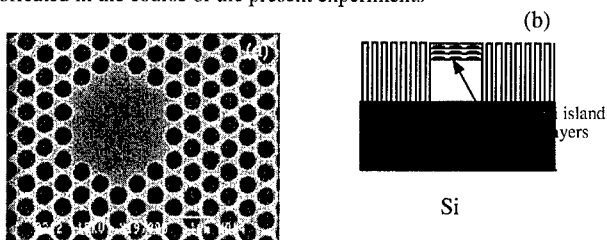
Figure 2. (a) Scanning electron micrograph of a photonic crystal H3 cavity fabricated on SOI. The PC period is 0.5 μm. The hole diameter is ~ 0.4 μm. (b) schematic of the layer profile.

The sample was grown on a SOI substrate with a 3.5 μm thick, buried oxide layer and a 0.2 μm thick silicon layer lying on top of the oxide. The active layer consisting of three Ge/Si self-assembled island layers separated by 20 nm silicon barriers was grown by low pressure chemical vapor deposition [9]. The islands had a typical base width of 120 nm and an height of 10 nm. The island density was around 1 x 10^9 cm^{-2}. The vertical correlation of the islands was observed by cross-section transmission electron microscopy. The total thickness of the waveguide core including Ge/Si island layers was 0.3 μm. This value was sufficiently small to ensure single-mode waveguiding at 1.5 μm once the whole PC structure was processed. After the island growth, a 0.2 μm thick oxide layer was deposited on top to provide an hard mask for silicon etching. The 2-D PC and microcavity (here a H3 hexagonal one [10]) were defined by electron beam lithography. The triangular lattice of holes with a 0.5 μm period was then processed. The pattern was transferred successively into the oxide layer and the guiding silicon-Ge/Si multilayers using RIE. The oxide layer and guiding silicon-Ge/Si

multilayers were etched with CHF_3 and SF_6 gases, respectively. The whole patterned surface was 50×50 μm^2. The holes drilled into the silicon-Ge/Si multilayers down to the buried oxide layer had presently diameters of ~0.4 μm. Correspondingly, the filling factor of the photonic crystals was ~65 %. After etching the holes, a thin oxide layer of the hard mask was kept on top of the structure, thus lowering the waveguide asymmetry.

PHOTOLUMINESCENCE RESULTS

Measurement set-up :

Photoluminescence (PL) measurements from Ge/Si islands were performed at room temperature with an Ar+ pump laser beam in a normal incidence configuration. The excitation and photoluminescence beams were focused and collected with the same objective of 0.65 numerical aperture. The excitation power was focused on a ~ 2 μm spot diameter. The luminescence was filtered with a 100 μm diameter pinhole located at the focal point of 15 cm focal lens. The luminescence was dispersed by a monochromator and detected with a liquid-nitrogen cooled germanium detector using standard lock-in techniques. The alignment of the pump beam on the cavity axis was achieved by imaging the sample surface with the argon laser.

Photoluminescence enhancement in PC microcavities :

At room temperature, the island photoluminescence measured on PC free regions of the samples was resonant around 0.91 eV and detected from 0.8 to 1.03 eV (0.11 eV full width at half maximum). The emission of silicon was detected between 1.030 eV and 1.15 eV with a resonance around 1.07 eV. Because of the relatively thick silica layer (~3 μm) and the optical arrangement used for PL detection, most of this high-energy PL originated from the silicon top layer, but not from the silicon substrate.

The Ge island PL was found to almost coincide with the photonic crystal bandgap in TE polarization (see fig.3, left). Indeed, for PC holes of 0.4 μm diameter and a PC period of 0.5 μm, the PC bandgap in TE is calculated to extend from 0.66 to 1.03 eV. In contrast, no gap exists for the TM polarization. Plane-wave calculations performed with the supercell method also show that numerous cavity modes (>13) are present within the TE gap, even for small hexagonal microcavities like H2 and H3.

Figure 3 (right) shows the measured PL spectra of H2 and H3 cavities compared to the PL spectrum of the same multilayer structure recorded outside the photonic crystal [11]. The pump power is 20 mW. The presence of the cavity leads to multiple resonances that modulate the PL spectra. These resonances correspond to the cavity modes that are coupled to the leaky continuum modes. In the case of the H3 cavity, the quality factor of these modes, defined as $Q = \omega/\Delta\omega$, reaches values between 200 and 300 at the lowest energies (i.e. at the longer wavelengths near 1.5 μm). As the major result, a significant enhancement of the room temperature PL is observed as the cavity size is decreased. A $\times 30$ enhancement is presently observed for the H2 cavity around 0.9 eV as compared to the reference. This is accompanied by a spectral broadening of the detected signal. A significant emission can be detected at 1.55 μm while no emission could be detected at this wavelength in the unprocessed sample under the same excitation conditions. Indeed, this result shows the great potential of two-

dimensional photonic crystal microcavities associated to Ge/Si self-assembled islands to enhance the light emission around 1.55 μm in silicon-based devices.
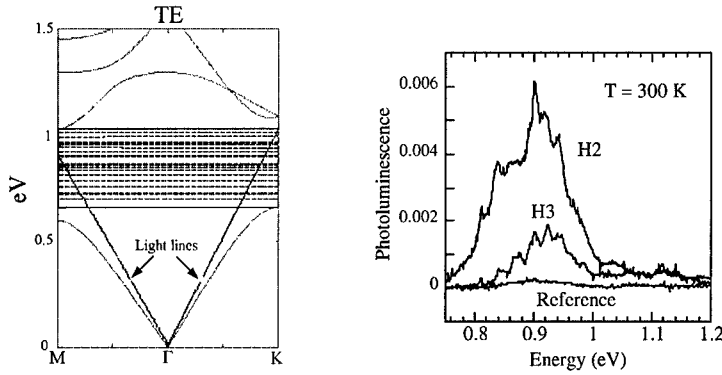
Figure 3. Left : Calculated dispersion diagram of the triangular PC on SOI for the TE polarization and the main crystal directions (same PC parameters as in fig. 2). The forbidden band gap is in gray. The dashed lines in the gap correspond to the defect modes of a H2 cavity. Right : room temperature PL of H2 (top curve) and H3 (bottom curve) cavities compared to the PL measured outside of the photonic crystal. The pump power is 20 mW.

PL dependence with pump power :

Beyond the performances, one of the most striking PL result is the nonlinear PL behavior with pump power when Ge/Si islands are embedded in small microcavities. This is illustrated in Figure 4, which shows the power dependence of the Ge/Si island photoluminescence measured on different kind of samples. The first sample (triangles) corresponds to a vertical stacking of Ge islands in a standard silicon matrix. The PL intensity measured at the energy peak (~0.91 eV) is characterized by a sublinear dependence with the excitation, as usually observed. The second sample (full dots) corresponds to Ge islands deposited on SOI, but without processing the photonic crystal. The presence of the silicon oxide layer blocks the diffusion of carriers towards the substrate and thus leads to an increase of the local carrier density. This local carrier density increase leads in turn to a superlinear emission that dominates above 30 mW as compared to the previous case. If we now consider H3 and H2 microcavities, we observe that the onset of the superlinear emission (laser-like) occurs at smaller excitation powers with a typical threshold around 10 mW for a H2 microcavity. We emphasize that this behavior is observed over the whole PL spectral range, but is not limited to a specific wavelength. We also note that the PL slope vs pump power increases for smaller cavities. Both effects lead to the drastic PL enhancement at room temperature that has been reported in fig.3.

As also seen in fig.4, the laser behavior is still more pronounced in the case of peculiar microcavities (called H2*) that have the same sizes as H2, but with a partially-removed

photonic crystal environment. A regular periodical patterning around the cavities is thus not required to observe the enhanced luminescence. However, the resonant character of the emission is lost in that case, and the photoluminescence spectrum is similar to the one of the original unprocessed structure (see fig. 3, right). Finally, let us note that the emission from the photonic crystal itself is always much weaker than that originating from a microcavity, whatever the type of microcavity is.
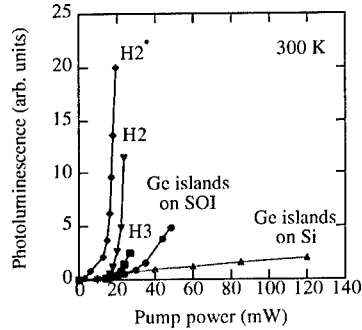
Figure 4. Peak photoluminescence amplitude at room temperature vs pump power. The triangles are for Ge islands embedded in a silicon matrix. Full dots are for Ge islands deposited on SOI. Squares and inverted triangles correspond to and H2 and H3 microcavities respectively. Diamonds correspond to an H2* microcavity with a partially-removed PC environment.

Comparison with a familiar III-V system :

To illustrate the PL efficiency of Ge/Si islands in SOI microcavities, a comparison was made with the emission of a high quality InGaAs quantum well (QW) pumped in the same conditions. The unprocessed III-V sample consisted of a single 7 nm thick $In_{0.38}Ga_{0.62}As$ quantum well surrounded by 100 nm thick GaAs barriers and 25 nm thick $Al_{0.3}Ga_{0.7}As$ barriers. Figure 5 (left) shows the PL evolutions of both the unprocessed InGaAs QW sample and the Ge/Si H2* microcavity. These evolutions are quite different. The peak photoluminescence amplitude of the InGaAs QW increases linearly at low pump powers, while it starts to saturate above 1 mW. Due to that, the gap between the optical efficiency of the Ge/Si islands and InGaAs QW regularly reduces with pump power. For an excitation of 20 mW, the integrated emitted power of the H2* cavity reaches 1 µW. The photoluminescence efficiency of the Ge/Si microcavity is then "only" two orders of magnitude lower than that of the bare III-V sample. Let us also note that the excitation delivered by the Argon ion laser is more efficiently absorbed in the GaAs matrix than in the top silicon layer. Figure 5 (right) shows a comparison between the spectral shapes of the two emissions. The PL linewidth is of the same order in both cases.
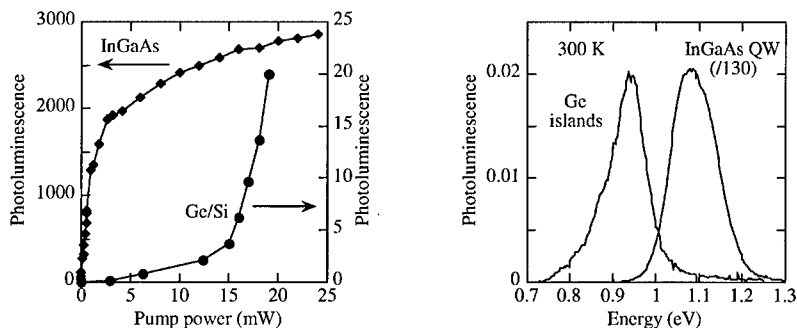
Figure 5. Left : photoluminescence signals from the InGaAs quantum well and Ge/Si islands versus pump power. The InGaAs quantum well is surrounded by AlGaAs barriers. The Ge/Si islands are in a H2* microcavity on SOI. (b) spectral shapes of the two emissions.

DISCUSSION

Previous studies have shown that two-dimensional PCs could be a powerful means to extract light from semiconductor slabs [12, 13]. They can act much as second-order gratings do. They can also help the vertical emission of PC microcavities for resonant modes whose wavefronts are aligned with the cavity edges [14]. This certainly occurs in our experiments when standard PC microcavities are used. However, the best performances are presently achieved with H2* (micropillar-like) cavities that are only partially surrounded by the photonic crystal. Similar performances were more recently obtained with true micropillars fabricated on SOI [15]. Therefore, light-extraction by the photonic crystal is not, by far, the dominant effect in our experiments. In turn, the origin of the PL enhancement must be sought in the carrier localization and recombination processes.

Note that a superlinear emission has already been reported for silicon devices, either in the case of bare silicon samples [16], p-n silicon diodes, p-mos silicon diodes [17] or silicon samples containing a high density of defects [18]. However, the non-linearity was relatively moderate in those cases as it scaled rather as the square of the excitation power.

Both the strong non-linearity and drastic PL enhancement observed in this work could be attributed to the high carrier densities achieved in the confined photonic structures. First, the buried SiO_2 barrier blocks the carrier diffusion towards the substrate [19]. Secondly, the lateral patterning of the structure tends to inhibit the lateral diffusion of carriers, thus leading to a local very dense electron hole plasma. The high plasma density provides additional scattering mechanisms for the carriers to the zone center, thereby enhancing the photoluminescence [20]. It is worth mentioning that the PL enhancement is only observed within the Ge islands and not in the silicon matrix. This *rules out thermal effects and black body radiation* since the whole material would be concerned in that case. Meanwhile, the trapping of holes in Ge islands limits the diffusion towards parasitic non radiative recombination centers, while it assists the optical recombination by Coulomb interactions. At

87

high carrier densities, strong band bending can occur around the Ge/Si heterostructure [21]. As the recombination is spatially indirect for Ge/Si islands between electrons in the silicon matrix and holes trapped in the islands, the band bending can enhance the overlap between electron and hole wavefunctions and thus enhances in turn the luminescence efficiency.

High electron-hole plasma densities in the system also favor many-body effects that can assist radiative recombination due to additional carrier scattering mechanisms [21,22]. Indeed, an abrupt (not thermal-type) decrease of the photoluminescence peak energy is observed for the H2* cavity simultaneously with the abrupt increase of the PL amplitude (fig.6). An opposite behavior would be expected for a classical band filling of the semiconductor heterostructures. Indeed, the present evolution could be the signature of an electron bandgap renormalization associated with exchange-correlation interactions between carriers.
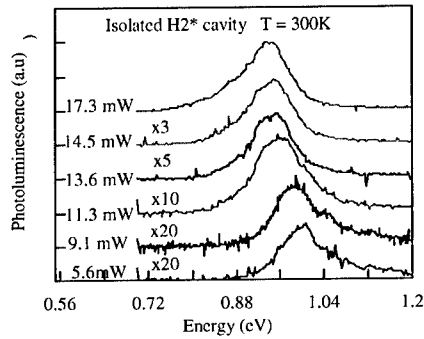
Figure 6. Spectral evolution of the room-temperature H2* photoluminescence with pump power.

PC WAVEGUIDE CHARACTERIZATION WITH Ge/Si ISLANDS

The characterization of 2-D photonic crystal waveguides is a key step toward the development of photonic circuits. There are basically two main experimental arrangements for the characterization of such waveguides : (i) the standard end-fire method where the light is injected from an external source through the cleaved facet of the semiconductor slab [23], (ii) the internal source method that uses the wideband luminescence of layers incorporated in the slab [24]. Both of these methods have their respective advantages and disadvantages, but their combination represent the most strategic way to have a full quantitative analysis of 2D-PC waveguide performances. Till now, due to the lack of internal sources, the characterization studies of silicon-based PC waveguides have been restricted to the end-fire method and its derivatives. From this viewpoint, the room-temperature luminescence of Ge/Si layers offers a very unique method to explore the internal source method for silicon-based photonics. First experiments were presently carried out with this aim.

Figure 7 (top) shows micrographs of linear PC waveguides that were fabricated on SOI. As usual, the linear PC- waveguides are obtained by omitting to drill one or several rows of

holes in the crystal. Correspondingly, they are labeled as W1, W2, W3...etc. The triangular lattice period, the hole diameters and the layer structure are the same as those used for the PC microcavities (see fig. 2). The propagation direction of the guides is ΓK. An Ar+ laser beam is focused onto the guide at a distance of ~15 µm of the cleaved facet. The laser spot diameter is around 2µm. The light emitted by the Ge/Si islands at the pump laser spot is then collected at the guide end after ~15 µm propagation. Actually, a fraction of the detected luminescence comes from the silicon substrate that is also pumped by the laser beam. This parasitic emission could not be eliminated as in the previous detection scheme used for PC microcavities.
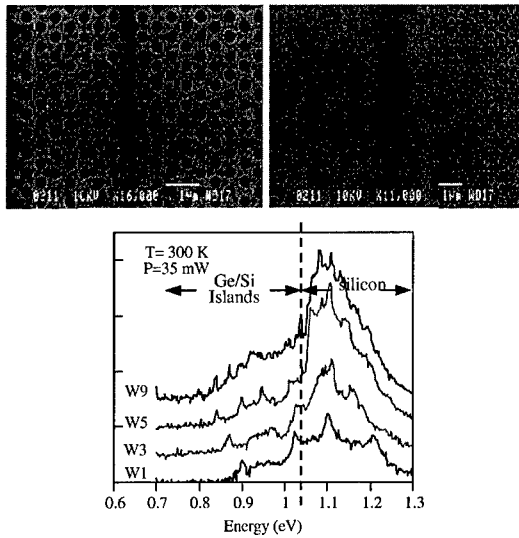
Figure 7. Top : micrographs of W1 (left) and W3 (right) PC waveguides including Ge/Si island layers. The PC characteristics and layer structure are the same as in fig.2. Bottom : room-temperature photoluminescence spectra measured at guide end for the W1, W3, W5 and W9 waveguides, respectively. The pump power is 35 mW. The respective contributions of the Ge/Si islands and the silicon substrate are indicated.

Figure 7 (bottom) shows the PL spectra measured at waveguide end for the W1, W3, W5 and W9 waveguides, respectively. The spectra are shifted from each other to better compare the different guide performances. Let us consider the PL contribution due to Ge/Si islands (below ~1.03 eV). The signal detected from the cleaved facet can be unambiguously attributed to guided modes, since it is not observed when Ge islands are excited either in the periodic PC or in a non structured region of the sample. As can be expected, the density of modes increases with the guide size. The wider the guide, the stronger the PL intensity. This

89

would suggest that smaller waveguides do ineluctably exhibit higher losses. However, a smaller guide width also leads to a smaller overlap with the laser excitation spot whose diameter is ~ 2 µm. Additional measurements and modeling are obviously required for a more detailed analysis.

CONCLUSION

We have shown that the incorporation of Ge islands in Si-based photonics has a great potential for the development of wavelength-scale, low-cost optical devices integrated on a silicon chip. Using classical Si substrates, the fabrication of low-refractive-index-contrast photonic-crystal waveguides has appeared to be feasible by inductively-coupled-plasma (ICP) etching of buried Si/SiGe/Si waveguides.

Using silicon-on-insulator substrates, a strong photoluminescence enhancement (×100) has been obtained for Ge islands in small micropillar-like cavities of ~1 μm^2 section. About 1 µW room temperature PL has been extracted from a single cavity near $\lambda \approx 1,35$ µm. The superlinear evolution observed with optical pumping has been attributed to the high carrier density that is achievable in such a highly confined structure on SOI. A further increase of the efficiency can be expected by optimizing the cavity geometry as well as the pump excitation. Indeed, Ge/Si self-assembled islands in a microcavity appear to be a challenging alternative to develop microsources operating at the telecommunication wavelengths that are monolithically integrated on silicon.

Finally, we have shown for the first time that the photoluminescence of Ge islands can be used to probe compact photonic structures and devices such as narrow photonic crystal waveguides on SOI. We believe that this internal-source probing method will be generalized soon in Si-based photonics.

ACKNOWLEDGMENTS

REFERENCES

1. A. Chelnokov, S. David, K. Wang, F. Marty, and J-M. Lourtioz, *IEEE Journ. Select. Topics in Quantum Electron.* **8**, 919 (2002).
2. J. Schilling, F. Müller, S. Matthias, R.B. Wehrspom, U. Gösele, K. Busch, *Appl. Phys. Lett.* **78**, 1180, (2001).
3. M. Notomi, A. Shinya, K. Yamada, J.-I. Takahashi, C. Takahashi, and I. Yokohama, *IEEE J. Quantum Electron.* **38**, 736 (2002).
4. J. Arentoft, T. Sondergaard, M. Kristensen, A. Boltasseva, M. Thorhauge, and L. Frandsen, *Electron. Letters* **38**, 274 (2002).
5. M.E. Castagna, S. Coffa, L. Caristia, A. Messina, *ESSDERC Proc.*, 439 (2002).
6. T. Brunhes, P. Boucaud, S. Sauvage, F. Aniel, J.-M. Lourtioz, C. Hernandez, Y. Campidelli, D. Bensahel, G. Faini, I. Sagnes, *Appl. Phys. Lett.* **77**, 1822 (2000).

7. H. benisty, P. Lalanne, S. Olivier, M. Rattier, C. Weisbuch, C.J.M. Smith, T.F. Krauss, C. Jouanin, and D. Cassagne, *Optical and Quantum Electronics* **34**, 205 (2002)
8. S. Rowson, A. Chelnokov, and J-M. Lourtioz, *J. Lightwave Technol.* **99**, 1989 (1999).
9. V. Le Thanh, V. Yam, P. Boucaud, F. Fortuna, C. Ulysse, D. Bouchier, L. Vervoort, and J. M. Lourtioz, *Phys. Rev.* **B 60**, 5851 (1999).
10. H. Benisty, C. Weisbuch, D. Labilloy, M. Rattier, C. J. M. Smith, T. F. Krauss, R. M. De la Rue, R. Houdre, U. Oesterle, C. Jouanin, and D. Cassagne, *J. Lightwave Technol.* **17**, 2063 (1999).
11. S. David, M. El Kurdi, P. Boucaud, A. Chelnokov, V. Le Thanh, D. Bouchier, and J-M. Lourtioz, Appl. Phys. Lett. **83**, 2509 (2003).
12. M. Boroditsky, T.F. Krauss, R. Coccioli, R. Vrijen, R. Bhat, and E. Yablonovitch, *Appl. Phys. Lett.* **75**, 1036 (1999).
13. D. Delbeke, R. Bockstaele, P. Bienstman, R. Baets, and H. Benisty, *IEEE J. Select. Topics Quantum Electron.* **8**, 189 (2002).
14. C.J.M. Smith, T.F. Krauss, H. Benisty, M. Rattier, C. Weisbuch, U. Oesterle, and R. Houdre, *J. Opt. Soc. Am. B* **17**, 2043, (2000).
15. M. El Kurdi, *PhD thesis,* Orsay, France (2003).
16. D. Guidotti, J. S. Batchelder, A. Finkel, and J. A. Van Vecheten, *Phys. Rev.* **B 38**, 1569 (1988).
17. C. W. Liu, M. H. Lee, M.-J. Chen, I. C. Lin, and C.-F. Lin, *Appl. Phys. Lett.* **76**, 1516 (2000).
18. E. O. Sveinbjörnsson, and J. Weber, *Appl. Phys. Lett.* **69**, 2686 1996).
19. M. Tajima, and S. Ibuka, *Journal of Applied Phys.* **84**, 2224 (1998).
20. B. E. Sernelius, *Phys. Rev.* **B 39**, 10825 (1989).
21. T. Baier, U. Mantz, K. Thonke, R. Sauer, F. Schäffler, and H. J. Herzog, Phys. Rev. B **50**, 15191 (1994).
22. D. Hulin, M. Combescot, J. Bok, A. Migus, J.Y. Vinet, and A. Antonetti, *Phys. Rev. Lett.* **52**, 1998 (1984).
23. M. Zelsmann, E. Picard, T. Charvolin, E. Hadji, B. Dal'zotto, M. Nier, C. Seassal, P. Rojo-Romeo, and X. Letartre, *Appl. Phys. Lett.* **81**, 2340 (2002).
24. D. Labilloy, H. Benisty, C. Weisbuch, C.J.M Smith, T.F. Krauss, R. Houdre, U. Oesterle, *Phys. Rev.* **B 59**, 1649 (1999).

Ultrasmall Lasers Based on Photonic Crystal Line Defects

Toshihiko Baba

Yokohama National University, Department of Electrical and Computer Engineering
79-5 Tokiwadai, Hodogayaku, Yokohama 240-8501, Japan

ABSTRACT

In this paper, we discuss unique light localization in a single line defect, which is effective for constructing photonic crystal light lasers. The localization is based on additional defect doping that breaks the symmetry of the line defect. Even though such a defect is opened to the line defect, the optical field is well confined around the defect at cutoff frequencies of the line defect. This concept expands the design flexibility of microcavities; for example, the composite of point and line defects and waveguide components such as bends and branches can be microcavities. It also allows effective mode controls such as the singlemode operation in relatively large cavities. The lasing operation of these cavities in a GaInAsP photonic crystal slab was experimentally observed by photopumping at room temperature. This paper reports lasing characteristics and the dependence on various structural details.

INTRODUCTION

Photonic crystals (PCs) are artificial multidimensional periodic structures with a period of the order of optical wavelength, which can be precisely designed by the photonic band theory. One of the most unique properties of PCs is a photonic bandgap (PBG). It inhibits or restricts the existence of optical modes and allows the strong control of light emission and propagation. The most fundamental applications of the PBG are cavities including lasers [1-7] and waveguides [8-14], which are composed of point and line defects, respectively. Those formed into two-dimensional (2D) PC slabs are now being studied worldwide. In these devices, the PBG acts as an angle-independent distributed Bragg reflector inside the 2D plane, and localizes or guides light in the defect region. To realize strong optical confinement in microcavities and microlasers, all sides of the point defect are normally surrounded and closed by the PC to completely suppress the light leakage. It simultaneously achieves a high Q factor and a small mode volume of, for example, > 10000 and $< 0.5(\lambda/n)^3$, respectively, where λ is the resonant wavelength and n the modal effective index. These values will be attractive for realizing a single photon emitter with a response speed enhanced by the Purcell effect, and a narrow band wavelength division multi/ demultiplexer with a wide free spectral range. But for other applications, such a small mode volume is not necessarily required. For example, for a standard microlaser in a photonic integrated circuit, the stable singlemode operation with a moderate output power is more desired.

In this paper, we discuss light localization, which is effective for the mode control in a PC cavity. It is different from the conventional point defect microcavity on the point that they utilize a line defect waveguide. Figure 1 shows a photonic band diagram of single line defect waveguide in a 2D PC of triangular lattice airholes. An important property seen in this figure is the cutoff frequency range of the waveguide band. As numerically demonstrated in [15], light is reflected at the input end of a PC waveguide at the cutoff range. In the case of Fig. 1, the cutoff range between the band-edge of the fundamental waveguide band (lower curve) and the top frequency of the lowest slab mode region acts as a full PBG even with the line defect.

If an additional defect is doped into the line defect, a mode having a resonant frequency at the cutoff range is strongly localized at the defect, while other modes overlapping with the waveguide band are not localized but radiated out through the waveguide. This concept provides wide variations in microcavity profiles, and allows useful mode controls such as singlemode resonance.

In the following sections, we describe various cavity profiles based on this concept, and experimentally demonstrate their lasing operation
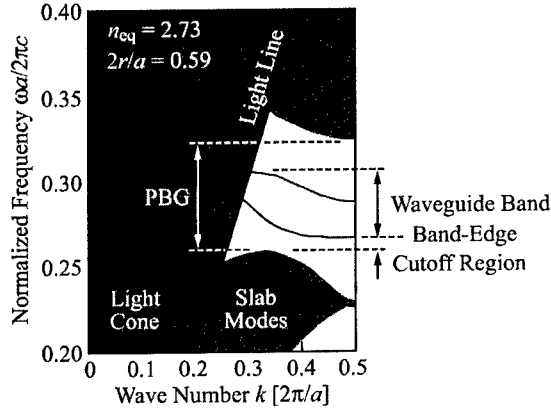
Figure 1. Photonic band diagram of single line defect in 2D PC of triangular lattice airholes. It was calculated by the plane wave expansion method with a plane wave number of 5253. In the 2D model, the diameter to lattice constant ratio $2r/a$ is 0.64. The background index is assumed to be 2.73, which is the same as an effective index of an airbridge semiconductor slab with an index of 3.5 and thickness of 243 nm at $\lambda = 1.55$ μm. Light line and light cone in an airbridge PC slab is displayed as a reference.
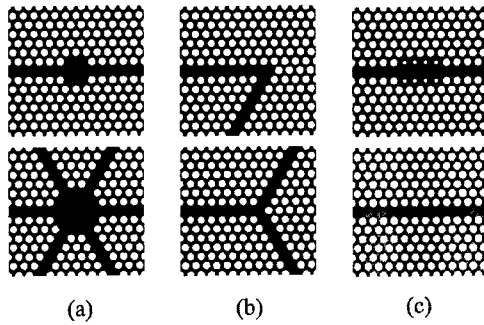
Figure 2. Various cavity profiles which utilize the cutoff frequency range of line defect. (a) Composites of point and line defect, (b) waveguide components, and (c) modified waveguides.

CAVITY STRUCTURES

Figure 2(a)-(c) shows schematics of three kinds of cavity structures in a 2D PC of triangular lattice airholes. Structure (a) has a point defect put into a line defect. We call it a point and line composite defect [16]. As an example, mode profiles and resonant spectra were calculated for a composite of so-called H2 point defect (hexagonal cavity of seven missing airholes) and three crossing line defects by using the finite difference time domain (FDTD) method, as shown in Fig. 3. Here, we modeled a PC slab by assuming an effective index of a semiconductor slab as a background index. In the simple H2 cavity, many resonant modes occur due to the wide PBG (the gap is ~22% of the midgap frequency) and the relatively large cavity size (an inscribed diameter is 2.8a). But in the composite defect, modes overlapping with the waveguide band are removed, and only a mode at the cutoff range (the gap is only ~4.5% of the midgap frequency) remains. The localized field profile in the composite defect is very similar to the one in the H2 defect (spectrum indicated by an arrow). Structure (b) is some simple waveguide element such as bends and branches [17, 18]. Even though they look like natural sequences of waveguides, they break the symmetry of a simple line defect. Therefore, they act as additional point defects and maintain a mode similar to those in composite defects. Structure (c) utilizes a heterostructure, in which some structural parameters are partly changed so that the modified region has a waveguide band at the cutoff range of the normal waveguide. (Here, the term "heterostructure" is used in the broader sense than in [19, 20], since the modified parameter is not limited to the lattice constant.) Similarly to the former two cases, the modified region acts as an additional point defect and maintains a cutoff mode.

Since the cutoff range is normally much narrower than the PBG, it is easy to obtain the singlemode resonance. Even in a larger composite defect, the singlemode will be maintained by adding an appropriate number of line defects. When the defect is several·μm in diameter,
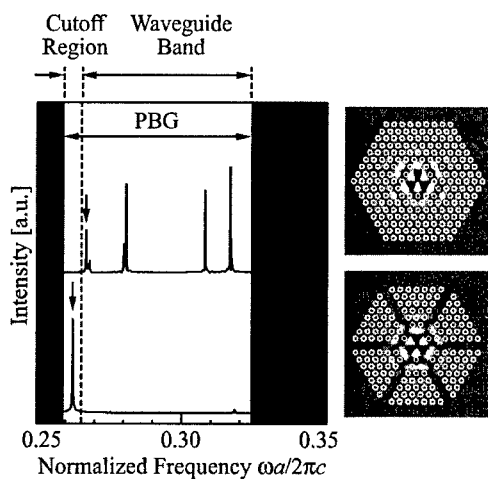
Figure 3. Resonant spectra and field profiles for H2 point defect (upper) and composite of H2 and three crossing line defects (lower), which are calculated by the FDTD method. Calculation parameters are the same as for Fig. 1.

95
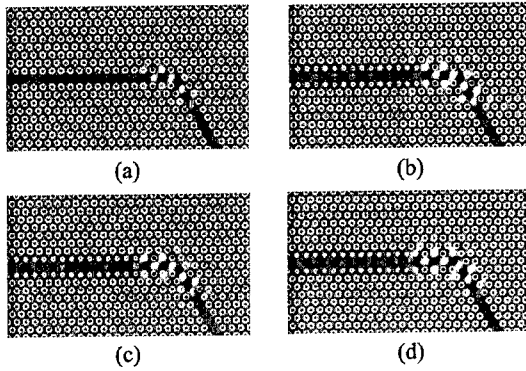
Figure 4. FDTD simulation of light extraction from 60° bend laser by using modified line defect waveguide. Design of modified waveguide in (a) – (d) correspond to those in Fig. 5.
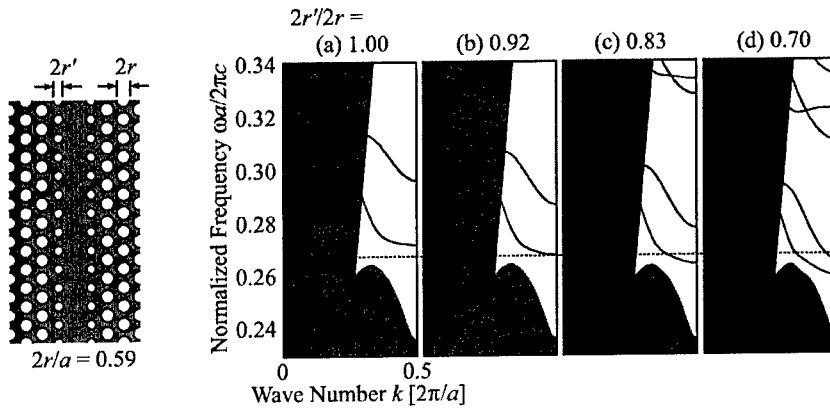
Figure 5. Schematic of modified line defect waveguide used for light extraction and its photonic band diagram with different airhole diameter $2r'$ beside the line defect.

an output power of mW order may be expected (cf. GaAs-based vertical cavity surface emitting lasers now commercially available normally have mW output in a similar cavity size). For the further stabilization of the singlemode, one has to take care of the symmetry of the cavity structure. It was experimentally shown that a cavity structure with a highly rotational symmetry causes a multimode resonance due to the splitting of degenerate modes. For example, the smallest point defect cavity of one missing airhole in a triangular lattice PC ideally has three degenerate modes with one resonance peak, but actually in an experiment, exhibits a multimode resonance arising from the break of the degeneracy in fabricated structures with a small disordering [1]. Since bends (b) and straight structures (c) have one- and two-fold rotational symmetry, respectively, they are free from the mode degeneracy problem and achieve a more stable singlemode operation. In addition, structures (a) – (c) are

suitable for extracting light because they are based on the PC waveguide. In these structures, a normal PC waveguide is used as a cavity mirror. By limiting the length of the normal waveguide and connecting a modified waveguide like that in (c), light in the cavity region tunnels to the modified waveguide. Therefore, light extraction is controlled by the length of the normal waveguide. Figure 4 shows an example of such light extraction by the FDTD simulation. Here, the modified waveguide has airholes with a reduced diameter $2r'$ just beside the line defect. The corresponding shift of the photonic bands is shown in Fig. 5. By reducing $2r'$ from $2r$, the fundamental waveguide mode shifts to lower frequency side, and finally the cutoff range disappeared. The horizontal line indicates a localized mode at the 60° bend. When $2r'/2r = 0.92$, the localized mode is extracted to this modified waveguide, as shown in Fig. 4(c). A peculiar light localization inside the waveguide in Fig. 4(b) and a zigzag propagation in Fig. 4(d) are caused by the overlap of the localized mode with the band-edge condition and by the overlap of two waveguide bands, respectively.

EXPERIMENT

In this study, some structures (a) and (b) in Fig. 2 were fabricated with normal hexagonal point defects and a single line defect in a GaInAsP PC slab to demonstrate the fundamental concept of using the cutoff condition of the line defect. In the experiment, an epitaxial wafer including five GaInAsP compressive-strained quantum wells grown on an InP substrate was prepared. The airhole array was formed by electron beam lithography and Cl_2/Xe inductively coupled plasma etching. The membrane structure of the PC slab was finally formed by the selective wet etching of InP substrate by HCl. The detail of the fabrication process is the same as that described in [16].Typical thickness t, lattice constant a and airhole diameter $2r$ were 0.243 μm, 0.42 μm and 0.22 μm, respectively. Cavity structures fabricated were H1, H2, H4 and H7 point defects, composite of H7 point defects and three line defects, a straight line defect, 60° and 120° bends, and a thee-fold symmetric branch in a line defect. Figure 6 shows pictures of fabricated PC slab, H2 point defect, and the composite defect. The maximum amplitude of roughness at the sidewall of airholes was less than 20 nm. The sidewall angle was 89 – 91°.

For all the structures, the lasing operation was observed at room temperature by pulsed photopumping at $\lambda = 0.98$ μm. Here, the pulse width, the repetition period and the focused spot diameter of the pump light were 75 ns, 500 μs and 5 – 6 μm, respectively. The light

━ 100 nm   ━━━ 1 μm   ━━ 1 μm

(a)   (b)   (c)
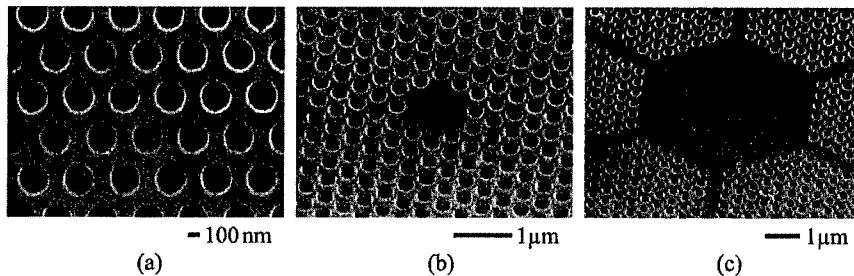
Figure 6. Scanning electron micrographs of (a) GaInAsP PC slab, (b) H2 point defect cavity, and (c) composite cavity of H7 point and three crossing line defects.
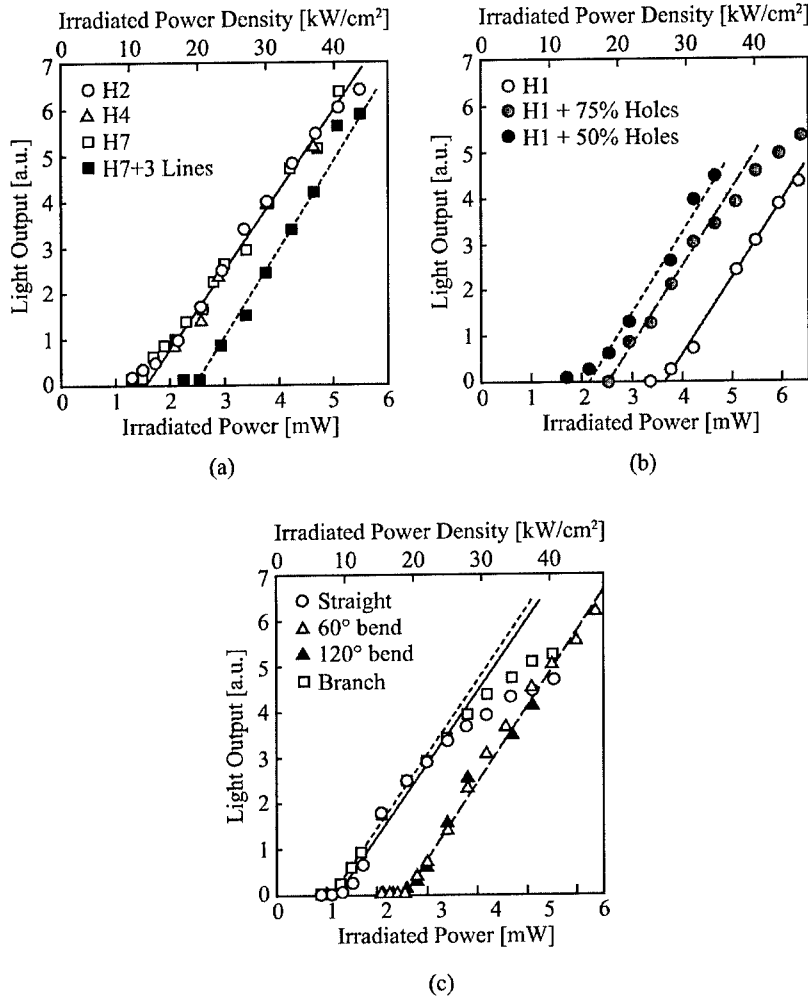
Figure 7. Lasing characteristics at room temperature by pulsed photopumping. (a) Point composite defect cavities. (b) H1 and its modified cavities. (c) Line, bend and branch cavities. These three were measured for devices fabricated in three different process cycles.

output from the device top was collimated and focused to a multimode fiber and analyzed by an optical spectrum analyzer. Observed lasing characteristics are shown in Fig. 7 and the corresponding spectra are shown in Figs. 8 and 9. Since devices shown in (a), (b) and (c) were fabricated by three different process cycles, we can compare the results in each figure. As shown in Fig. 7(a), the typical threshold power of external irradiation for H2 and larger point defects was nearly 1.5 mW. The corresponding absorbed power estimated by considering the filling factor of air, the effective mode area, the slab thickness, and an absorption coefficient
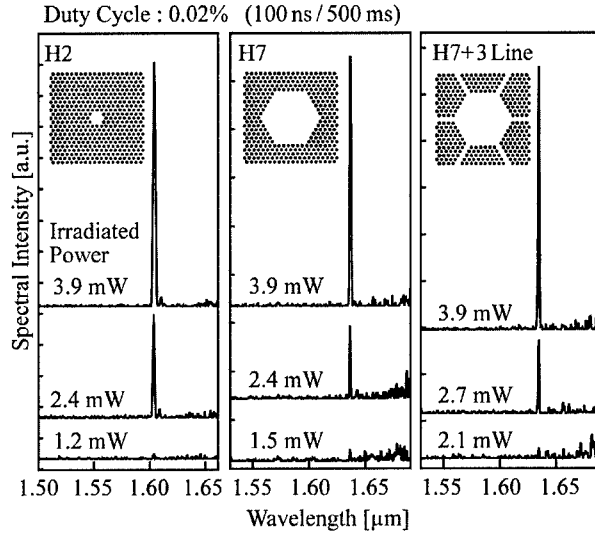
Figure 8. Lasing spectra for point and composite defects.

of the pump light at the slab of 20000 cm^{-1} was 70 μW. For different size point defects, no significant difference in threshold was observed. This is considered to be due to the large spot diameter of pump light, which completely covered these cavities, and due to the similar threshold power densities for them. Therefore, if the spot diameter of pump light is reduced to 3 μm for the H2 defect, a threshold of less than 0.3 – 0.5 mW will be possible, which is almost the same value as those recorded for an optimized H1 defect [21]. Regarding the normal H1 defect, the threshold was as high as 4 mW, as shown in Fig. 7(b). One main reason for this is a poor quality of the fabricated device. Another important reason is the lack of structural optimizations, which suppresses the optical leakage from the ultrasmall cavity toward the air. As a structural optimization, we fabricated modified H1 defects with a reduced diameter of six airholes surrounding the center defect. It is clear that smaller six airholes give lower threshold. By employing 50% diameter for the six airholes, the threshold was reduced to nearly half. This value was the same as that for H2 defect fabricated in this process cycle.

The threshold for the composite defect is slightly higher than the point defects, as seen in Fig. 7(a). It is considered to be due to the optical leakage and the carrier diffusion, which were enhanced by the line defects. Therefore, a structural modification and a carrier confinement structure should be considered in future, which are common issues for PC microcavity lasers. The threshold for the bends and the branch were also higher than those for the point defects. This must be due to their strongly asymmetric structures and corresponding mode profiles, which enhance the optical leakage. It is known from the result that the three-fold symmetric branch having a good consistency with the triangular lattice exhibited the lowest threshold of ~1 mW. The threshold for the simple line defect is also measured to be as low as 1.2 mW. However, we also observed strong position dependence; the threshold varied from 1.2 to 4 mW in different line defects and different photopumped positions. The reason for this is not clear, but we suppose some disordering in the line defects that can produce a light localization. Otherwise, it is difficult to explain this dependence and such a

low threshold against the small focused spot of the pump light, which cannot totally excite the widely expanded line defect mode. In the spectra shown in Fig. 9, however, we noticed a clear difference between the simple line defect and the waveguide components. Lasing wavelengths for the bends and the branch were longer than that for the line defect. This well corresponds to lower normalized frequencies for these waveguide components, which were calculated by the FDTD method.

(a)   (b)
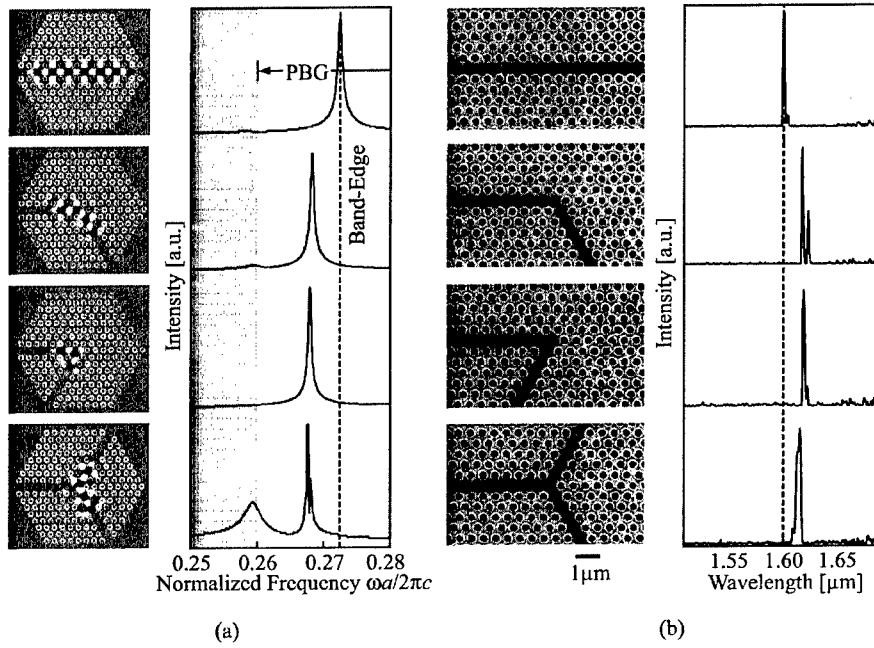
Figure 9. Comparison of resonant and lasing characteristics for straight waveguide and waveguide components between FDTD simulation and experiment. (a) Mode profiles (magnetic field in vertical direction) and resonant spectra by FDTD. (b) SEM views and observed lasing spectra in the experiment.

CONCLUSION

We proposed to use the cutoff condition of line defect for the construction of PC microcavities. Through the FDTD simulation, various cavity profiles with well localized modes were found to be available as microcavities. This expectation was experimentally verified by fabricating laser devices in a GaInAsP semiconductor PC slab. The lasing was observed at room temperature by pulsed photopumping. From the observation of lasing wavelengths, the operation at the cutoff frequency range was confirmed.

In this study, we limited our discussion to the demonstration of such a new cavity concept. Therefore, we did not investigate the detail of mode degeneracy issue and the cavity

Q mainly determined by the optical leakage into air. The low threshold obtained for the Y branch suggested that there is plenty of room for investigating an excellent cavity based on this concept. It is a next interesting issue.

ACKNOWLEDGMENTS

REFERENCES

1. O. J. Painter, A. Husain, A. Scherer, J. D. O'Brien, I. Kim, and P. D. Dapkus, *J. Lightwave Technol.* **17**, 2082 (1999).
2. H. G. Park, J. K. Hwang, J. Huh, H. Y. Ryu and Y. H. Lee, *Appl. Phys. Lett.* **79**, 3032 (2001).
3. C. Monat, C. Seassal, X. Letartre, P. Viktorovitch, P. Regreny, M. Gendry, P. Rojo-Romeo, G. Hollinger, E. Jalaguier, S. Pocas and B. Aspar, *Electron. Lett.* **37**, 764 (2001).
4. P. T. Lee, J. R. Cao, S. J. Choi, Z. J. Wei, J. D. O'Brien and P. D. Dapkus, *IEEE Photon. Technol. Lett.* **14**, 435 (2002).
5. C. J. M. Smith, T. F. Krauss, H. Benisty, M. Rattier, C. Weisbuch, U. Oesterle and R. Houdré, *J. Opt. Soc. Am. B* **17**, 2043 (2000).
6. M. Imada, S. Noda, A. Chutinan, M. Mochizuki and T. Tanaka, *J. Lightwave Technol.* **20**, 873 (2002).
7. S. Y. Lin, E. Chow, S. G. Johnson and J. D. Joannopoulos, *Opt. Lett.* **26**, 1903 (2001).
8. T. Baba, N. Fukaya and J. Yonekura, *Electron. Lett.* **35**, 654 (1999).
9. M. Tokushima, H. Kosaka, A. Tomita and H. Yamada, *Appl. Phys. Lett.* **76**, 952 (2000).
10. M. Lončar, D. Nedeljković, T. Doll, J. Vučković, A. Scherer and T. P. Pearsall, *Appl. Phys. Lett.* **77**, 1937 (2000).
11. S. Y. Lin, E. Chow, S. G. Johnson and J. D. Joannopoulos, *Opt. Lett.* **25**, 1297 (2000).
12. C. J. Smith, H. Benisty, S. Olivier, M. Rattier, C. Weisbuch, T. F. Krauss, R. M. De La Rue, R. Houdré and U. Oesterle, *Appl. Phys. Lett.* **77**, 2813 (2000).
13. M. Notomi, A. Shinya, K. Yamada, J. Takahashi, C. Takahashi and I. Yokohama, *Electron. Lett.* **37**, 293 (2001).
14. Y. Sugimoto, N. Ikeda, N. Carlsson, et al., *J. Appl. Phys.* **91**, 3477 (2002).
15. J. Yonekura, M. Ikeda and T. Baba, *J. Lightwave Technol.* **17**, 1500 (1999).
16. K. Inoshita and T. Baba, *IEEE J. Sel. Top. Quantum Electron.* **9**, (2003, to be published).
17. K. Inoshita and T. Baba, *Electron. Lett.* **39**, 844 (2003).
18. K. Inoshita and T. Baba, *Jpn. J. Appl. Phys.* **42**, 6887 (2003).
19. S. Kawakami, T. Sato, K. Miura, et al., *IEEE Photon. Technol. Lett.* **15**, 816 (2003).
20. B. S. Song, S. Noda and T. Asano, *Science* **300**, 1537 (2003).
21. M. Loncar, T. Yoshie, A. Scherer, P. Gogna and Y. Qiu, *Appl. Phys. Lett.* **81**, 2680 (2002).

Growth and Optical Properties of 2D Photonic Crystals Based on Hexagonal GaAs/AlGaAs Pillar Arrays by Selective-Area Metalorganic Vapor Phase Epitaxy

J. Motohisa, J. Takeda, M. Inari, and T. Fukui
Research Center for Integrated Quantum Electronics, Hokkaido University, North 13, West 8, Sapporo 060-8628, Japan

ABSTRACT

We report on the growth of GaAs and GaAs/AlGaAs heterostructured hexagonal pillar arrays using selective area (SA) metalorganic vapor phase epitaxy (MOVPE) for the application of two-dimensional photonic crystals (2D-PhCs). SA-MOVPE was carried out on SiO_2 masked (111)B GaAs substrates with circular or hexagonal hole openings. Extremely uniform array of hexagonal GaAs/AlGaAs pillars consisting {110} vertical facets with their diameter of order of 200 nm were obtained. Unexpectingly strong intense light emission was observed for the room temperature photoluminescence measurement, which suggests low surface nonradiative recombination and enhancement of the light extraction efficiency of the pillar arrays.

1 INTRODUCTION

Selective area (SA) growth on masked substrates is one of the most versatile methods to form semiconductor quantum nanostructures free from process induced damages in a self-organized fashion. Formation of various kind of nanostructures have been reported by SA growth both on (001) and (111)B substrates using metalorganic vapor phase epitaxy (MOPVE). In the case of SA-MOVPE growth on (111)B GaAs, nanostructures surrounded by vertical or inclined {110} facets are formed depending on the growth conditions, which makes this approach attractive and powerful to form quantum dots[1] and hexagonal structures[2]. Recently, SA-MOVPE growth of photonic crystals (PhCs) [3] consisting of periodic array of hexagonal GaAs pillar structures on (111)B GaAs is reported. We also have reported on the formation of the air-hole array of GaAs[4, 5], and pillar arrays of InGaAs[6] and InP[7] with their period a down to 0.4 μm by SA-MOVPE on (111)B- or (111)A-oriented substrates.

In this paper, we report the formation of GaAs/AlGaAs hexagonal pillar structures by SA-MOVPE on (111)B GaAs substrates for the application of two-dimensional (2D) PhCs. We will describe the formation of uniform pillar arrays and their photoluminescence (PL) characteristics for PhCs.

2 EXPERIMENTAL PROCEDURE

SA-MOVPE was carried out on GaAs (111)B substrates partially covered with SiO_2. The mask pattern of SiO_2 was defined by electron beam lithography and wet chemical etching, and triangular lattice array of holes with size d_0 were formed. The period a (or lattice constant of PhC) was varied from 0.2 μm to 3 μm. Although we designed to form hexagonal holes of SiO_2 with $d_0 \sim$ 50 nm, the actual size of the holes was much larger and their shape was triangular, due to the resolution limit of our fabrication process. With all such deterioration, we were able to obtain six-fold symmetric pillars and their uniform and high-density arrays owing to the evolution of sidewall {110} facets during the growth[6, 3] originating from the six-fold symmetry of vertical {110} surfaces on (111)B.

The growth was carried out in a horizontal, low-pressure system working at 0.1 atm. The hexagonal GaAs and AlGaAs pillar structures can be grown on appropriate growth conditions. The

growth temperature was 750°C for GaAs pillar arrays and 850°C for pillars containing AlGaAs. The detail of the growth procedure is reported elsewhere[8].

Structural characterization was carried out using a HITACHI S-4100 secondary electron microscope (SEM). Photoluminescence was measured at room temperature using ×20 microscope objectives with numerical aperture of 0.4 both for focusing and collection of the light normal to the surface (see inset of Fig. 2). Ar$^+$ laser operating at 514.5 nm and liquid-nitrogen cooled charge coupled device combined with spectrometer were used for excitation and detection, respectively.
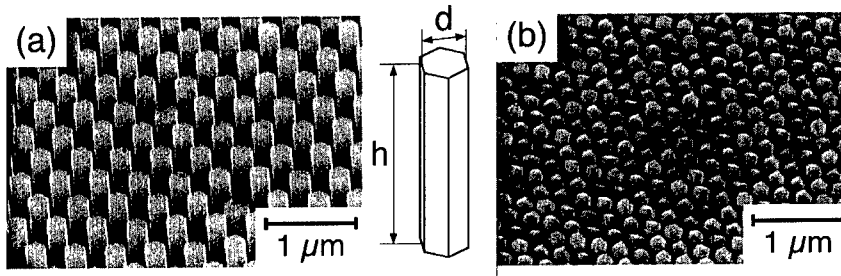
Figure 1: (a) Typical SEM images of GaAs hexagonal pillar arrays with $a = 0.4$ μm taken from an oblique angle. (a) Typical SEM images of GaAs/AlGaAs hexagonal pillar arrays with $a = 0.25$ μm. Inset shows the definition of size of the pillars.

3 RESULTS AND DISCUSSIONS

Figure 1(a) shows typical bird's eye view SEM images of the GaAs pillar arrays of $a = 0.4$ μm. We can see uniform arrays of vertical hexagonal pillars consisting of six {110} sidewall facets. The average lateral size d of the pillars was 0.24 μm, and their height h was about 1.4 μm for this sample. The standard deviation σ of the size distribution of the pillars were measured to be 7.1 nm, demonstrating excellent size uniformity of the hexagonal pillars. A measure of size uniformity σ/a was calculated to be 1.7%, and it is thought to satisfy the requirements ($\sigma/a < 5\%$) for the application to PhCs. We note that the pillar height is much larger than the growth thickness (0.19 μm) on reference (001) GaAs substrate grown simultaneously in the same run. This is ascribed to the diffusion of growth species from masked areas. The amount of enhancement in the growth rate is found to depend on the period a of pillar arrays and the initial opening d_0 of the mask as well as growth conditions. The detail will also be described elsewhere[8, 9].

Figure 1(b) shows typical bird's eye view SEM images of the GaAs/Al$_{0.25}$Ga$_{0.75}$As heterostructured pillar arrays. This heterostructured pillar arrays are used for PL study described below, and the layer structure is shown in Fig. 2(a) together with the designed thickness on (001) substrate. For this image, the period a is 0.25 μm, and the pillar size d is 0.18 μm. Uniform array of hexagonal pillars are also formed. We find the typical aspect ratio h/d of the pillars is about 3 and is much smaller than the GaAs pillars. This is because of the different preference of the growth on (111)B top and {110} sidewall surfaces between GaAs and AlGaAs, and AlGaAs has more tendency to proceed growth laterally from {110} sidewalls.
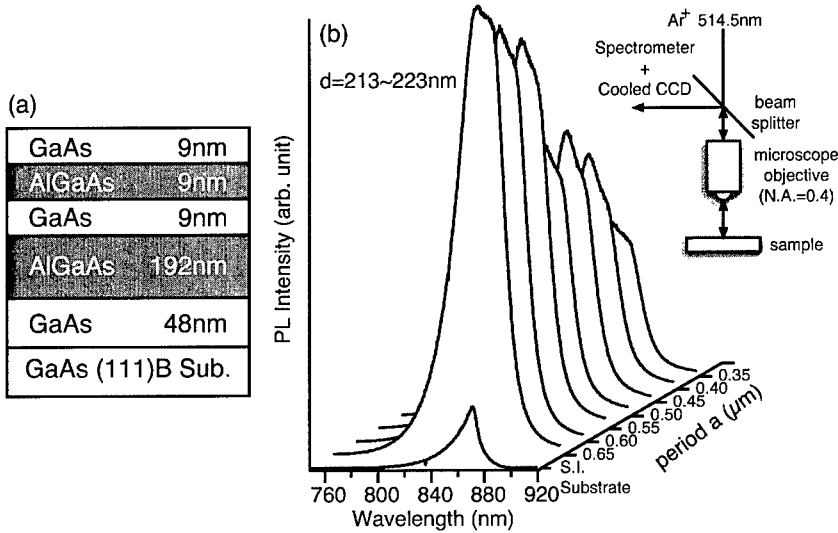
Figure 2: (a) Layer structure of AlGaAs/GaAs heterostructured pillars for the sample for PL measurement. The thickness is for the planar substrate and is much thicker for masked substrates. (b) PL spectra of the hexagonal pillar arrays with different period a of the triangular lattice. Inset shows the measurement setup.

Next, we measured the photoluminescence (PL) of the pillar arrays of the sample shown in Fig. 1(b). The room-temperature PL spectra of the pillar arrays with various a are summarized in Fig. 2(b). The pillar size d is somewhat dependent on a, but is in the range of 213 $\sim$ 223 nm. Strong emission was observed in each PL spectrum at around 860 nm close to the band edge of GaAs emission, which is attributable to the emission form GaAs quantum well (QW) formed top on the pillars. The integrated intensity was about 5 to 10 times stronger than that of a semi-insulating GaAs substrate. This emission is surprising considering the small diameter of the pillars. According to a simple estimation based on the diffusion equation which takes into account the nonradiative recombination of the sidewalls[10], the emission efficiency of pillars with $d \sim 200$ nm is three orders of magnitude smaller than that in the bulk GaAs. Such significant reduction of the emission efficiency seems to be absent in our pillar arrays. We think this is because AlGaAs layer caps over the {110} sidewall of pillars during the growth (lateral overgrowth)[11, 12], and bare sidewall surface of GaAs QW is not directly exposed to air. Such lateral overgrowth is possible if we consider the preference of the growth of AlGaAs described above. We recently found structural evidence of the such overgrowth and will be described elsewhere.

Next, we discuss about the effect originating from PhCs. Fan $et\ al.$[13] have shown that the light extraction efficiency from slab structures can be enhanced drastically in PhCs as compared to the slab structures. This is because the slabs having large refractive index should exhibit strong internal reflection at the surface, which gives rise to the propagating mode in the slab, and eventually, poor
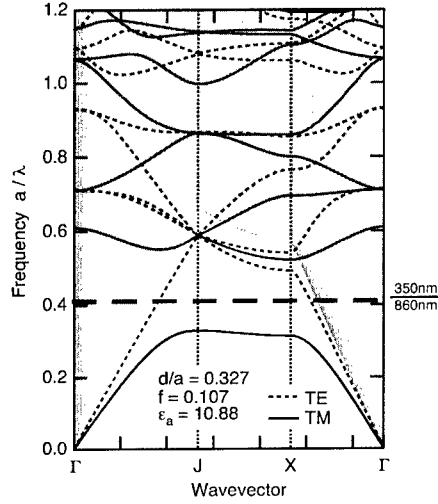
Figure 3: Calculated two-dimensional photonic bandstructure of pillar arrays in triangular lattice. The bandstructure is calculated for normalized pillar size d/a of 0.327, and dielectric constant of pillars of $\varepsilon_a = 10.88$. Solid and doted lines represent the bands for TM and TE polarization, respectively. Thick dashed lines indicates the position of normalized frequency a/λ of 350 nm/860 nm = 0.406. The shaded region indicates the mode above light line of the air.

light extraction from the surface. It can be eliminated, however, by fabricating periodic structure on the surface as the coupling to the leaky (radiation) mode is promoted by diffraction or by the photonic bandgap which prohibits lateral propagation. Some experimental demonstrations have already been reported[14, 15, 16, 17].

In the results shown in Fig.2(b), the PL intensity increases as a. It cannot be explained by the difference of surface recombination since we have larger pillars for shorter a. For qualitative understanding on the effect of 2D-PhC, we calculated the 2D-photonic bandstructure of the hexagonal pillar arrays for $d/a = 0.327$, as shown in Fig.3. For $a = 350$ nm and emission wavelength λ of 860 nm, the normalized frequency $\nu/(c/a) = a/\lambda$ lays at the thick dushed line in the figure. Assuming constant d/a, the increase of a simply pushes up the normalized frequency in the photonic bandstructure of Fig. 3. Therefore, more modes are pushed above the light line of the air as a is increased, which gives rise to the leakage of the light from the slab. Hence, PL extraction efficiency is increased as a becomes longer. We believe that our results are explained in this mechanism. Similar effect is experimentally observed by Ryu et al.[16, 17]. We must admit that present discussion neglects the change of normalized pillar size d/a, and the dependence of the light extraction efficiency on the parameters of PhCs is quite complicated[13]. Accurate numerical analysis on the light extraction efficiency is required and is left for future study.

4 SUMMARY

We have demonstrated the formation of hexagonal GaAs/AlGaAs pillars by selective area met-alorganic vapor phase epitaxial growth on (111)B GaAs masked substrates. Extremely uniform arrays of hexagonal pillars in triangular lattice have been obtained at optimized growth conditions. Photoluminescence study of GaAs/AlGaAs pillar array strongly suggests the small influence on the nonradiative recombination at the sidewall surfaces and the enhancement of light extraction efficiency in photonic crystals.

ACKNOWLEDGMENTS

References

[1] T. Fukui, S. Ando, Y. Tokura, and T. Toriyama, Appl. Phys. Lett. **58**, 2018 (1991).

[2] S. Ando, N. Kobayashi, and H. Ando, Jpn. J. Appl. Phys. **32**, L1293 (1993).

[3] T. Hamano, H. Hirayama, and Y. Aoyagi, Jpn. J. Appl. Phys. **36**, L286 (1997).

[4] M. Akabori, J. Takeda, J. Motohisa, and T. Fukui, Physica E **13**, 446 (2002).

[5] J. Takeda, M. Akabori, J. Motohisa, and T. Fukui, Appl. Surf. Sci. **190**, 236 (2002).

[6] M. Akabori, J. Motohisa, and T. Fukui, IEEE Conf. Proc. 27th Int. Symp. Compound Semi-conductors, 191 (2001); M. Akabori, J. Takeda, J. Motohisa, and T. Fukui, Nanotechnology **14**, 1071 (2003).

[7] M. Inari, J. Takeda, J. Motohisa and T. Fukui, in workbook of the 11th international con-ference of Modulated Semiconductor Structures (MSS-11) (Nara, Japan, 2003); M. Inari, J. Takeda, J. Motohisa and T. Fukui, to be published in Physica E (2004).

[8] J. Motohisa, J. Takeda, M. Inari, J. Noborisaka, and T. Fukui, accepted for publication in Physica E.

[9] J. Noborisaka, J. Motohisa, and T. Fukui, unpublished.

[10] V. Malyarchuk, J. W. Tomm, V. Talalaev, Ch. Linau, F. Rinner, and M. Baeumler, Appl. Phys. Lett. **81**, 346 (2002).

[11] S. S. Chang, S. Ando, and T. Fukui, Surf. Sci. **267**, 214 (1992).

[12] S. Ando, N. Koybayashi, and H. Ando, Jpn. J. Appl. Phys. **37**, L105 (1998).

[13] S. Fan, P. R. Villeneuve, J. D Joannopoulos, and E.F. Schubert, Phys. Rev. Lett. **78**, 3294 (1997).

[14] T. Baba, K. Inoshita, H. Tanaka, J. Yonekura, M. Ariga, A. Matsutani, T. Miyamoto, F. Koyama, and K. Iga, J. Lightwave Technol. **17**, 2113 (1999).

[15] M. Boroditsky, T. F. Krauss, R Coccioil, R. Vrijen, R. Bhat, and E. Yablonovitch, Appl. Phys. Lett. **75**, 1036 (1999).

[16] H. Y. Ryu, Y. H. Lee, R. L. Sellin, and D. Bimberg, Appl. Phys. Lett. **79**, 3573 (2001).

[17] H.-Y. Ryu, J.-K. Hwang, Y.-J. Lee, and Y.-H. Lee, IEEE Selected Topics on Quant. Electron. **8**, 231 (2002).

Design of a New Taper for Light Coupling Between a Ridge Waveguide and a Photonic Crystal Waveguide

Cécile Jamois[1], Torsten Geppert[1,2] and Ralf B. Wehrspohn[2]
[1]Max Planck Institute of Microstructure Physics, Weinberg 2, 06120 Halle, Germany.
[2]Nanophotonic Materials Group, Department of Physics, University of Paderborn,
  Warburger Strasse 100, 33098 Paderborn, Germany.

ABSTRACT

We propose the design of a new taper to improve light coupling between a photonic-crystal-based W1 waveguide and a ridge waveguide of similar width. The taper design is directly deduced from band structure calculations and allows an adiabatic mode conversion. The comparison between light propagation from the ridge waveguide through the W1 waveguide and through the taper, respectively, shows good improvement of the coupling efficiency.

INTRODUCTION

Photonic crystals (PCs) devices have gained large diversity in the last years. In particular, devices based on planar PCs (PPCs) are very exciting because they offer the possibility to fabricate PC devices or circuits fully integrated into a chip. An essential building block of PPC circuits is the waveguide. Depending on its design, a PPC waveguide can have very different functionalities. The aim of our project is to design a fully integrated dispersion compensator based on a PPC waveguide. Because it allows a low-cost fabrication using the standard silicon technology, the material system under study is the insulator-on-silicon-on-insulator (IOSOI) system, consisting of one thin silicon slab embedded between two thick silicon oxide cladding layers. A hexagonal array of air pores perforates the whole three-layers structure to build the bulk PPC lattice. It has been shown elsewhere [1] that a W1 waveguide consisting of one row of missing pores in the Γ-K direction, inserted in this system, is suitable for applications to dispersion compensation. However, several issues remain crucial to achieve a functional device, such as light coupling into the PC waveguide. In the case of a PPC waveguide integrated into a chip, the light is often coupled in and out through a ridge waveguide having a similar width. Although the efficiency is not always very high, Butt coupling is usually used in this case, as illustrated in figure 1 [2-4]. In this paper, we design a new kind of taper allowing an adiabatic mode conversion from the ridge waveguide into the W1 waveguide, following the principles presented in [5].

DESIGN OF THE TAPER

Besides the mismatch in the overlap of the field distributions, which may lead to a very bad coupling, two major issues play an important role in the coupling efficiency for the configuration

shown in figure 1: the mode propagation mechanism and the group velocity mismatch. Both of them will be addressed while designing the taper.

The band structure for the W1 waveguide made of one row of missing pores in the Γ-K direction in an IOSOI-based PPC is shown in figure 2a. The PPC has a relative silicon thickness $h/a = 0.4$, the two oxide claddings are assumed to be infinite, and the relative radius of the air pores is $r/a = 0.366$. For this special design, a defect band exists (red line in figure 2a), which is very flat below the light line (violet line in figure 2a), corresponding to the region where the mode is vertically confined within the silicon slab. Above the light line, the defect band has a quite steep and almost linear slope. In this region, the radiation losses due to the lack of vertical confinement are around 100 dB/mm [6]. Therefore, it is crucial to work below the light line where the defect band is very flat, i.e., the group velocity is very low. As shown in figure 2b, the relative group velocity in the guided region is $v_g/c \leq 5.10^{-3}$. On the other hand, the incident wave is propagating in a SOI-based integrated ridge waveguide, i.e., a medium with effective refractive index n close to that of silicon ($n_{Si} = 3.4$). In this case, the group velocity of the wave is $v_{gi} \approx c/n$. Consequently, the group velocity mismatch between the incident mode and the PPC mode is around two orders of magnitude, and light coupling from the ridge waveguide into the PPC waveguide may be very low.

The second issue to address is the mode propagation mismatch. Two different guiding mechanisms coexist in PC waveguides. The first one is classical index-guiding and the second one is based on the existence of the photonic band gap (PBG) [7]. To allow a good coupling between the modes of two waveguides, it is necessary that both of them are guided by the same mechanism [5]. Consequently, Butt-coupling from the ridge-waveguide into the PPC waveguide may lead to high losses, because ridge-waveguide modes are always index-guided and the W1 mode is PBG-guided in the region of interest below the light line.
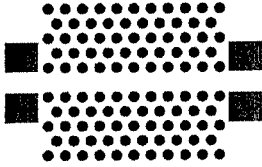
Figure 1. Principle of Butt coupling between a W1 photonic crystal waveguide and two ridge waveguides.
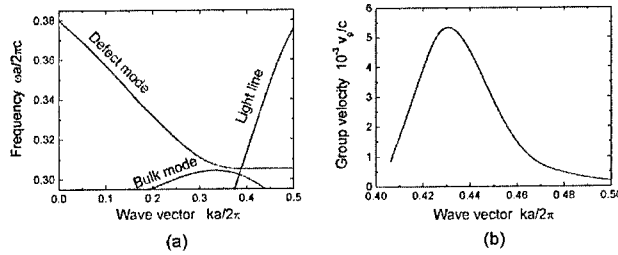
Figure 2. (a) Band structure showing the defect mode of interest and (b) group velocity of this mode in the region below the light line.

Therefore, to build a functional device, for application, e.g., to dispersion compensation, it is necessary to insert a taper improving the coupling between the ridge waveguide and the W1 waveguide. The taper should allow a smooth slowing down of the group velocity, as well as an adiabatic conversion of the mode propagation mechanism from index guidance to PBG guidance. This can be achieved by a smooth reduction of the defect width. Indeed, in the region above the light line, the defect mode is index-guided with a high group velocity, as in a ridge waveguide. Therefore, if the incident light from the ridge waveguide is coupled to the PPC defect mode in this region, the coupling should be quite good. As shown schematically in figure 3a, the position of the defect mode in frequency decreases with increasing defect width. If the taper consists of a waveguide with slightly larger width (e.g., W1.5) in its outer part, the incoming light will excite the waveguide mode in its index-guided region with large group velocity. Then, a very smooth reduction of the waveguide width, down to the W1, would lead to an adiabatic conversion of the waveguide mode to PBG guidance and to the extreme band flatness suitable for dispersion compensation, as illustrated in figure 3a. The design of such a taper is shown schematically in figure 3b.

(a)   (b)
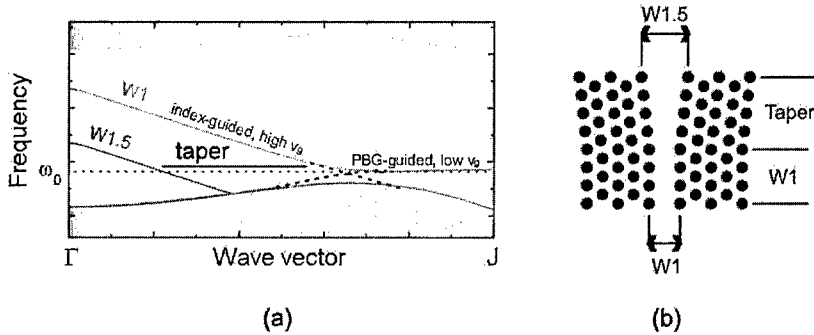
Figure 3. (a) Variation of the defect mode position with the defect width (schematic). At the given frequency ω_0, the defect band of the W1 waveguide is excited in the PBG-guided region with very low group velocity, while the larger waveguide W1.5 is excited in the index-guided region with large group velocity. (b) Principle of a taper based on limited waveguide width reduction (W1.5 →W1) to improve the group velocity matching as well as the mode matching between the incident wave and the PPC waveguide mode.

RESULTS

As a direct check of the taper performance, some transmission computations through the W1 waveguide and through the taper were performed, using the commercially available CrystalWave software by Photon Design. Because of the extremely low group velocity within the W1 waveguide, the transmission calculations require very long computation time. Therefore, in a first step only 2D calculations were performed, with waveguide lengths limited to few pore rows. Figure 4 shows a comparison between the results in the case of a direct coupling through a W1

waveguide having a length of five lattice constants, and a coupling into the same W1 waveguide through a taper having also a length of five lattice constants. The direct coupling of light from the ridge waveguide into the W1 waveguide (figure 4a) leads to very low transmission and strong reflection of the incident light. If the taper is inserted (figure 4b), a clear light propagation can be observed. This result highlights the good functionality of the taper from a qualitative point of view. In the case of a planar structure, the taper is used above the light line in the region of high radiation losses. However, very limited radiation losses are expected, because the small variation of the waveguide width requires only a short taper length of few lattice constants. For a taper length of $5a$, where the lattice constant a is typically around 500 nm, the radiation losses should be as low as 0.2-0.3 dB, for a transmission efficiency above 80 %. A larger 3D study, to be performed in the future, will allow a quantitative investigation of the taper efficiency.

1 μm   Taper   W1

(a)   (b)
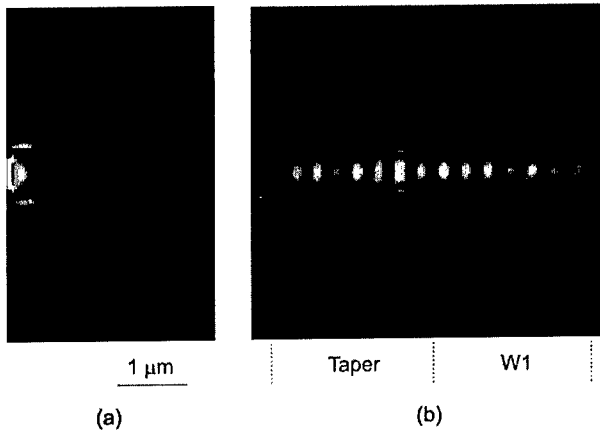
Figure 4. Comparison between light propagation through (a) the W1 waveguide and (b) the taper. Butt coupling of light from the ridge waveguide into the PPC waveguide (resp. the taper) is assumed (2D computations).

CONCLUSIONS

In this study, the design of a new type of taper for a better light coupling from an integrated ridge waveguide into a PPC-based W1 waveguide was presented. The taper design was directly deduced from band structure calculations and should allow an adiabatic mode conversion from an index-guided mode with high group velocity into a PBG-guided mode with very low group velocity. 2D transmission computations show a large improvement of the light propagation through the taper compared to the case without taper.

REFERENCES

1. R. März, S. Burger, S. Golka, A. Forchel, C. Hermann, C. Jamois, D. Michaelis and K. Wandel, "Planar High Index-Contrast Photonic Crystals for Telecom Applications", *Photonic Crystals: Advances in Design, Fabrication and Characterization*, ed. K. Busch, S. Lölkes, R. Wehrspohn and H. Föll, 308-329 (Wiley, 2004) (in press).
2. E. Miyai, M. Okano, M. Mochizuki, and S. Noda, *Appl. Phys. Lett.* **81**, 3729 (2002).
3. N. Moll and G.-L. Bona, *J. Appl. Phys.* **93**, 4986 (2003).
4. M. Qiu, K. Azizi, A. Karlsson, M. Swillo and B. Jaskorzynska, *Phys. Rev. B* **64**, 155113 (2001).
5. S.G. Johnson, P. Bienstman, M.A. Skorobogatiy, M. Ibanescu, E. Lidorikis, and J.D. Joannopoulos, *Phys. Rev. E* **66,** 066608 (2002).
6. L.C. Andreani and M. Agio, *Appl. Phys. Lett.* **82**, 2011 (2003).
7. C. Jamois, R.B. Wehrspohn, L.C. Andreani, C. Hermann, O. Hess and U. Gösele, *Photonics and Nanostructures: Fundamentals and Applications* **1**, 1 (2003).

Dispersion Engineering of Photonic Crystal Devices

David M. Pustai, Caihua Chen, Ahmed Sharkawy, Shouyuan Shi, Janusz Murakowski, and Dennis W. Prather
University of Delaware, Department of Electrical and Computer Engineering
140 Evans Hall, Newark, DE 19716

ABSTRACT

We present and experimentally validate self-collimation in planar photonic crystals as a new means of achieving structureless confinement of light in optical devices. We demonstrate the ability to arbitrarily guide and route light by exploiting the dispersive characteristics of the photonic crystal. Propagation loss as low as 2.17 dB/mm is measured, and the experimental validation of routing structures are presented.

INTRODUCTION

Since their introduction, [1, 2] photonic-crystals (PhC)s have enjoyed rapidly growing interest from both the academic and industrial communities due to their ability to manipulate light at the wavelength scale. One of the more common embodiments of PhCs is in semiconductor slabs with an air-hole lattice. Using this configuration, many useful devices have been proposed [3, 4] based on the introduction of defects into the lattice, which allow for the realization of cavities and optical waveguides. In this paper, we present and experimentally validate an alternative to a PhC waveguide—a device that does not require line defects for confinement, and yet can arbitrarily route light by exploiting engineered dispersion.

Our proposed device is based on engineering the dispersion properties of a two-dimensional slab PhC such that the propagation of light is permitted only in certain directions. In the vertical direction, we only consider field configurations that are bound to the slab by total internal reflection. However, in the lateral direction, the interaction is most appropriately interpreted through a dispersion diagram, which characterizes the relationship between the frequency, ω, of the wave and its associated wavevector, $\mathbf{k}$. Dispersion diagrams can be obtained by casting Maxwell's equations into an eigenvalue problem, in which the solution can be represented as a dispersion surface, as shown in Fig. 1a. To obtain such a rendering, one simply computes the eigenfrequencies for wavevectors at all k-points within the irreducible Brillouin zone, and then uses the appropriate symmetry operations to obtain the surface shown in Fig. 1a.

In the case of PhCs, dispersion surfaces can contain a variety of shapes depending on the lattice type, pitch, fill-factor, or index of refraction, in contrast to the strictly ellipsoidal surfaces of conventional materials. Taking cross-sections of the dispersion surface at constant frequencies, one obtains equi-frequency contours (EFCs), as shown in the bottom of Fig. 1a. By carefully choosing the frequency, one can obtain the square shape EFC shown by the dotted contour in Fig. 1b. The ability to shape the EFCs, and thereby to engineer the dispersion properties of the PhC, opens up a new paradigm for the design and function of optical devices. The importance of the EFC shape stems from the relation

$$\mathbf{v}_g = \nabla_k \omega(\mathbf{k}) , \qquad\qquad (1)$$

which means that the group velocity, $\mathbf{v}_g$, or the direction of light propagation coincides with the direction of the steepest ascent of the dispersion surface, and is perpendicular to the EFC, as indicated in Fig. 1(b).

(a)   (b)
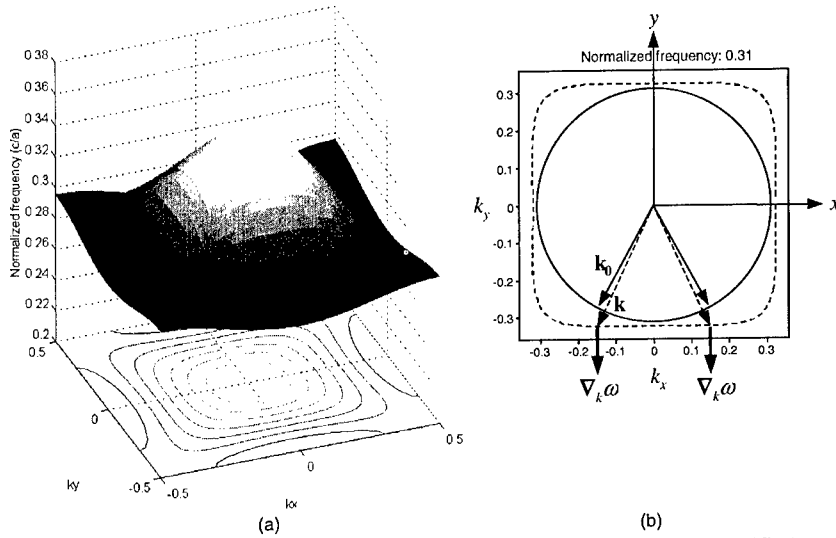
Figure 1. The dispersion surface for a PhC designed to have a square EFC for specified frequencies. The surface shown represents the second band. (a) A dispersion surface is a three-dimensional plot of the frequency versus planar wavevectors (k_x, k_y). (b) A square EFC is suitable for spatial beam routing applications. $\mathbf{k}_0$ is the incident wavevector, $\mathbf{k}$ is the wavevector in the PhC, and $\nabla_k \omega$ is the group velocity in the PhC corresponding to wavevector $\mathbf{k}$.

In the proposed application, we engineer a square EFC, in which case the wave is only allowed to propagate along those directions normal to the sides of the square. In this case, it is possible to vary the incident wavevector over a wide range of angles and yet maintain a narrow range of propagating angles within the PhC; this phenomenon is called "self-collimation" [5],[6] and was initially observed by Kosaka, et al.[5] and experimentally demonstrated by Wu, et al.[7]. This behavior can be used for a wide variety of applications, such as waveguiding and spatial beam routing, as well as for devices that have high misalignment tolerances, which could be very useful in facilitating high-efficiency in-plane coupling.

DISPERSION-BASED GUIDING

To illustrate this behavior, we simulated a point source located inside a square lattice of air holes within a thin silicon slab, with $r/a = 0.4$, using the FDTD method truncated by inhomogeneous Perfectly Matched Layers (PMLs). If the EFC for this material was a circle, representing an isotropic medium, light waves would emanate from the source and propagate equally in all directions within the plane. However, for the specified frequency, the EFC is nearly square. As a result, the propagation is limited to the x- and y-directions, as shown in Fig. 2(a).
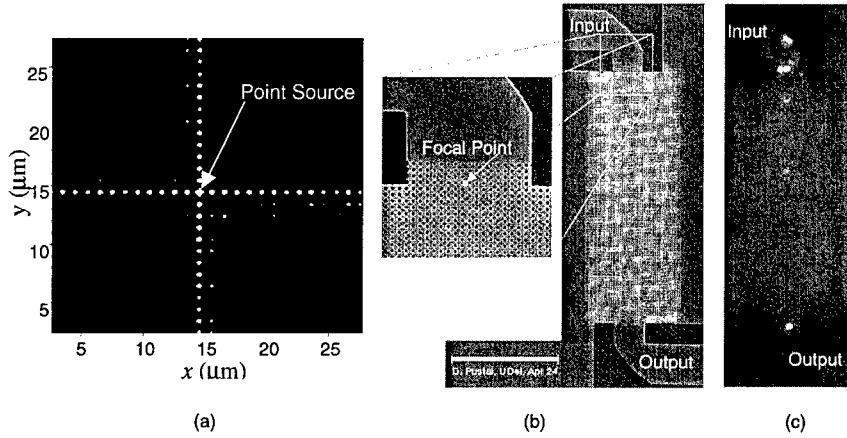
Figure 2. (a) FDTD simulation of a point source located within a dispersion guiding PhC lattice. (b) Scanning electron micrograph of a fabricated dispersion-based PhC waveguide. Scale bar: 20μm. (c) Image captured by a near-IR camera of the scattered light, where λ=1480nm, at the PhC/silicon boundaries. The point located at the output shows how the light is confined laterally within the PhC lattice.

To experimentally validate the lateral confinement of light within these dispersion-engineered waveguides, we used a tunable laser source end-fire coupled into a 260 nm thick silicon-on-insulator (SOI) ridge waveguide, within which we fabricated a J-coupler [8] to focus light into a square PhC lattice of $r = 133$nm and $a = 442$nm. The J-coupler is designed to tightly focus the light to a point located $4a$ within the lattice, as indicated in Fig. 2(b). This is done to generate a wider beam to ensure an area between two lattice sites is sufficiently illuminated, while at the same time narrow enough to observe lateral confinement. As seen in Fig. 2(c), the light enters the PhC lattice via the top J-coupler where some of the light is scattered by the silicon/PhC interface. We observe another scattered point of light at the opposite end of the PhC lattice, which demonstrates the lateral confinement of the initially divergent light as it propagates along the 63-μm length of the PhC. The underlying silicon dioxide layer is removed via a hydrofluoric acid wet etch in order to raise the light cone above the EFC of interest to reduce out-of-plane radiation.

The conspicuous absence of a light trail in Fig. 2(c) suggests low out-of-plane losses in this guiding structure. In order to quantitatively characterize propagation loss, we fabricated multiple PhC dispersion waveguides, with lengths ranging from 23.87 μm to 62.76 μm, on silicon-on-insulator (SOI) wafers and used the cutback method.[9] The cutback method entails analyzing waveguides of various lengths such that the loss is obtained from a linear fit of $\log(P_{out}/P_{in})$ vs. waveguide length, where P_{in} (P_{out}) is the scattered light at the beginning (end) of the PhC dispersion structure. In using this measure, we assume that the scattered light from each interface is proportional to the amount of light entering and exiting the PhC lattice. Propagation loss as low as 2.17 dB/mm is observed which is an improvement over loss measurements for

PhC line-defect waveguides.[9, 10] Further discussion of these results is presented in Reference [11].

ROUTING IN DISPERSION-BASED WAVEGUIDES

From the above, it should be clear that such a structure can be used to efficiently guide electromagnetic waves within a planar PhC without the use of channel defects or structural waveguides. However, for practical applications, these devices must also be capable of arbitrarily routing light. To do so, we use a dielectric mirror consisting of an etched rectangular air region to redirect the incident wave into its orthogonal direction.[12] The steady state Hz field shown in Fig. 3(a) demonstrates how sections of the directionally dispersive material can be combined with a reflecting mirror to route light in a very general manner. As shown in Fig. 3(a), the lateral extent of the optical fields is typically 2-3 lattice cells, which corresponds to about 800-900nm in the present example. This compares favorably with conventional PhC waveguides, which typically require at least one lattice period for waveguide cladding.

(a)   (b)
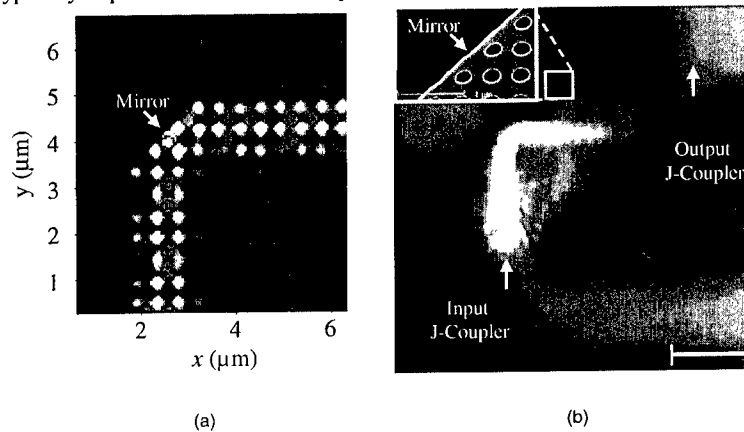
Figure 3. Routing capability of a material having a square-shaped equi-frequency dispersion contour. (a) Three-dimensional FDTD simulation of light guided through a PhC lattice and routed by reflection from a mirror. (b) Image of the scattered light as it is reflected by the mirror, where λ=1432nm. Scale bar: 10μm.

From observation of the fabricated device, as shown in Fig. 3(b), the lateral confinement of the light and mirror routing capability is demonstrated by the light path scattered out of the plane. Some light is scattered out-of-plane, as opposed to the guided light in Fig. 2(c), because the underlying oxide layer is left intact such that the operating frequency lies above the light cone. Detailed bending efficiency calculations are presented in Reference [12].

DISPERSION-BASED BEAM-SPLITTERS

A common use for PhCs in integrated optical applications is that of optical beam splitting. In this section, we present a PhC structure to realize a one-to-two beam splitter in a self-collimation lattice. The optical beam splitter consists of two sections as shown in Fig. 4(a): a

dispersion guiding PhC structure and a beam splitting structure. The PhC guiding structure has an air hole with a ratio $r_g = 0.3a$, and the splitting structure has an air hole of radius r_s, which varies from $0.3a$ to $0.435a$.
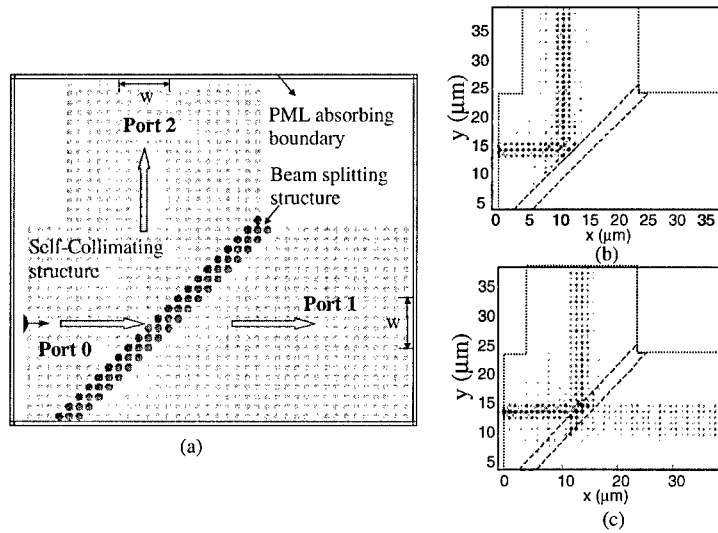
Figure 4. Dispersion-based beam splitting structure. (a) Schematic of the beam splitting region located within the self-collimating PhC lattice. Steady state result of Hz field with radii of air holes of (a) $0.42a$, (b) $0.36a$.
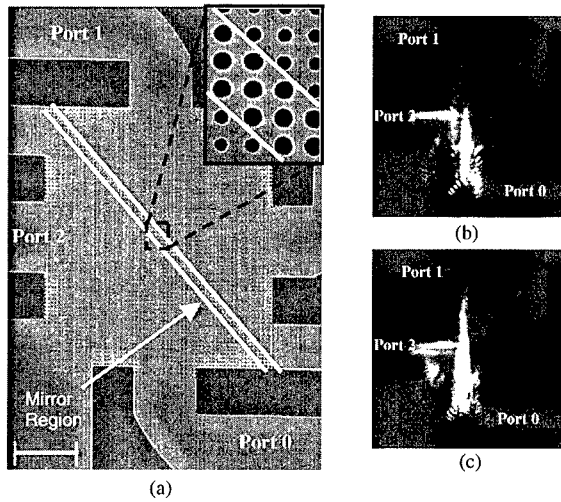
Figure 5. (a) Scanning electron micrograph of the dispersion guiding structure and beam-splitting region. Scale bar: 10μm Top-down view of the dispersion splitting structure at (b) λ=1503nm and (c) λ=1482nm.

The EFC at the operating frequency of $0.26c/a$ remains square-like in shape, therefore, if the radius of air holes in the splitting region is equal to those in the self-collimating structure, the wave will be self-collimated and completely output to port 1. Figure 4(b) shows the steady state result of the magnetic field (Hz) for a hole radius of $0.42a$ in the splitting structure, displaying most of the energy exiting at port 2. When $r_s = 0.36a$, one obtains approximately 3-dB splitting, and the corresponding steady state result of the magnetic field is shown in Fig. 4(c). Within the radius range $(0.3a < r < 0.345a)$, there is no stop band and a majority of the light will propagate in the same direction as the incident wave, with only a small amount entering port 2 due to the interface of the two slightly different types of PhC structures. As the radii of air holes continue to increase, the frequency $0.26c/a$ falls into the band gap and the beam is reflected.

This device was similarly fabricated on a SOI wafer consisting of air holes with a lattice constant $a = 442$nm and radii $r_g = 0.27a$ and $r_s = 0.33a$ for the guiding and splitting regions respectively. Figure 5(a) shows a scanning electron micrograph of the fabricated beam-splitting structure. The wavelength, or PBG, dependence on beam-splitting is observed in Fig. 5(b) and (c) when λ is tuned between 1503nm and 1482nm respectively. When $\lambda=1503$nm, the wavelength lies within the PBG, thereby much of the light is reflected into port 2. However, at $\lambda=1482$nm, the wavelength is located very close to the edge of the PBG producing a 3dB split between ports 1 and 2. A detailed analysis of these results is presented in Reference [13].

To summarize, we have demonstrated the application of dispersion engineering in photonic crystals for efficient waveguiding, routing, and splitting. We experimentally demonstrated self-collimation in planar PhCs, and a new means of achieving structureless confinement of light in optical devices. The applications of these devices are far-reaching in that they allow for very high-density photonic circuits due to the lack of structural interaction as well as their ability to propagate and route optical beams in an arbitrary fashion with low loss.

REFERENCES

1. S. John, *Physical Review Letters* **58**, 2486-2489 (1987).
2. E. Yablonovitch, *Physical Review Letters* **58**, 2059-2062 (1987).
3. D. W. Prather, A. Sharkawy and S. Shouyuan, *Design and Applications of Photonic Crystals*, (CRC Press, Boca Raton, FL, 2002) p. 211-232.
4. *IEEE Journal of Quantum Electronics* **38**, 724-963 (2002).
5. H. Kosaka, T. Kawashima, A. Tomita, M. Notomi, T. Tamamura, T. Sato and S. Kawakami, *Applied Physics Letters* **74**, 1212-1214 (1999).
6. J. Witzens, M. Loncar and A. Scherer, *IEEE Journal of Selected Topics in Quantum Electronics* **8**, 1246-1257 (2002).
7. L. Wu, M. Mazilu and T. F. Krauss, *Journal Of Lightwave Technology* **21**, 561-566 (2003).
8. D. W. Prather, J. Murakowski, S. Y. Shi, S. Venkataraman, A. Sharkawy, C. H. Chen and D. Pustai, *Optics Letters* **27**, 1601-1603 (2002).
9. M. Notomi, A. Shinya, K. Yamada, J. Takahashi, C. Takahashi and I. Yokohama, *IEEE Journal of Quantum Electronics* **38**, 736-742 (2002).
10. T. Baba, A. Motegi, T. Iwai, N. Fukaya, Y. Watanabe and A. Sakai, *IEEE Journal of Quantum Electronics* **38**, 743-752 (2002).
11. D. W. Prather, S. Shi, D. M. Pustai, A. Sharkawy, C. Chen, S. Venkataraman, J. Murakowski and G. Schneider, *Optics Letters* **29**, 50-52 (2004).
12. C. Chen, D. M. Pustai, S. Shi, A. Sharkawy and D. W. Prather, *Optics Express* **11**, 3153-3159 (2003).
13. S. Shi, A. Sharkawy, D. M. Pustai, C. Chen and D. W. Prather, *Optics Letters* (2004).

Light Guiding in Low Index Materials using High-Index-Contrast Waveguides

Vilson R. Almeida, Qianfan Xu, Roberto R. Panepucci, Carlos A. Barrios, and Michal Lipson
Cornell University, School of Electrical and Computer Engineering, 429 Phillips Hall
Ithaca, NY 14853, U.S.A.

ABSTRACT

We propose a novel high-index-contrast waveguide structure capable of light strong confinement and guiding in low-refractive-index materials. The principle of operation of this structure relies on the electric field (E-field) discontinuity at the interface between high-index-contrast materials. We show that by using such a structure the E-field can be strongly confined in a 50-nm-wide low-index region with normalized average intensity of 20 μm^{-2}. This intensity is approximately 20 times higher than that can be achieved in SiO_2 with conventional rectangular or photonic crystal waveguides.

INTRODUCTION

Recent results in integrated optics have shown the ability of efficiently guiding, filtering, bending and splitting light on chips using a variety of waveguide structures [1]. Extremely sharp curves, bends, and splitters have also been demonstrated, allowing a high level of integration [2,3]. Multiplexers and demultiplexers using resonant structures such as ring resonators have been shown [4]. All of these structures are based on total internal reflection (TIR) as the guiding mechanism. This mechanism is commonly thought to prohibit the light to be confined and guided in the lower-index region. In the last few years, guiding light in low-index materials has become increasingly important for applications such as optical sensing, interaction with low index materials, and avoiding nonlinearities in the high-index material.

Early attempts to guide light in the low-index material on high-index-contrast platform led to structures that are wavelength dependent and have relatively large transverse dimensions, which limited their optical intensity and ability for integration. The antiresonant reflecting optical waveguide (ARROW) structure uses the external reflection at the high-index-contrast interfaces as a guiding mechanism [5], in contrast to the total internal reflection used in standard waveguides; this structure was recently proposed for sensing applications [6]. Based on similar principles, the OmniGuide fibers and photonic band-gap fibers were investigated [7,8], where 1-D or 2-D periodic structures are used to provide the near-unity reflections for guiding. All aforementioned structures are wavelength dependent, inherently leaky, and present large cross sectional dimensions of at least several micrometers.

We propose a waveguide structure that can confine light inside a nanometer-wide area of low-index material with high E-field amplitude and optical intensity. In contrast to the leaky nature of the previously mentioned structures, the guided mode is an eigenmode of our proposed structure; therefore, it is fundamentally lossless. Our proposed structure, hereafter named slot-waveguide, consists of two parallel high-index contrast waveguides separated by a nanometer-sized low-refractive-index slot. Since the slot-waveguide does not rely on resonance principles, the eigenmode is almost wavelength insensitive. Furthermore, it is fully compatible with highly-

integrated photonics technology, retaining most of its important properties such as nanometer-sized cross-section dimensions and small minimum bend radius. For the quasi-TE eigenmode the slot is obtained by lithographic patterning, whereas for the quasi-TM counterpart appropriate multilayer design is requested. Potential applications for the slot-waveguide include host for active materials, sensing, non-linear optics, optical modulators and switches, near-field optical microscopy (NSOM), and efficient coupling to nanometer-sized waveguides and structures.

THEORY

The principle of operation of the slot-waveguide is based on the discontinuity of the normal component of the E-field E at the high-index-contrast interface. From Maxwell's equations, the normal component of the electric flux density D is continuous at the interface of two dielectric materials. Since $D = \varepsilon_r \varepsilon_0 E = n^2 \varepsilon_0 E$, where n, ε_r and ε_0 are the refractive index, dielectric constant and vacuum permittivity, respectively, the normal component of E shows discontinuity if n is different at opposite sides of the interface. The E-field is then higher at the low-index side and lower at the high-index side, with the ratio equal to the square of the index contrast $(n_{High}/n_{Low})^2$. This discontinuity has usually been overlooked because most of the investigated photonic structures rely on low-index-contrast. However, for high-index-contrast structures, this discontinuity is significant. For example, at the Si/SiO_2 interface, the normal component of E-field at the SiO_2 side is 6 times higher than that at the Si side. At the Si/air interface, the normal component of the E-field at the air side is 12 times higher than that at the Si side.

An example of a slot-waveguide is shown in figure 1; it consists of a low-index region embedded between two rectangular high-index regions. In such a structure, the major component of the E-field of the quasi-TE mode is in the horizontal direction, normal to the walls of the slot. Due to the high index contrast, the E-field has a discontinuity at the walls, with much higher amplitude in the slot than that in the high-index part of the structure. Due to the fact that the dimensions of the slot are comparable to the decay length of the field, the E-field amplitude will remain high over the whole region of the slot. Therefore, the average E-field amplitude in the slot becomes much higher than that in the high-index material. The optical intensity in the slot is also much higher than that in the high-index region, since the magnetic field (H-field) is continuous at the interface and varies slowly across the structure. On the other hand, the major E-field component of the quasi-TM mode is parallel to the interface of index contrast, resulting in an E-field that is continuous at the walls of the slot. As a result, the presence of the slot does not affect the quasi-TM mode as strongly as it affects the quasi-TE mode.
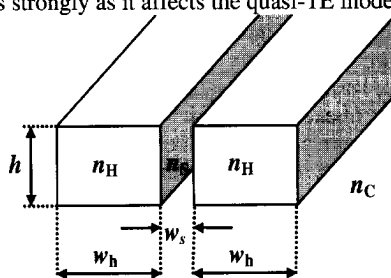
Figure 1. Schematic of a slot-waveguide

We numerically analyzed the performance of the structure shown in figure 1 for guiding and confining light in nanometer-size low index regions. A full-vectorial finite difference mode solver [9] with non-uniform grid mesh was implemented to simulate the quasi-TE eigenmodes of slot-waveguides with different dimensions and wavelengths. For concreteness, we assume that the slot-waveguide is built on the widely used Silicon-On-Insulator (SOI) platform, with the silicon being the high-index material, and the silicon dioxide being the low-index cladding; $n_H = 3.48$, $n_C = 1.46$, and a wavelength of $\lambda_0 = 1.55$ μm are assumed, unless otherwise specified. We also assume that the slot is filled with SiO_2 ($n_S = 1.46$), unless otherwise specified.

The E-field distribution across the structure shown in figure 1 can be seen in figure 2.a and 2.b for a slot-waveguide with silicon region width $w_h = 180$ nm, slot width $w_s = 50$ nm, and height $h = 300$ nm. Figure 2.a shows the contours of the E-field amplitude and the E-field lines of the quasi-TE mode. The center bright region shows a strong E-field inside the slot. The directions of the E-field lines in the slot confirm that the total transverse E-field is mostly normal to the walls of the slot, which causes its discontinuity at the interface between silicon and slot. The E-field distribution can be seen more clearly in the 3D profile shown in figure 2.b. The peak amplitude of the E-field in the slot is 4 times higher than that in the silicon region, and 2.5 times higher than that in the cladding.
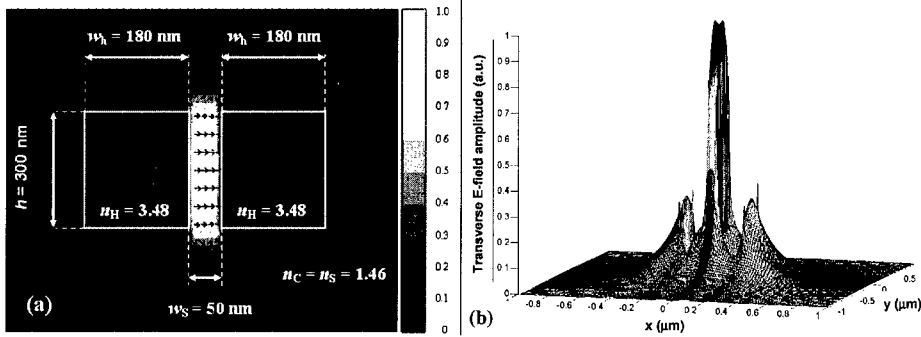
Figure 2. Transverse E-field profile of the quasi-TE mode. **(a)** E-field amplitude (contour) and lines. **(b)** 3D surface plot of the E-field amplitude. The origin of the coordinates system is located at the waveguide center; x-axis is horizontal direction and y-axis is vertical in part (a).

Figure 3.a shows the average optical intensity I_{slot} and the total optical power $P_{slot} = h \cdot w_s \cdot I_{slot}$ in the slot as a function of w_s and w_h for $h = 300$ nm. Both P_{slot} and I_{slot} are normalized with respect to the total optical power in the waveguide. For comparison, the normalized average optical intensity in the silicon region I_{Si} is plotted as well. The optical intensity is much higher in the slot than anywhere in the high-index region of the structure, which is a consequence of the E-field enhancement and the H-field invariance. Figure 3.a shows that P_{slot} remains nearly constant around 30% for $w_s \geq 50$ nm. For $w_s = 50$ nm, I_{slot} is as high as 20 μm^{-2}, which is 6 times higher than I_{Si}. One can also see from figure 3.a that w_h does not significantly affect the slot-waveguide performance.

In order to investigate the wavelength dependence, we simulated both P_{slot} and I_{slot} as a function of wavelength, as shown in figure 3.b. In the simulations, we used $w_h = 180$ nm, $w_s = 50$ nm, and $h = 300$ nm. The material dispersions have been taken into account in the simulations. One can see that the normalized power and intensity changed less than 10% over a wavelength

span of 400 nm. Therefore, the same slot-waveguide can be used to guide and confine light in a low-index material at a wide range of wavelengths, which greatly broadens its application scope.
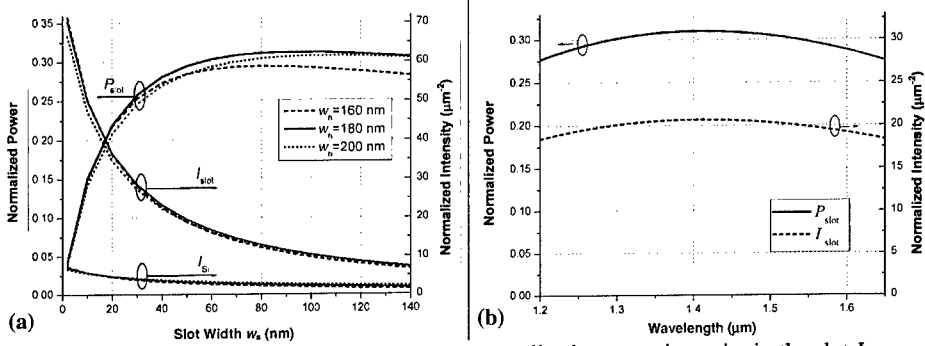
Figure 3. (a) Normalized power in the slot P_{slot}, normalized average intensity in the slot I_{slot}, and normalized average intensity in silicon I_{Si}, for quasi-TE mode in the slot-waveguide with SiO_2 slot. Normalization is relative to the total optical waveguide power. **(b)** Normalized power P_{slot} and normalized average intensity I_{slot} in the slot as a function of the wavelength of light.

Light propagating in the slot waveguide not only is confined to a low-index material, but also has a much higher intensity than that achievable using conventional rectangular waveguides or photonic crystal waveguides. In order to numerically compare the performance of the slot waveguide with conventional rectangular SOI waveguides [1], we calculated the average intensity inside the core of the conventional SOI waveguide. When the cross-sectional dimension of the waveguide is large, the intensity is low because of the large mode size. When the dimension of the waveguide is too small, the intensity is also low because the mode becomes delocalized [10]. Therefore, there is an optimal waveguide dimension for achieving the highest intensity. The highest normalized average intensity in the core of the conventional SOI waveguide is less than 9 μm^{-2}. Moreover, if the light is to be confined in a low-index material such as SiO_2 with the conventional waveguide structure, the highest possible index contrast that can be achieved is through the SiO_2/air platform; the maximum normalized intensity that can be obtained in this case is less than 1.1 μm^{-2}, which is almost 20 times lower than what we have calculated for the slot-waveguide. For the leaky-mode waveguides based on external reflections, such as the photonic crystal waveguide, the size of the low-index core is limited to be larger than half of the wavelength in the low-index material. Therefore, the normalized intensity can hardly exceed 1 μm^{-2} at 1.55-μm wavelength.

EXPERIMENTS

We fabricated directional couplers (see figure 4.a) and ring resonators (see figure 4.b) with slot waveguides on a SOI platform using a process similar to that described in [10]. The waveguide dimensions are $w_h = 220$ nm, $w_s = 100$ nm, and $h = 250$ nm. From the directional couplers, the effective index can be extracted from the dependence of the coupling ratio on the lateral distance between adjacent slot-waveguides that form the directional coupler. From the ring resonator transmission spectra, the group index can be extracted from the free spectral range

of their resonances.
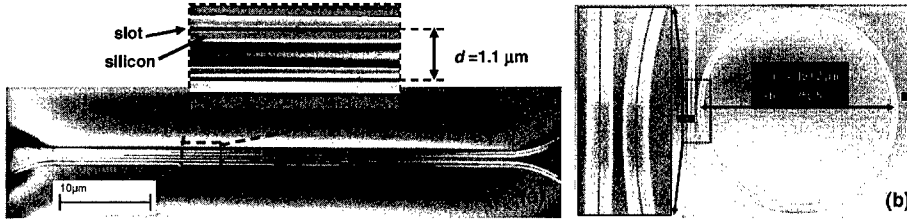
Figure 4. The top-view SEM picture of (a) a directional coupler and (b) a ring resonator, formed by two slot-waveguides fabricated using SOI platform.

The measured dispersion curves of the slot-waveguides that form the directional couplers are shown in figure 5.a, along with the ones obtained from simulations with actual device dimensions. Since the slots are found to be void, we used $n_H = 3.48$, $n_S = 1$, and $n_C = 1.46$. The dispersion curve for a conventional waveguide, i.e. $w_s = 0$, are also calculated. The effective index of the quasi-TM mode is barely affected by the presence of the slot. In contrast, the effective index of the quasi-TE mode is drastically reduced due to the presence of the slot, what represents direct evidence that the power is indeed concentrated in the low-index region. The measured quasi-TE group index of the slot-waveguide that form the ring-resonator is shown in figure 5.b, along with the one obtained from simulations with actual device dimensions.

One can see from figures 5.a and 5.b that there is good agreement between theoretical predictions and experimental results, evidencing that the slot-waveguide is capable of strongly confining light in the low-index slot region and that it is compatible with highly-integrated photonics technology.
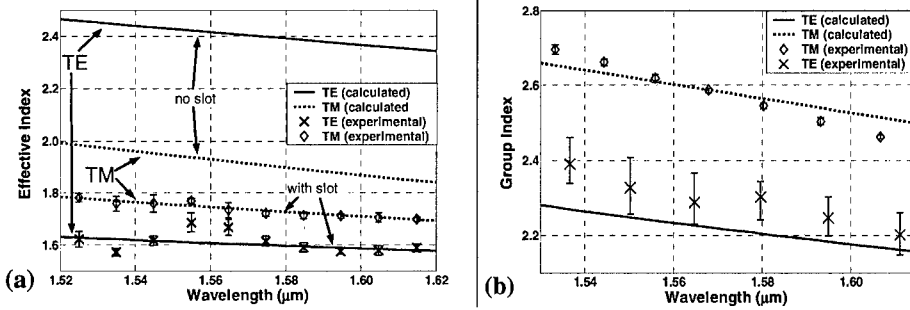
Figure 5. (a) Quasi-TE and quasi-TM modes; simulated (lines) and measured (marks with error bars) dispersion curves. Measurement was extracted from directional couplers with conventional and slot-waveguide ($w_s = 0$). (b) Quasi-TE mode; simulated (lines) and measured (marks with error bars) group index. Measurement was extracted from ring resonators with slot-waveguides.

CONCLUSIONS

In conclusion, we show experimental evidence that light can be efficiently guided and confined in low-index materials using E-field discontinuity in high-index-contrast material

systems. The slot-waveguide allows us to achieve high E-field amplitude and optical intensity in low-index materials at levels not attainable with conventional waveguides. This property enables highly efficient interaction between fields and active materials, which may lead to all-optical switch and parametric amplifier on Si integrated photonics. Since the E-field is strongly localized in a nanometer-sized low-index region, the slot-waveguide may be used to greatly increase the sensibility of optical sensing or to enhance the efficiency of near-field optical probes.

ACKNOWLEDGEMENTS

REFERENCES

1.   1. K. K. Lee, D. R. Lim, L. C. Kimerling, J. Shin, and F. Cerrina, "Fabrication of ultralow-loss Si SiO 2 waveguides by roughness reduction," Opt. Lett. **26**, 1888 (2001).
2.   A. Sakai, G. Hara, and T. Baba, "Sharply bent optical waveguide on silicon-on-insulator substrate," Proceedings of SPIE **4283**, 610 (2001).
3.   C. Manolatou, S. G. Johnson, S. Fan, P. R. Villeneuve, H. A. Haus, and J. D. Joannopoulos, "High-density integrated optics," J. Lightwave Tchonol. **17**, 1682 (1999).
4.   B. E. Little, J. S. Foresi, G. Steinmeyer, E. R. Thoen, S. T. Chu, H. A. Haus, E. P. Ippen, L. C. Kimerling, and W. Greene, "Ultra-compact Si-SiO2 microring resonator optical channel dropping filters," IEEE Photon. Technol. Lett. **10**, 549 (1998).
5.   M. A. Duguay, Y. Kokubun, and T. L. Koch, "Antiresonant reflecting optical waveguides in SiO2-Si multilayer structures," Appl. Phy. Lett. **49**, 13 (1986).
6.   R. Bernini, S. Campopiano, L. Zeni, and C.de Boer, and P. M. Sarro, "Planar antiresonant reflecting optical waveguides as sensors for liquid substances," Sensors, Proceedings of IEEE **2**, 1160 (2002).
7.   R. F. Cregan, B. J. Mangan, J. C. Knight, T. A. Birks, P. St. J. Russel, P. J. Roberts, and D. C. Allan, "Single-mode photonic band gap guidance of light in air," Science **285**, 1537(1999).
8.   S. G. Johnson, M. Ibanescu, M. Skorobogatiy, O. Weisberg, T. D. Engeness, M. Soljacic, S. A. Jacobs, J. D. Joannopoulos, and Y. Fink, "Low-loss asymptotically single-mode propagation in large-core OmniGuide fibers," Optics Express **9**, 748 (2001).
9.   C. L. Xu, W. P. Huang, M. S. Stern, and S. K. Chaudhuri, "Full-vectorial mode calculations by finite difference method," IEE Proc.-Optoelectron. **141**, 281 (1994).
10. V. R. Almeida, R. R. Panepucci, and M. Lipson, "Nanotaper for compact mode conversion," Opt. Lett. **28**, 1302 (2003).

Optical Properties of Dielectric and Magnetic Photonic Crystals in the Low-Frequency Limit

Arkady Krokhin[1,2], Jesús Arriaga[1], and Edgar Reyes[1]
[1]Department of Physics, University of North Texas, Denton, TX 76203, U.S.A.
[2]Instituto de Física, Universidad Autónoma de Puebla, Pue., 72570, Mexico

ABSTRACT

We consider the long-wavelength limit for two-dimensional photonic crystals – periodic arrangement of magneto-dielectric rods with dielectric and magnetic constant ε_a and μ_a embedded in a magneto-dielectric background (ε_b, μ_b). Using the Fourier expansion method in the low-frequency limit ($\omega \to 0$) we develop an effective medium theory and give a rigorous proof that, in this limit, a periodic medium behaves like a homogeneous one. We derive compact analytical formulas for the effective index of refraction of a 2D photonic crystal. These formulas are very general, namely the Bravais lattice, the cross-sectional form of cylinders, their filling fractions and the dielectric and magnetic constants are all arbitrary. For non-magnetic materials, $\mu_a = \mu_b = 1$, we show how to introduce index ellipsoid and demonstrate that the E-mode is an ordinary wave and the H-mode is an extraordinary wave. For magnetic materials the both modes turn out to be extraordinary. This unusual property is unknown for natural crystals.

INTRODUCTION

Photonic crystals (PC) are artificial semiconductor structures widely used in low-power micro-lasers, fiber optics communications, near-infrared devices and other optoelectronic applications [1]. Fabricated from two different dielectrics, arranged periodically in space, PC may possess a band-gap, i.e. a region of frequencies where electromagnetic signal cannot propagate due to destructive interference. Electromagnetic modes with frequencies above and below the band gap in a PC behave similar to electrons and holes in a semiconductor. This allows manipulating of the optical signal in a way comparable to that of the carriers of current into electronic devices. The materials of the PC's are high-quality dielectrics [1] possibly with a metallic fraction [2]. Recently PC's containing magnetic materials have been fabricated [3]. It is clear that these artificial periodic composites can be also employed in the region of linear dispersion, i.e. for the frequencies well below the gap. Here the PC's can be used as traditional optical elements, like prisms, lenses, and polarizers [4]. The advantage of the PC's in comparison to natural optical materials (e.g. quartz) is that the properties of the artificial structure may be specially designed and possess e.g. large optical anisotropy. Here we show that in the PC's with magnetic constituents reveals optical properties that do not exist for natural crystals. We develop an effective medium theory for 2D magneto-dielectric photonic crystals in the limit when the wavelength of the propagating wave is much larger than the lattice constant

of the PC. For natural crystals this limit corresponds to the region of visible light (and lower frequencies), i.e. to the Crystal Optics.

HOMOGENIZED WAVE EQUATION

Photon transport through a PC is characterized by dispersion law, $\omega = \omega_n(\mathbf{k})$, where ω is the frequency, $\mathbf{k}$ is the Bloch vector of photon, and $n = 1, 2, \ldots$ is the band index. Calculation of the band structure requires application of different numerical methods, however the most popular and universal one is the method of plane waves [5]. In what follows we apply the method of plane waves to calculate the long-wavelength limit

$$n_{eff} = \lim_{k \to \infty} \left(\frac{kc}{\omega} \right), \tag{1}$$

which by its definition gives the effective index of refraction of a PC.

We consider a 2D periodic structure of cylinders with their axes parallel to z. This 2D PC supports propagation of two uncoupled modes with either E-polarization (vector $\mathbf{E}$ is parallel to the rods) or H-polarization (vector $\mathbf{H}$ is parallel to the rods). The electric field of the E-mode is tangential to the cylinders. Due to the boundary conditions it is continuous across the structure. In this geometry the effective dielectric constant is known to be the space-average dielectric constant [6]

$$\varepsilon_{eff}^E = \overline{\varepsilon} = f\varepsilon_a + (1-f)\varepsilon_b. \tag{2}$$

Here f is the filling fraction of the component a. This result is valid not only for periodic systems, but also for any inhomogeneous dielectrics with dielectric constant that is independent of the coordinate z. If the constituents of the PC are non-magnetic, the effective index of refraction is simply $\sqrt{\varepsilon_{eff}}$. However, for magnetic materials one needs to calculate the effective permeability μ_{eff} in order to get the index of refraction, $n_{eff} = \sqrt{\varepsilon_{eff}\mu_{eff}}$. Since the magnetic field lies in the plane of periodicity (x-y), it is neither perpendicular nor parallel to the cylinders surfaces. Then the effective permeability should be calculated explicitly from the Maxwell equations. However, for the H-mode it is the effective permeability μ_{eff} that can be written in a form similar to Eq. (2),

$$\mu_{eff}^H = \overline{\mu} = f\mu_a + (1-f)\mu_b, \tag{3}$$

and to calculate ε_{eff} one should proceed with the Maxwell equations.

For 2D PC the equations for the E- and H-polarized modes have the following form

$$\nabla \cdot \left(\frac{1}{\mu(\mathbf{r})} \nabla E \right) = \frac{\omega^2}{c^2} \varepsilon(\mathbf{r}) E, \tag{4}$$

$$\nabla \cdot \left(\frac{1}{\varepsilon(\mathbf{r})} \nabla H \right) = \frac{\omega^2}{c^2} \mu(\mathbf{r}) H. \tag{5}$$

Here $\varepsilon(\mathbf{r})$ and $\mu(\mathbf{r})$ are coordinate-dependent permittivity and permeability of the PC. These equations are symmetric with respect to the replacement $E \leftrightarrow H$ and $\varepsilon \leftrightarrow \mu$. Therefore in what follows we calculate n_{eff} for the H-mode only. The effective index of refraction for the E-mode is obtained from that for the H-mode by interchanging $\varepsilon(\mathbf{r})$ and $\mu(\mathbf{r})$, i.e. $n_{eff}^E \{\varepsilon(\mathbf{r}), \mu(\mathbf{r})\} = n_{eff}^H \{\mu(\mathbf{r}), \varepsilon(\mathbf{r})\}$.

To obtain the long-wavelength limit from Eq. (5) we apply the method that was developed in Refs. [7,8] for 2D non-magnetic photonic crystal. Using the Bloch theorem and the periodicity of the functions $1/\varepsilon(\mathbf{r})$ and $\mu(\mathbf{r})$, we get the Fourier expansions,

$$H(\mathbf{r}) = \exp(i\mathbf{k} \cdot \mathbf{r}) \sum_{\mathbf{G}} h_k(\mathbf{G}) \exp(i\mathbf{G} \cdot \mathbf{r}),$$

$$\varepsilon^{-1}(\mathbf{r}) = \eta(\mathbf{r}) = \sum_{\mathbf{G}} \eta(\mathbf{G}) \exp(i\mathbf{G} \cdot \mathbf{r}), \tag{7}$$

$$\mu(\mathbf{r}) = \sum_{\mathbf{G}} \mu(\mathbf{G}) \exp(i\mathbf{G} \cdot \mathbf{r}),$$

where $\mathbf{G}$ are the reciprocal-lattice vectors. Substituting Eq. (7) into Eq. (5) we get a generalized eigenvalue problem in $\mathbf{G}$-space,

$$\sum_{\mathbf{G}} \eta(\mathbf{G} - \mathbf{G}') (\mathbf{k} + \mathbf{G}) \cdot (\mathbf{k} + \mathbf{G}') h_k(\mathbf{G}') = (\omega^2/c^2) \sum_{\mathbf{G}} \mu(\mathbf{G} - \mathbf{G}') h_k(\mathbf{G}') = 0. \tag{8}$$

The photonic dispersion relation $\omega = \omega_n(\mathbf{k})$ is obtained from the condition that the set of linear equations (8) has a nontrivial solution. It is easy to get from Eq. (8) that in the static limit, $\omega = k = 0$ the Fourier coefficients $h_k(\mathbf{G} \neq 0)$ vanish linearly. The only nonvanishing component is $h_k(\mathbf{G} = 0) = h_0$. In the long-wavelength limit, $ka \ll 1$, (a is the lattice period) this component determines the amplitude of the plane-wave solution, which is obtained from the first equation (7) by separating the term with $\mathbf{G} = 0$,

$$H(\mathbf{r}) \approx h_o \exp(i\mathbf{k} \cdot \mathbf{r}) + \sum_{\mathbf{G} \neq 0} h_k(\mathbf{G}) \exp(i\mathbf{G} \cdot \mathbf{r}). \tag{9}$$

Here we neglected $\mathbf{k}$ in the sum $\mathbf{G} + \mathbf{k}$ in the exponent. Since the sun over $\mathbf{G}$ vanishes when $k \to 0$, Eq. (9) means that the medium homogenizes, i.e. the solution of the wave equation

(5) approaches plane wave. Now the limit in Eq. (1) can be calculated using a perturbation theory with respect to small parameter ka. The following two equations are obtained from Eq. (8) in the linear and quadratic approximation respectively,

$$\mathbf{k} \cdot \mathbf{G}\ \eta\ (\mathbf{G})\ h_0 + \sum_{G \neq 0} \mathbf{G} \cdot \mathbf{G}' \eta\ (\mathbf{G} - \mathbf{G}')\ h_k\ (\mathbf{G}') = 0, \tag{10}$$

$$(\overline{\eta} k^2 - \overline{\mu}\ \omega^2 / c^2) h_0 + \sum_{G \neq 0} \mathbf{k} \cdot \mathbf{G}' \eta(-\mathbf{G}') h_k\ (\mathbf{G}') = 0. \tag{11}$$

Eliminating h_0 from Eqs. (10) and (11) and using the definition (1) we get a set of equations valid in the long-wavelength limit,

$$(\overline{\eta} - n_{eff}^{-2}\ \overline{\mu}) \sum_{G \neq 0} \mathbf{G} \cdot \mathbf{G}' \eta(\mathbf{G} - \mathbf{G}') h_k\ (\mathbf{G}') - \sum_{G \neq 0} (\hat{\mathbf{k}} \cdot \mathbf{G})(\hat{\mathbf{k}} \cdot \mathbf{G}') \eta(\mathbf{G}) \eta(-\mathbf{G}') h_k(\mathbf{G}') = 0. \tag{12}$$

EFFECTIVE INDEX OF REFRACTION

Set of linear equations (12) has nonzero solution if its determinant vanishes. Although this determinant equation is an infinite-order polynomial equation with respect to n_{eff}^2, it turns out that it has only a *unique* nonzero solution. Omitting mathematical details, we give the final result,

$$[n_{eff}^H(\hat{\mathbf{k}})]^2 = \overline{\mu} \bigg/ \left\{ \overline{\eta} - \sum_{G,G' \neq 0} (\mathbf{k} \cdot \mathbf{G})\ (\mathbf{k} \cdot \mathbf{G}') \eta(\mathbf{G}) \eta(-\mathbf{G}')\ [\mathbf{G} \cdot \mathbf{G}' \eta(\mathbf{G} - \mathbf{G}')]^{-1} \right\}. \tag{13}$$

Here $[...]^{-1}$ stands for the inverse matrix with respect to indices $\mathbf{G}$ and $\mathbf{G}'$, and $\hat{\mathbf{k}} = \mathbf{k}/k$ is a unit vector in the direction of propagation. The index of refraction for the E-mode is obtained from Eq. (13) by the abovementioned substitution $\varepsilon \leftrightarrow \mu$,

$$[n_{eff}^E(\hat{\mathbf{k}})]^2 = \overline{\varepsilon} \bigg/ \left\{ \overline{\xi} - \sum_{G,G' \neq 0} (\mathbf{k} \cdot \mathbf{G})\ (\mathbf{k} \cdot \mathbf{G}') \xi(\mathbf{G}) \xi(-\mathbf{G}')\ [\mathbf{G} \cdot \mathbf{G}' \xi(\mathbf{G} - \mathbf{G}')]^{-1} \right\}. \tag{14}$$

Here $\xi(\mathbf{G})$ is the Fourier component of a periodic function $\xi(\mathbf{r}) = 1/\mu(\mathbf{r})$. In the case of non-magnetic constituents, $(\overline{\mu} = \overline{\xi} = 1, \quad \xi(\mathbf{G}) = 0,)$ the index of refraction for the E-mode becomes $\hat{\mathbf{k}}$-independent, $n_{eff}^E(\hat{\mathbf{k}}) = \sqrt{\overline{\varepsilon}}$. Thus mode becomes the ordinary wave. The H-mode (13) remains the extraordinary wave even in a non-magnetic PC [7,8].
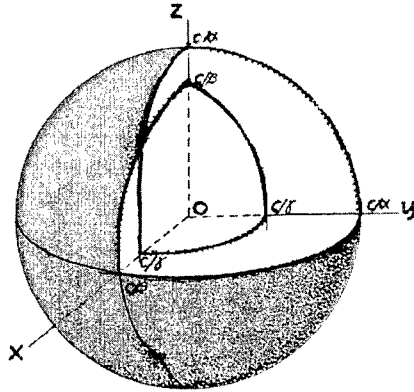
Figure. Fourth-order surface given by the Fresnel equation. The surface consists of two sheets, internal and external, which cross at four singular points. These points determine the directions of two optical axes of the crystal.

It is easy to demonstrate that Eqs. (13), (14) describe ellipses when the Bloch vector **k** sweeps all directions in the *x-y* plane,

$$n_{eff}^{-2}(\hat{\mathbf{k}}) = A_{ij} \hat{k}_i \hat{k}_j, \qquad i, j = x, y. \tag{15}$$

For the *H*-mode tensor A_{ij} is given by

$$A_{ij}^{(H)} = (\overline{\eta / \mu}) \delta_{ij} - (1/2\overline{\mu}) \sum_{\mathbf{G}, \mathbf{G}' \neq 0} (G_i G_j' + G_j G_i') \eta(\mathbf{G}) \eta(-\mathbf{G}') [\mathbf{G} \cdot \mathbf{G}' \eta(\mathbf{G} - \mathbf{G}')]^{-1}, \tag{16}$$

and for the *E*-mode one needs to interchange $\varepsilon \leftrightarrow \mu$.

The magnetic susceptibility of natural crystals (with respect to the magnetic field of propagating wave) is negligibly small. Therefore the Fresnel equation (the principal equation of Crystal Optics) is derived [9] for non-magnetic materials, $\mu_{ik} = \delta_{ik}$. Because of this limitation one of the solutions of the Fresnel equation turns out to be ordinary wave. The difference between ordinary and extraordinary wave is illustrated in Fig. 1. The self-crossing surface shown there is the fourth-order surface obtained from the Fresnel equation. For each direction of propagation there are two different indices of refraction. The contour

of the cross-section by plane $z = 0$ consists of a circle (ordinary wave) and an ellipse (extraordinary wave). However, if $\mu_{ik} \neq \delta_{ik}$ the curves in the x-y plane are ellipses, i.e. the both modes are extraordinary waves [10]. Thus Eqs. (13-16) obtained for 2D magnetic PC exhibits general property of the Fresnel equation that previously was not studied. Presence of two extraordinary modes in artificial magnetic PC strongly modifies the well-known phenomenon of conical refraction observed in biaxial natural crystals. This question requires further detailed study.

CONCLUSIONS

We have studied the low-frequency index of refraction for 2D magnetic photonic crystals. Analytical results show that the presence of magnetic material gives rise to the optical properties of magnetic photonic crystal that do not exist for natural crystals. In particular, two polarizations, the E- and H-modes, exhibit extraordinary-wave behavior.

ACKNOWLEDGEMENTS

REFERENCES

1. E. Yablonovich, Scientific American, December 2001, p. 47.
2. J.G. Flemming, S.Y. Lin, I. El-Kady, R. Biswas, and K.M. Ho, *Nature* **417**, 52 (2002); L.V. Panina, A.N. Grigorenko, and D.P. Makhnovskiy, *Phys. Rev. B* **66**, 155411 (2002).
3. F.X. Redl, K.-S. Cho, C.B. Murray, and S.O'Brien, *Nature* **423**, 968 (2003); Y. Saado, M. Golosovsky, D. Davidov, and A. Frenkel, *Phys. Rev. B* **66**, 195108 (2003).
4. P. Halevi, A.A. Krokhin, and J. Arriaga, *Appl. Phys. Lett.* **75**, 2725 (1999).
5. J. D. Joannopoulos, R.D. Meade, and J.N. Winn, *Photonic Crystals: Molding the Flow of Light*, (Princeton University Press, New Jersey, 1995).
6. R. Fuchs, *Phys. Rev. B* **11**, 1732 (1975).
7. P. Halevi, A.A. Krokhin, and J. Arriaga, *Phys. Rev. Lett.* **82**, 719 (1999).
8. A.A. Krokhin, P. Halevi, and J. Arriaga, Phys. Rev. B **65**, 115208 (2002).
9. M. Born and E. Wolf, *Principles of Optics* (Pergamon Press, Oxford, 1975).
10. A.A. Krokhin and E. Reyes (unpublished).

Photonic Crystal Tapers for Coupling Large Ridge Waveguides to Photonic Crystal Waveguides

Francis C. Ndi, Jean Toulouse
Physics Department, Lehigh University, 16 memorial drive east, Bethlehem PA 18015, USA

ABSTRACT

We present a study of various photonic crystal taper structures each characterized by the taper angle and roughness for coupling light into 2-dimensional photonic crystal waveguides from large ridge waveguides. The photonic crystal waveguide is made of a triangular lattice of holes in a dielectric. The objective is to find a taper structure that offers the best coupling efficiency over a range of widths of the ridge waveguide while leaving a small footprint. We show that such a structure indeed exists and can be further optimized as the width of the ridge waveguide gets even larger leading to more than 90% increase in coupling efficiency in some cases.

INTRODUCTION

Recently photonic crystal (PC) waveguides have received much attention due to their highly desirable optical properties such as non-radiative guiding of light within a plane which leads to unique optical characteristics such as high transmission through very sharp bends in the waveguide[1]. Additionally, the fact that these waveguides are of the order of microns in size provides an enabling technology for large scale optical integration on a single chip that involves the incorporation of many interconnected optical components on a monolithic substrate. Fabrication of PC devices is also amenable to methods developed in the microelectronics industry. In this respect, the photonic crystal made of a triangular lattice of holes in a dielectric promises to be one of the contenders in the first generation of optical integrated circuits. This is because it is relatively easy to make and offers a desirable frequency band gap at near infra-red frequencies for most conventional dielectrics. Unfortunately, because of their small sizes, it is very difficult to couple light from conventional waveguides into PC waveguides. This difficulty is primarily due to the disparity in the respective transverse mode profiles.

Various methods have been proposed to solve this problem such as the use of a parabolic mirror to focus the incident beam into the PC waveguide[2]. Another method involves coupling the light from the conventional waveguide into a ridge waveguide (RWG) of comparable dimensions and then adiabatically tapering the RWG into the PC waveguide[3].

The achievement of adiabaticity of the taper is a non-trivial task and is the focus of this paper. We present the transmission characteristics of a group of tapers made by omission of holes in the PC lattice and show that one of them offers the best coupling efficiency at a minimum taper length. We also propose a modification of this high-efficiency coupler that leads to an improvement in the coupling efficiency. Lastly, we also show that this result is valid for a range of widths of the ridge waveguide. The motivation for considering a range of widths being that, often, one would like to couple light from such sources as single and multi-mode fibers and even focused beams. These sources have widths ranging anywhere from a few microns to above ten microns.

The problems regarding photonic crystal tapers have been addressed in various studies. Happ et al.[4] have done a similar investigation but did not answer the question of the range of widths of the RWG or further optimization of the taper. Another study was also done for the case of tapers made of dielectric rods[5,6] but in these cases the taper walls are smooth extensions of the RWG and does not suffer from roughness due to contact with the lattice points and the ratio of PC waveguide width to RWG width was larger.

SIMULATION DETAILS

Our simulation was done using a two-dimensional finite-difference-time-domain program with perfectly-matched boundary conditions to eliminate back reflections[7]. The four diagrams in figure 1 depict the computational domains for four of the structures studied.
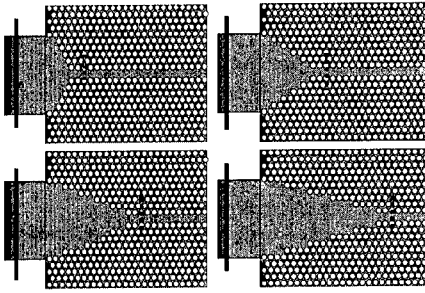
Figure1. Four of the five tapers investigated. The bold and dashed lines show approximately the locations where the input and coupled powers are measured respectively.

In each diagram, the grey area has a refractive index of 3.4 whereas the white circles are air holes. This is a simple model of a structure made using a Silicon substrate. The lattice constant a of the PC is 0.5 μm while the radius r is 0.42a. This structure has a bandgap from 1.15 μm to 1.89 μm[8] for light polarized in the plane of the lattice. The PC waveguide was made by removing a line of nearest-neighbor holes (ΓK direction). The tapers were made by removing a group of holes as shown in figure 1 and each can be characterized by the holes closest to the unperturbed dielectric. The one on the top left is made of nearest neighbor (nn) holes and the top right is made of next nearest neighbor (2nn) holes, etc.

In our simulation, a monochromatic beam with a Gaussian cross-section is launched into the taper from the RWG waveguide. The light has a wavelength of 1.55 μm and is linearly polarized with the electric field parallel to the plane of the lattice. The transmitted power is measured two lattice periods from the input of the PC waveguide as shown in figure 1. The coupling efficiency (defined as the transmitted power normalized to the input power measured 0.5 μm before the input to the taper) was then obtained. The simulation was run for different taper geometries with the width of the RWG kept constant at 6 μm. This width is more than thirteen times the width of the PC waveguide (0.45 μm).

RESULTS

The results are shown in figure 2. For the first three data points (nn, 2nn, 3nn), the coupling efficiency increases rapidly.
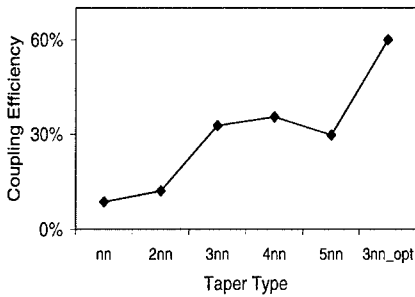
Figure 2. Coupling efficiencies of the various tapers investigated. The 3nn taper offers the best efficiency at a minimum taper length while the 3nn_opt taper offers the best overall coupling efficiency

The 4nn taper offers a slightly higher efficiency, but with almost 50% increase in taper length (from 7.5 μm to 11 μm). As the taper angle is further reduced in the 5nn taper, the efficiency drops. This is counter-intuitive because one would expect improved adiabaticity with a smaller taper angle. It is clear that among the five tapers investigated in our simulations, the 3nn taper offers the best coupling efficiency-to-taper length ratio.

The next question is whether the 3nn taper can be further improved in order to increase the coupling efficiency. We attempted to reduce the roughness of the walls of the taper by inserting smaller holes (with half the diameter of the holes making up the crystal) one lattice point to the left of the holes closest to the unperturbed dielectric in the taper. We refer to this taper, shown in figure 3, as 3nn_opt. The optimization leads to more than 90% increase in the coupling efficiency as shown in figure 2.
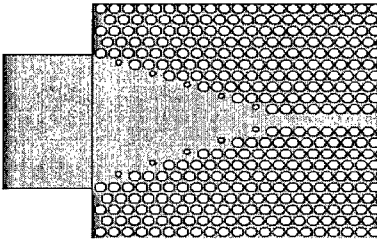
Figure 3. Optimized version of the 3nn taper, leads to more than 90% increase in coupling efficiency.

In order to investigate the influence of the width of the RWG, we ran the simulation for four different widths of the RWG (3 μm, 6 μm, 8 μm, 14 μm). The results are shown in figure 4.

135
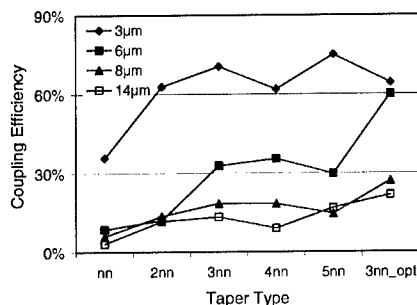
Figure 4. Coupling efficiency for different widths of the RWG.

The first obvious observation is that as the width of the RWG increases, the overall transmitted power drops. This is due to the increasing disparity between the widths of the modes of the two waveguides. Secondly, as the width of the RWG gets closer to the width of the PC waveguide, the taper structure does not play a significant role beyond the 3nn taper as shown in the graph corresponding to the 3 μm RWG. Thirdly, the 3nn taper does indeed provide the best coupling efficiency for all the tapers if one considers minimization of the taper length in the optimization process. Finally, the optimized version of the 3nn taper leads to an improvement in the coupling efficiency primarily for large ridge waveguides. We also note that, as the RWG widths gets larger, there are likely to be taper structures of higher order that are going to have higher coupling efficiencies than the 3nn taper but probably not giving a drastic improvement and most likely requiring a larger taper length. This is the case with the 5nn taper for the 14 μm width RWG.

CONCLUSION

We have shown that of the photonic crystal tapers made by simple omission of holes in a regular photonic crystal, the taper with the walls made of third nearest neighbor holes (3nn) offers the best coupling efficiency at a minimum taper length. This result is for the case of photonic crystals made of a triangular lattice of holes in a dielectric. We have also shown that this 3nn taper can be further optimized leading to a more than 90% increase in the coupling efficiency in some cases. Finally we have shown that the above results are valid for a range of widths of ridge waveguides that are comparable to the widths of conventional waveguides such as single and multimode fibers and focused beams. In particular, the optimized taper offers greater than 60% coupling efficiency for up to 6 μm wide ridge waveguide.

REFERENCES

[1]   J.D. Joannopoulos, R. D. Meade and J. N. Winn, *Photonic Crystals* (Princeton U. Press, Princeton, N.J., 1995)

[2] D. W. Prather, J. Murakowski, S. Shi, S Vankataraman, A. Sharkawy, C. Chen and D. Pustai, "High-efficiency coupling structure for a single-line-defect photonic crystal waveguide", Opt. Lett., **27**, 1601 (2002)

[3] P. Sanchis, J. Marti, A. Garcia, A. Martinez and J. Blasco, "High efficiency coupling technique for planar crystal waveguides", Electronics Letters, **38**, No. 17 (2002)

[4] T. D. Happ, M. Kamp and A. Forchel, "Photonic crystal tapers for ultracompact mode conversion", Opt. Lett. **26**, 1102 (2001)

[5] Y. Xu, R. K. Lee and A. Yariv, "Adiabatic coupling between conventional dielectric waveguides and waveguides with discrete translational symmetry", Opt. Lett. **25**, 755 (2000)

[6] A. Mekis, J. D. Joannopoulos, "Tapered couplers for efficient interfacing between dielectric and photonic crystal waveguides", J. Lightwave Technol. **19**, 861 (2001)

[7] M. N. O. Sadiku, "Numerical techniques in electromagnetics" (CRS, Boca Raton, Florida, 2001), pp 121-219

[8] This result was obtained using a commercial 2-dimemsional bandstructure calculation program based on the plane wave expansion method.

Phonon-Polariton Propagation, Guidance, and Control in Bulk and Patterned Thin Film Ferroelectric Crystals

David W. Ward, Eric Statz, Jaime D. Beers, Nikolay Stoyanov, Thomas Feurer, Ryan M. Roth[1], Richard M. Osgood[1], and Keith A. Nelson
The Massachusetts Institute of Technology,
Cambridge, MA 02139, USA
[1]Microelectronics Sciences Laboratories, Columbia University,
New York, New York 10027, USA

ABSTRACT

Using time resolved ultrafast spectroscopy, we have demonstrated that the far infrared (FIR) excitations in ferroelectric crystals may be modified through an arsenal of control techniques from the fields of guided waves, geometrical and Fourier optics, and optical pulse shaping. We show that $LiNbO_3$ and $LiTaO_3$ crystals of 10-250 μm thickness behave as slab waveguides for phonon-polaritons, which are admixtures of electromagnetic waves and lattice vibrations, when the polariton wavelength is on the order of or greater than the crystal thickness. Furthermore, we show that ferroelectric crystals are amenable to processing by ultrafast laser ablation, allowing for milling of user-defined patterns designed for guidance and control of phonon-polariton propagation. We have fabricated several functional structures including THz rectangular waveguides, resonators, splitters/couplers, interferometers, focusing reflectors, and diffractive elements. Electric field enhancement has been obtained with the reflective structures, through spatial shaping, of the optical excitation beam used for phonon-polariton generation, and through temporal pulse shaping to permit repetitive excitation of a phonon-polariton resonant cavity.

INTRODUCTION

At long wavelengths, the coupling of electromagnetic radiation to an optic phonon mode gives rise to a propagating excitation known as a phonon-polariton, henceforth referred to as a polariton, which displays the properties of both its phonon and photon constituents [1]. The exploitation of this dual-nature excitation is called polaritonics, in analogy to photonics. The phonon-polariton dispersion relation splits into two branches. The lower branch displays light-like dispersion for small wavevectors and evolves into phonon-like dispersion at higher wavevectors. The converse is true for the upper branch; however, the limited time resolution of our probe pulse precludes the resolution of upper branch polaritons. Exploitation of polariton electromagnetic wave character provides a direct channel of control over propagation and dispersion of not only electromagnetic but also lattice vibrational coherence and energy.

Coherent polaritons are generated by ultrafast optical pulses through impulsive stimulated Raman scattering (ISRS) [2]. The ability to spatially and temporally shape the optical excitation beam provides a channel of coherent control through which polariton spatial and temporal profiles may be specified.

EXPERIMENTAL DETAILS

We utilize two lasers for experiments and fabrication: a home-built Ti:sapphire multi-pass amplifier (800 nm, 50 fs, 1 KHz rep. rate, 700 μJ/pulse) seeded by a KM Labs oscillator (790 nm, 15 fs, 88 MHz rep. rate, 3 nj/pulse), and a Coherent RegA Ti:sapphire regenerative amplifier (800 nm, 200 fs, 250 KHz rep. rate, 6 μJ/pulse) seeded by a Coherent Mira oscillator.

Stoichiometric, X- or Y-cut, poled LiNbO$_3$ and LiTaO$_3$ crystals provide excellent conversion of optical light to polaritons due to their high electro-optic coefficients. In the experiments reported here, several types of samples were used. The thinnest samples, ~10 μm thick LiNbO$_3$, were fabricated by crystal ion slicing, which uses high-energy ion implantation at 3.8 MeV, combined with chemical etching, to exfoliate single-crystal sheets of metal oxide crystals [3]. 250 and 500 μm thick LiNbO$_3$ crystals were used for the patterned materials experiments, a 2 mm thick LiTaO$_3$ crystal with elliptically polished ends (curvature perpendicular to the optic axis) was used for large aperture focusing, and a 5 mm thick LiTaO$_3$ crystal was used for axicon experiments. All crystals are commercially manufactured with the exception of the 10 μm films.

In order to generate narrowband polariton waveforms of wavelength l , a spatially periodic optical intensity pattern is projected onto the sample. The excitation beam is passed through a binary phase mask, and the $\pm$ 1 orders of diffraction are overlapped at the sample to form an interference pattern of specified period l [4]. Polariton frequencies from ~0.1-7.5 THz with bandwidths on the order of 10 GHz are accessible with this setup.

The ionic displacements concomitant with polariton propagation modulate the index of refraction of the crystal, creating a unique time-dependent phase pattern that corresponds to the polariton amplitude distribution over the spatial extent of the crystal. Polariton imaging uses well known techniques of phase to amplitude conversion to image this phase pattern onto a CCD [5]. Images are acquired at different delays of an ultrafast probe pulse with respect to the pump, and the complete set of sequential images over a large range of delays constitutes a 'movie' that captures the propagating THz wave as a function of time [6]. Other probe techniques, including interferometric measurement, are used to monitor polariton propagation through a single point.

Patterning of a material with 10-20 μm lateral resolution is achieved by focusing a series of ultrafast laser pulses (100-200 μJ/pulse) onto a crystal using a microscope objective (NA~1.4), leaving a material void in the irradiated region. A computer actuated Burleigh 3-axis translation stage changes the position of the sample in the beam path in steps of 10 μm, allowing a user specified pattern to be cut into the sample with little to no user intervention [7].

Temporal shaping of the pump beam is achieved using the Deathstar pulseshaper, which consists of a system of two retroreflectors that divide a single ultrafast laser pulse into seven pulses that are evenly spaced temporally with repetition rate in the 5-1000 GHz range and whose intensities form a roughly Gaussian profile [8]. The resulting pulsetrain was focused to a 120 μm spot size at a polariton resonator structure. For the experiments reported here, pulsetrain repetition was tuned from 0.1 to 0.4 THz in 10 GHz steps to explore the frequency-dependent resonator response

RESULTS AND DISCUSSION

Polariton Slab Waveguide

Narrowband polariton generation and polariton imaging with a 400 nm wavelength probe were used to characterize the dispersive properties of a 10 μm thick slab of LiNbO$_3$ over a 6-100 μm range of polariton wavelengths. Figure 1a shows a typical CCD image of polaritons with 56 μm wavelength collected 5 ps after generation by crossed excitation pulses. The images at different probe delay times show the movement of the polariton peaks and nulls, and analysis of the set of results permits direct determination of the phase velocity. Since the images are redundant in the vertical dimension, signal-to-noise was enhanced by over an order of magnitude by integration and compression of each image along that dimension. The compressed images
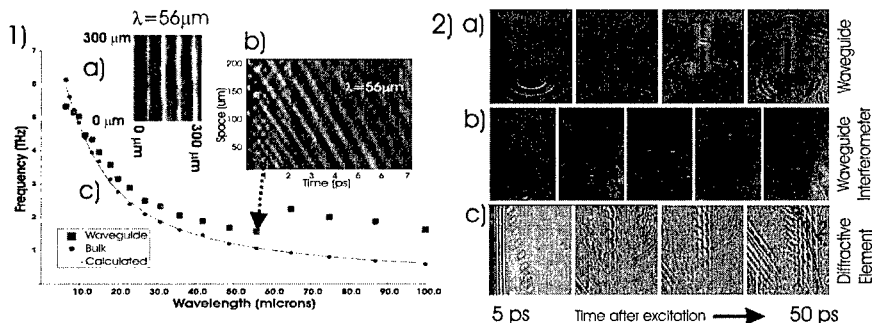
Figure 1: Crossed excitation beams generate narrowband polaritons in LiNbO₃, and their spatial and temporal evolution are monitored simultaneously by polariton imaging. a) CCD image of polaritons (56 μm wavelength) in a 10 μm thick LiNbO₃ film 5 ps after excitation. b) Space-time plot formed by compression and time ordering of images like that in (a), showing polariton propagation vs time. c) Polariton dispersion in a 10 μm thick film (squares) and bulk (circles and solid curve). **Figure 2:** Polariton propagation in several patterned materials demonstrating guidance, interference, and diffraction. a) 200 μm x 1.7 mm waveguide demonstrating polariton guidance. b) waveguide interferometer. c) Diffractive element consisting of ten 140 μm x 300 μm slits. The first two orders of diffraction are evident.

were rotated by 90 degrees and arranged in time order to generate a space vs. time graph as shown in figure 1b. Fourier filtering and examination of the spectral content for each polariton wavelength yielded the dispersion relation shown in figure 1c.

Comparison of the 10 μm slab waveguide to bulk LiNbO₃ in the limit of small polariton wavelength indicates similar dispersion properties. As the wavelength is increased, the dispersive properties deviate toward higher frequency than the corresponding bulk response, presumably under the influence of the lower-index exterior (air). At wavelengths much greater than the slab thickness, dispersion appears to be dominated by that of the exterior and has a group velocity very near that in air. Intermediate to these regimes, around 60 μm, the slab appears to undergo a rather sharp transition from predominantly bulk to predominantly exterior (i.e. "cladding" into which the polariton electromagnetic field extends) dispersion. We believe the abruptness of the transition may be due to the high dielectric contrast, 4.6 to 1.0. Assuming the transition is continuous, we expect to see a reversal of the group velocity over a short range of wavelengths in this region, but further investigation of this range is required.

Patterned Samples

Through ultrafast laser machining, we have fabricated a variety of components for polariton guidance and passive signal processing. The images of polaritons propagating through a 1700x200 μm waveguide in figure 2a illustrates direct visualization of polariton confinement in a manner that is not generally possible for optical waveguides [7]. As the polaritons travel the extent of the waveguide, the wave front remains planar. Only upon exiting does it start to diverge and radiate as from a point source. Polariton propagation through a waveguide interferometer, as shown in figure 2b, demonstrates the potential for functional THz devices.
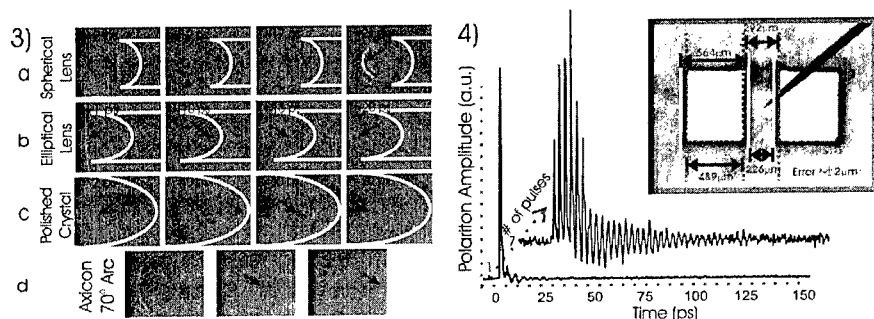
Figure 3 Polariton electric field enhancement of ~2 via focusing with a) a laser machined LiNbO₃ spherical lens, b) a laser machined elliptical lens (major axis 300 μm, minor axis 294 μm), c) and a LiTaO₃ crystal with elliptically polished ends (major axis 2778 μm, minor axis 2500 μm), d) and enhancement of ~5 with a spatially shaped pump pulse (axicon focus) in LiTaO₃. **Figure 4** The LiNbO₃ region of the polariton resonator is indicated by the pointer and is flanked with hollow (air) cavities on either side. The combined effect of the two cavities is an enhanced resonance at 321 GHz and a slightly weaker resonance at 239 GHz. Two interferometric time scans of the polariton signal in the resonator are shown. The first shows the response generated by a single 1μj optical pulse within the LiNbO3 region and the second shows the enhanced response (~6x in intensity) from a series of seven optical pulses generated by the Deathstar pulseshaper tuned to the 321 GHz resonance.

The diffraction grating in figure 2c illustrates the potential for conducting polaritonics in the frequency domain [9]. The figure illustrates first and second order diffraction of a broadband THz pulse centered around 150 μm. The grating consists of ten 140x300 μm slits spaced 200 μm apart in a LiNbO₃ crystal. Such structures allow for spectral discrimination along a spatial dimension and have potential applications in THz spectroscopy.

Passive enhancement of polariton amplitudes has been realized through various methods of focusing. Through femtosecond laser machining, we have fabricated both spherical (figure 3a) and elliptical (figure 3b) focusing reflectors. We have also polished the end of a 3x5x2 mm LiTaO₃ crystal to an ellipse (figure 3c), forming a larger reflecting element. A similar focusing effect is achieved by spatially shaping the pump beam to a circular shape at the sample in order to generate a curved polariton wavefront which focuses as it propagates (figure 3d) [10,11]. We achieve this by imaging an arc from the output of an axicon (a conical biprism that produces a circular beam profile) onto the crystal. We achieved electric field enhancements of order 2-5 and intensity enhancements of 4-25 through these methods; however, theoretical estimates suggest that field enhancement of about 10 are achievable in both cases. Comparable additional enhancement could be achieved through focusing in the other transverse dimension.

Coherent Control in a Polariton Resonator

We have used optical pulse shaping to repetitively drive polaritons trapped in a polariton resonator cavity (inset figure 4) with a primary resonance frequency of 321 GHz and an unloaded Q of approximately 10. There is also a weaker resonance at 239 GHz due to the coupling of hollow cavities to the central LiNbO₃ region as shown in the figure, but it is not explored in this report. Figure 4 presents interferometrically recorded data comparing the

polariton response due to a single excitation pulse to that of seven pulses from the Deathstar pulseshaper. The strength and persistence of the polaritons generated by the pulsetrain are attributed to the hollow cavities flanking the resonator and will be discussed in detail in a subsequent publication.

We amplified polariton energy by a factor of 6.25 using the seven pulses from the Deathstar, which is 95% of the theoretical maximum obtainable with an infinite number of pulses. Propagation loss in the resonator is negligible, but transmission loss at the interface is high. The low Q of the cavity is the chief impediment to amplification. If the dielectric resonator's walls are coated with silver then the theoretical amplification maximum rises to near 1600, but the seven pulses from the Deathstar can only realize 15% of this. Thus, not only does the Q need to be increased to achieve near maximal amplification, but the number of pulses in the pulsetrain must also be increased.

CONCLUSIONS

Two channels of control over polariton propagation have been demonstrated. The first channel exerts control through manipulation of the electromagnetic wave character of the polaritons, which we have effected by fabricating polaritonic structures using ultrafast laser machining. The second acts through spatial or temporal shaping of the optical field which is passed on to the polariton response through the ISRS excitation mechanism. Control over polariton guidance, generation, propagation, dispersion, and frequency content has been shown. The THz radiation from polaritons may be propagated out of the crystal in which they are generated. Polariton control therefore enables a robust source of coherent THz radiation and a host of capabilities for THz signal processing and spectroscopy [12].

ACKNOWLEDGEMENTS

REFERENCES

[1] M. Born and K. Huang, *Dynamical Theory of Crystal Lattices* (Clarendon Press, Oxford, 1954).

[2] Y.-X. Yan, E.B. Gamble, Jr., and K.A. Nelson,"Impulsive stimulated scattering: General importance in femtosecond laser pulse interactions with matter, and spectroscopic applications," J. Chem. Phys. **83**, 5391-5399 (1985).

[3] M. Levy, R.M. Osgood, Jr., R. Liu, E. Cross, G.S. Cargill III, A. Kumar and H. Bakhru, "Fabrication of Single-Crystal Lithium Niobate Films by Crystal Ion Slicing," Appl. Phys. Lett. **73**, 2293-2295 (1998).

[4] A.A. Maznev and K.A. Nelson, "How to make femtosecond pulses overlap," Opt. Lett. **23**, 1319-1321 (1998).

[5] R.M. Koel, S. Adachi, and K.A. Nelson, "Direct Visualization of Collective Wavepacket Dynamics," J. Phys. Chem. A. **103**, 10260-10267 (1999).

[6] Our website has a series of movies pertaining to the figures in this paper. http://nelson.mit.edu/movietheater.html.

[7] N.S. Stoyanov, D.W. Ward, T. Feurer, and K.A. Nelson, "Terahertz Polariton Propagation in Patterned Materials," Nature Materials **1** (2), 95-98 (2002).

[8]Manuscript in preparation.

[9]N.S. Stoyanov, T. Feurer, D.W. Ward, and K.A. Nelson, "Integrated Diffractive Terahertz Elements," Appl. Phys. Lett. **82** (5), 674-676 (2003).

[10]N.S. Stoyanov, D.W. Ward, T. Feurer, and K.A. Nelson, "Direct Visualization of Phonon-Polariton Focusing and Amplitude Enhancement," J. Chem. Phys. **117** (6), 2897-2901 (2002).

[11]T. Feurer, N.S. Stoyanov, D.W. Ward, and K.A. Nelson, "Direct Visualization of the Gouy Phase by Focussing Phonon-Polaritons," Phys. Rev. Lett. **88** (25), Art. No. 257402 (2002).

[12]T.F. Crimmins, M.J. Gleason, D.W. Ward, and K.A. Nelson, "A Simple Terahertz Spectrometer," presented at the Ultrafast Phenomena XII, Charleston, SC, 2001.

Fabrication of Two-dimensional Nonlinear Photonic Crystal by Electron Beam Lithography

Chiang Huen Kang[a], Ze Xiang Shen and Sing Hai Tang
Physics Department, National University of Singapore, Singapore 117542
[a] corresponding author: phimismy@yahoo.com

ABSTRACT

In this paper, we present a study on quasi-phase matched (QPM) two-dimensional $\chi^{(2)}$ lithium niobate (LN) nonlinear photonic crystal (NPC) for frequency doubling at $\lambda = 1064$nm. The NPCs were fabricated by electron beam lithography (EBL) through periodic polarization inversion of the ferroelectric domains and characterized with electrostatic force microscopy (EFM), atomic force microscopy and optical microscopy. Domain inversion occurred through the entire wafer thickness of 0.5mm as EFM images on the +c face of the z-cut wafer showed uniform domain structures throughout the corresponding electron beam irradiated regions of the -c face. In addition, the intended periodicity was observed. Moreover, domain inversion was also seen to have taken place in bulk from the optical images of the chemically etched samples. The EBL technique offers great flexibility in superlattice design and relative ease of fabrication as compared to the conventional poling techniques as pattern transfer is direct without the need for a mask and/or a coating of resist. Besides, micro- or sub-micro scale superlattices corresponding to wavelengths in the visible and into the ultraviolet are highly feasible, restricted only by the transparency of the crystals.

INTRODUCTION

Since the seminal paper by Armstrong et.al.[1] proposing the utilization of quasi-phase matching (QPM) as a solution to the problem of phase mismatch in frequency conversion, a large amount of research efforts had been done to realize one-dimensional QPM structures in a variety of ways[2-5]. It was until recently that Berger[6] extended the idea of QPM to two dimensions allowing us greater compensation for phase mismatch. These superlattices, nonlinear photonic crystals (NPC), have periodically modulated nonlinear susceptibilities in an otherwise spatially equivalent refractive index dielectric. The first experimental realization of such a two-dimensional NPC was accomplished by Broderick et.al.[7]. Amongst the fabrication methods, electro-poling of ferroelectrics, particularly lithium niobate (LN) had been the most prominent. Nevertheless, electro-poling requires a laborious multi-step process of resist coating, lithography patterning and subsequent metal deposition and resist removal for pattern transfer. Moreover, a mask had to be made for each intended pattern. Electron beam lithography (EBL) presents an edge over conventional poling in that pattern transfer is direct with the added bonuses of versatility in superlattice design and high resolution offering the possibility of submicron sized periodic ferroelectric domain features.[8] These domain inverted gratings had been imaged through diverse routes such as scanning electron microscopy (SEM)[9], transmission electron microscopy (TEM)[10], optical microscopy[11] and electric force microscopy (EFM)[12]. However, EFM presents a favorable technique in comparison to other imaging techniques in that it requires minimal sample preparation, ambient working conditions and provides a qualitative, if not quantitative, account of the electrostatic distribution of the grating with an achievable lateral resolution of 50nm[12]. Here, we emphasize on a particular type of EFM, electrostatic phase imaging (EPI). EPI works

through the detection of the phase differences of a resonantly driven cantilever induced by the surface charges or emanating electric fields on the dc bias tip. Nevertheless, no work has been done to employ this technique to probe ferroelectric features buried under a layer of dielectric which is common in integrated optics manufacturing.

In this paper, we present the fabrication of a two-dimensional NPC by EBL and its characterization by EPI. Buried structures under a thin layer of ZEP520 (an electron beam positive tone resist) were also examined. These studies may prove useful in integrated optics manufacturing.

EXPERIMENTAL

A systematic study of the dependence of domain inverted structures on charge density and current over a range of 50 to $650\mu C/cm^2$ (in steps of $50\mu C/cm^2$) and 0.2 to 1nA (in steps of 0.2nA) respectively was carried out. The superlattice was designed for frequency doubling of the wavelength of 1064nm with a periodicity of $12.8\mu m$ in a square lattice and a duty cycle of 50% corresponding to a second-order QPM superlattice. The repeating pattern was chosen to be a hexagon as earlier studies show that domain propagation conforms to the shape of the primitive cell[5]. These parameters were programmed into our JEOL JBX-5DII electron beam lithography system. A 100nm layer of Au was deposited on the +z face of the z-cut, two faces polished, optical grade $10\times10\times0.5$mm single domain LN single crystals through RF-magnetron sputtering. The gold layer was needed for homogenization of conductance to provide an ideal grounding. Subsequently, it was electron beam irradiated under the optimized electron beam conditions at an accelerating voltage of 25kV in a step and repeat vector scan. Figure 1 shows the cross-sectional view of the experimental configuration for electron beam exposure.
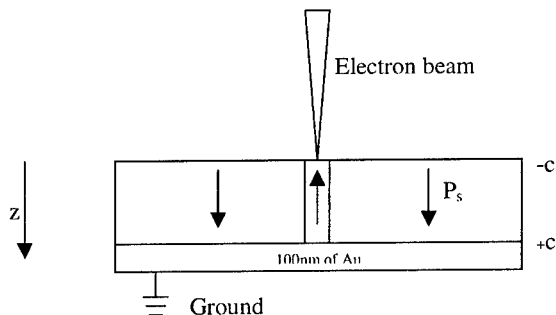
Figure 1 Cross-sectional view of the experimental configuration for electron beam exposure.

The entire artifact was placed in an etching mixture of HF and HNO_3 in 1:3 ratios at an elevated temperature of about 100°C for 1min and observed under an optical microscope. Using a Digital Instruments, Dimension 3000 Nanoscope IIIa controller with extender electronics, atomic force and electrostatic phase images were obtained under ambient conditions in tapping mode. A 300nm thick layer of ZEP520 was then spin-coated at a speed of 6000rpm for 2 minutes and baked for 20 minutes at a temperature of 170°C and EPI was also done on this buried periodic ferroelectric structure.

RESULTS AND DISCUSSIONS

It was found that lateral spreading increases with increasing charge density with no observable dependence on the current within our range of study. At a charge density of $450\mu C/cm^2$ and a current of 1nA, inversion took place in all electron beam irradiated regions through the wafer thickness and these inverted domains were most uniform. Nevertheless, it should be noted that these conditions may not be universal as domain reversal inevitably depends on the defect density[13] of the crystals which vary between different batches of crystals. Each electron beam impinged region results in a local poling field greater than the switching field of LN and lasts long enough to prevent back-switching of the newly inverted domains, inducing the inversion of the polarization of the ferroelectric domains through the entire wafer thickness of 0.5mm. Fig. 2 shows the optical image of an etched sample. Due to the differential etch rates of the dissimilarly polarized domains a ridge-like structure was obtained. The differential etch rates are the result of the difference in approach probability of H^+ ions to the positive and negative ends of the domain polarization; H^+ ions approach the negative ends with a higher probability due to Coulombic attraction.
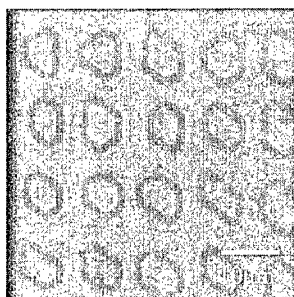
Figure 2 Optical image of the chemically etched two-dimensional nonlinear photonic crystal as seen on the +c face.

Atomic force images obtained under ambient conditions in tapping mode show a periodic topography as in Fig. 3. The dark hexagonal regions correspond to electron beam exposed area where domains are inverted. These regions are pits and together with the brighter regions form a ridge-like pattern. Through the height analysis of the atomic force image it was found that the height difference between the brighter and darker regions is approximately 140nm. We can also see that the intended periodicity of $12.8\mu m$ is observed with an appreciable uniformity of the expected hexagons. The duty cycle of 50% was not faithfully followed due to the lateral spreading of domain structures. The electron beam profile at the focal point which governs the interacting cross-section also contributes to the extent of domain spreading. Poorly defined boundaries yielding varying slopes in each pit are suggestive of non-anti-parallel domains near the domain walls.

Negative ends of
domain
polarization
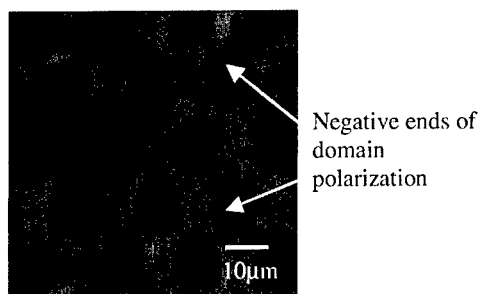
Figure 3 Atomic force image of the chemically etched two-dimensional domain inverted optical superlattice as seen on the +c face. The intended periodicity of 12.8µm is observed with appreciable uniformity of the expected hexagons. The scan size is 60×60µm.

To obtain electrostatic phase images, the cantilever with a cobalt coated tip was lifted to an optimized height of 50nm under the interleaved tapping lift mode in a 60×60µm retrace scan. This is a two-pass technique whereby the topographical data was first acquired and stored in computer memory. The cantilever was then lifted to a pre-determined height and scanned in accordance to the stored topographical data while maintaining a constant tip-sample distance. This process reduces the effects of topography on the electric force gradient data for which we are trying to obtain. To disregard the topographical effects on electrostatic distribution, a tip bias varying from -12 to 12V in steps of 3V was applied to the tip and the images compared as a function of tip voltage. It was found that changes in phase differences depend only on the magnitude and not the sign of the tip voltage as a consequence of the square dependence of the electrostatic force on the voltage. We can also observe that the contrast between the two differently polarized domains decreases along with increasing magnitude of the tip voltage and null at 12V as shown in Fig. 4. This trend was attributed to the fact that the effect of phase shifts on the tip by electrostatic polarized domains diminishes as tip voltages increases. In retrospect, we can also say that the Coulombic interactions were neutralized with increasing tip voltage.
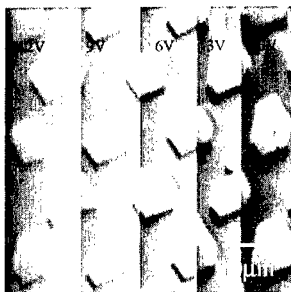
Figure 4 Electric phase image of the sample with varying tip voltages from 0V to 12V, as labeled, under continuous capture.

Phase images of buried structures were obtained in a similar approach as described above with a 20×20μm scan and shown in Fig. 5. It was hence proven that EPI is a reliable technique to image buried ferroelectric features. It was found that the contrast differs as the tip voltage was varied from -12V to 12V. This is an interesting phenomenon in that the presence of a polymeric
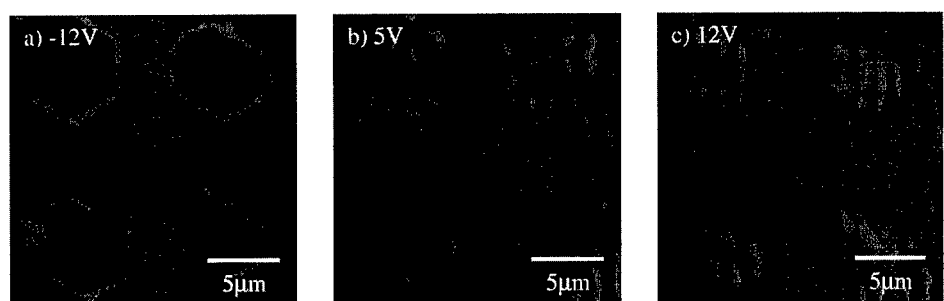
Figure 5 Electric phase images of buried ferroelectric structures under a resist with a tip voltage of a) -12V, b) 5V and c) 12V

layer actually gives a sign dependence of the imaged domains to the tip voltage and that this dependence, in our case, is only applicable to the domains with their negative ends of polarization imaged. One likely explanation to this behavior is as follows. The presence of a ferroelectric field causes the permanent dipoles of the uncharged polymer to align themselves in the direction of the field. The application of external electric fields from the tip results in the reorientation of the dipoles in the direction of the applied field when the field is larger than that due to the ferroelectric. This reorientation is only possible in the hexagonal regions where the electric field is relatively weaker as these regions are actually pits in the topographical image i.e. there is a thicker polymeric layer and since electric field decreases with the square of distance, the electric field aligning the dipoles is relatively smaller. The remaining regions would experience a larger electric field from the ferroelectric due to a thinner polymeric layer. Hence, more work has to be done to reorient the aligned dipoles in these regions implying a larger tip voltage is needed to induce the flip. Therefore, one should be able to obtain an EPI showing the electric field distributions with the intuitively correct contrast inversion along with the polarity of the tip voltage through the coating of a thick layer of polymer. This would imply that through this polymeric layer, EPI is indeed a nondestructive technique; without the need for mechano-chemical polishing to produce an extremely flat surface for EPI so as to disregard topographical interferences on electrostatic distribution.

CONCLUSIONS

In conclusion, we have realized the fabrication of a two-dimensional NPC with a period of 12.8μm in a square lattice using EBL under optimized conditions of 450μC/cm^2 and a current of 1nA. We have also demonstrated the feasibility of employing EPI to image buried ferroelectric features under a 300nm layer of resist, ZEP520. Through the imaging of these buried structures, we found the sign dependence of the contrast between dissimilarly polarized domains on the tip

voltage which can be fruitful to the de-convolution of electrostatic information from topographical data.

ACKNOWLEDGEMENTS

REFERENCES

1. J. A. Armstrong, N. Bloembergen, J. Ducuing, and P. S. Pershan, Phys. Rev. **127**, 1918 (1962)
2. S. Thaniyavarn, T. Finddakly, D. Booher, and J. Moen, Appl. Phys. Lett. **46**, 933 (1985)
3. C. J. Van Der Poel, J. D. Bierlen, J. B. Brown, and S. Colak, Appl. Phys. Lett. **57**, 2074 (1992)
4. G. Rosenman, Kh. Garb, A. Skliar, M. Oron, D. Eger, and M. Katz, Appl. Phys. Lett. **73**, 865 (1998)
5. J. He, S. H. Tang, Y. Q. Qin, P. Dong, H.Z. Zhang, C. H. Kang, W. X. Sun, and Z. X. Shen, J. Appl. Phys. **93**, 9943 (2003)
6. V. Berger, Phys. Rev. Lett. **81**, 4136 (1998)
7. N. G. R. Broderick, G. W. Ross, H. L. Offerhaus, D. J. Richardson, and D. C. Hanna, Phys. Rev. Lett. **84**, 4345 (2000)
8. C. Restoin, S. Massy, C. Darrud-Taupiac, and A. Barthelemy, Opt. Mater. **22**, 193 (2003)
9. M. Fujimura, K. Kintaka, T. Suhara, and H. Nishira, J. Lightwave Tech. **11**, 1360 (1993)
10. Z. Y. Zhang, L. C. Wang, Y. Y. Zhu and N. B. Ming, Ferroelectrics **215**, 113 (1998)
11. C. Restoin, C. Darraud-Taupiac, J. L. Decossas, J. C. Vareille, J. Hauden and A. Martinez, J. Appl. Phys. **88**, 6665 (2000)
12. H. Bluhm, A. Wadas, A. Roshko, J. A. Aust and D. Nam, Appl. Phys. Lett. **71**, 146 (1997)
13. V. Ya. Shur, E. L. Rumyantsev, R. G. Batchko, G. D. Miller, M. M. Fejer, and R. L. Byer, Phys. Solid State **41**, 1681 (1999)

W5.11

Creation and Optical Property of Microphotonic Crystals
by Electrophoretic Deposition Method Using Micro-counter Electrode

Jun-ichi Hamagami, Kazuhiro Hasegawa and Kiyoshi Kanamura
Department of Applied Chemistry, Graduate School of Engineering,
Tokyo Metropolitan University
1-1 Minami-Osawa, Hachioji, Tokyo 192-0397, Japan

ABSTRACT

In order to create micrometer-scale functional optical materials or devices, we have investigated on development of a novel electrophoretic deposition (EPD) method using a microelectrode as a counter electrode: This is so-called "μ-EPD method". The μ-EPD method was applied to fabricate micro colloidal crystals consisting of monodisperse submicron polystyrene latex spheres for micro photonic application. Scanning electron micrographs of the deposit prepared under the optimized μ-EPD parameters showed a formation of microdot consisting of three-dimensionally ordered polystyrene spheres. As a result of the microscopic transmittance spectra, the microdots exhibited a narrow absorption peak and the optical stopband was observed at 460 nm for 204 nm polystyrene spheres, 675 nm for 290 nm polystyrene spheres, and 755 nm for 320 nm polystyrene spheres, respectively. The observed position is due to the Bragg diffraction of light from (111) plane of face-centered cubic opal lattice.

INTRODUCTION

A development of micro-assembling technique for particle is very important to create functional optical materials or devices in future. In fact, two- or three-dimensional arrangement of monodisperse inorganic or polymer spheres on a flat substrate is of interest for photonic, electronic, magnetic, and sensor applications. A number of processes have been developed to fabricate desired materials consisting of highly ordered monodisperse spheres by using some external forces [1-11]. However, these techniques are not suitable for a formation of materials with nanometer- or micrometer-size periodic arrays. To solve this problem, we have proposed a novel micro-assembling technique for particle using an electrophoretic deposition (EPD) process.

The EPD process is one of promising techniques to assemble inorganic or organic particles from colloidal suspensions [8-10]. The EPD process utilizes an electric-field inducing deposition of electrically charged particles in the suspension. Recently, we have proposed to create micrometer-size deposit with a highly controlled microstructure onto a desired position of substrate by using a local electric field. The local electric field was generated by using a microelectrode as a counter electrode. This is so-called "μ-EPD process" [11] and the schematic illustration of the μ-EPD system is shown in Figure 1.

In this paper, the μ-EPD process to nearly monodisperse (standard deviation within 5 %) submicron polystyrene latex spheres was performed in order to create three dimensional microphotonic crystals. In addition, optical transmittance spectra for the electrophoretically fabricated polystyrene microdots were obtained from a microscopic visible spectroscopy.

EXPERIMENTAL DETAILS

Three kinds of polystyrene suspensions for the μ-EPD process were prepared as follows. Particles having a uniform particle size and true spherical shape, are necessary to produce a high quality colloid crystal with a good optical property. The commercial polystyrene microspheres with three kinds of particle size were used as particles dispersed in the suspensions. The mean diameters of polystyrene particles were selected 204, 290, and 320 nm, respectively. Because the colloid crystals made from these particle sizes have optical absorption peaks in visible region. Characteristics of the monodisperse polystyrene spheres are summarized in Table I. Ethanol (purity 99.5 %, Wako Pure Chem. Ind., Ltd.) was employed without further purification as a dispersion medium. The polystyrene spheres in the suspensions were well-dispersed with an ultrasonic bath for 30 minutes just prior to the electrophoretic deposition process.

A constant-voltage electrophoretic deposition of polystyrene latex spheres was carried out in a beaker cell. A μ-EPD apparatus with two electrodes system is schematically shown in Figure 1. An optically transparent indium-tin-oxide (ITO) coated glass was used as a working electrode (substrate) and a platinum wire of 50 μm in diameter embedded in a polytetrafluoroethylene tube was employed as a counter microelectrode.
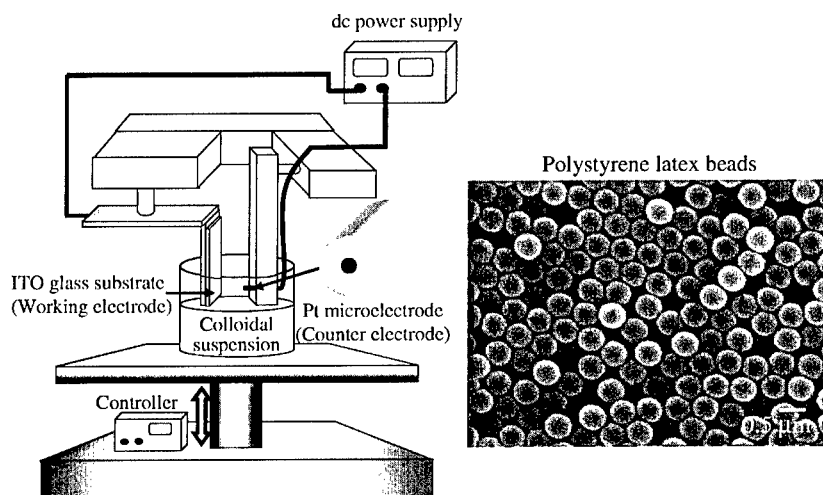
Figure 1. Schematic illustration of experimental setup for micro-electrophoretic deposition (μ-EPD) system and typical electron micrograph of monodisperse polystyrene spherical particles. Platinum wire of 50 μm in diameter and indium-tin-oxide coated glass were used as counter and working electrode (substrate), respectively.

Table I. Characteristics of polystyrene latex spherical particles used in this work.

Product company	Scradyn, Inc	Interfacial Dynamics Co.	Interfacial Dynamics Co.
Mean diameter / nm	204	290	320
Standard deviation / nm	6.9	12	6
Dispersion medium	Distilled de-ionized water	Distilled de-ionized water	Distilled de-ionized water
% solid / g/100 ml^{-1}	10.15	4.4	8.2
Charge group	Sulfate	Amidine	Sulfate
Sign of surface charge	Negative	Positive	Negative

Before deposition the ITO-coated glass substrate was cleaned with an ultrasonic cleaner in order to eliminate impurities on the surface. The two electrodes were fixed at 500 µm distance and connected to a dc power supply (HA-3001, Hokuto Denko Co.). The applied dc voltage of 300 ~ 600 mV was applied for up to 30 minutes to assemble the polystyrene spheres onto the substrate. After the deposition, the substrate was taken out from the suspension without applying the voltage, and then dried at room temperature.

The polystyrene particle deposited on the ITO-coated glass was examined with a scanning electron microscopy (SEM: JSM-5310, JEOL) to confirm the ordering structure of the polystyrene spheres. The optical property of the micro deposit of the monodisperse polystyrene spheres was examined by micro spectroscopy consisting of an optical microscope (BX51, Olympus Co.) and a spectrophotometer with charge coupled device (CCD) array (TFCAM-700C, Lambda Vision Inc.). By using the optical measuring system, the transmittance spectrum in wavelength region from 400 to 780 nm can be obtained from area of about a few µm in diameter of the deposit.

RESULTS AND DISCUSSION

Both microstructure and particle ordering for the deposit of polystyrene latex spheres obtained by the µ-EPD process were investigated by means of SEM. Figure 2 shows the scanning electron micrographs of the micro deposits of the polystyrene spheres with (a) 204, (b) 290, and (c) 320 nm in diameter. These deposits were prepared on the ITO-coated glass substrate under the optimized µ-EPD conditions. The deposits were formed just in front of the micro counter electrode in the EPD system and the sizes of all the deposits were roughly 5 µm. The size of the microdot is considerably smaller than that of the micro counter electrode (50 µm in diameter) used in the EPD system. This is due to ununiformity of the local electric field between both the working electrode (substrate) and the counter electrode, which strongly depends on both the surface of the platinum micro counter electrode and morphology of the substrate surface. SEM and AFM observation indicate that both the Pt electrode surface and the substrate surface were not completely smooth. As shown in Fig. 2, the microdots consist of three-dimensionally ordered polystyrene spheres. The monodisperse submicron polystyrene spherical particles were assembled into a face-centered cubic (fcc) lattice with (111) plane parallel to the surface of the ITO-coated glass substrate. Since the microdots prepared by the µ-EPD process are the almost single crystal without any defects, the microdots are seemed to have a high quality colloidal crystal or photonic crystal. In fact, the structural color of the
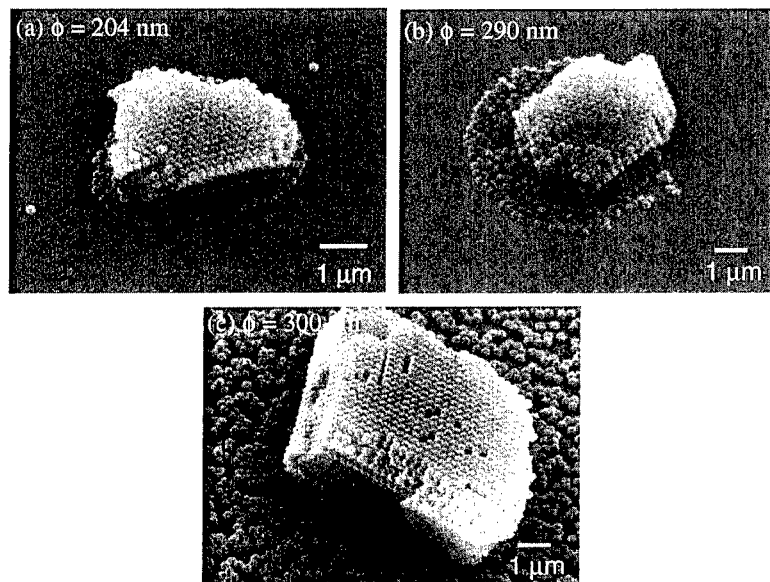
Figure 2. Scanning electron micrographs for the microdots of monodisperse polystyrene spheres with (a) 204 nm, (b) 290 nm, and (c) 300 nm in diameter prepared by using the μ-EPD process under the optimized conditions. An indium-tin-oxide coated glass was used as a substrate.

micro colloidal crystals, which is originated in an optical stopband, can be seen with an optical microscope.

Optical properties of the electrophoretically fabricated micro colloidal crystals on the ITO-coated glass substrate were examined with the microscopic transmission spectroscopy. Figure 3 shows normal incidence optical transmission spectra for three kinds of colloidal crystals in the wavelength region 400 ~ 780 nm. As shown in Fig. 3, a sharp transmittance peak is clearly observed at the specific wavelength depending on the diameter of monodisperse polystyrene spheres. This transmittance peak shows a presence of photonic stopband due to the Bragg reflection on (111) plane in the fcc lattice of colloid crystal. The minimum wavelength of each colloidal crystal was 460 nm for 204 nm polystyrene spheres, 675 nm for 290 nm polystyrene spheres, and 755 nm for 320 nm polystyrene spheres, respectively. Thus, the position of the stopband strongly depended on the polystyrene particle size in the colloidal crystal. On the other hand, the position of stopband for the crystal at normal incidence can be calculated by using the Bragg law. Figure 4 shows the relationship between the peak position of the transmittance spectra of micro colloidal crystals and the diameter of monodisperse polystyrene spheres. The calculated value from the Bragg equation is also shown in the Figure 4 as a dashed line. The experimental value of the stopband position is very close to the theoretical value. A small discrepancy may be assumed to be the shrinkage of polystyrene spheres in the colloidal crystal.
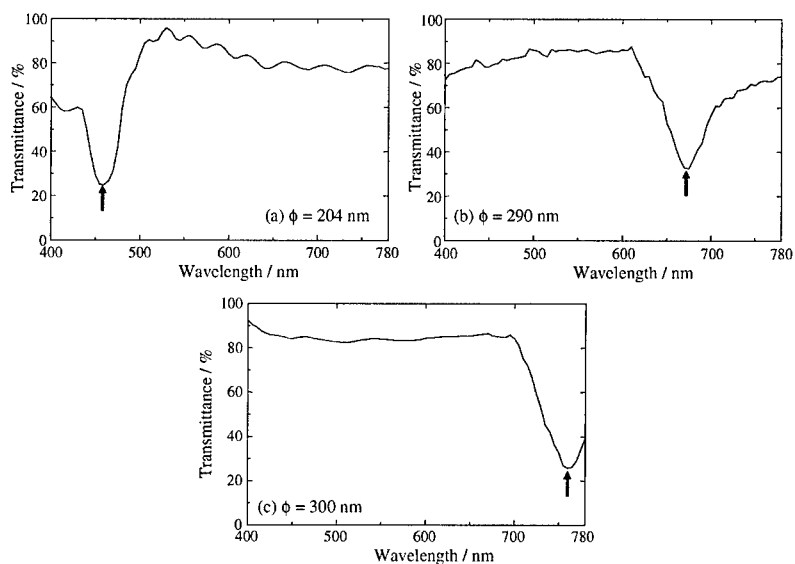
Figure 3. Normal incidence microscopic transmittance spectra of the electrophoretically fabricated microdots of the monodisperse polystyrene spheres with 204 nm, 290 nm, and 300 nm in diameter. The arrows in the figure corresponds to the optical stopband of the colloidal crystal.
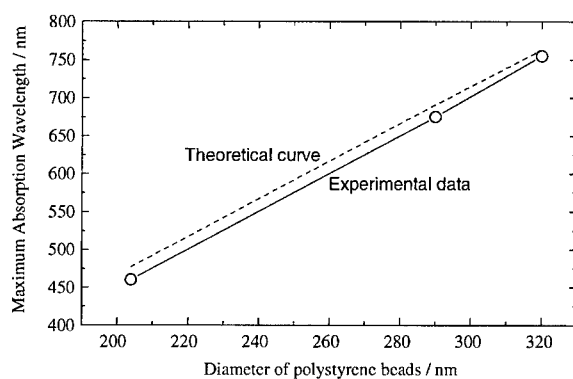
Figure 4. Dependence of the optical stopband on the diameter of monodisperse polystyrene spheres, open circle; the experimental data, dashed line; theoretical curve calculated from the Bragg's law.

CONCLUSION

We have been developed a novel micro-electrophoretic deposition (μ-EPD) method as one of micro-assembling technique of particle. Under the optimized μ-EPD conditions, a high quality photonic crystal (colloidal crystal) consisted of monodisperse submicron polystyrene spheres were successfully formed in front of the micro counter electrode onto an ITO-coated glass substrate. An optical measurement was conducted to examine the property of colloidal crystal prepared by the μ-EPD process. The measured microscopic transmittance spectra showed the minimum transmittance peak in a visible region, which corresponds to the value calculated from the Bragg's equation. From these results, it can be said that the micro photonic crystal with defect-free has been created by the μ-EPD method.

ACKNOWLEDGEMENTS

REFERENCES

1. F. Richetti, J. Prost and P. J. Barois, *J. Phys. Lett.*, **45** L1137 (1984).
2. P. J. Sides, *Langmuir*, **17**, 5791 (2001).
3. M. Giersig and P. Mulvaney, *Langmuir*, **9**, 3408 (1993).
4. M. Trau, D. A. Saville, and I. A. Aksay, *Science*, **272**,706 (1996).
5. R. C. Hayward, D. A. Saville and I. A. Aksay, *Nature*, **404**, 56 (2000).
6. H. Fudouzi and Y.Xia, *Langmuir*, **19**, 9653 (2043).
7. P. Sarker and P. S. Nicholson, *J. Am. Ceram. Soc.*, **79**, 1987 (1996).
8. M.Böhmer, *Langmuir*, 12 (1996), p. 5747.
9. A. L. Rogach, N. A. Kotov, D. S. Koktysh, J. W. Ostrander and G. A. Ragoisha, *Chem. Mater.*, **12**, 2721 (2000).
10. P. Sarkar, D. De, K. Yamashita, P.S. Nicholson and T. Umegaki, *J. Am. Ceram. Soc.*, **83**, 1399 (2000).
11. J. Hamagami, K. Hasegawa and K. Kanamura, *Key Engineering Material*, **248**, 195 (2003).

2-D Photonic Quasicrystal in Metallic Microcavity

J.Y.Zhang[1], H.L.Tam[1], W. H. Wong[2], Y. B. Pun[2], J. B. Xia[1] and K. W. Cheah[1]

[1]Department of Physics, Hong Kong Baptist University, Hong Kong SAR, PRC.

[2]Department of Electronic Engineering, City University of Hong Kong, Hong Kong SAR, PRC.

ABSTRACT

Photonic microcavity promises to be one of the photonic devices that can have immediate applications such as super bright LED and low threshold laser. Most photonic crystal structures currently used on microcavity are cubic or hexagonal, whose folding symmetry is no greater than 6. In this work, we fabricated 2-D photonic microcavity with Penrose quasicrystal pattern and measured the angular resolved transmission and photoluminescence spectra of the microcacity. From the experimental result it is found that isotropic photonic band gap exists in the microcavity with the Penrose quasicrystal pattern.

INTRODUCTION

Photonic crystals are artificial dielectric structures designed to control and manipulate the propagation of light [1]. Periodically corrugated metallic microcavity has similar photonic band gap to photonic crystals with the advantage of increasing the efficiency of extracting light [2-3]. But the photonic band structure of such micorcavity changes with different incident angles and sample orientations. By applying highly symmetric corrugation patterns onto the microcavity, the band structure can be maintained [4-7]. In this work, Penrose quasicrystal tiling with 5-fold symmetry is chosen as the corrugation pattern to enhance the isotropic property of photonic band structure. In addition, organic luminescence material tris (8-hydroxyquinoline) aluminum (Alq_3) is embedded into the microcavity to investigate the modification of photoluminescence by the photonic modes of the microcavity.

EXPERIMENTAL DETAILS

In the experiment, pre-cleaned glass plate with 40nm silver layer deposited on top by evaporation was used as substrate. The sample was then spin-coated with a layer of 60nm photo-resist. Texturing of the photo-resist was carried out by electron beam lithography. The peak-to-peak distance varies from 472 nm to 1418 nm. After etching out the un-exposed photo-resist, a layer of 100nm Alq_3 was evaporated, followed by another 40nm silver layer. Both the Alq_3 and top silver layers maintain the corrugation pattern.

Angle-resolved transmission spectra were measured in order to investigate the photonic band structure of the sample. A Xenon lamp (Oriel 6269; 1000W) was used as the light source. The sample was placed on a rotational stage with angular precision 0.1°. The stage allowed rotations both along the azimuthal axis and the in-plane axis. In the angle-resolved photoluminescence measurement, the 325nm line of He-Cd laser was used as excitation light source of Alq_3. Its output was guided by an optical fiber and focused on to the sample by a convergent lens. The incident angle of the excitation light was fixed at 30^0 while the emission angle can be varied from 0° to 60°. The output signal was captured by a monochromatic system similar to that in the transmission measurement.

DISCUSSION

Figure1(a)&(b) shows the angle-resolved transmission spectra in Transverse Electrical (TE) polarization mode with two different azimuthal angles ΓO and ΓP. The x-axis of the spectrum is in-plane k vector and the y-axis is wavelength of the light. The gray scale in the plot represents the transmittance of the sample with white having the highest transmission. Such spectrum demonstrates the allowed photonic modes inside the microcavity structure. Obvious photonic band gap exists at around 630nm with 20nm Full Width at Half Maximum (FWHM), which is very similar for ΓO and ΓP orientations. This demonstrates that absolute photonic band gap exists in microcavity with higher symmetric Penrose quasicrystal tiling comparing to microcavity with other tiling such as square [3] and hexagonal [8]. In this way, the position of photonic band gap is not restricted by the orientation of the sample. Theoretical calculations already show the existence of absolute photonic band gap in quasiperiodic tiling system [4-5].
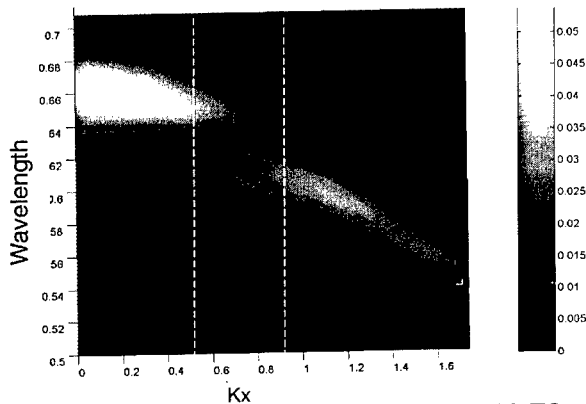
Figure 1(a).   Angle Resolved Transmission result with ΓO orientation
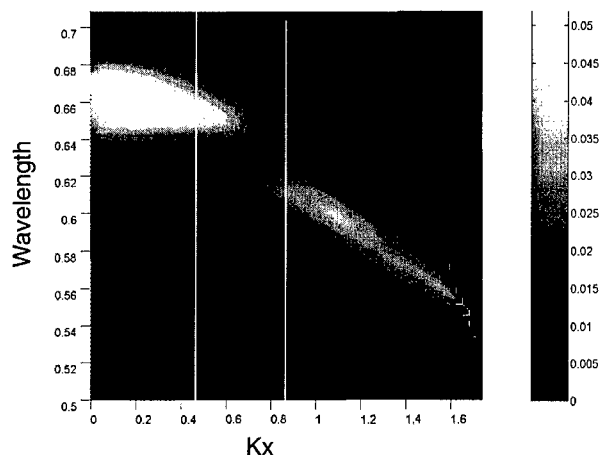
Figure 1(b). Angle Resolved Transmission result with ΓP orientation

Figure 2 shows the angle-resolved PL spectra with emission angles from 0° to 60°. As the sample is a microcavity structure, resonant effect due to the two metallic layers can also be observed. PL FWHM is 48nm at 0° emission angle and 34nm at 60° emission angle, much smaller than 100nm for bulk luminescence of Alq_3. Yet the resonant effect is not as strong as in planar metallic microcavity whose typical FWHM is 10nm because there are variations in cavity width in our corrugated microcavity. An obvious dip exists for all emission angles at around 630nm corresponding to the photonic band gap in transmission spectrum in Fig. 1(a). In Fig. 3(a), the peak wavelengths of PL for different emission angles are superimposed onto the transmission spectrum as dots. As the emission angle moves from 0° to 60°, the peaks follow the photonic band and blue shift from 600nm to 550nm. These indicate that the spontaneous emission of the luminescence material couples to the photonic modes of the microcavity. A detailed comparison between transmission and PL spectra is shown in Fig. 3(b). The two peaks at 586nm and 670nm in PL spectrum coincide with those in transmission spectrum. The difference lies in the relative intensity between the two peaks. The PL intensity is greater at 586nm but the transmission intensity is greater at 670nm. This is because the bulk PL peak of Alq_3 is at 520nm, which is closer to 586nm.

159
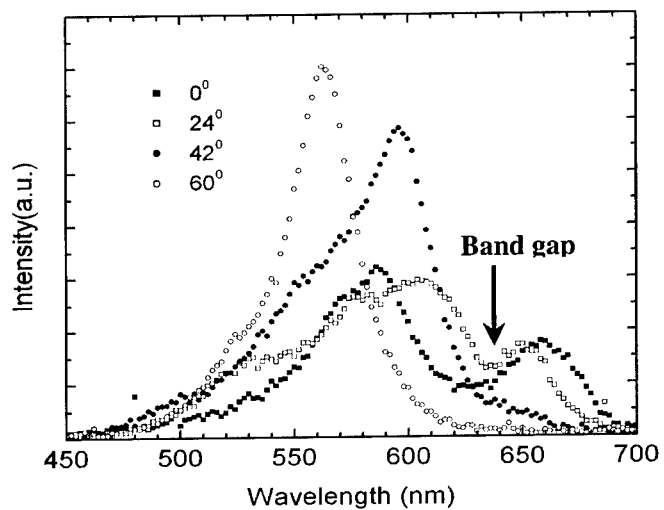
Figure 2 Angle resolved photoluminescence spectrum with ΓO orientation
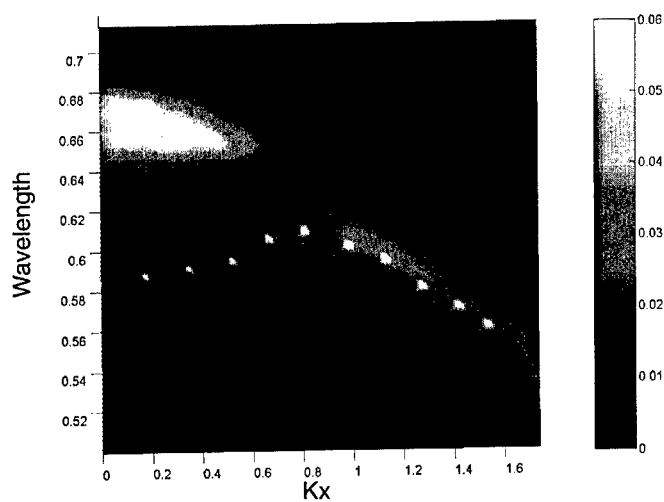
Figure 3(a) Merging of photoluminescence peaks into transmission result with ΓO orientation
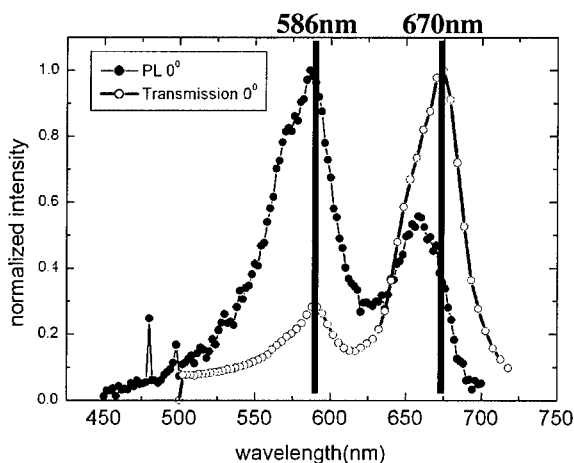
**Figure 3(b) Comparison of normalized transmission and photoluminescence
spectra with 0° incident angle**

CONCLUSIONS

From this work, it is observed that the 2-D photonic microcavity with Penrose
quasicrystal pattern has isotropic photonic band gap in both TE and TM modes. And
the photonic modes of the microcavity can be coupled to the photoluminescence
modes of the luminescence material that is placed inside the microcavity.

REFERENCES

[1] J.D.Joannopoulos, R.D.Meade & J.N.Winn, *"Photonic Crystals—Molding the
Flow of Light"*, Princeton University Press(1995).

[2] G. Parker and M. Charlton, *Physics World*, **August**, 29 (2000).

[3] M.G.Salt, W.L.Barnes, *Phys. Rev. B* **61**, 11,125 (2000).

[4] M.E.Zoorob, M.D.B.Charlton, G.J.Parker, J.J.Baumberg and M.C.Netti, *Nature*
404, 740-743 (2000).

[5] Xiangdong Zhang, Zhao-Qing Zhang and C.T.Chan, *Phys. Rev. B* **63**, 081105
(2001).

[6] Mehmet Bayindir, E. Cubukcu, I. Bulu, and E.Ozbay, *Phys. Rev. B* **63** 161104
(2001).

[7] Chongjun Jin, Bingying Cheng, Baoyuan Man, Zhaolin li, Daozhong Zhang,
Shouzheng Ban and Bo Sun, *Appl. Phys. Lett.* **75**, 1848 (1999).

[8] H.L.Tam, R.Huber, K.F.Li, W.H.Wong, Y.B.Pun, S.K.So, J.B.Xia and
K.W.Cheah, submitted.

Characterization By Variable Angle Spectroscopic Ellipsometry Of Dielectric Columnar Thin Films Produced By Glancing Angle Deposition

James Gospodyn, Michael J. Brett, and Jeremy C. Sit
Department of Electrical and Computer Engineering, University of Alberta,
Edmonton, Alberta T6G 2V4, Canada

ABSTRACT

Thin films composed of MgF_2 and TiO_2 were grown by glancing flux incidence, where the physical vapor flux arrives at the substrate between 80° and 90° with respect to substrate normal. The resulting films are composed of slanted columns inclined toward the incoming flux. The films were modeled using the Bruggemann effective medium approximation (EMA) and were found to be biaxial with one of the principal indices of refraction along the direction of the posts. The indices of refraction for MgF_2 and TiO_2 films were found to be in the range of 1.06 to 1.2 and 1.36 to 1.62, respectively, at a wavelength of 600 nm. The indices of refraction were found to decrease as the deposition angle increased. The film density was also found to be independent of the film thickness for films ranging in thickness from 500 nm to 3400 nm.

INTRODUCTION

The growth of thin films using the glancing angle deposition (GLAD) technique has been shown in the past to exhibit porous columnar microstructure [1, 2]. By using computer control of the substrate rotation and deposition angle with respect to substrate normal, $\alpha = 80°$ to 90°, tailored micro- and nano-structures can be achieved. For example, helices can be produced using a constant slow rotation of the substrate [3, 4], or square spirals [5, 6] can be produced using a rapid, intermittent 90° rotation. In order to fully exploit the potential of GLAD films for optical applications [6-9], it is first necessary to optically characterize columnar films grown at glancing flux incidence. Variable angle spectroscopic ellipsometry and Mueller matrix spectroscopy [10, 11] are ideal for this characterization, since the dispersion relations for the films can be extracted over a large range of wavelengths. In this study, we examine the optical properties of the (slanted post) columnar film structures composed of MgF_2 and TiO_2, since they form the basis for the more complex GLAD structures. These thin films, consisting of isolated columns inclined towards the substrate, are analyzed using the Bruggemann effective medium approximation and are shown to be biaxial, with one of the principal indices of refraction along the direction of the posts. We also examine how the principal indices and the birefringence vary with deposition angle and film thickness.

EXPERIMENTAL DETAILS

Columnar films, and solid films grown at normal incidence composed of MgF_2 and TiO_2 were deposited onto silicon wafers using thermal evaporation at pressures of 2×10^{-6} Torr, and e-beam evaporation at an O_2 partial pressure of 5×10^{-5} Torr respectively. An example of the resulting GLAD films is shown in Fig. 1, along with an illustration of the orientation of the three

principle indices of refraction. The films grown at normal incidence were optically characterized using variable angle spectroscopic ellipsometry (V-VASE, J. A. Woollam Co., Inc.) and modeled using the WVASE32 software [10, 11]. This was done in order to evaluate the film packing fraction, or density compared to the bulk, and the dispersion relation of the evaporated material for both MgF_2 and TiO_2. It was then assumed that the individual columns in the GLAD films would be of the same packing fraction and dispersion relation, and were then measured using Mueller matrix spectroscopy. The wavelength for the spectroscopic ellipsometry and Mueller matrix scans were from 400 nm to 1700 nm, and the angles of incidence for the measurements were 30°, 40°, and 50° for the MgF_2 films, and 40°, 50°, and 60° for the TiO_2 films, which were chosen to obtain a good data set and to acquire data near the Brewster angle. The GLAD films were then evaluated using Mueller matrix spectroscopy with the V-VASE and modeled using WVASE32 as a biaxial material composed of directionally dependent Bruggemann EMA in the modeling software. As an example, the solution to the dielectric constant, ε for an effective medium with a general microstructure for a two-phase composite is given by [12]:

$$\varepsilon = \frac{\varepsilon_a \varepsilon_b + \overline{\varepsilon}(f_a \varepsilon_a + f_b \varepsilon_b)}{\overline{\varepsilon} + (f_a \varepsilon_b + f_b \varepsilon_a)} \tag{1}$$

where f_a and f_b are the fractional composition of two materials with dielectric constants ε_a (void) and ε_b (material), respectively, and:

$$\overline{\varepsilon} = \frac{(1-q)\varepsilon_h}{q} \tag{2}$$

where ε_h is the host dielectric function, which in this case is the void and can be set to ε_a [12], and q is the depolarization factor, which describes the geometry of the inclusions. The main point to note here is that the birefringence arises from directionally dependent differences in q. Thus in the model template (as shown in Fig. 2), the films were modeled as a biaxial medium composed of three "dummy" EMA layers (note that the thickness is fixed to 0 nm in Fig. 2(a)) to describe each index of refraction and the film thickness, depolarization factors, and the % material were allowed to vary in the fit, with the % material was constrained to be equal in all 3 "dummy" layers. These dummy layers are then coupled into the biaxial anisotropic layer (Fig. 2(b)), which allowed us to fit for the optical properties of the dummy layers. An example of this is shown in Fig. 2 from the WVASE32 software, where θ and ϕ are the Euler angles describing

(a)   (b)
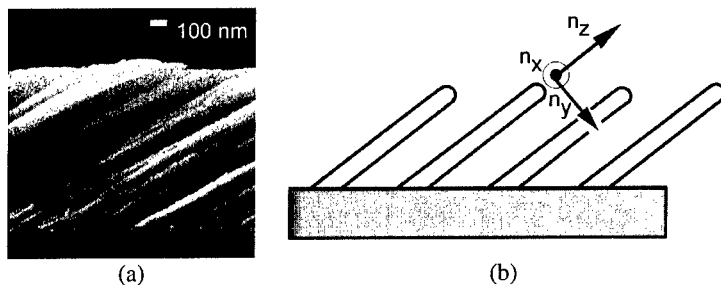
Figure 1. (a) SEM image of an MgF_2 GLAD film, $\alpha = 85°$, and (b) illustration of the three principal indices of refraction.

4	biaxial	1201.8 nm
3	ema3 void/34.4% mgf2_evap	0 nm
2	ema2 void/34.4% mgf2_evap	0 nm
1	ema void/34.4% mgf2_evap	0 nm
0	si_jaw	0.25 mm

Biaxial Anisotropic Layer

Comment: Biaxial material

Spectral range of optical constants: 1 - 20000 nm

Thickness: **1201.0** nm ☑Fit

Anisotropy Type — Mat. Name

- ◯ Isotropic (Ex): **Mat. #1** [ema3]
- ◯ Uniaxial (Ez): **Mat. #2** [ema]
- ◉ Biaxial (Ey): **Mat. #3** [ema2]

Euler Angles

Phi: 167.26 ☑
Theta: 55.536 ☑
Psi: 0 ☐

Ok   Delete Layer   Save

(a)   (b)

Figure 2. Example of the modeling of an MgF$_2$ GLAD film.

the post angle with respect to substrate normal, and the post alignment in the plane of the substrate, respectively.

RESULTS AND DISCUSSION

Effect on deposition angle

The principal indices of refraction for both MgF$_2$ and TiO$_2$ GLAD films were found to decrease as the deposition angle, α, increased. This was to be expected due to an increase in porosity with deposition angle. The relations describing indices as a function of deposition angle in this range of angles is linear, as shown in Fig. 3 for both film materials at a wavelength of 600 nm. The empirical linear relations corresponding to the best fit least squares are highlighted in Table 1 for both film materials, for relations of the form $n_i = A + B\alpha$ for α in degrees. It is

(a)   (b)
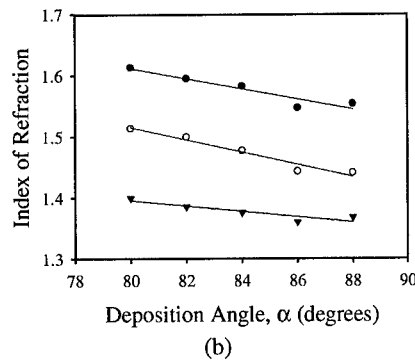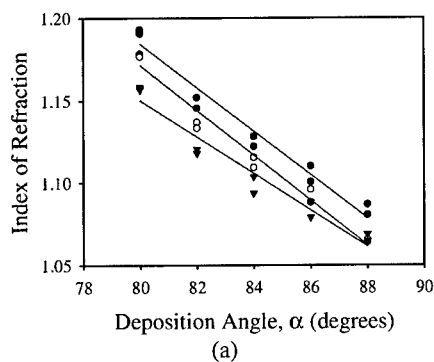
Figure 3. Indices of refraction n$_x$ (O), n$_y$ (▼), and n$_z$ (●) at a wavelength of 600 nm for (a) MgF$_2$ and (b) TiO$_2$ films grown at varying α. The best fit least squares linear fit is shown for all indices.

Table 1. Empirical parameters relating the index of refraction with deposition angle.

	MgF$_2$			TiO$_2$		
	n_x	n_y	n_z	n_x	n_y	n_z
A	2.2644	2.0381	2.2406	2.3253	1.7500	2.2772
B	-0.0137	-0.0111	-0.0132	-0.0101	-0.0044	-0.0083

important to note that n_z, the index of refraction along the direction of the posts, is highest. This is a result of the fact that $q = 0$ along the direction of the posts. It is also important to note here that $n_z > n_x > n_y$, and that based on the empirical linear fits, the birefringence between the principal indices also decreases as the deposition angle increase. By calculating the normal incidence birefringence, which is given by:

$$\Delta n = n_x - n_p \tag{3}$$

where n_p is given by:

$$n_p = \left(\frac{\sin^2 \theta}{n_z^2} + \frac{\cos^2 \theta}{n_y^2} \right)^{-1/2} \tag{4}$$

we find that our result corresponds with the work of Hodgkinson [13], who has shown deposition dependence on the normal incidence birefringence up to $\alpha = 70°$ for tantalum oxide, titanium dioxide, and zirconium oxide. His work demonstrated that there is a maximum normal incidence birefringence for a deposition angle at approximately 60°, with a sharp decrease in the normal incidence birefringence for greater deposition angles. Our normal incidence birefringence for TiO$_2$ is 0.018 for $\alpha = 80°$, with a post angle, $\theta = 45°$ (from the Euler angle, θ in the EMA model).

Effect on film thickness

Commonly in GLAD produced films the columns broaden as the film gets thicker. This has been attributed to column extinction in the earlier stages of growth [14]. That is, due to column competition, some of the columns from the initial seeds in the first few stages of growth become extinct, and as a result, columns that persist become wider in the later stages of growth. One of the questions to answer is whether or not the density of the film remains constant throughout growth. As evidenced in Fig. 4, using the Bruggemann EMA to model films of various thickness, the film density (or percent material in the EMA) appears to remain constant regardless of the film thickness over the range of 500 nm to 3400 nm. This result is also confirmed by earlier simulation work [15], and the density of the films here also corresponds to other simulations [16], which predict the film density as a function of deposition angle.
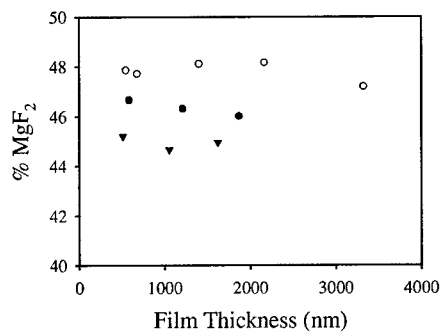
Figure 4. % MgF$_2$ from the Bruggemann EMA as a function of film thickness for $\alpha \cong 79.5°$ (**O**), $\alpha \cong 80°$ (**●**), and $\alpha \cong 80.5°$ (**▼**).

CONCLUSIONS

Slanted post GLAD structures composed of MgF$_2$ and TiO$_2$ have been modeled using the Bruggemann EMA to evaluate the Mueller matrix spectra corresponding to the films. Using this analysis technique, it was shown that both the principle indices of refraction and the birefringence of the films decrease as the deposition angle increases, and empirical linear fits were given for the indices in this range of deposition angles. It was also shown that the overall density of the film remained constant as a function of thickness, despite column thickening.

ACKNOWLEDGEMENTS

REFERENCES

1. K. Robbie, L. J. Friedrich, S. K. Dew, T. Smy and M. J. Brett, *J. Vac. Sci. Technol. A* **13**, 1032-1035 (1995).
2. K. Robbie and M. J. Brett, *J. Vac. Sci. Technol. A* **15**, 1460-1465 (1997).
3. K. Robbie and M. Brett, in *Proceedings of Electromagnetics of Complex Media BIANISOTROPICS*, edited by W. S. Weiglhofer, (Univ. Glasgow, Glasgow, UK, 1997) pp. 69-71.
4. P. I. Rovira, R. A. Yarussi, R. W. Collins, R. Messier, V. C. Venugopal, A. Lakhtakia, K. Robbie and M. J. Brett, *Appl. Phys. Lett.* **71**, 1180-1182 (1997).
5. M. O. Jensen, S. R. Kennedy and M. J. Brett, in *Nano-/Microstructured Materials*, edited by S. C. Moss, (Mater. Res. Soc., **728**, San Fransisco, CA, USA, 2002) pp. S9.10-15.

6.   S. R. Kennedy, M. J. Brett, O. Toader and S. John, *Nano Lett.* **2**, 59-62 (2002).
7.   S. R. Kennedy, J. C. Sit, D. J. Broer and M. J. Brett, *Liquid Crystals* **28** (12), 1799-1803 (2001).
8.   S. R. Kennedy and M. J. Brett, *Appl. Optics* **42** (22), 4573-4579 (2003).
9.   J. C. Sit, D. J. Broer and M. J. Brett, *Liquid Crystals* **27**, 387-391 (2000).
10.   J. A. Woollam, B. Johs, C. M. Herzinger, J. Hilfiker, R. Synowicki and C. L. Bungay, in *Optical Metrology*, edited by G. A. Al-Jumaily, (SPIE - The International Society for Optical Engineering, **CR72**, Denver, 1999) pp. 3-27.
11.   B. Johs, J. A. Woollam, C. M. Herzinger, J. Hilfiker, R. Synowicki and C. L. Bungay, in *Optical Metrology*, edited by G. A. Al-Jumaily, (SPIE - The International Society for Optical Engineering, **CR72**, Denver, 1999) pp. 29-58.
12.   D. E. Aspnes, *Thin Solid Films* **89**, 249-262 (1982).
13.   I. Hodgkinson, Q. H. Wu and S. Collet, *Appl. Optics* **40**, 452-457 (2001).
14.   D. Vick, T. Smy and M. J. Brett, *J. Mater. Res.* **17** (11), 2904-2911 (2002).
15.   T. Smy, D. Vick, M. J. Brett, S. K. Dew, A. T. Wu, J. C. Sit and K. D. Harris, *J. Vac. Sci. Technol. A* **18**, 2507-2512 (2000).
16.   R. N. Tait, T. Smy and M. J. Brett, *Thin Solid Films* **226**, 196-201 (1993).

Dispersion Properties of Photonic Crystal Fibers - Issues and Opportunities

J. Lægsgaard[1], S. E. Barkou Libori[1], K. Hougaard[1], J. Riishede[1], T. T. Larsen[1], T. Sørensen[1], T. P. Hansen[1,2], K. P. Hansen[1,2], M. D. Nielsen[1,2], J. B. Jensen[1], and A. Bjarklev[1]
1: Research center COM, Technical University of Denmark Bldg. 345w, DK-2800 Kgs. Lyngby 2:Crystal Fibre A/S, Blokken 84, DK-3460 Birkerød

ABSTRACT

The dispersion, which expresses the variation with wavelength of the guided-mode group velocity, is one of the most important properties of optical fibers. Photonic crystal fibers (PCFs) offer much larger flexibility than conventional fibers with respect to tailoring of the dispersion curve. This is partly due to the large refractive-index contrast available in silica/air microstructures, and partly due to the possibility of making complex refractive-index structures over the fiber cross section. We discuss the fundamental physical mechanisms determining the dispersion properties of PCFs guiding by either total internal reflection or photonic bandgap effects, and use these insights to outline design principles and generic behaviours of various types of PCFs. A number of examples from recent modeling and experimental work serve to illustrate our general conclusions.

INTRODUCTION

Photonic crystal fibers (PCFs), which are optical fibers with a cross-sectional microstructure of airholes and/or doped sections (for recent reviews we refer to Refs. [1, 2] and references therein), have in recent years attracted much scientific and technological interest. PCFs offer a number of novel design options, such as very large [3] or very small [4, 5, 6] mode areas, high numerical aperture [7], guidance of light in air [8, 9], and novel dispersion properties. The latter feature has been of particular importance for a number of current and potential PCF applications: All-optical signal processing utilizing nonlinear effects in fibers typically demands small dispersion in the wavelength range (around 1.55 μm) of interest [10]. Another popular application of nonlinearities, supercontinuum generation [5, 11], has in recent years benefited from the possibility of manufacturing small-core PCFs with low dispersion values at short (<1 μm) wavelengths. PCFs have also been shown to have considerable potential as dispersion compensating fibers (DCFs) for telecommunication [12, 13], although no practical application has as yet been made. In the present paper, we give a general discussion of the dispersion properties of PCFs, and illustrate it with a number of examples from recent modeling and experimental work, in order to elucidate the potential of PCFs for dispersion engineering.

In conventional optical fibers, electromagnetic modes are guided by total internal reflection in a core region whose refractive index is raised by doping of the base material. In PCFs, two distinct guiding mechanisms are possible: The guided modes may be trapped in a core with a higher average index than the cladding region by an effect similar to total internal reflection (often termed modified total internal reflection, or just index-guiding), or
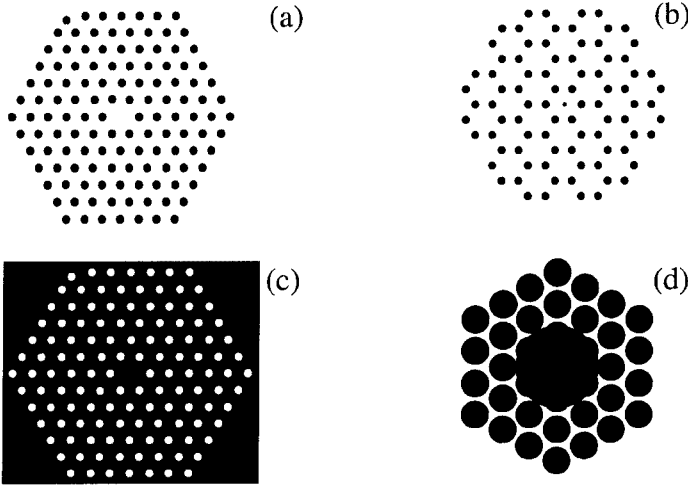
Figure 1: Some basic two-material PCF designs. Lighter color indicates a higher refractive index.

they can be trapped in a core of *lowered* average index by a photonic bandgap (PBG) effect [14, 15]. In Fig. 1 some typical two-material PCF designs are shown. Black color indicates the lowest refractive index in the structure. The design in Fig. 1(a) is the most common index-guiding design, in which the core is defined by a missing-airhole defect in a triangular array of airholes. The other three designs have cores with a lower average index than the cladding, and are thus PBG-guiding. The designs in Fig. 1(b), Fig. 1(c) have the majority of the guided mode propagating in silica, whereas the design in Fig. 1(d) has most of the field in air. All the fiber structures sketched in the figure have been realized experimentally (the structure in Fig. 1(c) can be obtained by infiltrating the holes of the structure in Fig. 1(a) with a high-index material [16, 17]). The existence of two different guiding mechanisms is one of the reasons for the versatile nature of PCFs, in particular with respect to the dispersion properties. In fact, we will show in the following, that the two fundamental types of PCFs have distinct differences in their generic dispersion behaviour.

PHYSICAL MECHANISMS DETERMINING DISPERSION BEHAVIOUR

The dispersion properties of a fiber are usually quantified by the group velocity dispersion (GVD) coefficient, D, defined as:

$$D = \frac{1}{c}\frac{dn_g}{d\lambda} \tag{1}$$

where n_g is the group index:

$$n_g = \frac{c}{v_g}, \qquad v_g = \frac{d\omega}{d\beta} \qquad (2)$$

Here ω, β are the frequency and propagation constant (wavevector along the fiber axis) of the guided mode, respectively, and $\lambda = 2\pi c/\omega$. The variation of n_g with wavelength is determined partly by the waveguide structure, and partly by the dispersion properties of the base material (which we here consider to be silica). In standard fibers the total dispersion coefficient is, to a good approximation, given by:

$$D = D_w + D_{SiO_2} \qquad (3)$$

where D_{SiO_2} is the dispersion coefficient of bulk silica and D_w is the so-called waveguide dispersion, calculated for a fixed material refractive index of suitable magnitude. In PCFs, the inclusion of material dispersion effects is more intricate, but in many cases Eq. (3) provides a reasonable first approximation to the dispersion coefficient. Therefore we will focus on obtaining an understanding of D_w, while giving a more brief discussion of material effects.

Theory of waveguide dispersion

In this subsection we will consider a fiber composed of two different materials with frequency-independent dielectric constants ε_1 and $\varepsilon_2 = \varepsilon_1 - \Delta\varepsilon$. We take $\varepsilon_1 > \varepsilon_2$. This covers both the standard step-index fibers with a doped silica core, and PCFs fabricated from pure silica with airholes. Quite generally, we may write the group velocity index as[18]:

$$n_g = \frac{\omega}{c\beta} \frac{\int_A \varepsilon(\mathbf{H} \times \mathbf{E}^*) \cdot \mathbf{z} dA}{\int_A (\mathbf{H} \times \mathbf{E}^*) \cdot \mathbf{z} dA}, \qquad (4)$$

for propagation in the z direction. Using the fact that ε is a two-valued piecewise constant function we can rewrite Eq. (4) as:

$$n_g = \frac{\varepsilon_1 - P_2 \Delta\varepsilon}{n_{ph}}, \qquad (5)$$

where we have introduced the phase index, $n_{ph} = \frac{c\beta}{\omega}$, and the fraction of power propagating in the region with $\varepsilon = \varepsilon_2$, P_2. Inserting Eq. (5) into Eq. (1) we obtain:

$$D_w = -\frac{dn_{ph}}{d\lambda} \frac{\varepsilon_1 - P_2 \Delta\varepsilon}{cn_{ph}^2} - \frac{dP_2}{d\lambda} \frac{\Delta\varepsilon}{cn_{ph}} \qquad (6)$$

This is an equation for D_w rather than D because we assumed the dielectric constants to be independent of wavelength.

The phase index of a guided mode varies between $\sqrt{\varepsilon_2}$ and $\sqrt{\varepsilon_1}$, so we can to some extent expect that $\frac{dn_{ph}}{d\lambda}$ will increase with increasing $\Delta\varepsilon$. In the second term, there is an explicit proportionality. Since the index contrast between silica and air is large, this means that silica/air PCFs will in general have larger values of D_w than ordinary fibers made from doped silica, where the index contrast is at least an order of magnitude lower. Since waveguide dispersion is engineerable through the design of the fiber, this difference in magnitude is

the most important reason for the increased flexibility in dispersion manipulation offered by PCFs.

It is also interesting to consider the sign of the two terms in Eq. (6). The group index of a guided mode is given by $n_g = n_{ph} - \lambda\frac{dn_{ph}}{d\lambda}$. Since in general $n_g > n_{ph}$, this implies that the first term in Eq. (6) always gives a positive contribution to D_w. The sign of the second term is determined by the sign of $dP_2/d\lambda$ since we have chosen $\Delta\varepsilon$ positive. In index-guiding fibers, $dP_2/d\lambda$ will in general be positive since the power gets increasingly confined in the high-index core as the wavelength decreases. Thus, the second term gives a negative contribution to D_w, whose sign is therefore dependent on the relative magnitude of the two terms. Typically, index-guiding PCFs will have negative waveguide dispersion in the wavelength region where the mode becomes confined to the core (and P_2 therefore shows a rapid decrease with wavelength), and positive D_w for shorter wavelengths where most of the power is confined to the high-index region, and the first term in Eq. (6) dominates. For PBG fibers, on the other hand, the situation is different. Here, as the wavelength is decreased, a guided mode enters the photonic bandgap at some treshold wavelength. As the wavelength decreases further, the mode becomes confined in the *low-index* core region, meaning that $dP_2/d\lambda$ is negative, and D_w is now given by the sum of two positive terms. Therefore, very high positive values of D_w can be obtained in PBG fibers. At still shorter wavelengths, the guided mode eventually leaves the photonic bandgap again, in which case $dP_2/d\lambda$ becomes positive. This can lead to quite large negative D_w values, but usually in a narrow wavelength interval. In the left panel of Fig. 2 we show waveguide dispersion curves for the two PCF designs in Fig. 1(a), 1(c). Both curves have been calculated with a hole diameter, $d=0.5\Lambda$, where Λ is the center-to-center hole spacing (commonly denoted the pitch). In one case (solid curve) the holes are filled with air and the fiber is index-guiding. In the other (dashed curve), the holes are filled with high-index material with a refractive index of 1.6. Here the core constitutes a low-index defect, and the fiber guides in a finite wavelength interval by the PBG effect. It can be seen that the two designs have distinctly different dispersion properties, in accordance with the reasoning outlined above: The index-guiding fiber has negative waveguide dispersion in the long-wavelength limit, and moderately positive waveguide dispersion in the short-wavelength limit. The PBG fiber has very large and positive waveguide dispersion on the long-wavelength side of the transmission window, which then decreases and eventually becomes negative shortly before the mode leaves the bandgap.

Material dispersion effects

Real dielectric materials have frequency-dependent refractive indices, which influence the dispersion properties of waveguides. From a modeling point of view, this material dispersion has the unfortunate effect of breaking the scale invariance of Maxwells equations. In the absence of material dispersion one can derive the simple scaling relation:

$$D_w(\Lambda) = \frac{\Lambda_0}{\Lambda}D_w(\Lambda_0) \qquad (7)$$

for the dispersion coefficient, where Λ is an overall scaling parameter, e.g. the pitch. Therefore, a calculation of the waveguide dispersion for one value of the fiber size gives the waveguide dispersion for all sizes, so that one dimension of the design parameter space becomes
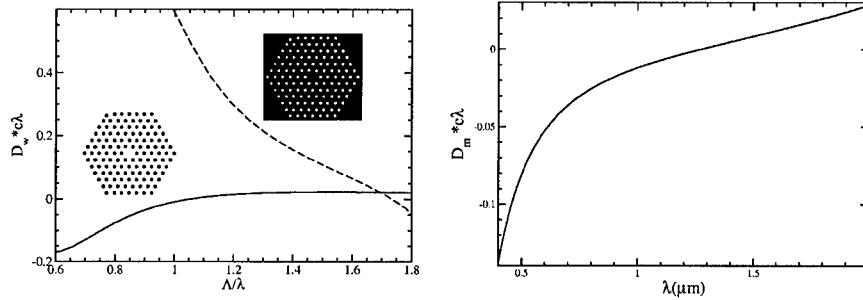
Figure 2: Left: Waveguide dispersion versus normalized frequency for the two fiber designs shown in the inset. Lighter color indicates a higher refractive index. λ is the wavelength, and Λ the pitch (center-to-center hole spacing). Right: Material dispersion of silica in the visible and near-infrared region.

trivial to explore. When material dispersion is included, this simple scaling behaviour is lost, and in principle a full calculation of the modal structure is needed for each value of Λ.

The bulk material dispersion, D_{SiO_2}, of silica is shown in the right panel of Fig. 2, in units of $(c\lambda)^{-1}$, λ being the wavelength. The curve was calculated from the Sellmeier formula with the coefficients given by Okamoto [19]. An estimate of the dispersion properties of a silica-based fiber may be obtained from Eq. (3). Thus, if one for instance wants to design a fiber having $D=0$ at a particular wavelength, the waveguide dispersion should approximately balance D_{SiO_2} at this wavelength, and a comparison of the waveguide and material dispersion curves in Fig. 2 can give a quick estimate of the Λ-parameter needed. However, at least for PCFs, more sophisticated modeling is required to obtain quantitatively accurate results [20, 21].

Airguiding PBG fibers constitute a special case in this regard. In these fibers more than 90% of the field energy is usually guided in air, and Eq. (3) obviously becomes invalid. However, material dispersion is still found to play a role in these fibers [22]. In Fig. 3, some dispersion curves for a particular airguiding fiber design, calculated with either fixed or frequency-dependent material index are shown. While it is evident that material dispersion effects are much smaller than the waveguide dispersion, they are still comparable in magnitude to D_{SiO_2} at these wavelengths. This can be understood in the following way: The group velocity in the presence of material dispersion can be shown to be given by the formula:

$$v_g = \frac{v_g^0}{1 + \frac{\omega}{2}E_d \frac{d\ln\varepsilon}{d\omega}}, \qquad (8)$$

where E_d is the fraction of the electric field energy present in the dielectric, and $\varepsilon(\omega)$ is the frequency dependent dielectric constant [21]. The derivative of v_g, which determines the dispersion coefficient through Eq. (1), will then have terms proportional to both E_d and its frequency derivative. For airguiding fibers it turns out, that although E_d is small
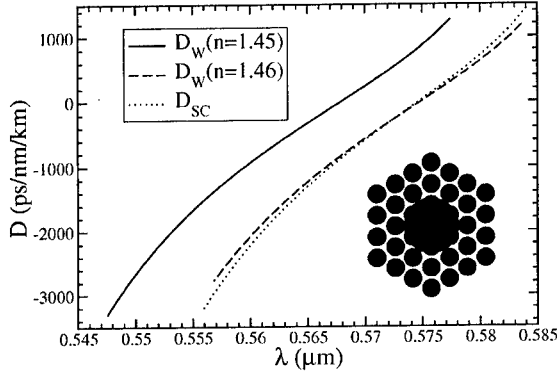
Figure 3: Dispersion curves for the hollow-core PBG fiber design shown in the inset. The curves labeled D_w are calculated using a fixed refractive index, whereas the curve labeled D_{SC} is calculated using the index corresponding to the wavelength.

(<0.1), its frequncy derivative is substantial due to the narrow transmission windows, so a non-negligible effect of the material dispersion arises [22]. This finding raises the interesting prospect of engineering the dispersion properties of airguiding fibers through the choice of highly dispersive base materials.

APPLICATIONS

PCFs with short zero-dispersion wavelengths

In standard optical fibers it is difficult to shift the zero-dispersion wavelength (ZDW) significantly below the bulk silica value of $\sim 1.27 \mu m$ due to the small magnitude of the waveguide dispersion. One of the earliest and most important applications of PCFs was to fabricate fibers with a ZDW shifted towards the visible part of the spectrum [5, 6]. This is possible due to the large index contrast between silica and air, which makes the magnitude of the waveguide dispersion much larger than in standard fibers, as argued in the previous section. A short ZDW is important for a number of nonlinear applications, most notably supercontinuum generation in the visible or near-infrared part of the spectrum [5, 11].

From Fig. 2 it is seen that the waveguide dispersion of an index-guiding fiber becomes positive with increasing frequency, and reaches a maximum value, relative to $1/(c\lambda)$. Since the material dispersion curve decreases monotonically with frequency, there is a lower limit to the ZDW obtainable in an index-guiding fiber. In Fig. 4 ZDW curves for two index-guiding designs with $d/\Lambda=0.5$ and 0.95 are shown as a function of pitch. The fiber with the largest airholes attains ZDW values as low as 520 nm. A problem in this connection is, that the smallest ZDW values are found to occur in a multimode regime [6].

One way to overcome these limitations is to use a PBG-guiding fiber. These fibers have strong positive waveguide dispersion in the long-wavelength part of the transmission window,
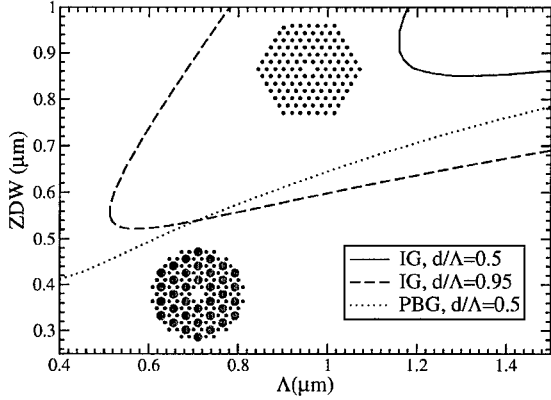
Figure 4: Shortest zero-dispersion wavelength (ZDW) as a function of pitch for two index-guiding PCF designs (IG, upper inset) with different holesizes and one PBG-guiding design (PBG, lower inset).

which means that very short ZDWs can be reached while staying in a single-mode regime [23]. An example (the F0340 design of Ref. [23]), is shown by the dashed line in Fig. 4. In this design, a perfect honeycomb array of airholes has been doped to increase the refractive index of the cladding region. The absence of a doped region defines a low-index core. The value of d/Λ is 0.5 (for further details of this fiber we refer to Ref. [23]). It is noteworthy that very short ZDW values can be obtained with moderate-sized airholes, and that, perhaps more importantly, the fiber is single-moded at the zero-dispersion point for all pitches considered. The main technological obstacle towards going to very short ZDW values is likely to be the very small Λ-values needed.

Dispersion-flattened PCFs

Dispersion control is an all-important issue when using optical fibers for telecommunication. A flat dispersion curve with small magnitude is highly desirable for transmission fibers, along with equally important requirements of low loss and nonlinearity coefficients. The possibility of using PCFs as basic transmission fibers is currently being investigated in the laboratory [24], but given the huge investments made in standard fiber networks in recent years, a practical implementation of PCF-based networks is not to be expected in the near future. A more realistic application of PCFs is as a fiber component in nonlinear devices for all-optical signal processing [10]. Here the main design requirements are usually small and flat dispersion around the important telecommunication wavelength of 1.55 μm. In Fig. 5, the dispersion curves of two index-guiding designs are shown. In both cases the zero-dispersion point is close to 1.55 μm. It can be seen that small airholes and a fairly large pitch is needed to obtain a flat dispersion profile [25]. This has the effect of increasing the mode area, which is undesirable for nonlinear applications, and also implies higher propagation and bend losses
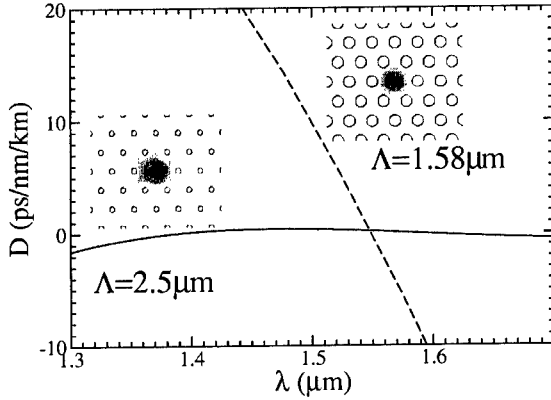
Figure 5: Dispersion behaviour around $\lambda=1.55\mu$m for two PCF designs with $d/\Lambda=0.24$ (left inset) and 0.5 (right inset). The shading in the insets indicates the field energy distribution of the guided mode.

[26].The design with the larger airholes, on the other hand, was succesfully used to fabricate an all-optical time-domain demultiplexer based on a nonlinear fiber loop mirror [10], but the steep slope of the dispersion curve makes it difficult to use this design for applications over a broad wavelength range.

An improved design,recently demonstrated both theoretically and experimentally by Hansen [27], is shown in Fig. 6. Instead of reducing the dispersion slope by making the airholes smaller, three of the airholes nearest to the core are removed and replaced by Flourine-doped low-index regions. The central region is Germanium-doped to increase the refractive index, and the nonlinear coefficient. In the right panel of the figure some calculated dispersion curves are shown. The relative holesize has been decreased from $d/\Lambda=0.56$ to 0.44 while simultaneously increasing the pitch from 1.24 μm to 1.61 μm (the dispersion coefficient at 1.3 μm wavelength increases with relative holesize). It is evident, that both the dispersion and dispersion slope can be made very small around 1.55 μm wavelength by appropriately tuning the pitch and holesize. At the same time the fiber has a reasonably large nonlinear coefficient of about 11 $(\text{Wkm})^{-1}$. This fiber is a good example of how the structural flexibility of PCFs may be used to meet specific design requirements.

PCFs for dispersion compensation

The pulse-broadening that results from transmitting a signal through a dispersive fiber can be nullified by subsequently propagating the signal through a second piece of fiber with a dispersion coefficient of the opposite sign, a technique known as dispersion compensation. The larger the magnitude of the dispersion in a dispersion compensating fiber (DCF), the shorter the length of the DCF should be to compensate a given transmission line. PCFs are of interest for dispersion compensation because, as shown in Section 2, they can have very
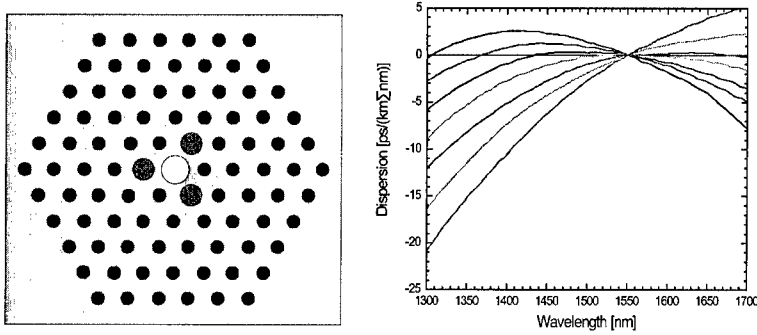
Figure 6: The generic structure of a Ge/F-doped PCF with flattened dispersion around 1500 nm wavelength (left). Darker regions have lower refractive index. In the rigth panel, some simulated dispersion curves are shown.

large dispersion, and both positive and negative signs of the dispersion coefficients can be obtained.

The most important application of DCFs has to date been to compensate standard fiber transmission lines, to boost the performance of existing fiber links. Since standard transmission fibers have a positive dispersion coefficient this calls for DCFs with large negative D-values. For systems operating over a range of wavelengths (wavelength division multiplexing) the ratio between the dispersion coefficients of the transmission fiber and the DCF should preferably be constant with wavelength, which translates into the requirement that the ratio between dispersion and dispersion slope in the DCF should equal that of the fiber to be compensated ('slope compensation'). Index-guiding PCFs turn out to have the desired generic behaviour in the wavelength region where the waveguide dispersion is negative (see Fig. 2). The magnitude of the negative dispersion is generally found to increase with increasing airhole size, in accordance with the reasoning outlined in Section 2.

Early modeling work, approximating large-airhole PCFs by a silica strand in air, found dispersion coefficients at 1.55 μm wavelength as low as -2000 ps/nm/km [12], which should be compared to the $\sim$ -100 ps/nm/km obtainable in ordinary DCFs [28] and 17 ps/nm/km of standard SMF28 transmission fiber. If slope compensation was required, the minimum value of D was found to be of smaller magnitude, around -680 ps/nm/km. Recently, modeling results for a PCF with a triangular airhole array in the cladding were presented by Poli et al [13]. For d/Λ=0.9 and Λ=0.9 μm, approximate slope compensation could be obtained with a dispersion coefficient of D=-590 ps/nm/km at λ=1.55 μm.

While an increase by a factor of 5-6 in the magnitude of the dispersion coefficient compared to standard DCFs is certainly of interest, it must be noted that a useful DCF must meet a range of other requirements, in particular low loss, and low nonlinearity. The latter is particularly important for high-bitrate networks (40 Gb/s and beyond). Therefore, the extremely small core size of the designs discussed above may constitute a serious obstacle to applications in real networks. In Fig. 7 we plot the dispersion coefficient at 1.55 μm
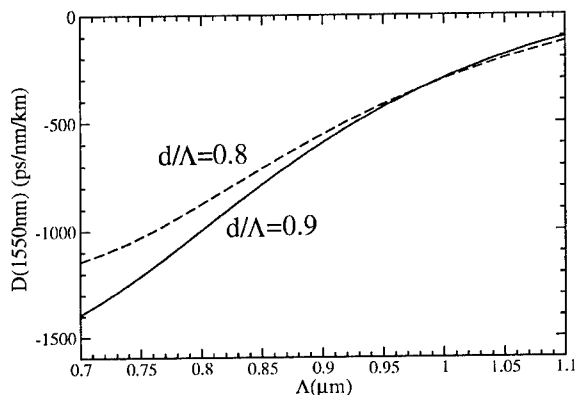
Figure 7: Dispersion coefficient at 1.55 μm wavelength as a function of pitch for index-guiding PCFs with d/Λ=0.8 and 0.9 respectively.

as a function of Λ for two PCF designs with d/Λ=0.8 and 0.9 respectively. It is clearly seen, that the extreme values of the dispersion coefficient are obtained at the expense of a strongly reduced core area, which leads to an increased nonlinear coefficient, and possibly large coupling losses. It seems likely that more sophisticated PCF designs for dispersion compensation will have to be invented in order to overcome this problem.

CONCLUSION

The novel and highly flexible dispersion properties of photonic crystal fibers have a number of important applications within various branches of optics. In this contribution, we have shown some general results on the dispersion properties of two-material fibers, which explains the trends and differences found in the dispersion properties of index- and PBG-guiding PCFs. On the practical level, PCFs have been shown to be useful for devices requiring short zero-dispersion wavelengths, or a flattened dispersion curve. PCFs also have potential as dispersion compensating fibers in present-day telecommunication networks, however in this case several technological challenges remain.

ACKNOWLEDGMENT

References

[1] J. C. Knight and P. St. J. Russell. Applied optics: New ways to guide light. *Science*, 296:276–277, 2002.

[2] T. A. Birks, J. C. Knight, B. J. Mangan, and P. St. J. Russell. Photonic crystal fibres: An endless variety. *IEICE Trans. Electron.*, E84-C:585–591, 2001.

[3] J. C. Knight, T. A. Birks, R. F. Cregan, P. St. J. Russell, and J.-P. De Sandro. Large mode area photonic crystal fibre. *Electron. Lett.*, 34:1347–1348, 1998.

[4] N. G. R. Broderick, T. M. Monro, P. J. Bennett, and D. J. Richardson. Nonlinearity in holey optical fibers: measurement and future opportunities. *Opt. Lett.*, 24:1395–97, 1999.

[5] J. K. Ranka, R. S. Windeler, and A. J. Stentz. Visible continuum generation in air–silica microstructure optical fibers with anomalous dispersion at 800 nm. *Opt. Lett.*, 25:25–27, 2000.

[6] J. C. Knight, J. Arriaga, T. A. Birks, A. Ortigosa-Blanch, W. J. Wadsworth, and P. St. J. Russell. Anomalous dispersion in photonic crystal fiber. *IEEE Photonic Tech. L.*, 12:807–809, 2000.

[7] K. Furusawa, A. Malinowski, J. H. V. Price, T. M. Monro, J. K. Sahu, J. Nilsson, and D. J. Richardson. Cladding pumped ytterbium-doped fiber laser with holey inner and outer cladding. *Optics Express*, 9:714–20, 2001.

[8] R. F. Cregan, B. J. Mangan, J. C. Knight, T. A. Birks, P. St. J. Russell, P. J. Roberts, and D. C. Allan. Single-mode photonic band gap guidance of light in air. *Science*, 285:1537–1539, 1999.

[9] N. Venkataraman, M. T. Gallagher, C. M. Smith, D. Müller, J. A. West, K. W. Koch, and J. C. Fajardo. Low loss (13 db/km) air core photonic bandgap fiber, 28th European Conference on Optical Communication, ECOC '02, September 2002, Copenhagen, Denmark, post-deadline paper PD1.1.

[10] L. K. Oxenløwe, A. J. Siahlo, K. S. Berg, A. Tersigni, A. T. Clausen, C. Peucheret, P. Jeppesen, K. P. Hansen, and J. R. Jensen. A photonic crystal fibre used as a 160 to 10 gb/s demultiplexer, OECC 2002 post deadline paper PD-1-4.

[11] G. Genty, M. Lehtonen, H. Ludvigsen, J. Broeng, and M. Kaivola. Spectral broadening of femtosecond pulses into continuum radiation in microstructured fibers. *Optics Express*, 10:1083–98, 2002.

[12] T. A. Birks, D. Mogilevtsev, J. C. Knight, and P. S. J. Russell. Dispersion compensation using single-material fibers. *IEEE Photon. Tech. Lett.*, 11:674–676, 1999.

[13] F. Poli, A. Cucinotta, M. Fuochi, S. Selleri, and L. Vincetti. Characterization of microstructured optical fibers for wideband dispersion compensation. *J. Opt. Soc. Am. A*, 20:1958–62, 2003.

[14] J. Broeng, S. E. Barkou, A. Bjarklev, J. C. Knight, T. A. Birks, and P. S. J. Russell. Highly increased photonic band gaps in silica/air structures. *Opt. Commun.*, 156:240–244, 1998.

[15] J. C. Knight, J. Broeng, T. A. Birks, and P. St. J. Russell. Photonic band gap guidance in optical fibers. *Science*, 282:1476–1478, 1998.

[16] R. T. Bise, R. S. Windeler, K. S. Kranz, C. Kebage, B. J. Eggleton, and D. J. Trevor. Tunable photonic band-gap fibre, OFC 2002, ThK3.

[17] T. T. Larsen, A. Bjarklev, D. S. Hermann, and J. Broeng. Optical devices based on liquid crystal photonic bandgap fibres. *Optics Express*, 11:2589–96, 2003.

[18] A. W. Snyder and J. D. Love. *Optical Waveguide Theory*. Chapman & Hall, London, 1996.

[19] K. Okamoto. *Fundamentals of optical waveguides*. Academic Press, San Diego, 2000.

[20] A. Ferrando, E. Silvestre, P. Andrés, J. J. Miret, and M. V. Andrés. Designing the properties of dispersion-flattened photonic crystal fibers. *Optics Express*, 9:687–697, 2001.

[21] J. Lægsgaard, A. Bjarklev, and S. E. Barkou Libori. Chromatic dispersion in photonic crystal fibers: Fast and accurate scheme for calculation. *J. Opt. Soc. Am. B*, 20:443-8, 2003.

[22] J. Lægsgaard, N. A. Mortensen, J. Riishede, and A. Bjarklev. Material effects in air-guiding photonic bandgap fibers, to appear in J. Opt. Soc. Am. B.

[23] J. Lægsgaard and A. Bjarklev. Doped photonic bandgap fibers for short-wavelength nonlinear devices. *Opt. Lett.*, 28:783–5, 2003.

[24] B. Zsigri, C. Peucheret, M. D. Nielsen, and P. Jeppesen. Transmission over 5.6km large effective area and low-loss (1.7 db/km photonic crystal fibre. *Electronics Letters*, 39:796–8, 2003.

[25] A. Ferrando, E. Silvestre, J. J. Miret, , J. A. Monsoriu, M. V. Andrés, and P. St. J. Russell. 'designing a photonic crystal fibre with flattened chromatic dispersion'. *Electronics Letters*, 35:325–327, 1999.

[26] W. H. Reeves, J. C. Knight, P. St. J. Russell, and P. J. Roberts. Demonstration of ultra-flattened dispersion in photonic crystal fibers. *Optics Express*, 10:609–13, 2002.

[27] K. P. Hansen. Dispersion flattened hybrid-core nonlinear photonic crystal fiber. *Optics Express*, 11:1503–9, 2003.

[28] L. Grüner-Nielsen, S. N. Knudsen, B. Edvold, T. Veng, D. Magnussen, C. C. Larsen, and H. Damsgaard. Dispersion compensating fibers. *Opt. Fiber Tech.*, 6:164–80, 2000.

W7.2

Design and Fabrication of Dispersion Controlled and Polarization Maintaining Photonic Crystal Fibers for Optical Communications Systems

Satoki Kawanishi[1], Takashi Yamamoto[1], Hirokazu Kubota[1], Masatoshi Tanaka[2], and Syun-ichiro Yamaguchi[2]
[1]NTT Network Innovation Laboratories
Room 807-A, 1-1 Hikari-no -oka, Yokosuka, Kanagawa, 239-0847 Japan
[2]Mitsubishi Cable Industries, LTD., 4-3 Ikejiri, Itami-City, 664-0027 Japan

ABSTRACT

Recent progress on photonic crystal fibers (PCFs) is reviewed aiming at their application to high performance optical communications sytems. The optical properties, for example dispersion characteristics, can be set by selecting the appropriate combination of air hole diameter and air hole pitch. A noteworthy characteristic of PCFs is their strong birefringence, which suggests optical components with better polarization maintaining characteristics.

This paper describes the characteristics of dispersion controlled PCFs and polarization maintaining PCFs. It describes theoretical analyses and experimental results of fabricated PCFs that have short wavelength zero dispersion at 810 nm, polarization maintaining capability with birefringence of 1×10^{-3}, polarization maintaining dispersion flattened functions, and absolute single polarization state support with polarization dependent loss of 1 dB/m at 1550 nm. A supercontinuum generation experiment with PM-PCF in the 1550 nm region is shown with symmetrical spectral broadening to over 40 nm. The potential of PCFs will be discussed with reference to the next generation optical communications systems.

INTRODUCTION

A PCF has an array of air holes surrounding the silica core region as shown in Figure 1. Light is confined to the core by the refractive index difference between the core and the array of air holes. Since the initial demonstration of a PCF [1], research has concentrated on PCF analysis and fabrication. PCFs have special characteristics compared to conventional single mode fibers. Theoretical analyses [2] and measurements [3] of initial PCF variants showed zero dispersion wavelengths shorter than 1280 nm [3] or large normal dispersion values [4] suitable for dispersion compensation at 1550 nm. The PCFs with zero dispersion wavelength in the 800 nm region had core diameters of around 2 μm and this is suitable for nonlinear applications, for example supercontinuum generation [5] and soliton generation [6]. PCFs with zero dispersion
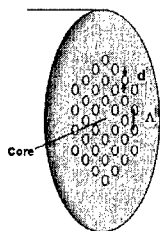

Figure 1. Schematic configuration of a photonic crystal fiber.

wavelengths in the 1550 nm region were recently proposed [7]-[8]. In addition, low dispersion slope (i.e. dispersion flattened) PCFs with small core diameter [8]-[10] are attracting interest because they offer nonlinearity over a wide wavelength range. PCFs can exhibit single mode performance from the visible to infrared (>1550 nm) if appropriately designed [11]. This enables the realization of a single mode fiber for any wavelength for wavelength-division multiplexed (WDM) transmission systems. Another characteristic of PCFs is their strong birefringence, which is set by the size and arrangement of the air holes. A theoretical analysis [12] and experiments [13], [14] showed high birefringence of the order of 1×10^{-3}, three times larger than that of conventional polarization maintaining fibers and so optical components with better polarization maintaining characteristics are expected. The loss of initial PCFs was 80 dB/km, but recent developments in fabrication technology have drastically reduced [14]-[15]. Therefore, PCFs are expected to become key optical devices.

This paper describes the characteristics of dispersion controlled PCFs and of polarization maintaining PCFs that offer supercontinuum generation, as well as absolute single polarization characteristics for various types of optical devices in high performance optical network systems.

FABRICATION OF PCF

One merit of a PCF is its fabrication technique because it uses present fiber fabrication techniques, for example, multiple-capillary drawing method or the vapor-phase axial deposition (VAD) method. The fabrication process of the multiple-capillary drawing method is shown in Figure 2. Three components are combined to create the preform: silica capillaries, silica core rod, and jacketing tube. The silica capillaries and silica core rod are made by drawing a silica tube and silica rod, respectively. These capillaries and rod are packed and inserted into the jacketing tube. By heating and drawing the assembly, the capillaries and rod fuse to form a PCF. One important fabrication goal is reducing fiber loss. Early results yielded propagation losses in the order of 80 dB/km, but this was drastically reduced by using purified material and the loss of 1.3 dB/km was realized in 2001 [14] with this method. To date, the lowest fiber loss is 0.28 dB/km with the VAD method [15]. This fabrication method uses a high purity silica glass made by the VAD process. This result strongly suggests the possibility of low-loss photonic crystal fiber comparable to conventional single-mode fibers.
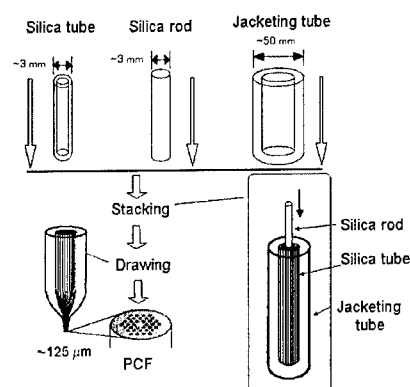

Figure 2. Fabrication of PCF by multiple-capillary drawing method.

OPTICAL PROPERTY OF PCF

PCFs have several unique optical characteristics in terms of mode and dispersion because the refractive index contrast between core and surrounding region is large and the refractive index of the surrounding region strongly depends on wavelength.   Therefore, a PCF shows single mode characteristics over a broad wavelength range.   These properties are determined by selecting the appropriate combination of air hole diameter d and air hole pitch Λ.   The normalized frequency V given by

$$V = \frac{2\pi\rho}{\lambda}(n_0^2 - n_1^2)^{1/2}$$

(1)

stays at a fixed value even if the wavelength shortens because of the strong wavelength dependence of the effective refractive index of the air-hole-array section.   Here ρ, n_0, and n_1 are the core diameter, the refractive index of core, and the effective refractive index of air-hole-array section, respectively.   This means that a PCF can offer single mode operation from the visible to infrared region if V satisfies a single mode condition.   This is not possible with conventional single mode fiber, where V rises as the wavelength shortens.   When parameter d/Λ becomes large and Λ is comparable to the wavelength (small core diameter and large refractive index difference), the contribution of the fiber structure to the fiber dispersion strengthens and the zero dispersion wavelength shifts to wavelengths shorter than 1280 nm, the zero dispersion wavelength of bulk silica [5]-[6], [16]-[17].   Figure 3 shows an example of a PCF with zero dispersion of 810 nm [16].   The air hole diameter d and air hole pitch Λ are 1.5 µm and 2.3 µm, respectively.   It is also possible to realize dispersion shifted (DS) PCFs with 1550 nm zero dispersion wavelength.   There are two approaches to realizing a DS-PCF.   One is to make use of the second zero dispersion of the PCF with the first zero dispersion wavelength set at around 900 nm [7] as shown in Figure 4(a).   As seen in the figure, the zero dispersion wavelength is 1550 nm if the parameter d/Λ is set to 0.35.   The other is to use a PCF structure that lowers the zero dispersion wavelength of a fiber whose basic zero dispersion wavelength is longer than 1550 nm [8]-[10] as shown in Figure 4(b).   Since PCF has greater freedom in fiber design because d and Λ can be independently chosen, a dispersion shifted and dispersion flattened PCF can be achieved with the appropriate design [8]-[10].

(a)   (b)
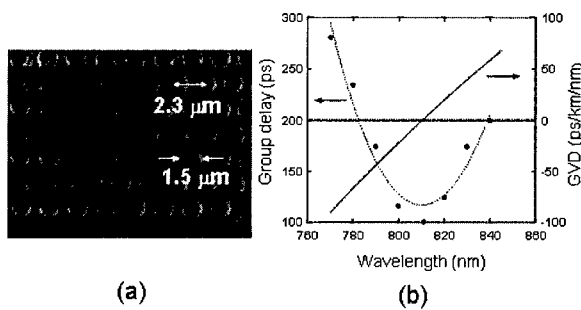
Figure 3.   (a) Micrograph of the PCF with zero dispersion in the 810 nm region.   (b) Measured dispersion characteristics of the PCF.

183
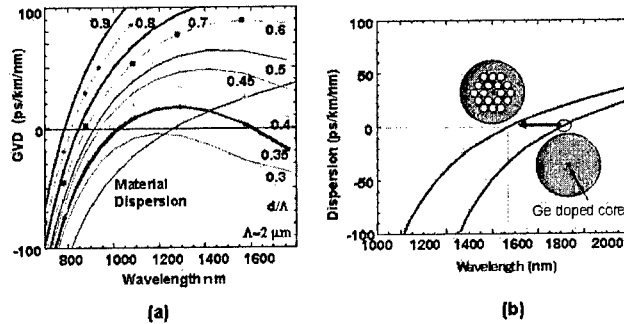
Figure 4. (a) Dispersion shifted PCF with with the first zero dispersion wavelength set at around 900 nm. (b) Dispersion shifted PCF that has lower zero dispersion wavelength than a fiber without PCF structure.

Several methods have been proposed for analyzing PCFs. Examples include the finite element method [12], [18], plane wave method [19], hybrid orthogonal function method [20], and multipole method [21].

POLARIZATION MAINTAINING PCF

Polarization maintaining (PM) fibers can stabilize the polarization state in the fiber and therefore, stabilize the operation of optical devices. Accordingly, they are expected to play an important role in optical communications. PCFs make it easier to realize fiber PM devices that is possible with existing PM fiber because anisotropy in the hole arrangement around the core region induces birefringence in the fiber, whereas the core region of existing PM fibers must be stressed [22]. Several configurations of PM-PCFs have been reported as shown in Figure 5. The configurations of Figure 5(a) [12], (b) [14], and (c) [13] have different air-hole diameters along two orthogonal axes near the core region and Figure 5(d) has two defects in the hole arrangement [23]. A theoretical analysis using the finite element method for the structure of Figure 5 (a) showed that it offers birefringence of 1×10^{-3} if the hole diameter ratio between small and large holes exceeds two [12]. We used the configuration of Figure 5(b) when fabricating PM-PCFs because of its simplicity. Figure 6(a) show a micrograph of a fabricated PM-PCF. The birefringence of the PM-PCF was measured by the beat length between the two orthogonal polarization modes.
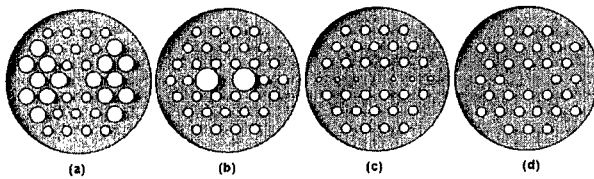
Figure 5. Polarization maintaining (PM) photonic crystal fiber configuration.
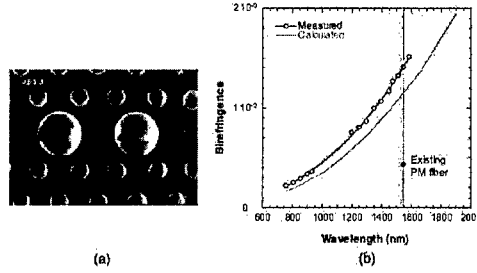
Figure 6. (a) Micrograph of fabricated PM-PCF. (b) Wavelength dependence of the birefringence.

The relationship between the polarization beat length L_B and the modal birefringence B is given by [24]

$$L_b = \frac{2\pi}{|\beta_x - \beta_y|} = \frac{\lambda}{|n_x - n_y|} = \frac{\lambda}{B},$$ (2)

where β_x and β_y are the propagation constants of the two orthogonal modes, and n_x and n_y are the effective refractive indexes for each polarization mode; λ is the wavelength of light in a vacuum. The linearly polarized light was launched at 45 degrees from the principal axis into the PM-PCF and the output power was measured as a function of wavelength. Figure 6(b) shows the wavelength dependence of the fiber birefringence. Its birefringence, 1.4×10^{-3}, at 1550 nm is three times larger than that of existing PM fiber. The birefringence increases with the wavelength. This is because the mode field diameter falls as the wavelength shortens, and this results in a reduction in modal asymmetry. The dotted curve in Figure 6(b) shows calculated results obtained using the fiber parameters. The experimental and calculated results agree well. The group velocity dispersions for the two polarization modes at 1550 nm are 59.5 and 66.8 ps/km/nm, respectively; the difference is as much as 7.3 ps/m/nm. The dispersion slopes for each polarization mode are 0.070 and 0.071 ps/nm^2/km, respectively. In order to control the dispersion characteristics of a PM-PCF with low dispersion or gentle dispersion slope at 1550 nm, a new design technique is necessary; our solution is dercribed in the next section.

DISPERSION CONTROLLED PM-PCF FOR SUPERCONTINUUM GENERATION

Nonlinear fiber with low dispersion and dispersion slope can yield the supercontinum (SC) generation needed to create WDM signals [25]. It should be noted that polarization maintainability is indispensable for stable SC generation. A PCF can meet this requirement [7]-[10], [25]-[27]. Figure 7(a) shows a micrograph of a PM-PCF designed for SC generation. The four central air holes with large diameter provide high birefringence, which realizes PM operation. The parameters of center core diameter d_2, air hole diameter d_1, and air hole pitch Λ were designed to achieve low dispersion, low dispersion slope, and high nonlinearity. This fiber has a silica core with an elliptical Ge-doped center core. The Ge-doping enables us to control the dispersion characteristics of the PM-PCF as well as to reduce the confinement loss [6]
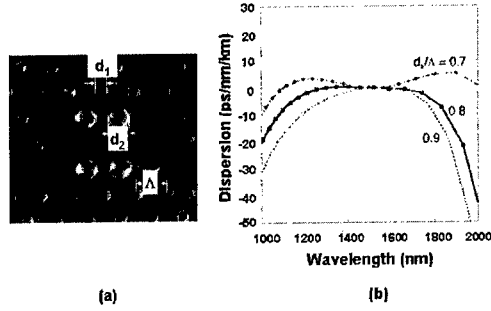
Figure 7. (a) Micrograph of dispersion controlled PM-PCF for SC generation.
(b) Calculated chromatic dispersion characteristics of the PM-PCF.

The dimensions of the Ge-doped elliptical core are 1.4 μm x 1.1 μm. The low dispersion of the PCF is essential for SC generation [6], [26]. The dispersion slopes of reported PCFs for nonlinear applications are quite high (approximately -0.25 ps/km/nm^2 [6]), but because of the design optimization, the configuration in Figure 7(a) realizes low dispersion slope characteristics, and thus low dispersion over a wide wavelength range. Figure 7(b) shows the calculated PCF dispersion characteristics for three ratios of d_2 / Λ. It is clear from the figure that dispersion-flattened characteristics are obtained with d_2 / Λ values of between 0.7 and 0.8. The d_2 / Λ value of the fabricated PM-PCF was approximately 0.77, close to the dispersion flat condition. The length of the PM-PCF used in the experiment was 200 m and optical loss at 1.55 μm was 22 dB/km. Figure 8 shows the measured chromatic dispersion characteristics of the PM-PCF. Measured dispersion and dispersion slope at 1.55 μm were -0.23 ps/km/nm and 0.01 ps/km/nm^2, respectively. The value of modal birefringence at 1.55 μm was 1.3 x 10^{-3}, which is comparable to that of Figure 6(b). The nonlinear parameter γ (= $n_2\omega/c/A_{eff}$) of the PM-PCF at 1.55 μm was 19 [W^{-1} km^{-1}], which is about ten times that of dispersion shifted fiber (~ 2 [W^{-1} km^{-1}]). In the experiment, the pumping optical pulse source was a mode-locked erbium doped
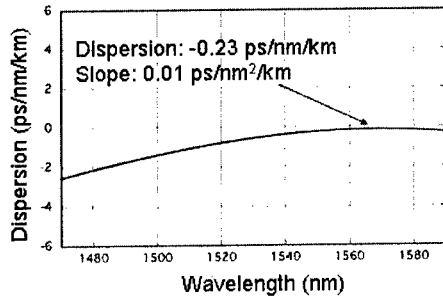
**Figure 8.** Measured chromatic dispersion characteristics of the PM-PCF.
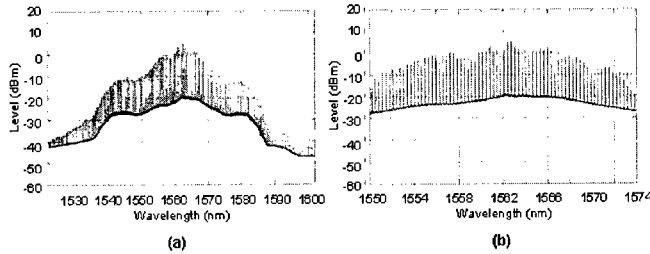
Figure 9. Optical spectra of the supercontinuum generated in a 200 m PM-PCF. (a) Supercontinuum spectrum at the output of the PM-PCF with coupled average power of 28 dBm. (b) Longitudinal mode structure around the center wavelength in (a).

fiber laser with center wavelength of 1562 nm and pulse width of 2.2 ps. Average coupled power into the PM-PCF was 28 dBm, which corresponds to the peak power of 6.3 W. Figures 9 show the generated supercontinuum spectra. It is clear from the figure that the optical spectrum was broadened symmetrically over 40 nm. Although the peak level decreased as the spectrum broadened, no increase in the noise level was observed. By reducing the optical loss of the PM-PCF, supercontinuum generation with less pumping power, around 20 dBm, is expected. This fiber is applicable to a multi channel optical source for WDM communication systems and photonic networks.

ABSOLUTELY SINGLE POLARIZATION PCF

Absolutely single polarization (ASP) fiber is an optical fiber, which, unlike other optical fibers, guides only one polarization mode of the light signal. ASP fiber is expected to eliminate polarization mode dispersion (PMD). A PM-PCF with high birefringence can offer ASP characteristics. The structure of an ASP-PCF is shown in the inset of Figure 10. d_1 and d_2 are the diameters of the small air holes and large air holes, respectively, and Λ is the air hole pitch.
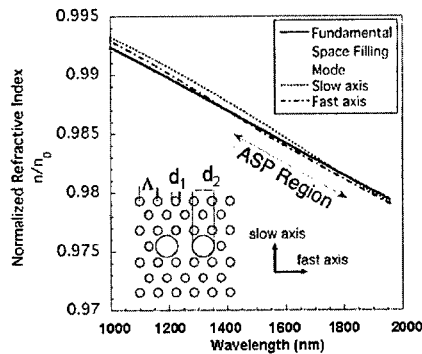
Figure 10. Effective indices of two orthogonal polarization modes and fundamental space-filling mode in an ASP-PCF.

187
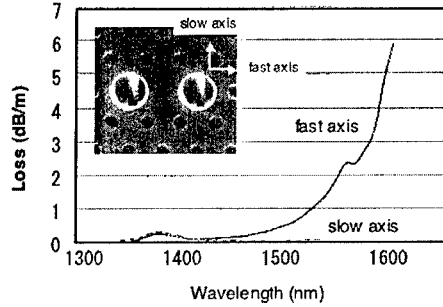
Figure 11. Spectral loss profile of two orthogonal modes in a 2-m ASP-PCF. Inset shows a micrograph of the fiber's cross-section.

Parameter d_2 / d_1 must be larger than 1, which results in a W-shaped effective index profile. Fiber with a W-shaped refractive index profile offers fundamental mode cutoff in the long wavelength region [28]. PM fiber with a W-shaped refractive index profile has different cutoff wavelengths for the two polarization modes because of the non-degenerated fundamental mode. Figure 10 shows the effective indices of the slow axis, n_s, the fast axis, n_f, and the fundamental space-filling mode (FSFM), n_{clad} as functions of wavelength. The degree of modal birefringence B of the ASP-PCF is defined by

$$B = (\beta_s - \beta_f)/k .\qquad(3)$$

β_s and β_f are the propagation constants of the two orthogonal polarization modes corresponding to the slow and fast axis, respectively and k is the wavenumber. The effective index of the cladding region, n_{clad}, is defined by the FSFM of the cladding structure. When n_s or n_f is larger than n_{clad}, the guiding mode is present. When both are smaller than n_{clad}, the leaky mode dominates, that is, the fundamental mode is cutoff. When n_s is larger than n_{clad} and n_f is smaller than n_{clad}, the fiber guides only one polarization mode. The wavelength range of the ASP is indicated in the figure. It should be noted that fibers with large B are important in realizing an ASP-PCF with a wide operating wavelength range. The inset in Figure 11 shows a cross-section of the fabricated ASP-PCF. The ratio between d_1 and d_2 is greater than two in order to induce large modal birefringence [12]. The n_f, n_s, and n_{clad} were calculated to determine the cutoff wavelengths of the fabricated fiber. The cutoff wavelengths of the fast and slow axes were 1420 and 1810 nm, respectively. A numerical simulation also showed that the fiber exhibits ASP at 1550 nm. Figure 11 shows the measured spectral loss profile of the fabricated ASP-PC for both polarization modes. The polarization dependent loss (PDL) is about 1 dB/m at 1550 nm, and more than 5 dB/m at 1650 nm, while it is less than 0.1 dB/m at 1310 nm. The propagation loss was less than 0.1 dB/m for the entire measured wavelength range, 1300 to 1650 nm, except for the OH base absorption peak around 1400 nm. The PDL decreases as the wavelength shortens because both polarization modes are well confined in the core region at short wavelengths. The loss of the fast axis begins to increase at 1450 nm. This wavelength agrees well with the numerical simulation results shown in Figure 10. Long wavelength cutoff of the guiding mode was not observed within the measured wavelength range. A numerical simulation indicates that the cutoff wavelength of the slow axis occurs at a wavelength longer

than the measured range. This fiber will help to stabilize optical systems and improve their SN ratio by suppressing the crosstalk between the two principal axes.

APPLICATION OF PCF FOR OPTICAL COMMUNICATIONS SYSTEMS

The next generation photonic network will use generalized multi-protocol label switching (GMPLS) and achieve high performance. In order to realize GMPLS, multi-channel WDM signal sources, optical cross connects (OXCs), optical add/drop multiplexer/demultiplexers (OADMs), and high performance optical routers (O-routers) are necessary and optical paths are dynamically controlled from the Internet Protocol (IP) layer. PCFs will be used as pigtails in optical devices in the optical equipments or to couple the output power of a laser diode to PCF without a coupling lens. SC sources based on dispersion controlled PM-PCF will yield multi-wavelength, stable optical signal sources that have simple configuration and low pumping power. These optical system devices will help to enhance the high performance optical subsystems mentioned above and realize next generation photonic networks.

CONCLUSIONS

The characteristics of dispersion controlled PCFs and polarization maintaining PCFs were described. Theoretical analyses and experimental results of fabricated PCFs were shown; they offered short wavelength zero dispersion at 810 nm, polarization maintenance with birefringence of 1×10^{-3}, polarization maintaining dispersion flattened functions, and absolutely single polarization with polarization-dependent loss of 1 dB/m at 1550 nm. A supercontinuum generation experiment with PM-PCF in the 1550 nm region confirmed symmetrical spectral broadening to over 40 nm. The potential of PCFs was discussed for use in the next generation high performance networks.

ACKNOWLEDGEMENTS

REFERENCES

1. J. C. Knight, T. A. Birks, P. St. J. Russel, and D. M. Atkin, "All-silica single mode fiber with photonic crystal cladding," *Opt. Lett.*, vol. 21, pp. 1547-1549, 1996.
2. D. Mogilevtsev, T. A. Birks, and P. St. J. Russel, "Group-velocity dispersion in photonic crystal fibers," *Opt. Lett.*, vol. 23, pp. 1662-1664, 1998.
3. M. J. Gardner, R. McBride, J. D. C. Jones, D. Mogilevtsev, T. A. Birks, J. C. Knight, and P. St. J. Russel, "Experimental measurement of group velocity dispersion in photonic crystal fibre," *Electron. Lett.*, vol. 35, No. 16, pp. 63-64, 1999.
4. T. A. Birks, D. Mogilevtsev, J. C. Knight, and P. St. J. Russell, "Dispersion compensation using single-material fibers," *IEEE Photon. Technol. Lett.*, vol. 11, pp. 674-676, 1999.
5. J. K. Ranka, R. S. Windeler, and A. J. Stentz, "Visible continuum generation in air-silica microstructure optical fibers with anomalous dispersion at 800 nm," *Opt. Lett.*, vol. 25, pp. 25-27, 2000.
6. W. J. Wadsworth, J. C. Knight, A. Ortigosa-Blanch, J. Arriaga, E. Silvestre, and P. St. J. Russell, "Soliton effects in photonic crystal fibres at 850 nm," *Electron. Lett.*, vol. 36, No. 1, pp. 53-55, 2000.

7. K. P. Hansen, J. R. Jensen, C. Jacobsen, H. R. Simonsen, J. Broeng, P. M. W. Skovgaard, A. Petersson, and A. Bjarklev, "Highly nonlinear photonic crystal fiber with zero-dispersion at 1.55 μm," *Tech. Digest of Optical Fiber Communication Conference (OFC) 2002*, vol. 70, postdeadline paper FA9.
8. W. Reeves, J. Knight, P. Russell, P. Roberts, and B. Mangan, "Dispersion-flattened photonic crystal fibers at 1550 nm," *Tech. Digest of Optical Fiber Communication Conference (OFC) 2003*, paper FI3.
9. K. P. Hansen, "Dispersion flattened hybrid-core nonlinear photonic crystal fiber," *Optics Express,* vol. 11, pp. 1503-1509, 2003.
10. T. Yamamoto, H. Kubota, and S. Kawanishi, M. Tanaka and S. Yamaguch, "Supercontinuum generation at 1.55 μm in a dispersion-flattened polarization-maintaining photonic crystal fiber" *Optics Express,* vol. 11, pp. 1537-1540, 2003.
11. T. A. Birks, J. C. Knight, and P. St. J. Russel, "Endlessly single-mode photonic crystal fiber," *Opt. Lett.*, vol. 22, pp. 961-963, 1997.
12. S. Kawanishi and K. Okamoto, 'Polarization maintaining holey optical fiber', *IEICE Soc. Conf. 2000*, Nagoya, B-10-153 (in Japanese).
13. A. Ortigosa-Blanch, J. C. Knight, W. J. Wadsworth, J. Arriaga, B. J. Mangan, T. A. Birks, and P. St. J. Russell, "Highly birefringent photonic crystal fibers," *Opt. Lett.*, vol. 25, pp. 1325-1327, 2000.
14. K. Suzuki, H. Kubota, S. Kawanishi, M. Tanaka, and M. Fujita, "High-speed bi-directional polarisation division multiplexed optical transmission in ultra low-loss (1.3 dB/km) polarisation-maintaining photonic crystal fibre," *Electron. Lett.*, vol. 37, No. 23, pp. 1399-1401, 2001.
15. K. Tajima, J. Zhou, K. Kurokawa, and K. Nakajima, "Low water peak photonic crystal fibers," *Tech. Digest of European Conference on Optical Communication (ECOC) 2003*, paper Th4.1.6.
16. H. Kubota, K. Suzuki, S. Kawanishi, M. Nakazawa, M. Tanaka, and M. Fujita, "Low-loss, 2 km-long photonic crystal fiber with zero GVD in the near IR suitable for picosecond pulse propagation at the 800 nm band," *Tech. Digest of Conference on Lasers and Electro-Optics (CLEO) 2001*, Baltimore, paper CPD3.
17. J. C. Knight, J. Arriaga, T. A. Birks, A. Ortigosa-Blanch, W. J. Wadsworth, and P. St. J. Russell, "Anomalous dispersion in photonic crystal fiber," *IEEE Photon. Technol. Lett.*, vol. 12, pp. 807-809, 2000.
18. M. Koshiba and Y. Tsuji, "Curvilinear hybrid edge/nodal elements with triangular shape for guided-wave problems," *IEEE J. Lightwave Technol.*, vol. 18, No. 5, pp. 737-743, 2000.
19. A. Ferrando, E. Silvestre, J. J. Miret, J. A. Monsoriu, M. V. Andres, and P. St. J. Russell, "Designing a photonic crystal fibre with flattened chromatic dispersion," *Electron. Lett.*, vol. 35, pp. 325-327, 1999.
20. T. M. Monro, D. J. Richardson, N. G. R. Broderick, and P. J. Bennett, "Holey optical fibers: An efficient modal model," *IEEE J. Lightwave Technol.*, vol. 17, pp. 1093-1102, 1999.
21. T. P. White, R. C. McPhedran, "Multiple method for efficient microstructured optical fiber calculations," *Tech. Digest of Conference on Lasers and Electro-Optics (CLEO) 2001*, Baltimore, paper JTuC6, pp. 597-598.
22. T. Hosaka, K. Okamoto, T. Miya, Y. Sasaki, and T. Edahiro, 'Low-loss single polarisation fibres with asymmetrical strain birefringence', *Electron. Lett.*, vol. 17, pp. 530-531, 1981.
23. T. P. Hansen, J. Broeng, S. E. B. Libori, E. Knudsen, A. Bjarklev, J. R. Jensen, and H. Simonsen, "Highly birefringent index-guiding photonic crystal fibers," *IEEE Photon. Technol. Lett.*, vol. 13, pp. 588-590, 2001.
24. D. N. Payne, A. J. Barlow, and J. J. R. Hansen, "Development of low- and high-birefringence optical fibers," *IEEE J. Quantum Electron.*, vol. QE-18, pp. 477-488,

1982.

25. H. Takara, T. Ohara, K. Mori, K. Sato, E. Yamada, Y. Inoue, T. Shibata, M. Abe, T. Morioka, and K-I. Sato, "More than 1000 channel optical frequency chain generation from single supercontinuum source with 12.5 GHz channel spacing," *Electron. Lett.*, vol. 36, pp. 2089-2090, 2000.

26. Z. Yusoff, P. Teh, P. Petropoulos, K. Furusawa, W. Belardi, T. Monro, and D. Richardson, "24 channel x 10 GHz spectrally spliced pulse source based on spectral broadening in a highly nonlinear holy fiber," *Tech. Digest of Optical Fiber Communication Conference (OFC) 2003*, paper FH3.

27. P. Petropoulos, T. M. Monro, H. Ebendorff-Heidepriem, K. Framoton, R. C. Moore, H. N. Rutt, and D. J. Richardson, "Soliton-self-frequency-shift effects and pulse compression in an anomalously dispersive high nonlinearity lead silicate holey fiber," *Tech. Digest of Optical Fiber Communication Conference (OFC) 2003*, postdeadline paper PD3.

28. S. Kawakami and S. Nishida, "Characteristics of doubly clad optical fiber with a low-index inner cladding", *IEEE J. Quantum Electron.*, vol. QE-10, No. 12, pp. 879-887, 1974.

Interfacial Energy and Materials Selection Criteria in Composite Microstructured Optical Fiber Fabrication

Shandon D. Hart, Yoel Fink
Department of Materials Science & Engineering and Research Laboratory of Electronics
Massachusetts Institute of Technology
Cambridge, MA, 02139 U.S.A.

ABSTRACT

The recently expanding field of microstructured optical fibers relies on the controlled fabrication of sub-micron features in a fiber drawn in the viscous fluid state. Microstructured fibers have generated great interest owing to their potential in areas such as photonic bandgap guidance of light in low-index media; high-energy laser transmission; and unique control over waveguide non-linearities, dispersion and modal properties [1-6]. These fibers have been made from a single material with air holes [7, 8] and as multi-material 'composite' fibers where air is not a part of the microstructured region [6, 9]. While single-material microstructured fibers generally rely on the established technology base of fused silica, the use of less conventional materials may enable applications not possible using silica [6]. Multi-material fibers may also present certain fabrication advantages due to their incompressible domains and simple cylindrical geometries. However, the use of more than one material raises questions about which types of materials can be combined in the drawing of a microstructured fiber. This problem can be approached by analyzing the relative importance of different materials properties such as viscosity, interfacial energy, and thermal expansion. In this study we focus on the effects of interfacial energy in composite microstructured fibers. We measure the interfacial energies at high temperature of a chalcogenide glass and an organic polymer recently employed in the fabrication of composite photonic bandgap optical fibers. We discuss the effect of interfacial energy during fiber draw, as well as the interplay between surface and viscous forces. Finally, we comment on the implications of this analysis for understanding what classes of materials can be used in composite microstructured fiber fabrication.

INTRODUCTION

In a microstructured optical fiber, 100-1000 nm size features exist with sharply defined interfaces. These features are created by high-temperature drawing of the fiber in the viscous fluid state, and the associated feature size is 2-3 orders of magnitude smaller than those found in conventional optical fiber technology (figure 1). This creates large interfacial areas in these systems. Neglecting viscosity, surface forces should drive the capillary instability and breakup of these microstructures, with the magnitude of the instability increasing approximately as $(1/r)^{3/2}$, where r is the characteristic feature size [10, 11]. The fabrication of optical fibers in general involves a competition between surface forces, which drive the breakup of fluid filaments, and viscous forces, which slow or even arrest this breakup through kinetic limiting of the approach to equilibrium. In microstructured fibers the small feature sizes should heighten the effect of surface forces / interfacial energy. Elucidating the role of interfacial energy in these structures may lead to a more general understanding of what types of materials can be employed in these fibers.
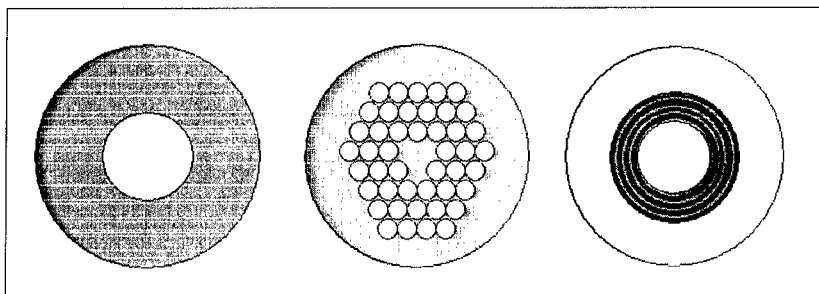
Figure 1. Schematic (not to scale) of three types of optical fiber. Left: conventional fiber with silica cladding and doped silica core. Middle: '2-D' photonic crystal fiber, usually made from silica filled with air holes. Right: cylindrical multilayer or 'Bragg' fiber, the layer composition alternating between two different solid materials.

We begin this analysis by measuring the high-temperature interfacial energy between a chalcogenide glass, arsenic triselenide (As_2Se_3) and an organic polymer, poly(ether sulfone) (PES). These materials have recently been employed in the fabrication of hollow photonic bandgap optical fibers [6]. Through isolating interfacial energy, we gain insight into its importance as well as the importance of viscosity in materials selection for these fiber structures. This will aid in the further development of these fibers, which may find important technological applications in areas such as high-energy laser transmission for communications or therapeutic surgery, spectroscopy for chemical sensing or diagnostic medicine, and ultrafast laser physics.

Chalcogenide glasses are amorphous semiconductors that are of general scientific and technological interest in their own right owing to properties such as mid-infrared transparency, optical non-linearities, and photoconductivity. These glasses are used in IR optical elements such as fibers and lenses that are often fabricated by processing in the fluid state, where surface energy is an important parameter. Chalcogenides have also recently been explored for use in microstructured 'holey' fibers, as in the middle of figure 1 [12]. Although high-temperature surface energy values have been reported for various polymer and oxide glass systems [13, 14], to the best of our knowledge literature values do not exist for the surface energies of any chalcogenide glasses. In addition to measuring the surface energies of As_2Se_3 and PES individually, we also measure the interfacial energy between the two materials to aid our discussion of materials property criteria in composite photonic bandgap fibers. The study of organic/inorganic interfacial energy where both materials are in the viscous state is also of interest for the processing of low-melting glass/polymer composites for various other optical and structural applications [15-17].

EXPERIMENTAL

The determination of fluid surface energy through the fitting of droplet surface coordinates to the Laplace-Young equation has been well-described in the literature [18, 19]. This technique generally relies on a numerical integration of the Laplace-Young equation:

$$\frac{d\phi}{ds} = 2b + \frac{(\Delta\rho)gz}{\gamma_{LV}} - \frac{\sin\phi}{x} \tag{1}$$

194
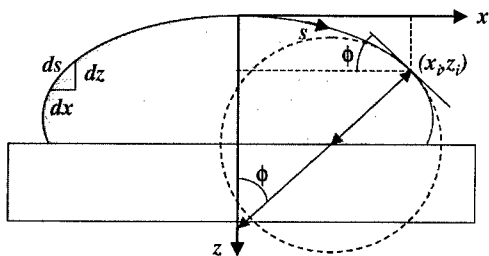
Figure 2. Geometry for numerical solution of the Laplace-Young equation using droplet surface profile coordinates.

where the drop coordinate variables are defined as in figure 2, $\gamma_{l.v}$ is the drop/ambient interfacial energy, b is the mean curvature at the apex of the droplet, g is the gravitational constant, and $\Delta\rho$ the density difference between the drop and ambient phases.

Systems and software are commercially available that measure surface energy using this framework. Our measurements were carried out using a Dataphysics OCA-20 system outfitted for high-temperature analysis. Calculations were performed using Laplace-Young fitting in Dataphysics analysis software. PES sessile drop tests were used to determine the PES surface energy, while sessile and pendant drop tests were both performed with As_2Se_3. In order to obtain the PES/As_2Se_3 interfacial energy, a molten droplet of As_2Se_3 was placed on a PES film. Testing temperatures were chosen to coincide with the previously employed composite photonic bandgap fiber drawing regime [6, 9]. All tests were performed under flowing nitrogen gas.

RESULTS

PES droplets in sessile drop experiments were allowed to equilibrate for greater than 30 minutes. Less time was needed for equilibration of the As_2Se_3 droplets owing to its lower viscosity at the temperatures of interest; these shorter relaxation times are helpful in avoiding surface crystallization of the As_2Se_3 which often begins after ~30 min under these conditions. Figure 3 shows an As_2Se_3 pendant drop image and computer generated Laplace-Young profile fit. Good agreement was found between both sessile and pendant drop results for As_2Se_3.
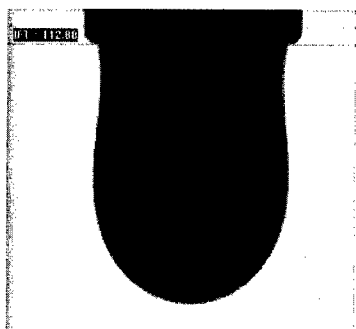
Figure 3. Image of As_2Se_3 pendant drop and calculated Laplace-Young surface profile fit.

**Table I.** High-temperature surface energy data for As_2Se_3 and PES.

Interface	Temp. (°C)	Density (g/cm³)	Surface Energy (mJ/m²)
As_2Se_3 / N_2	~292	4.43 +/- 0.07	**112.8 +/- 0.8**
PES / N_2	295	1.32 +/- 0.04	**46.9 +/- 4.5**

Results for the surface energies of As_2Se_3 and PES are summarized in table I. Using the contact angle between an As_2Se_3 drop and a PES film (figure 4) with the individual values of surface energy obtained for each material, the interfacial energy between As_2Se_3 and PES can be obtained using the well-known Young equation:

$$\gamma_{SL} - \gamma_{SV} = \gamma_{LV} \cos\theta \tag{2}$$

This test is complicated by the fact that at the temperatures of interest, both the chalcogenide glass and the polymer film are above their respective softening temperatures. Thus, "γ_{SL}" in this case is actually an interfacial energy between two viscous fluids. Under these conditions, the polymer itself will have a tendency to rearrange into droplets on the surface of the solid substrate, and the dense chalcogenide glass will tend to indent the surface of the polymer. Fortunately, the viscosity of the polymer is high enough at the experimental temperatures to greatly delay these effects. The high viscosity and adhesion of the polymer to the solid (silicate glass) substrate allowed the polymer to remain in a film geometry for the duration of the test. The experimental contact angle data were obtained within ~30 seconds of chalcogenide droplet deposition on the polymer film, avoiding significant penetration of the chalcogenide into the polymer. Although the chalcogenide glass relaxes quite quickly at these temperatures, it is best not to assume that this test represents an equilibrium case. Nevertheless, the near-equilibrium contact angle obtained should still provide meaningful information for assessing the interfacial energy between the two materials. An image of the freshly deposited As_2Se_3 droplet on a 25 micron thick PES film supported by a glass substrate is shown in figure 4. The calculated value of interfacial tension between the two materials is given in table II.
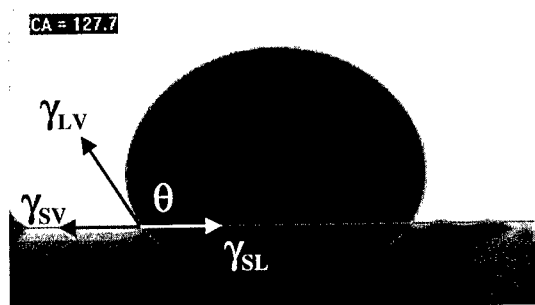
Figure 4. As_2Se_3 sessile drop freshly deposited on 25 micron PES film supported by a glass substrate at 295°C.

Table II. As_2Se_3 – PES measured contact angle and calculated interfacial energy.

Interface	Temp. (°C)	Contact angle	**Interfacial Energy (mJ/m^2)**
As_2Se_3 / PES	~292	126.6 +/- 2.5	**114 +/- 9**

ANALYSIS AND DISCUSSION

A cylindrical multilayer microstructured fiber is characterized by a large amount of interfacial area; the total amount of interfacial area is increased by a factor of ~100 during the fiber draw process. Thus, with appreciable interfacial energy it would obviously be energetically favorable for the layers to rearrange into rods or droplets during fiber drawing. To quantify our understanding of the PES/As_2Se_3 interface, it is helpful to present certain derived quantities, which are summarized in table III. The wetting tendency of this materials system is illustrated by a common parameter called the spreading coefficient, S:

$$S_{(\alpha\beta)} = \gamma_{\beta v} - (\gamma_{\alpha v} + \gamma_{\alpha\beta}) \tag{3}$$

(where in this case α denotes one phase, β another phase, and v the vapor). A negative spreading coefficient for two materials means that one material will not spread spontaneously on the other. In this case, a strong tendency toward droplet formation is obvious. Nevertheless, there is some interaction (wetting) between the materials. This condition is characterized by a non-zero work of adhesion (w_a), the amount of work that is needed to separate the materials from one another:

$$w_{a(\alpha\beta)} = \gamma_{\alpha v} + \gamma_{\beta v} - \gamma_{\alpha\beta} \tag{4}$$

The fact that the materials do not have strong wetting tendencies leads to significant implications for the relative importance of viscosity and interfacial energy in composite microstructured fiber drawing. As mentioned previously, the traditional optical fiber draw process is dominated by high viscosity, which prevents the surface-driven capillary breakup of the drawn fiber. The achievable drawing viscosities in a polymer-based composite system are not as high as in the traditional silica-glass based system. A natural hypothesis would be that high surface wetting would be necessary in a polymer-glass composite drawn microstrucutured fiber [6, 9]; however, this study shows that high surface wetting is not a strict requirement. The effects of high interfacial energy can be counter-acted by high viscosity in these drawn fiber structures.

A first-order estimate of the importance of viscosity can be obtained by modeling what would happen if viscosity were *not* a factor. Utilizing these interfacial energy data, we can analyze what should be the effect of drawing very fine capillaries under the influence of surface forces alone. We make use of the theory of Rayleigh [10], who first analyzed the instability of an inviscid fluid cylinder (neglecting viscosity effects) due to surface energy. Rayleigh's

Table III. Derived interfacial quantities for PES and As_2Se_3 glass at ~295°C.

Interface	Spreading coefficient	Work of adhesion (mJ/m^2)	Rayleigh time scale (sec)
As_2Se_3 / PES	-180 +/- 15	46 +/- 14	6.0×10^{-6}

conclusions included a characteristic time associated with the breakup of a fluid cylinder due to surface forces, which we call the Rayleigh time scale (t_R):

$$t_R = \left(\frac{r^3 \rho}{\gamma_{\alpha\beta}} \right)^{1/2} \tag{5}$$

t_R is proportional to the time in which a capillary perturbation will grow according to the ratio 1:e in the absence of viscous forces. In the case of PES/As$_2$Se$_3$, using $r = 10$ μm to approximate the initial condition in a microstructured fiber preform [6, 9], we find that $t_R = 6.0 \times 10^{-6}$ seconds. Although t_R is calculated for a cylinder rather than a film, it nevertheless gives an expected time scale for the growth of instabilities due to surface forces. Furthermore, this time scale continually decreases as the instability grows, rapidly leading to capillary breakup. This clearly demonstrates that if surface forces were dominant in the PES/As$_2$Se$_3$ system, a drawn microstructured fiber would not be sustainable using these materials. In this system, as in the fused silica/air system [2, 3], a viscosity-dominated draw process is what allows the fabrication of well-ordered microstructured fibers. Fused silica has an advantage in its high-viscosity, 'strong liquid' behavior [20]; two key benefits of a multi-material system are the incompressibility of the entire microstructure and the potentially high viscous forces in both material domains that work together to prevent capillary breakup.

CONCLUSIONS AND FUTURE WORK

The data and analysis presented here provide a framework for understanding the importance of interfacial energy in microstructured fiber systems. It has been shown that polymer-based composite systems with high interfacial energies may perform well, provided the viscosity of one or both materials is high during fiber drawing. This is encouraging for the future exploration of various materials systems for composite microstructured fiber devices. This analysis suggests that it is not necessarily viscosity *matching* between the composite fiber materials that is required for successful fiber drawing, but rather *high viscosity* in one or both fiber materials that leads to the maintenance of controlled microstructures. It is not a requirement that the materials be highly wetting (although for a fixed viscosity level, improved wetting will decrease the driving force towards capillary breakup). This indicates that it should be possible to employ a wider suite of materials than those that have been employed thus far in composite microstructured fibers, provided that at least one of the fiber components has a high viscosity during fiber draw.

The measurements reported here must be reproduced in the future to gain greater confidence in their statistical accuracy, and it may be useful to repeat the PES/As$_2$Se$_3$ interfacial energy measurement using a different sample geometry to corroborate the present results. In addition, it is of interest to explore the effects of interfacial energy on other important phenomena, such as the crystallization that may occur at the material boundaries. A major step forward in defining the materials selection criteria for these fibers will be to model the viscous flow during draw using a complete Navier-Stokes description. This model ideally should be coupled with the ability to measure the anisotropic viscosities (particularly in extension) of these materials. This viscosity analysis will help to define how high the material viscosities need to be, as a function of their interfacial energy or t_R, to maintain order in drawn composite microstructured fibers.

REFERENCES

1. T.A. Birks, J.C. Knight and P.S. Russell, Optics Letters, **22**(13): p. 961-963, 1997.
2. R.F. Cregan, B.J. Mangan, J.C. Knight, T.A. Birks, P.S.J. Russell, P.J. Roberts, and D.C. Allan, Science, **285**: p. 1537-1539, 1999.
3. C.M. Smith, N. Venkataraman, M.T. Gallagher, D. Muller, J.A. West, N.F. Borrelli, D.C. Allan, and K.W. Koch, Nature, **424**(6949): p. 657-659, 2003.
4. W.H. Reeves, D.V. Skyrabin, F. Biancalana, J.C. Knight, P.S. Russell, F.G. Omenetto, A. Efimov, and A.J. Taylor, Nature, **424**(6948): p. 511-515, 2003.
5. T. Engeness, M. Ibanescu, S.G. Johnson, O. Weisberg, M. Skorobogatiy, S.A. Jacobs, and Y. Fink, Optics Express, **11**(10): p. 1175-1196, 2003.
6. B. Temelkuran, S.D. Hart, G. Benoit, J.D. Joannopoulos and Y. Fink, Nature, **420**(6916): p. 650-653, 2002.
7. B.J. Eggleton, C. Kerbage, P.S. Westbrook, R.S. Windeler and A. Hale, Opt. Express, **9**(13): p. 698-713, 2001.
8. J.C. Knight, Nature, **424**(6950): p. 847-851, 2003.
9. S.D. Hart, G.R. Maskaly, B. Temelkuran, P.H. Prideaux, J.D. Joannopoulos and Y. Fink, Science, **296**: p. 510-513, 2002.
10. L. Rayleigh, J.W.S., Proc. Royal Soc. London, **29**: p. 71-97, 1879.
11. J. Eggers, Rev. Modern Physics, **69**(3): p. 865-928, 1997.
12. T.M. Monro, Y.D. West, D.W. Hewak, N.G.R. Broderick and D.J. Richardson, Electronics Letters, **36**(24): p. 1998-2000, 2000.
13. S. Wu, Journal of Colloid and Interface Science, **31**(2): p. 153-161, 1969.
14. A. Kucuk, A.G. Clare and L. Jones, Glass Technol., **40**(5): p. 149-153, 1999.
15. E. Bormashenko, R. Pogreb, Z. Pogreb and S. Sutovski, Opt. Eng., **40**(5): p. 661-662, 2001.
16. N.H. Ray and F.R. Sherliker, United States Patent No. 3,732,181, 1973.
17. C.J. Quinn, P. Frayer and G.H. Beall, in *Polymeric materials encyclopedia*, J.C. Salamone, Editor. 1996, CRC Press, Inc. p. 2766-2777.
18. S. Hartland and R.W. Hartley, *Axisymmetric fluid-liquid interfaces*. 1976, New York: Elsevier.
19. S. Lahooti, O.I. del Rio, P. Cheng and A.W. Neumann, in *Applied Surface Thermodynamics*, A.W. Neumann and J.K. Spelt, Ed. 1996, Marcel Dekker: New York.
20. A.K. Varshneya, *Fundamentals of inorganic glasses*. 1994, New York: Academic Press.

Aperiodic lattices for photonic bandgap engineering

Subhasish Chakraborty, David G. Hasko and Robert. J. Mears[1, 2]
Microelectronics Research Centre, Cavendish Laboratory, Department of Physics, University of Cambridge, Madingley Road, Cambridge CB3 0HE.
[1] Department of Engineering, University of Cambridge, Trumpington Street, Cambridge CB2 1PZ
[2] Present address: R. J. Mears 189 Wells Avenue, Newton MA 02459

ABSTRACT

A new method is presented, based on the discrete Fourier Transform, for the design of aperiodic lattices to be used in photonic bandgap engineering. Designing an aperiodic lattice by randomly choosing defects is unlikely to result in useful optical transmission characteristics. By contrast, this new method allows an aperiodic lattice to be designed directly from the desired optical characteristic. The use of this method is illustrated with a design for a structure to realise two transmission wavelengths in the stopband of a one-dimensional photonic lattice. This design has been fabricated in silicon-on-insulator and some optical characteristics are given.

INTRODUCTION

Previously, photonic band gap engineering has been carried out mainly using periodic lattices with single defects [1,2]. If further defects are introduced into the structure the lattice is rendered aperiodic. However, it is highly unlikely that a randomly chosen aperiodic lattice will have any useful transmission characteristics, either for use in WDM systems or for use in photonic integrated circuits. With large numbers of defects, the increase in the number of scattering sites makes the problem of identifying "useful" aperiodic lattices computationally difficult.
This paper describes the design of a one-dimensional aperiodic photonic lattice using an optimization procedure based on Discrete Fourier Transform (DFT) theory [3]. A one-dimensional microstructural aperiodic superlattice, for second harmonic generation with quasi phase matching technique, has been studied in detail [4]. The question of finding aperiodic optical superlattices (AOS), which contain plentiful Fourier spectral components, necessary to implement complex optical characteristics, has been raised [5]. However, for the design of useful aperiodic lattices, the present research uses an approach similar to computer-generated holography. In particular, the reciprocal (i.e. Fourier) space representation of an aperiodic lattice is mathematically similar to the far field diffraction pattern of a computer-generated hologram (CGH) illuminated with a monochromatic electromagnetic wave [6].
This paper describes a novel method to produce tailored bandgap properties for a 1D photonic lattice using an overall aperiodic distribution of scatterers. A two defect lattice, giving two independently chosen transmission wavelengths in the stopband is used to illustrate the ability to of this method to tailor the bandgap properties. Such structures are useful in microphotonic integrated circuits at optical telecommunication wavelengths, which requires microscale optical elements. We have used the silicon-silicon dioxide system, which provides a sufficiently large contrast (the refractive index difference Δn is about 2) to realize an efficient optical waveguide at the important communications wavelength of 1.54 μm. The optical wave is strongly confined, so

that the waveguide cross-section can be made very small (in this case 0.5 μm wide and 0.26 μm thick). The aperiodic lattice is implemented using a number of 200 nm diameter holes placed along the centre line of the waveguide. Particular attention has been paid to sidewall roughness of the waveguide, which leads to undesirable scattering of the optical wave and transmission losses [7]. The techniques used to fabricate the waveguides used in this study have been developed to minimize the roughness. It is important that the propagation loss is minimised for any photonic structure in an integrated circuit, and the magnitude of the loss can be measured using the Fabry-Perot resonance method [8].

THEORY

This theory is based on two ideas. First, for bandgap engineering it is important to dope an otherwise pure (i.e. periodic) real space lattice with defects (missing or extra scattering sites). Second, a useful aperiodic lattice, doped with multiple defects, can be distinguished from any randomly chosen aperiodic lattice (non-useful) by defining a well-defined spatial frequency set $\{G_i\}$. It is important to realize that the spectral response of an aperiodic lattice is closely related to its Fourier Transform; the spatial frequency set is found by taking the Fourier transform of the lattice. It is well-known that a single defect, in an otherwise periodic structure, leads to an allowed "defect" transmission state within a wide photonic stop band (Fig. 2). We have extended this approach to design a structure with multiple defects, which results in overall aperiodicity, to achieve two completely isolated high transmission defect states within a wide photonic stop band. The design process is as follows: We start with a length of periodic scatterers to form a trial lattice. The spectral response of the trial lattice is calculated using the Discrete Fourier Transform method described elsewhere [3]. The difference between the desired spectral characteristics and the actual spectral response is then calculated and used as the cost function of an iterative optimization process. The process proceeds by randomly either inserting or removing defects in at least one of the scattering sites and recomputing the cost function; if the recomputed cost function falls below a predetermined cost function value the corresponding now aperiodic lattice is selected and the process continues for further optimization. Small increases in the cost function are also accepted, in the early stages of the optimization process, according to Maxwell-Boltzmann classical probability statistics. This is essential to make sure that the search process avoids being trapped in any local minima. The process is terminated after a predetermined number of iterations or when the overall aperiodic lattice provides the desired spectral response. Fig. 1(b) shows an optimal aperiodic lattice solution for the spectral characteristic shown in Fig. 3. This optimized structure may not necessarily be a globally optimized structure, which is mathematically difficult to obtain unless the entire search space is investigated. However because the number of scattering sites is small (only eight in this case), the possibility of further optimization is limited. The design was carried out using a software program written in MATLAB™. The spectral characteristics shown in Fig. 2 and 3 were carried out using a commercial software package, FIMMPROP-3D, and has been discussed in detail elsewhere [9].
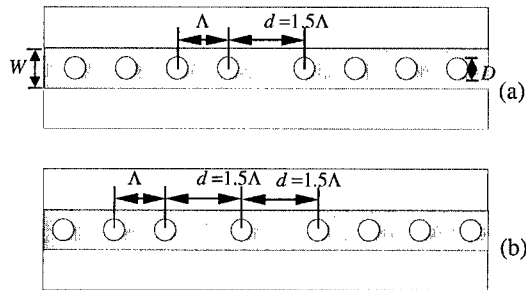
Figure 1. Schematic diagrams of single (a) and double (b) defect one-dimensional photonic lattices.
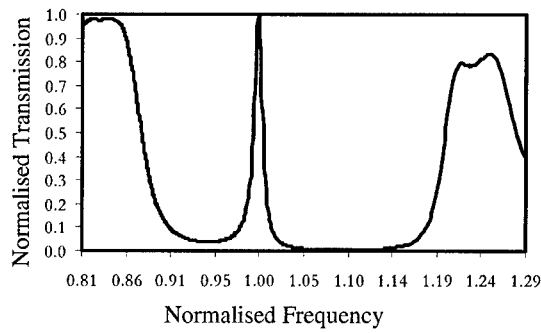
Figure 2. Optical transmission characteristics of the lattice in Fig. 1(a).
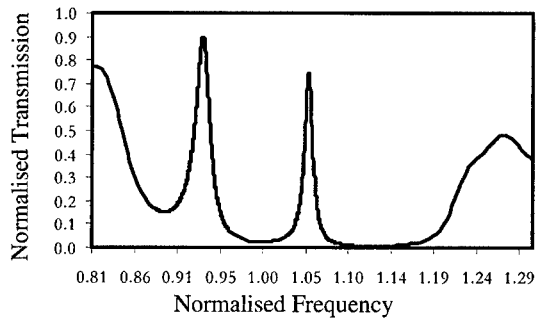
Figure 3. Optical transmission characteristics of the lattice in Fig. 1(b).

FABRICATION

The fabrication techniques used to form the low loss aperiodic waveguides have been discussed elsewhere [10], a brief description follows: Waveguides are made using Unibond silicon-on-insulator (SOI), consisting of a lightly doped single crystal silicon layer of 0.26μm thickness, isolated by a 1μm thick silicon dioxide layer from the undoped silicon substrate. Electron beam lithography is used to pattern a hard mask against reactive ion etching using CF_4:$SiCl_4$ to form the waveguide.

This has been found to produce waveguides with lower roughness than when the resist is used as an etch mask directly. Finally, optical facets were formed at the ends of the waveguide in unthinned SOI substrates using a custom made tool. A schematic drawing of the device and SEM image of the hard mask to form the device are given in Fig. 4.

The cleaved facets at the ends of the waveguide act as mirrors, due to internal reflection at the air-silicon interface, so defining a FP cavity with the length of the waveguide defining the cavity length.

OPTICAL PROBING

The effective index (group index of the guided mode) and the propagation loss around the wavelength of 1550nm have been measured using a Fabry-Perot (FP) resonance technique. In this measurement, light from a tuneable laser source laser source was coupled into the waveguide using a conical-shaped lensed fibre (minimum spot size of ~5 μm and focal length of ~15 μm) and the transmitted light was measured using a power meter.

The intensity of the transmitted light from the optical mode in the waveguide is measured, for a constant power of the input light, in the FP resonance technique, resulting in the transmission spectrum shown in Fig. 5.

$$\Lambda = \frac{\lambda_{BR}}{2n_{eff}}$$

$$d = 1.5\Lambda$$
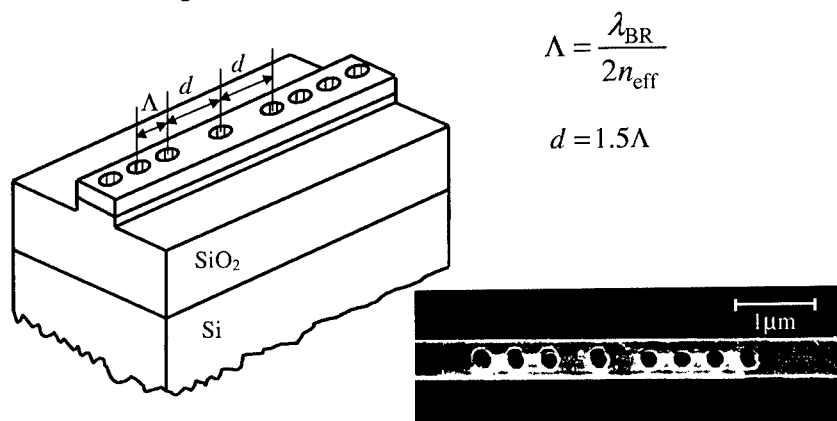
Figure. 4 Schematic drawing of the device and SEM image of the hard mask used to form the device.
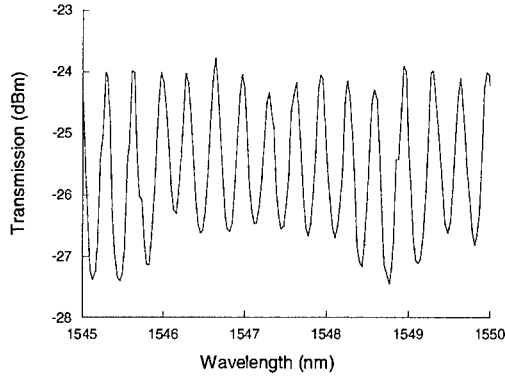
Figure. 5 Transmission spectrum in the passband for a typical device.

If the two facets have identical power reflectivity R, the propagation loss coefficient α is given by [9]

$$\alpha = -\frac{1}{L}\ln\left(\frac{1}{R}\cdot\frac{\sqrt{P_{max}/P_{min}}-1}{\sqrt{P_{max}/P_{min}}+1}\right)$$

where P_{max} and P_{min} are the maximum and minimum power of each resonance respectively. The reflectivity R is given by

$$R = \left(\frac{n_0 - n_{eff}}{n_0 + n_{eff}}\right)^2$$

n_{eff} is the effective refractive index of the waveguide mode, n_0 the refractive index of air, i.e.=1. The effective refractive index can be measured from the FP spectral characteristics using the formula for Free Spectral Range (FSR), which is given by

$$n_{eff} = \frac{\lambda^2}{2L\Delta\lambda}$$

where L is the length of the waveguide, λ is the wavelength and $\Delta\lambda$ is the spacing between neighboring resonance peaks in FP spectral characteristic (FSR). For the aperiodic waveguide described earlier the cavity length L was 1mm and the spacing $\Delta\lambda$ was found to be 0.3nm, so that n_{eff} was ~4. The reflectivity R and the ratio P_{max}/P_{min} were 36% and ~2.5 respectively, so that the average propagation loss α was better than 5 cm^{-1} (or ~20dB/cm).

CONCLUSIONS

A new method, based on the discrete Fourier Transform, for the design of aperiodic lattices, for use in photonic bandgap engineering, has been described. The use of this method has been illustrated by the design of a two-defect structure giving two transmission lines in the stopband.

Devices have been fabricated in silicon-on-insulator and characterised optically. This system is shown to realise structures with very low loss.

ACKNOWLEDGEMENTS

REFERENCES

1. J. S. Foresi, P. R. Villeneuve, J. Ferrera, E. R. Thoen, G. Steinmeyer, S. Fan, J. D. Joannopoulos, L. C. Kimerling, H. I. Smith and E. P. Ippen, *Nature*, **390**, 143, (1997).
2. A. Yariv, Y. Xu, R. K. Lee, and A. Scherer, *Opt. Lett.* **24**, 711, (1999).
3. S. Chakraborty, Aperiodic lattices for photonic bandgap engineering and light localization, *PhD Thesis, Cambridge University*, (2003).
4. B. Gu, B. Dong, Y. Zhang, and G. Yang, *Appl. Phys. Lett.* **75**, 15, 2175, (1999).
5. B. Gu, Y. Zhang, and B. Dong, *J. Appl. Phys.* **87**, 11, 7629, (2000).
6. R. W. Cohn, S. F. Lyuksyutov, K. M. Walsh, and M. M. Crain, *Opt. Rev.* **6**, 4, 345, (1999)
7. K. K. Lee, D. R. Lim, H. Luan, A. Agarwal, J. Foresi and L. C. Kimerling, *Appl. Phys. Lett.* **77**, 1617 (2000).
8. A. Sakai, G. Hara, and T. Baba *Jpn. J. Appl. Phys.* **40**, L383, (2001).
9. D. F. G. Gallagher and T. P. Felici, *Photonics West*, San Jose, (2003) Paper 4987-10.
10. S. Chakraborty, D. G. Hasko and R. J. Mears, Accepted for MNE 2003 issue of Microelectronic Engineering.

Plasmonics

W2.4

Modeling of a Surface Plasmon Polariton Interferometer

Victor Coello[*1], Thomas Søndergaard[2], and Sergey I. Bozhevolnyi[2]
[1]CICESE Monterrey,
P. de Alba S/N Posgrado FCFM-UANL, C. P. 66450 S. N. de los Garza N. L., Mexico.
[2]Micro Managed Photons A/S, Institute of Physics and Nanotechnology, Aalborg University, Pontoppidanstræde 103, DK-9220 Aalborg Øst, Denmark

ABSTRACT

We model the operation of a micro-optical interferometer for surface plasmon polaritons (SPPs) that comprises an SPP beam-splitter formed by equivalent scatterers lined up and equally spaced. The numerical calculations are carried out by using a vector dipolar model for multiple SPP scattering. The SPP beam-splitter is simulated for different angles of the incident SPP beam, radii of the particles, and inter-particle distances in order to find a suitable configuration for realization of a 3dB SPP beam-splitter. The results obtained are in good agreement with experimental data available in the literature. The feasibility of fabricating an interferometer is thereby corroborated and the calculated intensity maps are found rather similar to those experimentally reported.

INTRODUCTION

Surface plasmon polaritons (SPPs) i.e., collective oscillations of surface electron charge density, represent (quasi) two-dimensional waves [1]. Associated with SPPs there exist electromagnetic fields propagating along the (metal-dielectric) interface and exponentially decaying perpendicular to it. Due to their electromagnetic nature, SPPs propagating along the surface can diffract and reflect by surface features and interfere. These properties are clearly exhibited in the course of elastic (in the plane) SPP scattering. Usually, elastic scattering of SPPs and related phenomena [1] have been generated because of randomly situated surface defects. However in the last years, several studies of two-dimensional optics of SPPs based on artificially fabricated micro-components were reported. Thus, first examples of SPP micro-lens, micro-mirrors [2] and SPP band gap structures [3] have been demonstrated. Additionally, SPP propagation along thin metal stripes was performed showing a potential tool for optical addressing purposes at nanometer scales [4]. In general, this new direction of SPP investigations has revealed several features such as wavelength dispersion and stability (with respect to geometric parameters) of the micro-components that have to be elucidated. One could gain more understanding in this context illustrating several configurations (e.g. varying the number of single scatterers, and orientation) of a particular micro-component. This task seems to be more reliable and less time demanding when carried out by means of numerical simulations. The problem is not simple, as even a circularly symmetric surface defect requires elaborated numerical calculations [5] and a complete theory that could deal with the scattering of SPPs by surface roughness has not yet been established. A scalar multiple scattering approach was used for simulation of SPP optical micro-components and photonic band gap structures formed by sets of point scatterers [6]. The micro-scatterers were considered in a two-dimensional geometry as

---

* Corresponding author: e-mail: vcoello@cicese.mx, Phone: +52 81 8478 0507, Fax: +52 81 8478 0508

isotropic point-like scatterers characterized by their effective polarizabilities (related directly to the total scattering cross sections). Despite the apparent success, the model has some limitations, one of them being that the effective polarizability of an individual scatterer is a phenomenological quantity which is difficult to relate to scatterer's parameters (e.g., size, susceptibility, etc). Recently, such an approach has been extended into a vector dipolar multiple-scattering theory and used to calculate SPP scattering produced by band-gap structures [7]. Based on this new approach, here we report the results of numerical simulation of a SPP beam-splitter and interferometer. We investigate in detail the overall *sensitivity* of the SPP beam-splitter to the angle of beam incidence, size (radius) of the particles, and inter-particle distance. Based on the configuration most suitable for realization of a 3dB SPP beam-splitter, the feasibility of fabricating an interferometer was corroborated. The results obtained are in good agreement with experimental data available in the literature [8]. The combination of several SPP optical elements could lead, in principle, to two-dimensional SPP optical circuits with high potential benefits for nanotechnology and nanoscience, e.g., by designing SPP based optical interconnects.

MODEL FOR ELASTIC SCATTERING OF SURFACE POLARITONS

Our modeling is based in the assumption that the elastic SPP scattering is dominant with respect to the inelastic (out of the plane) SPP scattering. Therefore it is possible at least to some extent to avoid the complicated mathematical treatment involved in the problem of SPP scattering by surface inhomogeneities [5]. The assumption lead to the construction of an approximate Green's tensor describing scattering by a dipolar point-like scatterer located on a metal/dielectric interface. The validity of the model has been established for relatively large inter-particle distances, whereas for smaller distances it is more accurate to include multipolar contributions in the scattered field ([7] and references therein). First, the polarization of each nano-particle is obtained by solving the following equation:

$$P_i = \alpha_i \cdot E^0(r_i) + k_0^2 \sum_{n \neq i} \alpha_i \cdot G(r_i, r_n) \cdot P_n, \tag{1}$$

where P_i is the polarization of the particle i, α_i is the polarizability tensor for particle i with the multiple scattering between the particle and the metal surface taken into account (surface dressing effect), E^0 is an incoming electric field, k_0 is the free space wave number, and $G(r_i, r_n)$ is the Green's tensor for the reference structure (total field propagator). The Green's tensor G is the sum of a direct contribution G^d, in this case the free space Green's tensor, and an indirect contribution G^s that describes both reflection from the metal/dielectric interface and excitation of SPPs. The incoming E^0 describes a gaussian SPP field impinging on the arrangement of nanoparticles. The polarizability tensor is given by:

$$\alpha = \left(I - k_0^2 \frac{\alpha^0}{\varepsilon_0} \cdot G^s(r, r) \right)^{-1} \cdot \alpha^0, \tag{2}$$

where I is the unit dyadic tensor and the free space polarizability tensor in the long-wave electrostatic approximation is given by

$$\alpha^0 = \varepsilon_0 I 4\pi a^3 \frac{\varepsilon-1}{\varepsilon-2} , \qquad (3)$$

with ε_0 being the vacuum permittivity, a the radius of the nano-particle, and ε the dielectric constant of the particle. Finally, using the dipole electrostatic approximation for G^S [9], the polarizability tensor is given by the next relation:

$$\alpha \approx \left[I - \frac{\varepsilon-1}{\varepsilon+1}\frac{\varepsilon-1}{\varepsilon+2}\left(\frac{1}{8}\hat{x}\hat{x} + \frac{1}{8}\hat{y}\hat{y} + \frac{1}{4}\hat{z}\hat{z}\right)\right]^{-1} \cdot \alpha^0 \qquad (4)$$

where $\hat{x}, \hat{y}, \hat{z}$ are unit vectors in a cartesian coordinate system with $\hat{z}$ being perpendicular to the air-metal interface.

The polarizations [eq (1)] and the total field,

$$E(r) = E^0(r) + k_0^2 \sum_n G(r, r_n) \cdot P_n , \qquad (5)$$

can be calculated using the appropriate Green's tensor for the reference structure $G(r, r')$. Based on the initial assumptions, it was proposed to use a three-dimensional dyadic Green's tensor approximation which accounts only for the SPP elastic scattering channel. The Green's tensor approximation is expressed in the following form [7] that takes into account the exponential decay of the SPP field away from the interface as well as different angular dependencies of the SPP's excited by different field components i.e.:

$$G^{SPP}(\rho, \phi, z, h) = a_{zz}(\lambda)\exp[i\kappa_z(z+h)]H_0^1(\kappa_\rho\rho)\times\left[\hat{z}\hat{z} + (\hat{z}\hat{\rho} - \hat{\rho}\hat{z})\frac{\kappa_z}{\kappa_\rho} - \hat{\rho}\hat{\rho}\left(\frac{\kappa_z}{\kappa_\rho}\right)^2\right], \qquad (6)$$

where H_0^1 is the zero-order Hankel function of the first kind, $\rho = |r_\| - r'_\||$, $\hat{\rho} = (r_\| - r'_\|)/\rho$, ($\hat{\rho}$ points in the direction specified by the angle ϕ), with $\|$ referring to the projection of the radius vector on the xy plane at the metal air interface ($\rho\phi$ plane for cylindrical coordinates), z is the height of the observation point r above the surface, and h is the height of the observation point r'. Finally,

$$\kappa_\rho = k_0\sqrt{\frac{\varepsilon}{\varepsilon+1}} , \qquad (7)$$

$$\kappa_z = \sqrt{k_0^2 - \kappa_\rho^2} , \qquad (8)$$

are the components of the three dimensional SPP wave vector. The validity domain of the model was determined by calculating the exact Green's tensor components normalized with respect to the radial and height dependencies of the approximate Green's tensor components. Thus, it was established that for large ρ (>10 µm) and small h and z (< 500 nm) that the exact Green's tensor exhibit the same radial and height dependencies as the cylindrical SPP fields. The complete

analysis of the validity of such a domain is beyond the scope of this report and can be found elsewhere [7].

NUMERICAL CALCULATIONS

In order to numerically build step by step an SPP interferometer first, we investigated the in-plane scattered field created with a 5-μm-wide Gaussian SPP beam (λ=750nm) of a unit amplitude impinging on an equally spaced line of scatterers which acts as a beam-splitter. Using the calculation area of 50x50 μm^2 and considering a line of equivalent scatterers forming an SPP beam-splitter, we elucidated the density, inter-particle distance, and particle radius to realize the most suitable configuration for a 3dB SPP beam-splitter. For example, the inter-particle distances were investigated in the range from 200 to 400 nm with 10 nm step. Additionally, several angles θ_0 of SPP beam incidence with respect to the normal to the nano-particles' line were considered. Thus, it came out that, for a line of 200 scatterers with distance between the nano-particles of 280nm and with particle radius of 64 nm, a nearly 50/50 beam-splitter is conceivable [Fig. 1(a,b)]. The angle of incidence was set at $\theta_0 = 16^0$. Note that these values match well to the experimentally reported ones [8] including equivalence in volume of the experimental cylindrical scatterer and the calculated spherical particle in our case. In our simulations, the incident SPP propagates from left to right and the dielectric constant used was ε=-23.11+1.4i which corresponds to gold at 750nm.

The SPP interferometer has been completed by adding a second beam impinging at the incident angle of -θ_0 (Fig. 2). The numerical simulations showed that the two output beams, which result from the interaction of the incident beams with the beam-splitter, vary as a function of the introduced phase shift φ in the incident beams switching from one side to another of the beam-splitter. When the values of φ are $\pi/2$ and $3\pi/2$, the SPP intensity exhibits a maximum and a minimum in the outputs of the beam-splitter [cf. Figs. 2(b) and 2(d)]. This fact suggests


(a)	(b)
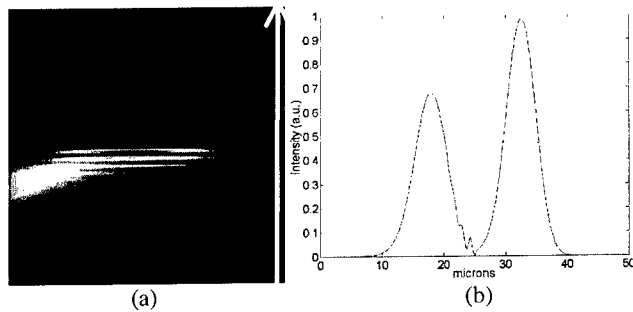
Figure 1. Pseudo-color scale representations of the total field intensity distributions in the area of 50x50 μm^2 calculated for a SPP beamsplitter composed of 200 nanoparticles with radius of 64 nm and for the wavelength of light: λ = 750 nm. The angle of the incident field set at 16^0 with regard to the normal of the beamsplitter (a). The white arrow in (a) indicates the cross section shown in (b).
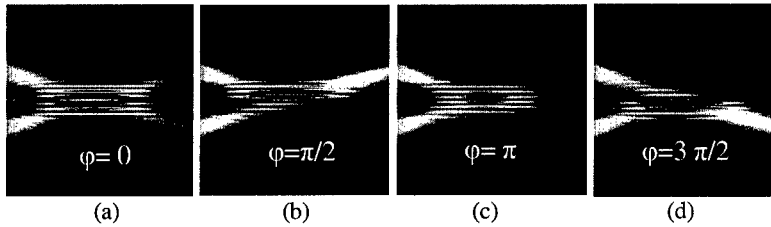
Figure 2. Pseudo-color scale representations of the total field intensity distributions in the area of 50×50 μm² calculated for a SPP interferometer. The SPP maps has been calculated for relative phase shifts between the incident fields of φ=0 a), φ=π/2 b), φ=π c), and φ=3π/2 rad. d). All else is as in Figure 1.

that after passing via the beam-splitter there exist a phase shift of π between the transmitted and reflected SPP as one would also expect to occur in a conventional interferometer. This conjecture has been verified further by directly superimposing an incident SPP beam at $-\theta_0$ on the single incident SPP field which produces the reflected and transmitted beam in the beam-splitter [e.g. Fig. 1(a)]. An adjustable phase shift between these two superimposed beams was introduced allowing us to determine the phase shift resulting in the minimum SPP field in the reflected direction. These simulations showed that the relative phase difference between the reflected and transmitted beams in a beam-splitter corresponds to ~π rad. Note that the SPP intensity distributions simulated in Figs. 2 (b) and 2(d) very closely resemble the experimental images of an SPP interferometer reported in the literature [8]. The switching in the relative intensities values of the two output beams of the SPP interferometer as a function of the phase shift between the incident beams is clearly seen in Figure 3, where the intensities levels were calculated by considering cross sections of the beams similar to that of the Figure 1.
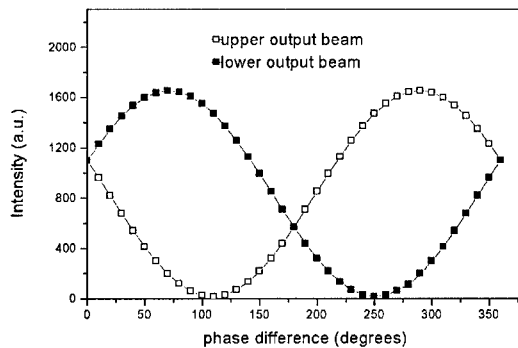
Figure 3. Switching in intensity level of the output beams of the SPP interferometer as a function of the phase shift between the incident beams. The introduced phase shift was calculated for values from 0-2π with the step of π/10 rad.

CONCLUSIONS

We have modeled the SPP scattering by an SPP interferometer by making use of a vectorial model for multiple scattering by surface nanoparticles via surface polariton-to-polariton interactions. The interferometer is based on a 3dB SPP beam-.splitter built of a line of 200 equivalent scatterers with inter-particle distance of 280nm and radius of 64 nm. The SPP intensity distributions for the interferometer exhibited switching of the intensity values of the output beams from one side to another as a function of an introduced phase shift. This effect is in agreement with the reported experimental images [8], and the simulated intensity distributions were found to resemble rather well the experimental images obtained with the line of particles whose parameters were also rather similar to those used in our simulations. We believe that the present investigation suggests a way for further progress in two-dimensional SPP micro-optics by complementing experimental investigations with numerical simulations.

REFERENCES

1. H. Raether, *Surface Plasmons*, Springer Tracts in Modern Physics Vol. 111.

2. I. I. Smolanyinov, D. L. Mazzoni, and C. C. Davis, Phys. Rev. Lett.**77**, 3877 (1996). S. I. Bozhevolnyi and F. A. Pudonin, Phys. Rev. Lett. **78**, 2823 (1997). S. I. Bozhevolnyi and V. Coello, Phys. Rev. B. **58,** 10899 (1998).

3. S. I. Bozhevolnyi, J.E. Erland, K. Leossson, P. M. W. Skovgaard, and J. M. Hvam. Phys. Rev. Lett. **86**, 3008 (2001). S. Bozhevolnyi, V. Volkov, and K. Leosson, Opt. Commun. **196**, 41 (2001).

4. B. Lamprecht, J. R. Krenn, G. Schider, H. Ditlbacher, M. Salemo, N, Felidj, A. Leitner, F. R. Aussenegg, and J.C. Weeber App. Phys. Lett. **79,** 51 (2001).

5. A. V. Shchegrov, I. V. Novikov, and A. A. Maradudin, Phys. Rev. Lett. **78**, 4269 (1997).

6. S. I. Bozhevolnyi and V. Coello, Phys. Rev. B **58**, 10 899 (1998). S. I. Bozhevolnyi and V. Volkov, Opt. Commun. **198**, 241 (2001).

7. T. Søndergaard and S. I. Bozhevolnyi, Phys. Rev. B. **67**, 165405 (2003).

8. H. Dittlbacher, J.R. Krenn, G. Shider, A. Leitner, and F.R. Aussenegg. Appl. Phys. Lett. **81** 1762 (2002).

9. O. Keller, M. Xiao, and S. Bozhevolnyi, Surf. Sci. **280**, 217 (1993). Z. Li, B. Gu, and G. Yang, Phys. Rev. B **55**, 10883 (1997). P. Gay-Balmaz and O. Martin, Opt. Commun. **184**, 37 (2000).

Subwavelength Structured Optical Elements and Resonant Grating Filters

Hisao Kikuta and Koichi Iwata
College of Engineering, Osaka Prefecture University,
1-1 Gakuen-cho, Sakai, Osaka, 599-8531, Japan
Akio Mizutani, Hiroshi Toyota and Wanji Yu
Osaka Science and Technology Center,
2-7-1, Ayumino, Izumi, Osaka, 594-1157, Japan

ABSTRACT

We developed several optical elements with subwavelength-structured surfaces. Antireflection surfaces were fabricated on a diffraction grating. A micro-retarder array realized by the form-birefringent effect has been made for an application to a polarization camera system. And we developed narrow-band reflection wavelength filters called "guided-mode resonant grating filters". This filter bases on a coupling of guided mode and radiation mode. After describing some examples of the filters, we mention a grating structure for an optical switch with nonlinear optical material.

INTRODUCTION

Subwavelength structured (SWS) surfaces are attractive for new optical elements. The subwavelength structure has the optical features of artificial refractive index, form birefringence, and resonance effects. Since the grating period is shorter than light wavelength, an incident light wave passes through the grating structure without diffraction. The structure can be regarded as a substance with effective refractive index. The effective refractive index can be controlled by the filling factor of the structure, and the effective index is called the "artificial refractive index" [1]. When a shape of lattice point is asymmetric, the effective refractive index will be anisotropic. This effect is known as the "form birefringent" [2]. Moreover, when the grating period is in the same order of light wavelength, the transmittance and reflectance are sensitive to the wavelength and incident angle because of the resonance of light waves in the structure. This optical feature is called the "anomaly" in the field of diffractive optics [3].

Figure 1 shows examples of the SWS elements in the passive element regime. Since the effective refractive index can be controlled by the filling factor, the efficient diffractive optical elements can be realized by the binary grating structure [4]. When the grating structure is a micro-cone array, it acts as antireflection surface [5]. The light reflection is reduced by the gradual change of effective refractive indices from the air to the substrate. Such the low reflectance effect is valid for broad spectral bandwidths and a wide angle of incidence. The antireflection-structured surfaces are useful to applications not only to a display panel but also to Solar cell and infrared optics [6].

Form birefringent elements are also useful. A simple line-and-space grating structure acts as a birefringent phase retarder [7]. And polarization beam splitters and polarization computer generated holograms have been demonstrated [8,9]. We have fabricated a micro-retarder array for imaging polarimetry [10].

Some SWS elements operating in the resonance domain have been developed. The guided-mode resonant grating filter is a narrow-band reflection filter [11,12]. The filter having
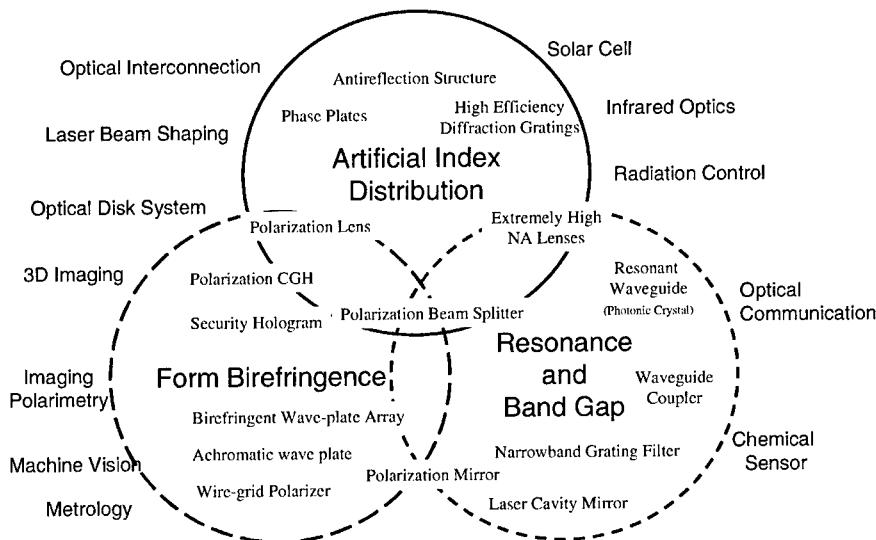
Figure 1. Passive optical elements with subwavelength structured surfaces and applications.

over 90% reflectance with a few nanometer full-width-at-half-maximum (FWHM) has been fabricated [13]. This filter can be used as a wavelength selective mirror and a polarization selective mirror.

In this paper, after introducing some SWS elements we developed [14], a guided-mode resonant grating filter operating in a finite small area has been demonstrated. And we describe a study on an optical switch based on the grating filter by numerical simulation. When the wave-guide material is optically nonlinear, the transmittance of the grating filter can be controlled by other light waves.

SWS ELEMENTS

We fabricated antireflective structured (ARS) surfaces on a fused silica substrate [15]. To obtain a high aspect structure, a micro-disk array of chromium thin film was used as an etching mask for a high-density plasma. Because the Cr disks are etched not only from the top surface but also from the disk edges, the resultant surface profile becomes a micro-cone array with a smooth taper. Figure 2 (a) shows the fabricated ARS surface with a 250nm period and 750nm heights. The measured reflectance was less than 0.5% at wavelengths from 400 to 800 nm. Figure 2 (b) is the ARS on a diffraction grating. In this example, the structure height is reduced to be equal to the period for easy replication with the injection molding.

Figure 3 is the form-birefringent quarter-wave plate, which is less sensitive to the wavelength [16]. When the grating period is in the same order of the light wavelength, the form birefringent depends on the wavelength very much. Especially for the filling factor close to unity, i.e., narrow grating grooves, the phase retardance will be less sensitive to the change of light wavelength [17]. In this example, the narrow groove structure was realized by sputtering ZTO
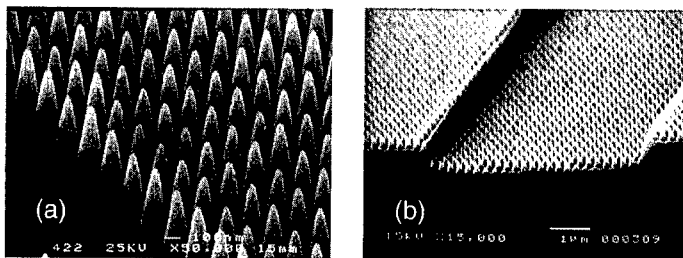
Figure 2. Antireflection structured surfaces on a flat silica surface (a) and a diffraction grating (b). The structure on the flat surface has a period of 250nm and cone height of 750nm (aspect ratio: 3). The structure of the diffraction grating has an aspect ratio of 1.
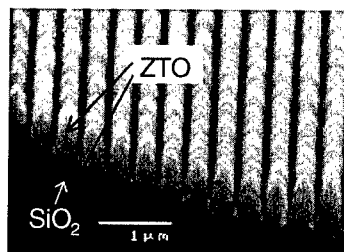

Figure 3. Form birefringent quarter wave plate consisting of a high refractive-index thin film sputtered on the silica subwavelength grating

(Zn_2SnO_4, n=2.03) on a silica grating substrate. The silica grating has a period of 340nm and grating height of 500nm. The phase retardance was 85° at 633nm wavelength. The dependency of phase retardance on wavelength was reduced to the half of the dependency of a conventional zero-order quarter-wave plate. When TiO_2, Ta_3O_5 and HfO_2 thin films were sputtered on the grating substrates, high aspect structures could not be obtained. The sputtered ZTO thin film was amorphous, and the other thin films were crystallized. We suspect that the amorphous feature contributes to forming the high aspect structure.

A real-time imaging polarimetry will be useful to many applications such as machine vision, polarization interferometers, retina cameras, remote sensing. We fabricated an array of micro wave-plates for the imaging polarimetry [10]. The system configuration of the imaging polarimetry is shown in Fig.4. The phase retarder array consists of 652×494 subwavelength gratings. The retarder array and a polarizer thin film are put on the black-and-white CCD image sensor with careful alignment. The minimum unit to determine a polarization state is composed of 2×2 wave-plates with different orientations of grating grooves. From outputs of the 2×2 pixels, the polarization state can be determined completely including the unpolarized component.

Each micro wave-plate is 7.4mm×7.4mm, which is equal to a pixel size of the CCD image sensor. The micro wave-plate is a deep-groove grating of fused-silica glass. Figure 5 shows a
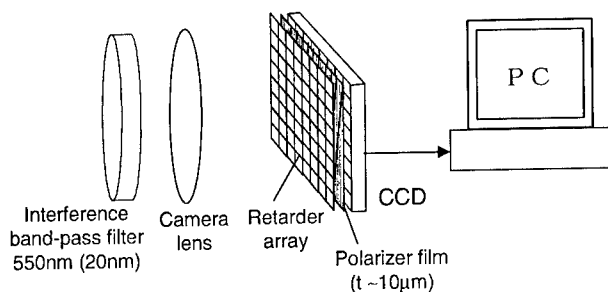
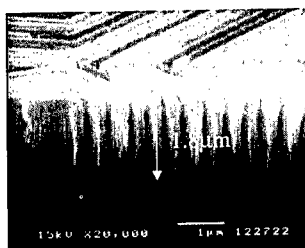Figure 4. System configuration of the imaging polarimetry with a micro-retarder array.

Figure 5. Cross-section of the fabricated form-birefringent micro-retarder array of fused silica grass. The grating period is 0.3μm. Each micro-retarder is a square of 7.4μm×7.4μm.

cross section of the fabricated grating structure. The grating period is 300nm, and the groove depth is 1.8μm. The phase retardation was ~90° for 550nm wavelength light. We succeeded in obtaining polarization images without any mechanical system.

GUIDED-MODE RESONANT-GRATING FILTERS

The guided-mode resonant grating filter is a narrow-band reflection filter based on the resonance effect of light waves in the grating structure [11,12]. This filter is a kind of input/output grating couplers. The filter consists of diffraction grating on wave-guide. A periodically index-modulated slab wave-guide also acts as the resonant grating filter. Figure 6 (a) shows the principle of the resonant reflection. The modulation period is shorter than the light wavelength, but diffracted light waves are generated in the wave-guide because of a high refractive index of the wave-guide. When the diffracted light wave has a wave-number equal to a propagation constant of the wave-guide, the diffracted light wave propagates in it and is diffracted again due to the grating structure. In this condition the incident light wave is reflected by the wave-guide grating. On the other hand, when the wave number of the diffracted light wave is not equal to the propagation constant of the wave-guide, the light wave cannot enter it and passes through the grating wave-guide. Such the resonant reflection occurs in a limited condition of wavelength and angle of incidence, so that the grating wave-guide acts as the narrow-band wavelength selective mirror. The peak reflectance is 100% theoretically, and 98% reflectance with a few nanometers FWHM were achieved experimentally [13].
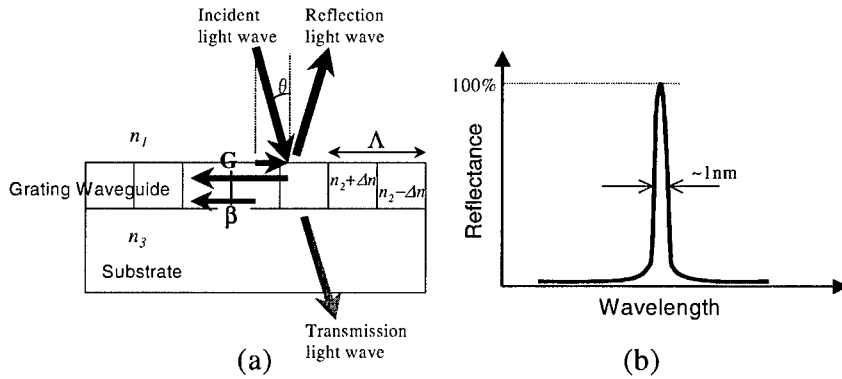
Figure 6. Principle of the guided-mode resonant grating filter (a) and a typical reflectance with respect to wavelength (b).
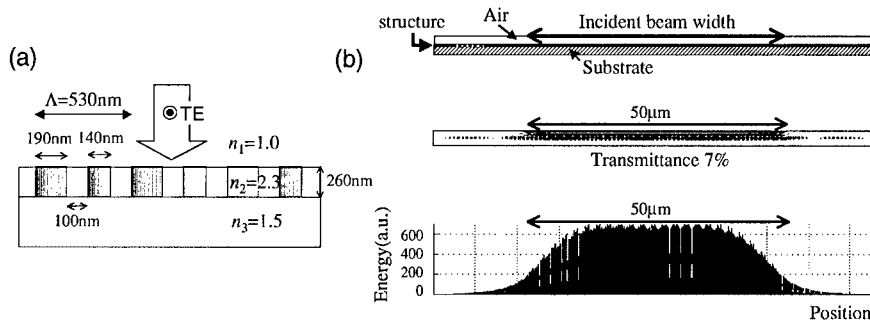

Figure 7. A resonant grating filter with a large second harmonic component (a), and a simulation result of wave localization in the wave-guide layer (b). The incident light beam has a width of 50μm. The bottom figure shows the field energy distribution in the wave-guide layer.

A non-polarization grating filter for oblique incidence and a low-sideband grating filter with ARS surface had been proposed. The non-polarization grating filter was realized by a two-dimensional rhombic lattice structure [18]. The low sideband filter consists of a high-index film deposited on the ARS surface [19]. The ARS effect suppresses the reflection of non-resonant light waves in broad spectral bandwidth.

We fabricated a narrow-band grating filters operating in a finite small area. For a conventional configuration of the guided-mode resonant grating filter, the mean propagation length in the wave-guide is inversely proportional to the FWAM. Then large widths of grating and incident beam are needed to obtain the narrow-band feature. The filter operation in a small area can be realized by a grating structure with a large second-harmonic component. The original idea has
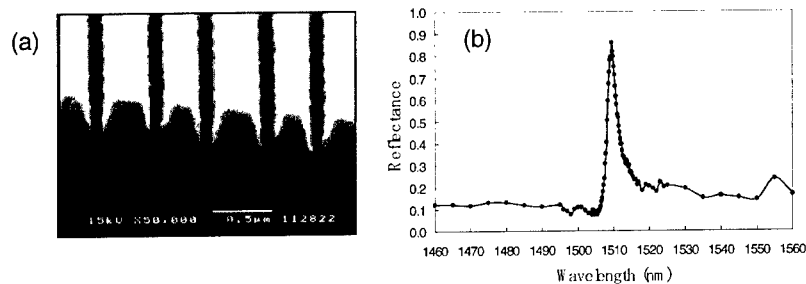
Figure 8. The fabricated resonant grating filter with a large second harmonic component for 1.5μm wavelength. (a) A Cross section of the grating structure. The grating is Si₃N₄, and the substrate is fused silica grass. (b) Measured spectral reflectance.

been proposed by F. Lemarchand et al [20]. They studied theoretically on the principle of the wave confinement in the small area. The proposed grating structure consists of a diffraction grating on a short period and deep index-modulated wave-guide layer. The short period index-modulation acts as a Bragg reflector, so that the light waves do not propagate far away in the wave-guide and they are confined in small area.

In order to confirm the confinement of the light wave in small area experimentally, we redesigned a grating structure with a large second-harmonic component for easy fabrication. Figure 7 (a) shows the grating structure we designed for a resonant wavelength of ~1μm. This structure consists of only one grating layer. The refractive index changes two times in a grating period $\Lambda=530nm$. The high index layers have widths of 190nm and 140nm. The dominant spatial spectrum is the second harmonic $2/\Lambda$, not the base spectrum $1/\Lambda$. A small component of the base spectrum relates to the FWHM directly, and the large component of $2/\Lambda$ contributes to the confinement of the light wave in small area. The calculated resonant wavelength and FWHM are 1014.2nm and 1.7nm, respectively, for the normally incident TE polarized. The Q factor is ~600. The expected angular tolerance of the incident light beam was 3.6°, which is about ten times as wide as that of a conventional grating filter with the same FWHM.

Figure 7 (b) shows an example of a numerical simulation for a finite incident beam. The incident beam is 50μm in width. The middle figure shows the electric filed distribution calculated with the finite differential time domain (FDTD) method. The light waves are well confined in the small area, and the reflectance is higher than 90%. The bottom figure shows the field energy distribution in the wave-guide. The maximum energy normalized by the incident field is almost the same as the Q factor.

The fabricated grating filter is shown in Figure 8 (a). For experiments at 1.5μm wavelength the dimensions are 50% large compared with those of Figure 7 (a). The structure consists of Si₃N₄ grating on a fused silica substrate. The grating grooves are tapered to the bottoms. Measured spectrum reflectance is shown in Figure 8 (b). The resonant frequency was 1509nm, and the FWHM was 3nm. The resonant peak reflectance was higher than 85%. The measured angler tolerance was 2°, which corresponds to the mean propagation length of 14μm.
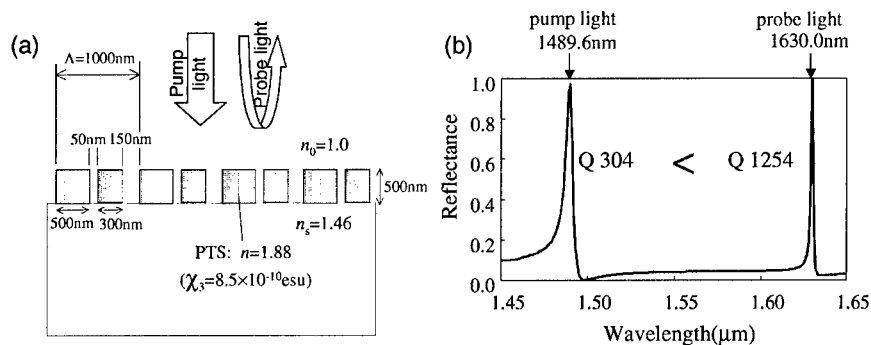
Figure 9. An asymmetric grating wave-guide for a nonlinear optical switch. (a) An asymmetric grating structure with the large second harmonic component. The grating material has third-order susceptibility. (b) Spectral reflectance of the asymmetric grating wave-guide for TE polarized light. There are two resonant peaks with different FWHMs.
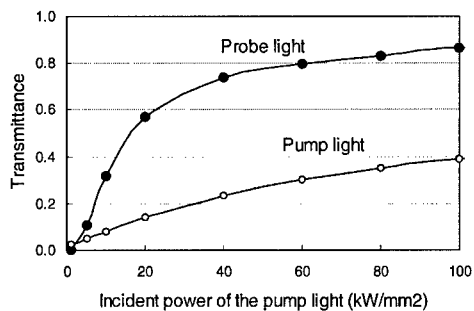

Figure 10. Transmittance of the probe light and pump light with respect to the incident power of the pump light.

A GRATING FILTER WITH NONLINEAR OPTICAL MATERIAL

The guided-mode resonant grating filter with nonlinear optical material will be an optical switch. Especially the grating filter with the large second-harmonic component is valid, because a pump laser beam can be focused on the small area. This section describes a grating configuration of the optical switch based on the grating wave-guide with the nonlinear material.

Figure 9 (a) shows an asymmetric grating wave-guide for the optical switch. This structure has a large second-harmonic component of grating structure to occur the resonant reflection in the finite small area. We suppose the Kerr effect in the grating wave-guide. The grating material has the refractive index of 1.8 and the third-order susceptibility χ_3 of 8.5×10^{-10} esu. Figure 9 (b) shows a calculated spectral reflectance of TE polarized light in the linear regime. The reflection curve has two resonant peaks at 1489.6nm and 1630.0nm wavelengths. These correspond to the

lower and upper band-edges of the grating wave-guide. The Q factors are 304 and 1254, respectively.

The one of the resonant peaks is used for the pump light and the other peak is for the probe (signal) light. The probe light is reflected by the grating for no pump light. When the intense pump light is incident on the grating, the refractive index of grating is changed by the Kerr effect and the grating wave-guide transmits the probe light. In this example, we set the pump light of 1489.6nm wavelength and the probe light of 1630nm wavelength, because the Q factor of 1630nm wavelength is narrower than that of 1489.6nm wavelength. The high Q factor, i.e. a narrow-bandwidth, realizes the high sensitivity of the transmittance to the refractive index change.

It is noted that the pump light also resonates in the grating wave-guide and its field energy increases very much. According to the result of Fig. 7 (b), it is expected that the field energy is Q times as much as that of the incidence. Then the refractive-index change will be increased by the resonance of the pump light. However, if the Q factor of the pump light is too high, the electric field will not be accumulated, because the intense pump light shifts the resonant wavelength of itself. Q factors of both the resonant peaks can be controlled by a degree of the asymmetry.

Figure 10 shows a simulation result of the reflectance of probe light as a function of the incident power of pump light. The transmittances were calculated with the non-linear FDTD method. The transmittance is over 80% at the incident pump power of 60kW/mm^2. This value corresponds to the incident power of 150W in case of the effective grating area of 50μm×50μm. At the incident power of 60kW/mm^2 the transmittance of the pump light is 30%. This result means that the pump light is not accumulated much in the grating wave-guide because the pump light changes the resonant wavelength of itself.

CONCLUSIONS

Optical elements with the subwavelength structred surface were described. The development of ARS is in the stage of product commercialization. The real-time polarization imaging system with the micro-retarder array will be used for many applications such as as machine vision and remote sensing.

The guided-mode resonant grating filter is attractive as a narrow-band wavelength filter and a polarization mirror. We designed and fabricated the grating filter operating in the finite small area. A study on the optical switch based on the nonlinear grating filter has been made by numerical simulations. The asymmetric grating wave-guide with the Kerr effect has been proposed for the optical switch. Two resonant peaks were used for the pump light and probe light. The transmittance of the probe light was controlled by the input power of pump light.

ACKNOWLEDGMENTS

REFERENCES

1. E. B. Grann, M. G. Moharam, and D. A. Pommet, *J. Opt. Soc. Am. A*, **11**, 2695 (1994).
2. A. Yariv and P Yhe, Chap.6 in *Optical Waves in Crystals* (John Wiley & Sons, New York, 1984).
3. R. Petit, Electromagnetic Theory of Gratings (Springer-Verlag, Berlin, 1980).
4. M. W. Farn, *Appl. Opt.* **31**, 4453 (1992).
5. S. J. Wilson and M. C. Hutley, *Optica Acta*, **29**, 993 (1982).
6. D. Raguin, M. Morris, *Opt. & Photon. News*, **3**, 33 (1995).
7. D. C. Flanders, *Appl. Phys. Lett.*, **42**, 492 (1983).
8. F. Xu, R. Tyan, P. Sun, Y. Fainman, C. Cheng, and A. Scherer, *Opt. Lett.*, **21**, 1513 (1996).
9. W. Yu, T. Konishi, T. Hamamoto, H. Toyota, T. Yotsuya, and Y. Ichioka, *Appl. Opt.* **41**, 96 (2002).
10. H. Kikuta, K. Mumata, M. Muto, et al, Technical Digest of OSA Annual Meeting 2003, ThRR3.
11. L. Mashev and E. Popov, *Opt. Commun.* **55**, 377 (1985).
12. S. S. Wang and R. Magnusson, *Appl. Opt.* **32**, 2606 (1993).
13. Z. S. Liu, S. Tibuleac, D. Shin, P. P. Young, and R. Magnusson, *Opt. Lett.* **23**, 1556 (1998).
14. H. Kikuta, H. Toyota, and W. Yu, *Optical Review*, **10**, 63 (2003).
15. H. Toyota, K. Takahara, M. Okano, T. Yotsuya and H. Kikuta, *Jpn. J. Appl. Phys.* **40**, L747 (2001).
16. W. Yu, H. Kikuta, T. Konishi, *Jpn. J. Appl. Phys.* (submitted).
17. H. Kikuta, Y. Ohira, H. Kubo and K. Iwata, *J. Opt. Soc. Am. A*, **15**, 1577 (1998).
18. A. Mizutani, K. Nakajima, H. Kikuta and K. Iwata, *J. Opt. Soc. Am. A*, **18**, 1261 (2001).
19. A. Mizutani, H. Kikuta, K. Iwata, H. Toyota, *J. Opt. Soc. Am. A*, **19**, 1346 (2002).
20. F. Lemarchand, S. Sentenac, and H. Giovannni, *Opt. Lett.*, **23**, 1149 (1998).
21. A. Mizutani, H. Kikuta and K. Iwata, *Optical Review*, **10**, 13 (2003).

Hexagonal Lattice Photonic Crystal in Active Metallic Microcavity

H. L. Tam[a], R. Huber[b], K. F. Li[a], W. H. Wong[c], Y. B. Pun[c], S. K. So[a], J. B. Xia[a] and K. W. Cheah[a,#]

[a]Department of Physics, Hong Kong Baptist University, Hong Kong SAR, PRC
[b]Physik-Department E11, TU München James-Franck-Strasse, 85748 Garching, Germany
[c]Department of Electronic Engineering, City University of Hong Kong, Hong Kong SAR, PRC

ABSTRACT

A hexagonal lattice photonic crystal was fabricated inside the metallic microcavity. And a thin film of Alq_3 was incorporated inside the textured cavity as an active medium. The microcavity is designed such that the modified photonic modes due to the textured structure can couple to the excited electronic states of Alq_3. This leads to changes in the emission characteristics of Alq_3. From the angle-resolved transmission (ARTR) results, the photonic bandgap was observed at all angles from normal incident to 60°. The presence of surface plasmon (SP) was observed in both TM and TE modes of the transmission. Compare to the bulk Alq_3 photoluminescence spectrum, significant modification of the photoluminescence (PL) spectrum was observed in the angle-resolved photoluminescence (ARPL). The photoluminescence spectra showed clear suppression in luminescence intensity for the range inside the photonic bandgap. We use decouple approximation for the standing wave modes and derive the photonic waveguide characteristics for two-dimensional textured metallic microcavities. The theoretical result is in good agreement to the experimental result.

INTRODUCTION

Planar microcavity structures are commonly used for controlling the spectral, spatial and lifetime characteristics of light emission from optical devices [1-6]. For most microcavities, highly reflecting dielectric stacks are used as mirrors, however, metallic mirror is equally suitable due to that it maintains relatively high reflection and almost independently of the incident angle. In addition it has short penetration depth and can simultaneously serve as the conductive electrodes [4, 7-9].

The modification of the photonic density of states may be significantly enhanced when a periodic corrugation is introduced to one of the cavity mirrors [9, 10]. Such lateral texturing can reduces energy flux getting into lossy waveguide modes [6]. Recently, Salt et al. [11] have demonstrated that Bragg scattering can provide flat photonic band edges and large continuous photonic band gaps in metallic microcavities with square like periodic texturing in two dimensions. It was pointed out that a hexagonal lattice structure would perform even better in terms of flat photonic bands and large bandgaps [9]. In this work, we fabricated a hexagonal

#: To whom all correspondence should be addressed to

textured metallic microcavity with an optically active dielectric medium, tris(8-quinolinolate) Aluminum (Alq_3). It is an organic semiconductor with well characterizes optical property. Alq_3 has a strong but broad luminescence spectrum centered at 530 nm with FWHM about 100nm [12]. It is expected that the coupling of its excited electronic state with the modified microcavity photonic modes will change its optical characteristics.

EXPERIMENTAL PROCEDURE

Sample fabrication processes starts with a glass substrate with 40nm silver layer deposit on its top by evaporation. Then a hexagonal periodic pattern of photo-resist with 750nm periodicity which was achieved by electron beam lithography was deposited on the silver layer. Next the active medium (Alq_3) was deposited onto the patterned photo-resist followed by another 40nm silver layer. A schematic diagram of the sample structure is shown in Fig.1.

(a)

(b)
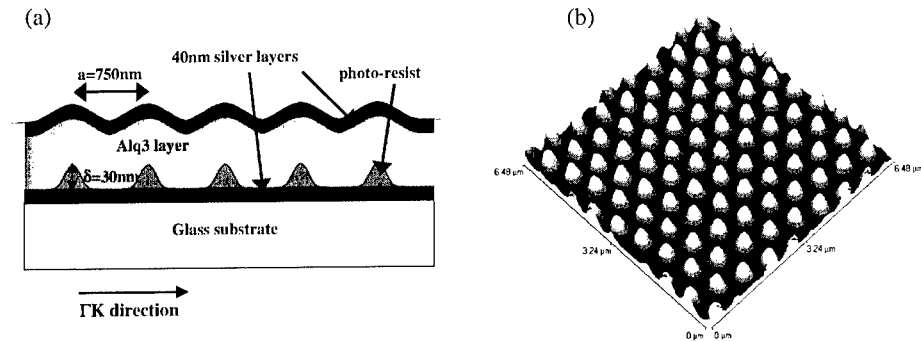
Figure 1. a) Cross-section diagram of the textured metallic microcavity sample. b) The AFM image of the surface profile of hexagonal patterned photo-resist layer

Since high transmittance occurs whenever the incident photon matches the photonic mode inside the cavity, ARTR measurement was performed. Samples were placed on a rotational stage such that transmittance at different wavelengths and in-plane wavevectors can be scanned by varying the incident angles and wavelengths.

To see how the luminescent material changes its emission properties after placing it in a microcavity, we take the ARPL measurement. The incident laser, He-Cd (325 nm), is guided by the optical fiber and focus on the sample by the convergent lens. The incident angle is fixed and the PL was detected by the PMT and monochromator system at different emission angles.

RESULTS AND DISCUSSIONS

From the ARTR results, we can see clearly the photonic mode structure of the planar microcavity (Fig.2a) and textured microcavity (Fig.2b and c). The whiter in colour represents higher transmittance in the grey scaled colour-mapped figure. For planar microcavity, the continuous guiding mode can be clearly seen. And for textured microcavity, bandgap opened up at Brillouin zone edge along the in-plane wavevector k_x (defined as $\frac{1}{\lambda}\sin\theta$ where θ is the incident angle) at about 0.75µm^{-1} (ΓM) and 0.9µm^{-1} (ΓK) which matched with the derived value 0.77µm^{-1} ($\frac{2\pi}{0.75}\frac{1}{2}\frac{2}{\sqrt{3}}\frac{1}{2\pi}$) and 0.8889 µm^{-1} ($\frac{2}{\sqrt{3}}\frac{1}{\sqrt{3}}\frac{1}{0.75}$) for ΓM and ΓK directions respectively for the corrugation periodicity 750nm. The bandgap width for TM mode (~12nm) was narrower than that of TE mode (~20nm). Their bandgap overlaps at 630nm.

A theoretical model is used to support the experimental result. Treating the metal as an ideal conductor, the tangential component of the electric field and the normal component of the magnetic field should be zero at the metal-dielectric interface. Considering that in the microcavity there is only one dielectric medium, i.e. ε(r) is a constant over the whole region.

We consider the textured case as shown in Fig.1, with one planar mirror and the other corrugated. Light is incident in the x-z plane, and propagates in the x direction in the microcavity. The TE modes can be described by

$$E(r) = f(x,y)\sin(\frac{m\pi z}{d}) \tag{1}$$

where f(x,y) and d(x,y) are periodic functions of x and y, m is an integer. The electric field of equation (1) satisfies the boundary condition at the metallic surface and can be simplified to

$$-\nabla^2 E(r) = (\frac{\omega}{c})^2 \varepsilon E(r) \tag{2}$$

For the 2D triangular photonic structure, we approximate it as triangular array texture in the model and can be taken as parabolic corrugation. The parabolic corrugation can be defined below:

$$d = \begin{cases} d_0, & |x| > r_0 \\ d_0 + \delta[1-(\frac{x}{r_0})^2], & |x| \le r_0 \end{cases} \tag{3}$$

Inserting equation (1) into equation (2), and using the decouple approximation, we obtain

$$-\frac{\partial^2 f}{\partial x^2} - \frac{\partial^2 f}{\partial y^2} + (\frac{m\pi}{d(x,y)})^2 f = (\frac{\omega}{c})^2 \varepsilon f \qquad (4)$$

The periodic function f(x,y) can be expanded by plane waves

$$f(x,y) = \sum_G C(G)e^{i(k+G)\cdot\rho} \qquad (5)$$

where G is the reciprocal vector and ρ is the displacement.

The Fourier expansion coefficients in two-dimensional case in the secular equation is,

$$\sum_{G'}(k+G)^2 \delta_{G'G} + \pi^2 d^{-2}(G-G')]C(G') = (\frac{\omega}{c})^2 \varepsilon C(G) \qquad (6)$$

By solving the secular equation, the dispersion relationship was obtained. Taking the parameters for triangular array $r_0/a = 0.5$ and $\delta/d_0 = 0.174$, which is fitted quite well with the parameters obtained from the Atomic Force Microscopy, the theoretical calculation is plotted as solid line in Fig.2b&c. And it agrees with the experimental results.

From the ARPL results for planar microcavity sample (Fig.3a), we can see that the PL peak wavelength blue shift with increasing emission angle. And this shift agrees with the ARTR results (Fig.2a), i.e. the photonic states inside the planar microcavity. Compare with the planar microcavity, the blue shift of peak wavelength in the textured microcavity sample is less at small angles (Fig.3b&c). However, we can see the spectrum for the textured sample is broader than the planar case. This could be due to structural homogeneity or inter-mode interference arose from the presence of several photonic modes inside the microcavity. From Fig.3b&c, we can see that the luminescent properties of the Alq_3 mainly controlled by the cavity photonic mode, and it agree well with the results in Fig.2b&c. We can also see that the spectrum for the textured sample has a dip at where the photonic of bandgap is, reflecting the inhibitation of the spontaneous emission for the Alq_3 in the bandgap energy (Fig.4). The periodic corrugation also enables the coupling of the photon and the surface plasmon at different metal/dielectric interface inside the metallic microcavity by Bragg scattering. The simulated curves shown in Fig.3b&c are the dispersion curve for the photon can couple with the corresponding SP. The silver/air interface SP coupling enhanced the transmittance of the corrugated silver mirror, and thus higher PL intensity are observed at the specific emission angle and wavelength which is dictated by the SP dispersion curve. The simulation for the SP modes at different interfaces is based on the scatter matrix method for the planar microcavity. We traced the dip of the TM mode reflection minimum in the prism coupling structure for the planar microcavity and thus find the SP dispersion. According to different orders in Bragg scattering, we got the dispersion curve shown in Fig3b&c and the theoretical and experimental results are in good agreement.
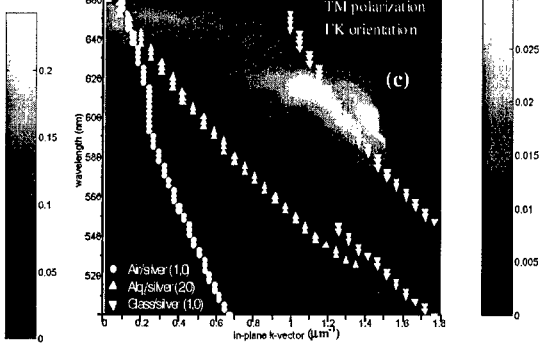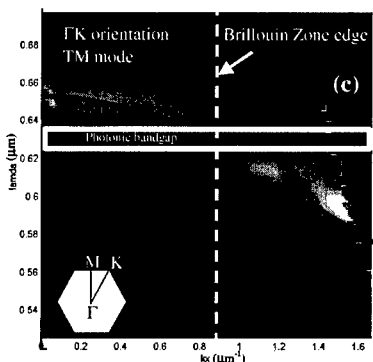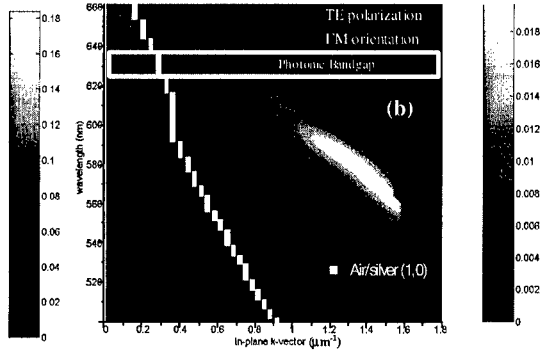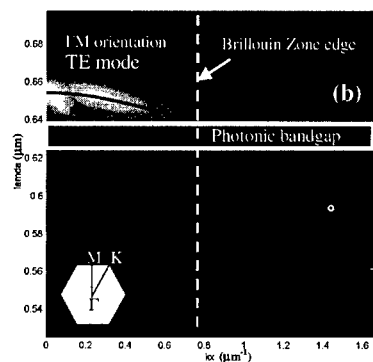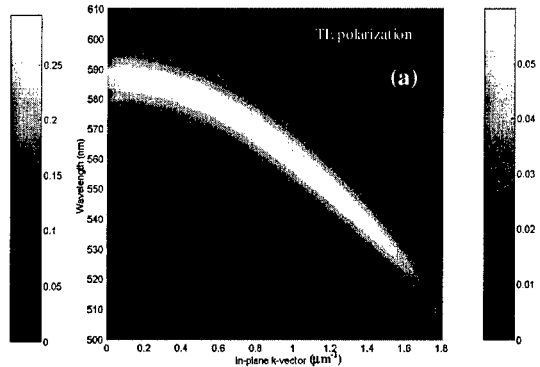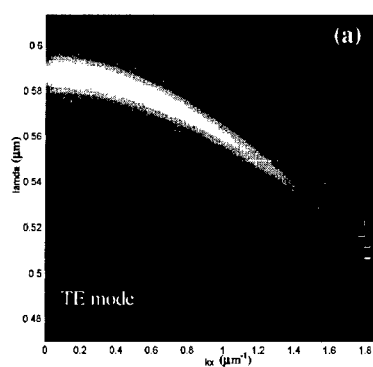
Figure 2. Angle resolved transmission result of the a) planar microcavity and b),c) textured metallic microcavity sample and the theoretical calculation on the photonic modes of the textured sample. Inset shows the first Brillouin zone and the symmetry directions.

Figure 3. ARPL results of the a) planar microcavity and b),c) textured metallic microcavity sample and the theoretical simulations on the surface plasmon coupling in different interfaces

229
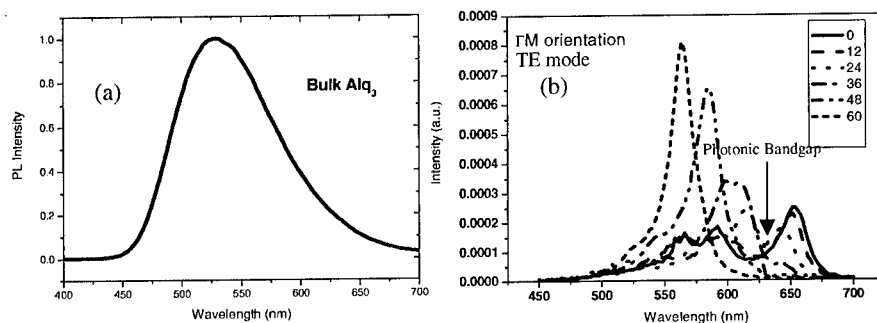
Figure 4. The PL spectrum of Alq₃ in (a) free space and (b) textured metallic microcavity

CONCLUSION

The ARTR and ARPL results have shown that the photonic band structure of the cavity modes are greatly altered for the laterally textured sample and also the bandgap can be observed at Brillouin zone edge which matched with predicted value. Also, it is shown that the PL peak shift with the viewing angle from the textured sample is less compare to the planar microcavity sample. The present study shows that the 2-D patterned metallic microcavity has the potential in application such as super bright LED, super monochromatic light emission and also fundamental emission study of luminescent materials.

ACKNOWLEDGEMENT

REFERENCES
1. Y. Yamamoto and R. E.   Slusher, Phys. Today **46**, 66 (1993)
2. Dodabalapur, L. J. Rothberg, R. H. Jordan, T. M. Miller, R. E. Slusher, and J. M. Phillips, J. Appl. Phys. **80**, 6954 (1996)
3. Abram and G. Bourdon, Phys. Rev. A **54**, 3476 (1996)
4. Abram, I. Robert, and R. Kuszelewicz, IEEE J. Quantum Electron. **34**, 71 (1998)
5. P. T. Worthing, R. M. Amos, and W. L. Barnes, Phys. Rev. A **59**, 865 (1999)
6. H. Rigneault, F. Lemarchand, A. Sentenac, and H. Giovannini, Optics Letters **24**, 148 (1999)
7. P. Kaminow, W. L. Mammel, and H. P. Weber, Applied Optics **13**, 396 (1974)
8. R. J. Ram, D. I. Babie, R. A. York, and J. E. Bowers, IEEE J. Quantum Electron. **31**, 399 (1995)
9. S. C. Kitson, W. L. Barnes, J.R. Sambles, J. Appl. Phys. **84**, 2399 (1998)
10. M. G. Salt and W. L. Barnes, Phys. Rev. B **61**, 11125 (2000)
11. M. G. Salt, W. C. Tan, and W. L. Barnes, Appl. Phys. Lett. **77**, 193 (2000)

Very large plasmon band shift in strongly coupled metal nanoparticle chain arrays.

L. A. Sweatlock[1], J. J. Penninkhof[2], S. A. Maier[1], A. Polman[2], and H. Atwater[1]
[1]Thomas J. Watson Laboratories of Applied Physics, Caltech
Pasadena, CA 91125, USA
[2]FOM Institute for Atomic and Molecular Physics (AMOLF)
Kruislaan 407, 1098 SJ Amsterdam, The Netherlands

Abstract

30 MeV silicon ion irradiation of silica glass containing 10 nm silver nanocrystals causes alignment of the nanocrystals in closely spaced linear arrays along the ion tracks. Optical transmission measurements show a 1.5 eV splitting of the surface plasmon resonant absorption bands for polarizations longitudinal and transversal to the arrays. The resulting material is a highly anisotropic glass that absorbs blue light of one polarization, and near-infrared light of the orthogonal polarization. Finite-difference time domain simulations are used to explore the effects of interparticle spacing and total array length on the absorption properties.

Introduction

The optical extinction properties of small metal particles have been studied for many years [1, 2]. Noble metal nanoparticles embedded in a dielectric exhibit a strong absorption peak due to a collective motion of free electrons, that is, a surface plasmon resonance. For isolated spherical particles, the resonance peak occurs generally in the visible part of the spectrum. The particular frequency depends on the particle size, and the dielectric constants of the metal and of the surrounding medium. For particle ensembles, however, electromagnetic coupling between neighboring particles shifts the plasmon absorption bands [3]. Numerical calculations have demonstrated that nanoparticle size, nearest neighbor spacing, and the overall ensemble size and shape have a critical effect on extinction spectra [4].

In linear arrays of particles the optical response is anisotropic, since the character of interparticle coupling depends on whether incident light is polarized longitudinal or transversal to the chain axis. In particular, the longitudinal collective extinction resonance can be significantly red-shifted throughout the technologically relevant visible and near-infrared spectrum. Wavelength tuning is achieved by engineering the strength of interparticle coupling. The transverse mode extinction is modestly shifted to higher frequencies.

It has been experimentally demonstrated that nanoparticle chains are capable of guiding electromagnetic energy via dipolar near-field interactions comparable to Forster transfer [5]. These structures exhibit lateral mode confinement smaller than the optical diffraction limit, which cannot be achieved with conventional waveguides [6], nor with other novel technologies such as photonic crystals [7] or plasmonic stripe waveguides [8]. Therefore metal nanoparticle chains are of interest for applications in photonics

where local concentration of electromagnetic fields is critical, including nonlinear devices and sensors.

We have previously explored nanoparticle arrays fabricated by electron beam lithography with 50 nm particles and 25 nm next-neighbor spacing. [5, 9] Motivated by potential technological applications, we consider shrinking these length scales in order to increase the strength of interparticle coupling. In this note we discuss an experimental method for producing quasi-ordered arrays of 10 nm particles spaced by 2 nm or less. We then connect the experimental far-field optical extinction results with finite-difference time domain (FDTD) simulations.

Method

Our collaborators have shown that anisotropic core-shell particles can be fabricated by megaelectron-volt (MeV) ion irradiation of colloidal spheres consisting of a metal core surrounded by a silica shell [10]. The shape change of the metal core is attributed to an anisotropic deformation of the silica matrix, which is known to occur in amorphous materials [11]. This led us to investigate the effect of MeV ion irradiation on silver (Ag) nanocrystals in a glass film.

Ionic silver is introduced into sodalime glass by immersing the substrate into a melt of Ag salts. The silver replaces native sodium via an ion exchange interaction. Nucleation of Ag nanocrystals is induced by 1 MeV irradiation with xenon ions. These heavy, relatively low energy particles cause atomic displacements that enhance mobility of the embedded Ag. Nucleation could alternatively be accomplished by thermal annealing. Finally, the sample is exposed to 30 MeV silicon ions with an incident angle 60 degrees from normal, while cooled to a temperature of 77 K. Under these conditions the primary stopping mechanism for the energetic ions is electronic braking rather than atomic collisionrents. Electronic braking causes a thermal spike along the ion trajectory, which is thought to be responsible for anisotropic deformation of the matrix. No deformation of the individual particles is observed. Please refer to our recent letter [12] for additional information regarding our fabrication method.

An established method for fabricating optically dichroic glass is via ultrafast laser pulse deformation of embedded Ag nanoparticles [13]. Intense femtosecond optical pulses are found to induce various morphological changes to the Ag nanoclusters [14]. In contrast, the ion irradiation procedure we propose in this report induces plastic flow in the glass matrix, and results in the ordering of particles into chain arrays without noticeably altering the morphology of individual particles. The two methods produce significantly different nanostructure as well as distinct optical extinction spectra, and each promises interesting technical applications.

Results

Optical extinction is determined by normal-incidence transmission spectroscopy for polarizations parallel and perpendicular to the projection of the ion trajectories onto

the surface. Also, plan-view TEM samples were prepared via ion milling with a kiloelectron-volt argon beam.

Figure 1 (a & b):
TEM of samples before (a)
& after (b) high energy
ion irradiation. Inset,
FFT of image confirms
particle orientation along
ion tracks.
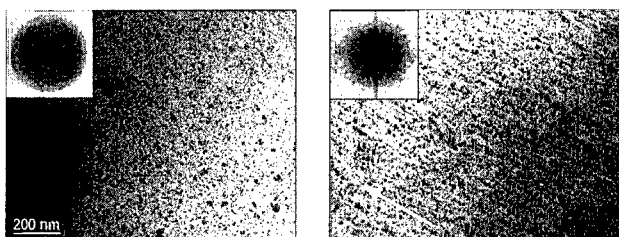
Normal incidence plan-view TEM images appear in Figure 1. The first panel shows Ag particles with diameters typically in the range 2-15 nm, dispersed throughout the glass after annealing with 1 MeV Xe ions. Particles appear to be randomly arranged throughout the matrix, and indeed, the inset spatial fast fourier transform (FFT) of the image shows no directionality. The second panel shows the sample following high-energy Si irradiation, with the direction of the ion tracks indicated by an arrow. In this case, quasi-linear arrays of nanoparticles are observed, and FFT confirms that the arrays are oriented parallel to the ion beam.

Figure 2.
Optical extinction of Ag nanoparticles in BK7-type
glass irradiated with 30 MeV Si, including optical
polarizations longitudinal ("s-pol") and
transversal ("p-pol") to the projection of the ion
beam direction into the normal plane. Also shown
is the extinction of an isotropic control sample with
randomly oriented nanoparticles (solid line) and
*with only unannealed ionic Ag (dashed line).*
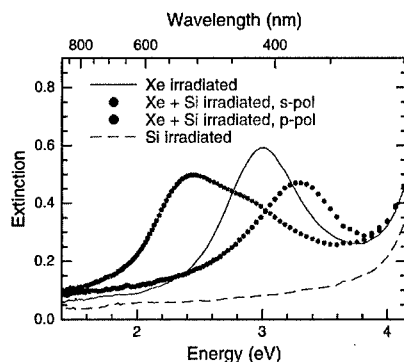
Figure 2 presents optical extinction spectra of the samples consisting of Ag nanoparticles in glass following irradiation with 30 MeV Si for optical polarizations longitudinal ("s-pol") and transversal ("p-pol") to the projection of the ion beam direction into the surface plane. A solid line indicates the isotropic response of an annealed sample without Si ion irradiation, which contains only randomly oriented nanoparticles. The broken line is the extinction of a sample containing only unannealed ionic Ag. In this typical example, the longitudinal plasmon extinction peak redshifts by 0.6 eV relative to the isotropic response of the control sample while the transversal peak blueshifts by a smaller amount. We have shown elsewhere [12] that the magnitude of the peak splitting can be tuned by controlling the total ion fluence. This result is summarized in Figure 3.

Figure 3.
Peak position [eV] of collective plasmon extinction
resonance for Ag nanoparticles in BK7 glass
irradiated with various fluences [1e15 ions/cm^2] of
30 MeV Si, including optical polarizations
longitudinal (lower branch) and transversal (upper
branch) to the projection of the ion beam into the
normal plane. Particularly in the longitudinal
direction, the resonance frequency is a strong
function of fluence.
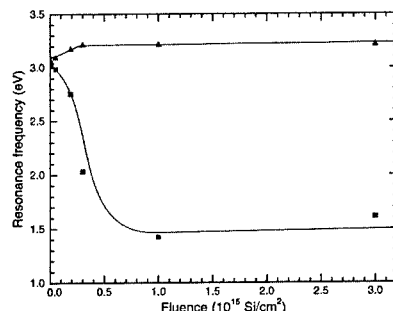
From literature results [4, 15], we understand that the dependence of resonance peak frequency on ion fluence may result from either a decreasing typical interparticle spacing, or from an increasing average nanoparticle chain length, or from a combination of several effects. We use FDTD simulation to understand the relative importance of these effects in idealized chains with critical dimensions similar to those observed in TEM. Simulations have the added benefit of helping bridge the gap between optical far-field extinction and interesting near-field effects, which would be challenging to address directly in experiment.

Because it is difficult to explicitly perform a simulation of frequency scanning spectroscopy with a time domain algorithm, a two-step process is used to simulate the plasmon resonance frequencies. First, the simulation volume is irradiated by a pulse with an off-resonance center frequency that allows the particle chain to absorb energy into any modes that may exist. The particles' relaxation is then observed in the time domain. Fourier transform of this data gives the frequency position of any resonant absorption peaks. Once the spectrum is outlined in this way, on-resonance excitation may be used to excite individual modes, for example, to examine the corresponding energy density profile.

Figure 4
Simulated longitudinal extinction spectra for four-
particle chains of 10 nm Ag particles in glass with
various interparticle spacings; and for comparison
the simulated spectra of a single nanoparticle.
Decreasing spacing leads to stronger interparticle
coupling, and thus an increasing peak shift towards
lower frequency.
Peaks of magnitude less than 1 are non-
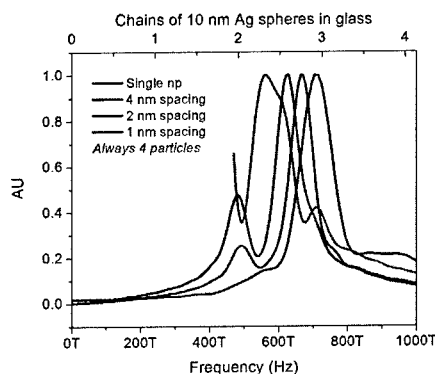*dipole modes, artifacts of the simulation mesh.*

Figure 4 shows a simulated longitudinal polarization extinction spectrum for four-particle chains of 10 nm Ag particles. The particle size and chain length are chosen as
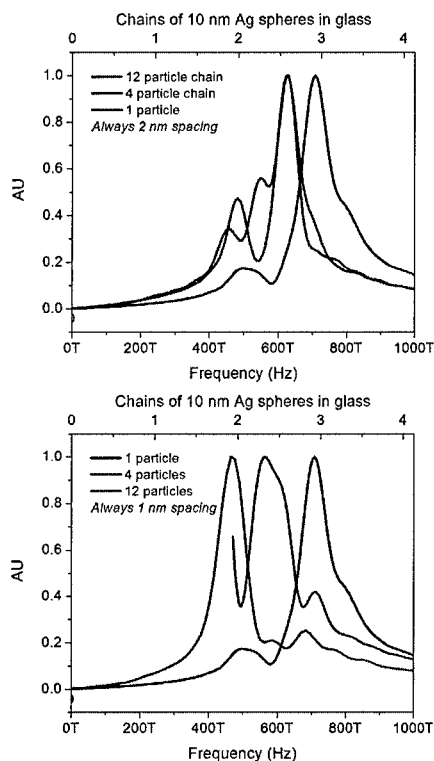
234

typical of chains observed in TEM. The data series in Figure 4 represent arrays with various interparticle spacings, and also isolated particles. The simulated peak for isolated particles at 2.9 eV is in good agreement with the experimental control, suggesting that the as-annealed sample consists of essentially uncoupled nanoparticles. Decreasing interparticle spacing leads to stronger coupling, and thus to a peak shift of increasing magnitude towards lower frequencies. Secondary peaks (with amplitude less than 1 in Figure 4) were investigated by selective excitation, and were found to correspond to non-dipole modes that occur as artifacts of the simulation mesh.

Figure 5
Simulated longitudinal extinction spectra for chains of 10 nm Ag particles in glass with fixed interparticle spacing and variable chain length; and for comparison the simulated spectra of a single nanoparticle.

Peaks of magnitude less than 1 are non-dipole modes, artifacts of the simulation mesh.

In panel (a), the spacing is fixed at 2 nm. In this case there is no difference between long and short chains of nanoparticles.

However in panel (b), the spacing is fixed at 1 nm. For this very close interparticle spacing, the particle chain length is also a critical parameter.

Chains of 10 nm Ag spheres in glass

12 particle chain
4 particle chain
1 particle
Always 2 nm spacing

Chains of 10 nm Ag spheres in glass

1 particle
4 particles
12 particles
Always 1 nm spacing

In Figure 5 the effect of total chain length on the extinction properties of Ag nanoparticle chains is explored, again considering only the longitudinal polarization. The two panels correspond to chains with interparticle spacing of 1 or 2 nm. In the first panel, the overall length of the array is not a critical factor. However, for the very close interparticle spacing seen in the second panel, the length of the array becomes an important parameter.

Discussion

Here we have demonstrated a method for fabrication of an exceptionally anisotropic bulk glass. The optical anisotropy results from resonant absorption into longitudinal and transverse collective plasmon modes in chains of silver nanoparticles. The longitudinal resonance can be tuned by 1.5 eV or more, throughout the visible and near infrared.

Comparison of finite element simulation with TEM images helps relate the material nanostructure to optical extinction. Although important questions still remain, we are progressing toward understanding the dynamics of the process by which ion irradiation leads to nanoparticle alignment. Simulation also allows connection between far-field measurements and near-field parameters such as local enhancement of electric field amplitudes that would be difficult to measure directly. Indeed, the very small length scales accessible by this fabrication technique suggest potential use in applications in which the local field amplitude is critical.

Acknowledgements

References

[1] Mie, G. *Ann. Phys.* **25**, 377-445 (1908).
[2] Kreibig, U. and M. Vollmer, Optical Properties of Metal Clusters. (Springer, 1995).
[3] Gérardy, J. M. and M. Ausloos, *PRB* **25**, 4204 (1982).
[4] Quinten, M. and U. Kreibig, *Appl. Opt.* **32**, 6173 (1993).
[5] Maier, S. A. et al., *Nature Materials* **2**, 229 (2003).
[6] Saleh, B. E. and M. C. Teich, Fundamentals of Photonics. (Wiley, 1991).
[7] Mekis, A. et al., *PRL* **77**, 3787-3790 (1996).
[8] Lamprecht et al., *APL* **79**, 51 (2001).
[9] Maier, S. A., P. G. Kik, and H. A. Atwater, *APL* **81**, 1714-1716 (2002).
[10] Roorda, S., T. van Dillen, C. Graf, A. M. Vredenberg, B. J. Kooi, A. van Blaaderen, and A. Polman, in press 2003.
[11] Snoeks, E., A. van Blaaderen, T. van Dillen, C. M. van Kats, M. L. Brongersma, and A. Polman, *Adv. Mat.* **12**, 1511 (2000).
[12] Penninkhof, J. J., L. A. Sweatlock, A. M. Vredenberg, B. J. Kooi, S. A. Maier, H. A. Atwater, and A. Polman, *APL* **83**, 4137 (2003).
[13] Kaempfe, M., T. Rainer, K.-J. Berg, G. Seifert, and H. Graener, *APL* **74**, 1200 (1999).
[14] Kaempfe, M., H. Hofmeister, S. Hopfe, G. Seifer, and H. Graener. *J. Phys. Chem. B* **2000**, 11847-11852.
[15] Lamprecht, B. et al., *PRL* **84**, 4721-4724 (2000).

ANGULAR ROLL-OFF DEPENDENCE OF SPECTRAL EMISSION FROM A METALLODIELECTRIC PHOTONIC CRYSTAL

Puscasu, Irina; Pralle, Martin U.; McNeal, Mark P.; Moelders, Nicholas ; Daly, James T
Greenwald, Anton C.; Ludwiszewski, Alan ; Johnson, Edward A.; Schaich, William L.[*]
Ion Optics Inc., Waltham, MA 02452, USA.
[*]Indiana University, Bloomington, IN, USA.

ABSTRACT

We are reporting on the analysis of a new design for a thermal source exploiting Si-based suspended micro-bridge structures. A device consists of a metal film perforated by a periodic array of apertures extending into the Si substrate and each of size on order of the wavelength of the light. This perforated film permits resonant coupling of the incident radiation from the underlying silicon photonic crystal with surface plasmons at the metal surface. The coupling provides for unusually high optical emission efficiencies when the structure is thermally excited. The radiation emitted exhibits an enhancement over a narrow wavelength range in the infrared and its spectral response is highly dependent on the direction of observation. The positions of the main resonances, for both reflection and emission from our structures, scale linearly with the periodicity of the metallo-dielectric structure. As one moves off normal incidence, a single main resonance splits into several smaller resonances whose locations scale roughly linearly with observation angle. These structures have been used as emitter/detector sensor chips to selectively detect industrial pollutants like carbon dioxide. Control of the wavelength of resonance, bandwidth and direction of emission play an important role in improving the sensitivity and selectivity of these gas sensors.

INTRODUCTION

Sensors of trace gases are of outmost importance to diverse fields such as meteorology, environmental protection, household safety, bio-hazardous material identification and industrial environments. The current era of high technology and advanced industry is pushing the limits of science when it comes to enhancing the performance of traditional devices and creating new candidates through microengineering for sensors manufacturers.

Infrared sensors remain the most accurate and reliable because they don't rely on catalytic or electrochemical interactions which are prone to interference from other chemical species and poisoning or depletion with prolonged use. Because each gas has a unique infrared absorption line, infrared sensors provide conclusive identification and measurement of the target gas with little interference from other gases. Since the sensor element does not touch the gas, they are not poisoned by contact with the environment.

The principle of operation of Ion Optics' innovative sensor[1-2] is shown in Figure 1. This single microelectro-mechanical system (MEMS) replaces all the components of bulky conventional NDIR instruments. The key to this device is precise control of the infrared wavelengths so that the device only emits (and is only sensitive to) infrared light

that is useful for the measurement. This is possible through the use of newly discovered technology using a 2-D photonic crystal as the surface coating. By design of the pattern of the coating, the narrow band emission is tuned to the absorption line of a specific gas. Reflected light is re-absorbed by the hot silicon membrane which quickly achieves a thermal steady-state. Gas present in the light path absorbs reflected radiation and reduces optical power incident upon the sensor element. This affects the sensor temperature and, in turn, such properties as resistance, output signal that is used to monitor the gas concentration.
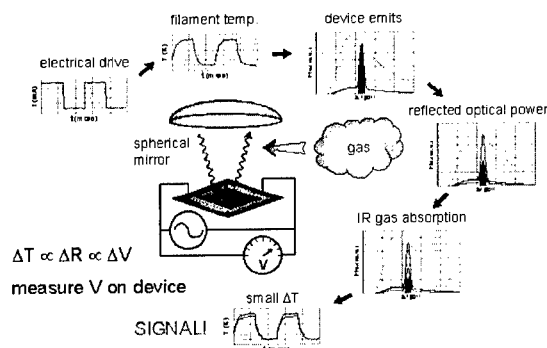
Figure 1. Ion Optics' novel, low-cost infrared gas sensor concept using a heated bolometer element as both source and detector in an open path gas measurement.

FABRICATION

Test structures for 2-D photonic crystal patterns were fabricated on passivated, bulk n-doped Si. The periodic structure was photolithographily defined, then transferred into the metal layer via a plasma etch technique. This was followed by deep reactive ion etch into the silicon wafer. An alternative approach first defined the holes in silicon followed by a "lift off" lithographic process to deposit the metal only on the top surface.

FTIR MEASUREMENTS

Room temperature reflectance and emission measurements at 325 °C were carried out on a Nicolet Nexus 670 FTIR equipped with an external emission port. Reflectance measurements were collected close to normal incidence and also at variable angles of incidence, in the range of 7000–500 cm^{-1} at a resolution of 4 cm^{-1}. Transmission measurements showed that our samples are opaque to radiation in the infrared, which implies that the absorption, A is given by: 1-R, where R represents reflection. Emission and absorption of radiation are related processes. Indeed Kirchhoff's law[3] states that the spectral emissivity equals the spectral absorption under the same conditions. Our experimental measurements of absorption and emission show a good agreement (Fig.2a and b) to the theory.
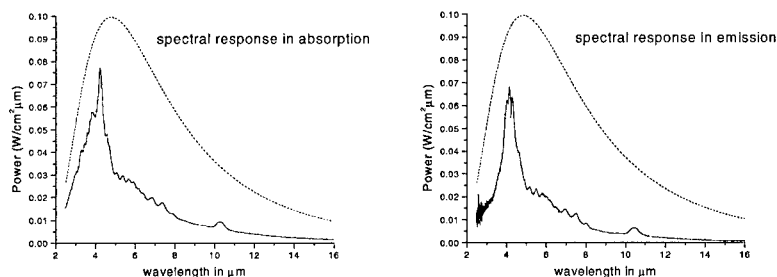
Figure 2. a) Spectral response in absorption vs. blackbody at 325 C; b) Spectral response in emission vs. blackbody at 325 C

For emission measurements, samples were mounted on a hot stage and heated to 325 °C for several minutes to ensure they reached set point temperature. The infrared radiation was collected, using a parabolic right angle mirror and imaged into the interferometer.

EXPERIMENT AND DISCUSSIONS

We have developed a novel thermally stimulated narrow-band infrared source/detector by combining the unique advantages of two different structures: a photonic crystal[4] that consists of an array of holes etched into a dielectric substrate (silicon for example) and a periodically perforated metallic thin film (Fig. 3.). The dielectric photonic crystal structure is passive and exhibits a strong absorption at resonance. This acts as a radiation reservoir for the conductive array, which plays an active role through plasmon[5] interactions and is opaque at all wavelengths except those at which coupling occurs. The perforated metal film, where the apertures are on order of the wavelength of the light, permits resonant coupling of the incident radiation (from the underlying silicon) with surface plasmons at the metal surface. This coupling provides for unusually high optical transmission efficiencies, where again, the periodicity of the structure is employed.

The emission process begins in the bulk silicon, where thermal stimulation produces blackbody-like radiation.
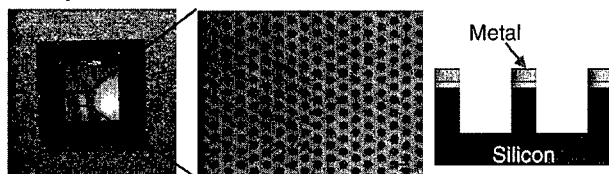
Figure 3. Photonic crystal structure: hexagonal array of holes

239

The silicon/air pattern of the photonic crystal reshapes this spectrum of radiation and centers it around a specific wavelength of resonance defined by the lattice spacing of the crystal. (Fig. 4).
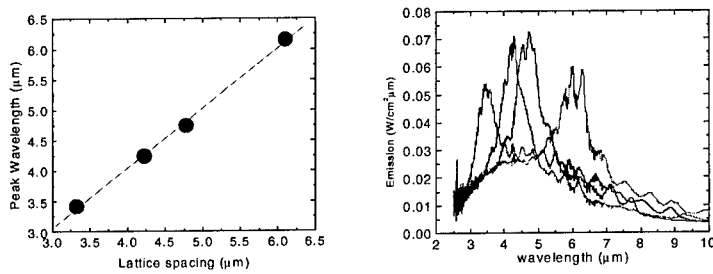
**Figure 4.** Tunability of the device's wavelength response by controlling the geometry of the photonic crystals

The photons cannot penetrate through the thin metal on the top surface. Instead they excite surface plasmon modes at the lower substrate/metal interface, where the vertical trenches create a boundary condition. There is a resonant interaction of the incident light with the surface plasmons on both surfaces of the metal film, the interaction is allowed by coupling through the grating momentum, which combined with the surface plasmon dispersion for smooth films results in the following equation that governs the resonance:

$$\left(\left(\left(i+\frac{j}{2}\right)\frac{2}{\sqrt{3}}\right)^2 + j^2\right)^{\frac{1}{2}} \lambda = a\left(\frac{\varepsilon_1\varepsilon_2}{\varepsilon_1 + \varepsilon_2}\right)^{\frac{1}{2}} \tag{1}$$

Where ε_1 is the dielectric constant of the interface medium, and ε_2 is that of the metal, a is the lattice periodicity, λ is the wavelength, and i,j are integer numbers. From this equation it results that the dielectric layer in contact with the metal along with the lattice constant of the array will influence the position of the resonant wavelength. . These surface plasmons then decay into photons, which are emitted from the surface.

Samples were prepared with hexagonal arrays having lattice parameters between 2 and 9 μm (Fig. 4). We observe a linear dependence between the wavelength of resonance and the periodicity of the array (Fig. 4).

It is important to note that this behavior only works when all of these processes occur together in one continuous sequence. If we separate the system into its individual components, i.e. a bulk silicon wafer, a silicon photonic crystal and a perforated metal film we do not observe the same effects. The emission from an array of holes in a thin metal layer on top of an unpatterned Si substrate does not exhibit spectral resonances and resembles a gray-body emission. (Fig. 5). Therefore this interaction cannot be described as a filtering type mechanism but rather as an enhanced emission mechanism.
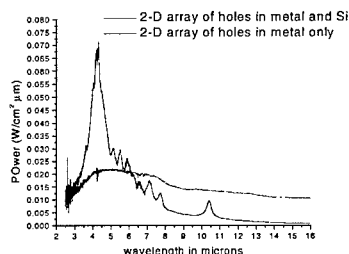
Figure 5. Emitted radiation from a 2-D array of holes in a thin metal layer with or without an array of holes in the underlying Si substrate

Influence on the spectral response of different parameters has been studied. Orientation of the structure plays an important role. Reflection measurements were taken at different incident and azimuthal angles (Fig. 6). Dependence over phi reflects the hexagonal symmetry of the array. Dependence over theta changes more dramatically the response of the structures, with the appearance of new resonances, shifted from the main resonance at normal incidence.
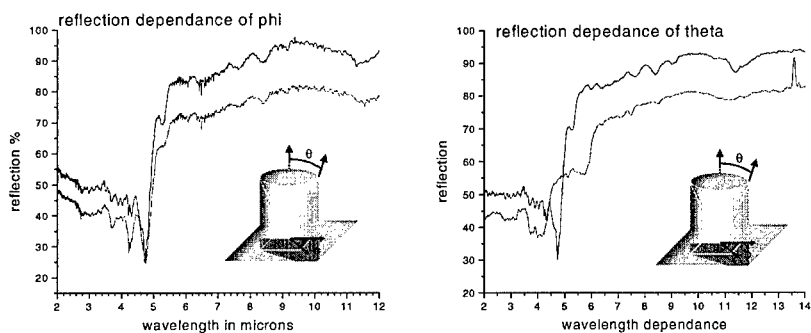
Figure 6. a) Spectral dependence of reflection vs. $\phi = 0$ and $\phi = 90$ degrees; b) Spectral dependence of reflection vs. $\theta = 0$ and $\theta = 30$ degrees; θ = angle made by the incoming radiation with the normal to the structure and ϕ = in-plane angle made by the incoming radiation with a principal reciprocal lattice vector.

Variation with theta is further studied in emission. As one moves off normal incidence, a single main resonance splits into several smaller resonances whose location scale roughly linearly with observation angle (Fig. 7a). For gas measurement purposes, the useful radiation is contained in a narrow range of wavelengths centered around a certain resonance. A potential concern with regard to employing these planar photonic crystal devices as frequency selective emitters/detectors, is their spectral angular dependence. The calculations indicate very sharp peaks for the absorption/emission spectra at individual angles; however the peak wavelength of these spectra changes with

241

viewing angle, consistent with the plasmon dispersion relation. In practical applications, the signal to the detector integrates over a range of angles for light emitted from the surface. This angular dependence of wavelength could contribute to broadening of the peak and reduced selectivity to target gases. As we can see in figure 6, the emission for a hexagonal array (with lattice periodicity of 3 µm) has a main resonance at 1x the periodicity, for normal incidence. As one moves off normal, the radiation emitted at 3 microns decreases. If we integrate the power emitted at 3 µm (within a 1 µm bandwidth) as a function of angle, we observe that the useful radiation at 3 microns is emitted mainly forward (Fig. 7b). This helps the gas detection, as useful radiation is easily captured by the optics (Fig. 1). While the radiation at wavelengths outside the range of interest, being emitted at large angles, it is not captured by the optics, thus it does not interfere with the gas measurement.
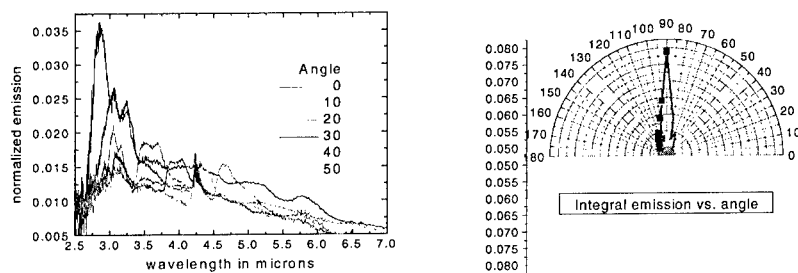
Figure 7. a) Emission measurements as a function of incident angle; b) Integrated power at 3 µm (with a 1 µm bandwidth) as a function of incident angle

CONCLUSIONS

In this work we have presented the properties of a novel thermally excited infrared source based on a photonic crystal type structure. Spectral measurements in reflection, absorption and emission have been performed. The effect of different parameters: lattice constant and angle of observation has been studied. These parameters define the tunability of the radiation and the width of the emission at a designed wavelength. This technology promises a new class of tunable infrared emitters with high power in a narrow spectral band that are critical for sensing, spectroscopy, and thermophotovoltaic applications.

REFERENCES

1. M. U. Pralle, I. El-Kady, E. A. Johnson, N. Moelders, M. P. McNeal, I. Puscasu, A. C. Greenwald, J. T. Daly,T. F. George, D. S. Choi, and R. Biswas, *"Photonic Crystal Enhanced Narrow-band Infrared Emitters,"* Journal of Applied Physics Letters, vol. 81, 4685-4689 , 2002.
2. E.A. Johnson, Patent No. 5838016
3. W. L. Wolfe, "Introduction to Radiometry" (vol. TT29, SPIE Press, 1998).
4. J.D. Joannopoulos, R.D. Meade, and J.N. Winn, Photonic Crystals (Princeton University Press, Princeton, 1995)
5. H. Raether, Surface Plasmons (Springer, Berlin, 1988)

W4.8

Standing Wave Reflectivity in Photonic Structures Using a Scattering Type Optical Near-Field Optical Microscope

A. Bruyant, S. Aubert, G. Lérondel, S. Blaize, R. Bachelot P. Royer and V.Minier[1]
Laboratoire de Nanotechnologie et Instrumentation Optique, UTT - CNRS (FRE 2671), 10010
TROYES cedex, France
[1] Groupement d'Electromagnétisme Expérimental et d'Optoélectronique, 38240 Meylan, France

ABSTRACT

A method for measuring locally the normalised reflectivity spectrum in waveguiding photonic structures is presented. The latter is obtained by imaging the standing wave pattern upstream of the structure with a scattering type Scanning Near-field Optical Scanning Microscope (s-SNOM) and normalised with a simple Fourier analysis . Two kinds of sample are investigated. The first one is a corrugated integrated waveguide, the second is a fiber Bragg grating. The s-SNOM technique applied to waveguiding structures is first introduced with the case of a straight waveguide.

INTRODUCTION TO s-SNOM : A STRAIGHT WAVEGUIDE STUDY

SNOM is an attractive tool for the characterisation of integrated devices such as waveguides or Bragg gratings [1-4]. In this microscopy, a tapered optical fiber is usualy used to collect the evanescent light in near-field optic. The scattering-SNOM (s-SNOM) or apertureless SNOM (ASNOM) uses scattering tip. This alternative technique has proved its ability to map the intensity profile of guided modes of integrated optical structures on large area with a high resolution [5]. There are several motivations for the s-SNOM approach. One is the wide choice (dielectric, metallic) of commercial AFM tips. Those nanometric probes should provide an highly increased resolution on the topographic and near-field optic images. Moreover those scattering tips do not have a cut-off wavelength, it is hence possible to work on a wide wavelength range. Finally the s-SNOM allows to localise and to estimate the losses of the guiding structure [6].

As an introduction, we consider the s-SNOM experiment depicted in Figure 1a that we have already reported [5,6]. In this experiment, a pigtailed waveguide is scanned under the scattering tip of an Atomic Force Microscope. The tip oscillating in intermittent contact at its vertical frequency resonance is kept at a typical amplitude of a few tenth of nanometers. A part of the guided mode energy is hence periodically converted in radiating modes. The light scattered by the tip is collected by a confocal microscope. In addition to this field, the losses in the small detection zone propagating with wavevectors within the numerical aperture of the microscope objective are also collected. Hence, the intensity detected by the quadratic detector as a function of the tip-sample position (x,y) is given by:

$$I(x, y) = I_{tip}(x, y) + I_{losses}(x, y) + 2 \ E_{tip}(x, y) \times E_{losses} \times \cos(\phi(x, y)) \qquad (1)$$

Where ϕ is the phase between the E_{tip} and E_{losses} approximated by two plane waves. This intrinsic interferometric behaviour of the ASNOM will be used later to distinguish the forward and backward propagating guided modes in reflectivity measurements.
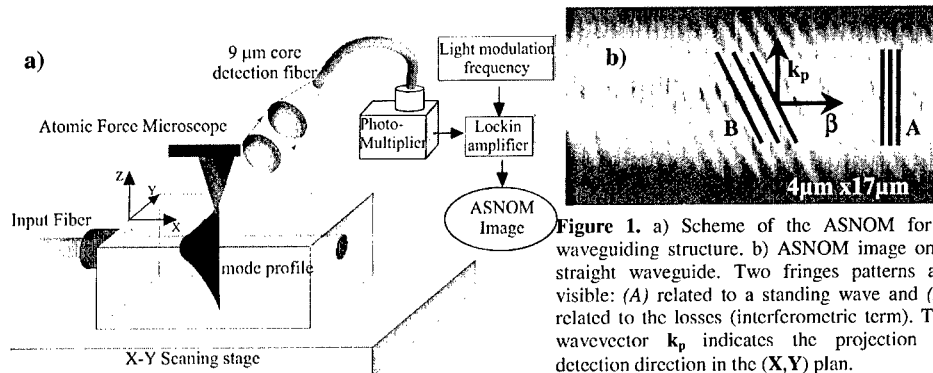
Figure 1. a) Scheme of the ASNOM for a waveguiding structure. b) ASNOM image on a straight waveguide. Two fringes patterns are visible: *(A)* related to a standing wave and *(B)* related to the losses (interferometric term). The wavevector k_p indicates the projection of detection direction in the (**X,Y**) plan.

A lock-in detection at the tip resonance frequency allows to extract the weak signal from the noise. Consequently, the intensity corresponding to the losses which is not modulated is not revealed by the ASNOM image (Figure 1b) . Nevertheless the detected intensity is still sensitive to the local losses via the interferometric term in (1) which produce oblique fringes noted *B* on the ASNOM image. We can also observe the standing wave pattern due to the small reflection at the exit facet. The vertical fringes frequency allows a precise measure of the effective refractive indexes [5] whereas the oblique fringe pattern allows to estimate and localise the losses [6] with the precision of the confocal detection (here $3\mu m$) .

Another interesting parameter for photonic devices is the *in situ* reflection coefficient [3,7]. In this paper, we report a method for measuring, with the same setup, the absolute complex reflection spectrum of Bragg gratings. The basic of this method lies on the standing wave imaging upstream the periodic structure and will now be detailed.

ASNOM IMAGES ON PERIODIC STRUCTURES

The first sample is a singlemode corrugated waveguide made by reactive ion etching over an Ag^+-Na^+ diffused waveguide realised in silicate glass substrate. Details about the structure fabrication can be found elsewhere [8]. The experimental setup, similar to the previous one is shown in Figure 2 (see caption for details). In order to retrieve the complex reflection coefficient in the structure, we have imaged the standing waves appearing near the Bragg wavelength $\lambda = 2.\Lambda.n_{eff}$. The scans in figure 3 were performed in tapping mode upstream of the
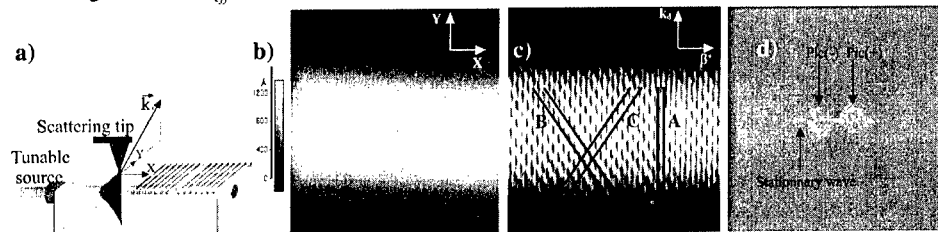
Figure 2. Experimental setup for reflectivity determination of guiding photonic devices. A tuneable source (OSICS ECL 1560) is coupled in the guide, and the confocal microscope collects the scattered light in a direction k perpendicular to the propagation (X). AFM image upstream of the grating (b) and simultaneously recorded ASNOM image near the resonance (1528 nm) showing three fringe patterns (c) with the corresponding fast Fourier transform (d)

The AFM image (fig. 3(b)) reveals the graded topographic profile (100 nm high stripe) of the diffused waveguide and several scattering centers are visible. The ASNOM image (fig. 3(c)) exhibits three fringe patterns related to 3 interference terms: the standing wave pattern indicated by A and the non-local interference between the forward (resp. backward) mode scattered by the tip and the losses in the detection zone indicated by B (resp. C). On the fast Fourier transform of the image, the peaks corresponding to the fringe patterns A, B, C are noted *stationary wave, peak(+)* and *peak(-)*, respectively.

ASNOM SIGNAL ANALYSIS AND REFLECTIVITY SPECTRUM

Field scattered by the tip and field related to the losses

We note β the optical constants of the guided modes (forward and backward), $E_s^+(x,y)$ and $E_s^-(x,y)$ the real and positive amplitudes of the modes and $\Delta\phi$ the phase shift induced by the grating on the backward mode. The field scattered by the tip at the *(x,y)* position in the $(\vec{X},\vec{Y})$ plan of the surface sample is supposed to be proportional to the total field $E(x,y)$ at the surface:

$$E_{tip} \propto E(x,y) = E_s^+(x,y)e^{-i\beta.(x-x_g)} + E_s^-(x,y)e^{i\beta.(x-x_g)}e^{i\Delta\phi} \tag{2}$$

where the front grating boundary position x_g is taken as phase reference for the forward guided mode. The phase shift can be then expressed as $\Delta\phi = 2.\beta(x_g - x_{eff})$, where x_{eff} is an effective or equivalent reflection point. Hence:

$$E_{tip} \propto E_s^+(x,y).e^{-i\beta.(x-x_g)}.(1+r(x)) \quad , \text{ with } \quad r(x) = \left|\frac{E_s^-}{E_s^+}\right|.e^{i.2\beta(x-x_{eff})} = |r|.e^{i.2\beta(x-x_{eff})} \tag{3}$$

where *r(x)* is the complex reflection coefficient of the structure at the tip position. Compared to the complex reflection coefficient at the grating front, $r(x_g) = |r|.e^{i.2\beta(x_g-x_{eff})}$ *r(x)* includes the phase variation due to the propagation between x_g and x.

As mentioned before, losses induced by any scattering centers (small dusts) or intrinsic losses in the small confocal detection zone will interfere with the field scattered by the tip. This field E_{losses} can be correctly approximated, by a plane wave propagating towards the detector [6] with a constant wavevector $\vec{k}_d$ whose projection in the $(\vec{X},\vec{Y})$ plane, $\vec{k}_p$ is along the $\vec{Y}$ direction. The phase of E_{losses} depends on the distance between the scattering centers and the detector during the scan:

$$E_{losses} \propto E_L.e^{-i.k_p.y} \tag{4}$$

Detected intensity

In the general case of a mode $\vec{\beta}$ in the $(\vec{X},\vec{Y})$ scanning plan, the phase difference at the detector between the tip scattering and the losses (both considered as plane waves) can be expressed as:

$$\phi(x,y) = \vec{\beta} \ .(x\vec{X}+y\vec{Y}) - \vec{k}_p.(x\vec{X}+y\vec{Y})$$

In our case, $\vec{\beta}$ is along $\vec{X}$ or $-\vec{X}$ and $\vec{k}_p$ is along $\vec{Y}$. The total intensity detected by the quadratic detector can be expressed as:
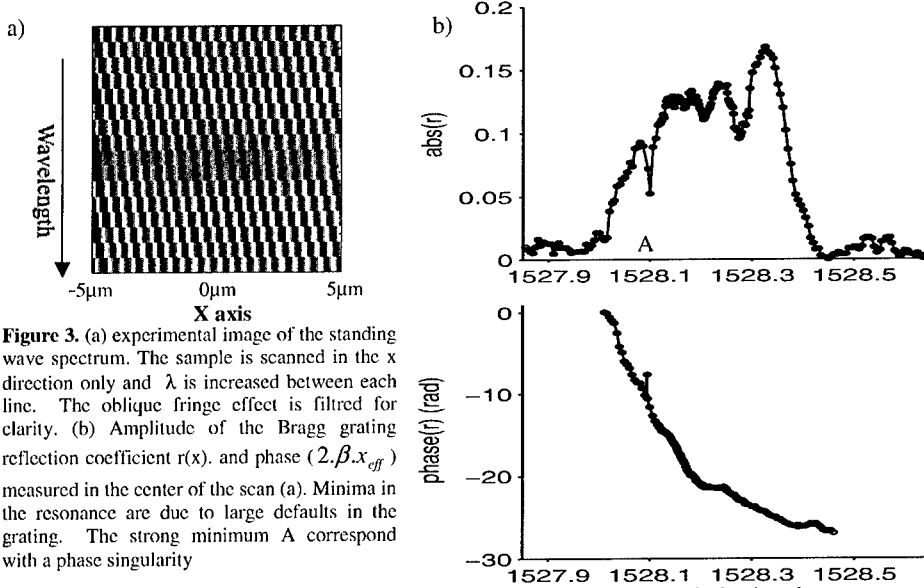
$$I(x, y) = \left| E_{tip}(x, y) + E_{losses}(x, y) \right|^2 \propto \left| E_s^+(x, y) \right|^2 \cdot \left(1 + \left|r\right|^2\right) + \left|E_L\right|^2$$
$$+ 2 \; E_s^+(x, y) E_s^-(x, y) \; \cos\left(2\beta.(x - x_{eff})\right) \qquad (5)$$
$$+ 2 \; E_s^+(x, y) E_L . \cos \; \left[\beta x - k_p y + K\right]$$
$$+ 2 \; E_s^-(x, y) E_L . \cos \; \left[\beta x + k_p y + K'\right]$$

where K and K' are two constants and the three sinusoidal terms correspond to the fringe patterns (A,B,C) on the fig. 2.(b). The Fourier transform of the signal is given by:

$$F(fx, fy) \propto \left(\left|E_L\right|^2 + \left|E_s^+\right|^2 + \left|E_s^-\right|^2 \right).\delta(fx + fy)$$
$$+ 2 \; E_s^+ E_s^- \; \left(e^{-i2\beta.x_{eff}}.\delta(fx - 2\beta) + e^{+i2\beta.x_{eff}}.\delta(fx + 2\beta) \right)$$
$$+ 2 \; E_s^+ E_L \left(e^{+i.K}.\delta(fx + fy \; -\beta \; +k_p) + e^{-i.K}.\delta(fx + fy \; +\beta \; -k_p) \right) \qquad (6)$$
$$+ 2 \; E_s^- E_L \; . \; \left(e^{+i.K'}.\delta(fx + fy \; -\beta \; -k_p) + e^{-i.K'}.\delta(fx + fy \; +\beta \; +k_p) \right)$$

Standing wave spectrum

In Eq.(6), the second term $F(/2\beta/,0)$, proportional to the amplitude of the reflection coefficient (proportional to E_s^-) corresponds to the standing wave peak. In the figure 3, an experimental spectrum of standing wave patterns measured along the same scanning line (y constant) but for different wavelengths is shown.

a)

b)

Figure 3. (a) experimental image of the standing wave spectrum. The sample is scanned in the x direction only and λ is increased between each line. The oblique fringe effect is filtred for clarity. (b) Amplitude of the Bragg grating reflection coefficient r(x). and phase ($2.\beta.x_{eff}$) measured in the center of the scan (a). Minima in the resonance are due to large defaults in the grating. The strong minimum A correspond with a phase singularity

246

A modification of both the phase shift and the intensity is observed. The reflection spectrum of the grating centred at the Bragg wavelength is displayed in fig. 3.(b). It has been obtained by plotting for each wavelength (e.g. for each scanning line) the amplitude of $F(/2\beta/,0)$ corresponding to the standing wave peak in the power spectrum. Furthermore the phase variation of $F(/2\beta/,0)$ gives us directly the phase variation $2\beta.x_{eff}$ of the complex reflection coefficient and has been plotted in fig. 3.(b).

Normalisation

In Eq.(6), the third $F(\pm\beta,\mp k_p)$ and fourth $F(\pm\beta,\pm k_p)$ terms are interference terms between the forward (resp. backward) wave and the losses and. They correspond to the peaks noted (+) and (-) on the fig. 2.(d). The normalisation of the spectrum is straightforward since we have:

$$\frac{\left|F(\pm\beta,\pm k_p)\right|}{\left|F(\pm\beta,\mp k_p)\right|} = |r|.$$

A "full" image (scan in X and Y direction) was done at one wavelength λ_o (fig 3.b). The ratio of the amplitudes of peak (+) and peak (-) gives us the absolute value of $|r(\lambda_o)|$. Compared to the value of $|r(\lambda_o)|$ obtained directly from the standing wave contrast, values reported here do not depend on local variation in real space or on the sampling in frequency analysis and over all on the microscope resolution (e.g. the tip diameter).

Result on a fiber Bragg grating

The same technique was applied to a commercial single mode fiber Bragg grating whose spectral characteristic is well known. This device consists in a periodic modulation of the index of refraction along the fiber core. This fiber was chemically thinned in order to enable the scattering of the exponentially decaying field close to the core and the standing wave imaging.

Figure 4. ASNOM Characterisation of a fiber bragg grating:
a) Experimental setup: the bare fiber was thined around the grating in order to image the standing wave pattern.
b) Normalised complex reflectivity obtained by standing wave imaging and classical transmission measure.
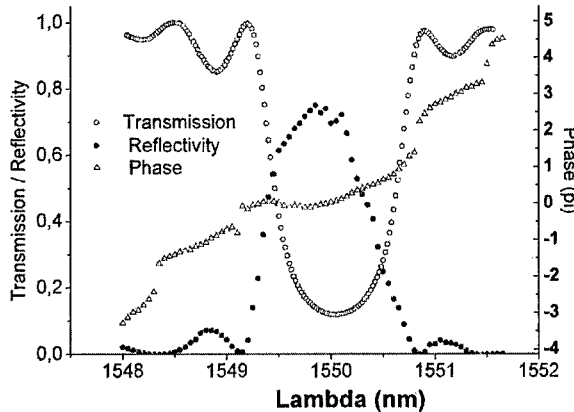
The setup and the complex normalised reflectivity spectrum are shown in figure 4. The far field transmission measured is in agreement with the *in situ* reflectivity spectrum. In this case, the standing wave pattern was registered at the beginning of the grating. We believe that the observed differences mainly arise from mechanical instability and sensitivity to leaky modes that are not considered in this analysis.

CONCLUSION

In conclusion, a method for complex reflection coefficient measurement has been presented. This method is based on a standing wave pattern imaging using a scattering type near-field optical microscope. The spectrum is obtained and normalised using a simple Fourier analysis. The technique was successfully applied to a corrugated waveguide and a fiber Bragg grating. The same method can also be directly applied upstream photonic crystals or hybrid structures such as active guide-mirror to allow an in-situ determination of the coupling losses. Besides the local intensity mapping, the possibility of assessing the complex reflection coefficient brings to the fore the potentiality of ASNOM for the characterisation of photonic chips.

REFERENCES

[1] J. C. Gates, J. D. Mills and W.S. Brocklesby Appl. Phys. Lett. **83** 1890 (2003)
[2] E. Flück, M. Hammer, A. M. Otter, J. P. Korterik, M. L. M. Balistreri, L. Kuipers and N. F. Van Hulst J. Opt. Soc. Am. B **21** 1384 (2003).
[3] G. H. Vander Rhodes, B. B. Goldberg, M. S. Ünlü, S. T. Chu, W. Pan, T. Kaneko, and Y. Kokobun, B. E. Little Appl. Phys. Lett. **75** 2368 (1999)
[4] P. L. Phillips, J. C. Knight, B. J. Mangan, and P. St. J. Russel, M. D. B. Charlton and G. J. Parker J. of Appl. Phys **85** 6337 (1999)
[5] S. Blaize, S. Aubert, A. Bruyant, R. Bachelot, G. Lerondel, P. Royer, J. E. Broquin, V. Minier Journal Of Microscopy **209** 155 (2002)
[6] S. Aubert, A. Bruyant, S. Blaize, R. Bachelot, G. Lerondel, S. Hudlet, and P. Royer J. Opt. Soc. Am. B **20** 2117 (2003)
[7] E. Flück, A. M. Otter, J. P. Korterik, M. L. M. Balistreri, L. Kuipers and N. F. Van Hulst, Journal Of Microscopy **202** 104 (2000)
[8] S.Blaize, L. Bastard, C. Cassagnetes, G. Vitrant and J-E Broquin Proc. of the SPIE Opto2002, 4640 (2002)

W5.16

Microscopic theory of electromagnetic energy transport in nanostructured media

Yongqiang Xue and Mark A. Ratner
Department of Chemistry and Materials Research Center
Northwestern University
Evanston, Illinois 60208

ABSTRACT

We present a microscopic theory of electromagnetic energy transport in nanostructured media based on the Lagrangian formulation of semiclassical electrodynamics. We show the importance of the interplay between transverse and longitudinal local fields in determining the light-matter interaction in nanostructured media. We derive rigorously the coupled-dipole equation of the local fields and apply the theory to analyze energy transport in metal nanoparticle chain waveguide.

INTRODUCTION

As is the case for microelectronics, the further miniaturization of integrated optical devices requires investigating optical elements with dimensions on the nano-scale. Methods are therefore needed for detecting and guiding light on a scale much smaller than the wavelength of the light. Near-field optics, which exploits evanescent rather than propagating light fields, attracts a lot of attention as a promising way of circumventing the diffraction limit [1]. Since the evanescent fields bound to the nanostructures decay in intensity within a fraction of the light wavelength, they carry information about sample features on a sub-wavelength scale [2] and provide a new mechanism for guiding light through near-field coupling among closely-packed nanostructure assemblies [3,4]. It is clear that to investigate light-matter interaction in a spatial extension much less than the optical wavelength, one can not in general have confidence in the macroscopic electrodynamics so far popular in near-field optics and photonic band-structures [1,2]. Instead a microscopic approach treating rigorously the local-field effect is highly desirable [5].

In this work we present a microscopic description of electromagnetic wave propagation in nanostructured media. Our theory is based on the Lagrangian formulation of semiclassical electrodynamics, where we treat the media response quantum-mechanically and the electromagnetic fields classically. We derive rigorously the couple-dipole equation of electromagnetic wave propagation in linear chain of metal nanoparticles for analyzing energy transport in such nano-scale waveguide.

LAGRANGIAN APPROACH TO MICROSCOPIC ELECTRODYNAMICS OF NANOSTRUCTURED MEDIA

In semiclassical electrodynamics, the Lagrangian for light interacting with a quantized many-electron system is [6]

$$L = \int d^3\mathbf{q}\,\psi^\dagger(\mathbf{q})[\sum_i \frac{1}{2m_i}(-i\hbar\nabla_i + e_i\mathbf{A}(\mathbf{q}_i))^2 - V_{ext}(\mathbf{q}_i) - V_{Coul}(\mathbf{q}_i,\mathbf{q}_j)]\psi(\mathbf{q}) + \int d^3\mathbf{r}\mathbf{j}(\mathbf{r})\bullet\mathbf{A}(\mathbf{r})$$

$$+\frac{i\hbar}{2}\int d^3\mathbf{q}[\psi^\dagger(\mathbf{q})\frac{\partial}{\partial t}\psi(\mathbf{q}) - \frac{\partial}{\partial t}\psi^\dagger(\mathbf{q})\psi(\mathbf{q})] + \frac{\varepsilon_0}{2}\int d^3\mathbf{r}[(\frac{\partial}{\partial t}\mathbf{A})^2(\mathbf{r}) - c^2\nabla\times\mathbf{A}^2(\mathbf{r})] \tag{1}$$

where $\psi(\mathbf{q})$ is the many-electron wave function of the nanostructures, V_{ext}, V_{Coul} describe the nuclei potential and Coulomb interaction between electrons respectively. We use Coulomb gauge with the transverse vector potential $\mathbf{A}$ here. Given the Lagrangian (1), the equations of motion for the coupled light-matter system are easily derived.

Since $\mathbf{E}_T = -\frac{\partial\mathbf{A}}{\partial t}, \mathbf{B} = \nabla\times\mathbf{A}$, the variation with respect to $\mathbf{A}$ gives the transverse part of the Maxwell equation for $\mathbf{B}$: $\nabla\times\mathbf{B}(\mathbf{r}) = \frac{1}{c^2}\frac{\partial}{\partial t}\mathbf{E}_T(\mathbf{r}) + \frac{1}{c^2\varepsilon_0}\mathbf{j}_T(\mathbf{r})$, where the transverse current density is $\mathbf{j}_T(\mathbf{r}) = \int d^3\mathbf{q}\psi^\dagger(\mathbf{q})[\sum_i(-i\hbar\nabla_i + e_i\mathbf{A})\delta_T(\mathbf{r}-\mathbf{q}_i)]\psi(\mathbf{q})$. The longitudinal part, $\frac{\partial}{\partial t}\mathbf{E}_L(\mathbf{r}) + \frac{1}{\varepsilon_0}\mathbf{j}_L(\mathbf{r}) = 0$, follows from the charge conservation equation $\frac{\partial}{\partial t}\rho + \nabla\bullet\mathbf{J}_L(\mathbf{r}) = 0$, and the equation for the longitudinal electric field $\nabla\bullet\mathbf{E}_L = \frac{\rho}{\varepsilon_0}$. Here the transverse and longitudinal current density is related to the current density through the transverse and longitudinal Dyadics $\delta_{T(L)}(\mathbf{r})$ respectively [6]. The equation of motion for the electron field is just the many-electron Schrödinger equation

$$i\hbar\frac{\partial}{\partial t}\psi(\mathbf{r}) = \{\sum_i[\frac{1}{2m_i}(-i\hbar\nabla_i + q_i\mathbf{A}(\mathbf{r}_i))^2 + e_iV_{ext}(\mathbf{r}_i,t)] + \frac{1}{8\pi\varepsilon_0}\sum_{ij}\frac{e_ie_j}{|\mathbf{r}_i-\mathbf{r}_j|}\}\psi(\mathbf{r}), \tag{2}$$

The other Maxwell equations follow from the definition of the field $\nabla\times\mathbf{E}_T(\mathbf{r}) = -\frac{\partial}{\partial t}\mathbf{B}(\mathbf{r})$, and $\nabla\bullet\mathbf{B} = 0$, from which one obtains the following local energy balance relation for the transverse field: $\nabla\bullet(\frac{1}{\mu_0}\mathbf{E}_T\times\mathbf{B}) + \frac{\partial}{\partial t}(\frac{\varepsilon_0}{2}\mathbf{E}_T^2 + \frac{1}{2\mu_0}\mathbf{B}^2) = -\mathbf{E}_T\bullet\mathbf{J}_T$, where $\frac{1}{\mu_0}\mathbf{E}_T\times\mathbf{B}$ is the transverse Poynting vector, and $\frac{\varepsilon_0}{2}\mathbf{E}_T^2 + \frac{1}{2\mu_0}\mathbf{B}^2$ is the energy density stored in the transverse field. A similar equation applies to the longitudinal field $\frac{\partial}{\partial t}(\frac{\varepsilon_0}{2}\mathbf{E}_L^2) = -\mathbf{E}_L\bullet\mathbf{j}_L$. Note that there is no Poynting vector associated with the longitudinal field, so this part of the field cannot transport energy from one place to another. The energy stored in the longitudinal field is simply the Coulomb electrostatic potential energy $\frac{\varepsilon_0}{2}\mathbf{E}_L^2 = \frac{1}{8\pi\varepsilon_0}\iint d^3\mathbf{r}d^3\mathbf{r}'\frac{\rho(\mathbf{r})\rho(\mathbf{r}')}{|\mathbf{r}-\mathbf{r}'|}$ of the system of charges [6]. The cross coupling between the transverse and longitudinal fields leads to $\nabla\bullet(\frac{1}{\mu_0}\mathbf{E}_L\times\mathbf{B}) = -\mathbf{E}_T\bullet\mathbf{j}_L - \mathbf{E}_L\bullet\mathbf{j}_T$. The energy balance equation for the total field is obtained by summing over the above three equations,

$$\nabla \bullet (\frac{1}{\mu_0} \mathbf{E} \times \mathbf{B}) + \frac{\partial}{\partial t} (\frac{\varepsilon_0}{2} \mathbf{E}^2 + \frac{1}{2\mu_0} \mathbf{B}^2) = -\mathbf{E} \bullet \mathbf{j}, \tag{3}$$

The right hand side corresponds to an energy sink for the electromagnetic field. Since the total energy of the coupled light-matter system is conserved, the energy lost by the electromagnetic field can only go into the kinetic energy of the many-electron system. The Hamiltonian of the coupled light-matter system is [6]

$$H = \sum_i \frac{1}{2m_i} (-i\hbar\nabla_i + e_i \mathbf{A}(\mathbf{r}_i))^2 + e_i V_{ext}(\mathbf{r}_i) + \frac{1}{8\pi\varepsilon_0} \sum_{i \neq j} \frac{e_i e_j}{|\mathbf{r}_i - \mathbf{r}_j|} + \frac{\varepsilon_0}{2} \int d^3\mathbf{r}[\mathbf{E}_T^2(\mathbf{r}) + c^2 \mathbf{B}^2(\mathbf{r})] \tag{4}$$

Since the kinetic energy density of the system of charges is $\mathrm{E}_{KT} = Tr\{\rho\hat{T}\}$, where ρ is the many-body density matrix and $T = \sum_i \frac{\hat{\mathbf{P}}_i^2}{2m_i} = \sum_i \frac{1}{2m_i} [-i\hbar\nabla_i + e_i \mathbf{A}(\mathbf{r}_i, t)]^2 \delta(\mathbf{r} - \mathbf{r}_i)$. The time variation of the kinetic energy density is thus

$$\frac{\partial}{\partial t} \mathrm{E}_{KT} = Tr\{\frac{\partial\rho}{\partial t}\hat{T} + \rho \frac{\partial\hat{T}}{\partial t}\} = Tr\{[\rho, H]\hat{T}\} + Tr\{\rho \sum_i \delta(\mathbf{r} - \mathbf{r}_i) \frac{e_i \hat{\mathbf{P}}_i}{m_i} \bullet \frac{\partial}{\partial t} \mathbf{A}(\mathbf{r}, t)\} .$$

The second term on the right gives $\mathbf{j} \bullet \mathbf{E}_T$. The first term follows from the Liouville equation of the many-body density matrix. Using the cyclic property of trace, it gives

$$Tr\{[\rho, H]\hat{T}\} = Tr\{\rho[H, \hat{T}]\} = Tr\{\rho \sum_i \delta(\mathbf{r} - \mathbf{r}_i) \frac{\hat{\mathbf{P}}_i}{m_i} \bullet (\nabla V_{Coul})\} = \mathbf{j} \bullet \mathbf{E}_L .$$ We obtain therefore the desired

result $\frac{\partial}{\partial t} \mathrm{E}_{KT} = \mathbf{j} \bullet \mathbf{E}$. The energy transport equation for the coupled light-matter is

thus $\nabla \bullet (\frac{1}{\mu_0} \mathbf{E} \times \mathbf{B}) + \frac{\partial}{\partial t} (\frac{\varepsilon_0}{2} \mathbf{E}^2 + \frac{1}{2\mu_0} \mathbf{B}^2 + E_{KT}) = 0$, and we can define rigorously the

speed of energy transport through the media as $v_E = |\frac{1}{\mu_0} \mathbf{E} \times \mathbf{B}| / (\frac{\varepsilon_0}{2} \mathbf{E}^2 + \frac{1}{2\mu_0} \mathbf{B}^2 + E_{kT})$,

whose magnitude is in general space-time dependent and is always smaller than the speed of light in vacuum. Note that in the presence of other relaxation mechanism of the materials excitation, additional term needs to be added to the Liouville equation [7], which gives rise to a dissipation term in the energy balance equation describing, e.g., various sources of heat.

The above formulation can also be recast into a form more amenable to numerical calculation by expressing the media response in terms of the optical response functions. Given the Hamiltonian of Eq. (4), we obtain the following general relation between current density and the electric field after Fourier transforming to the frequency domain $\mathbf{j}(\mathbf{r}, \omega) = \int d^3\mathbf{r}' \sigma(\mathbf{r}, \mathbf{r}'; \omega) \bullet \mathbf{E}(\mathbf{r}'; \omega)$, where $\sigma(\mathbf{r}, \mathbf{r}'; \omega)$ is the many-body conductivity tensor.

Since $\mathbf{j}(\mathbf{r}, t) = \frac{\partial}{\partial t} \mathbf{P}(\mathbf{r}, t)$ for nonmagnetic materials, the conductivity tensor is related to the

electric susceptibility and dielectric tensor as $\sigma(\mathbf{r}, \mathbf{r}', \omega) = -i\omega\chi(\mathbf{r}, \mathbf{r}', \omega) = -i\omega[\varepsilon(\mathbf{r}, \mathbf{r}', \omega) - \delta(\mathbf{r} - \mathbf{r}')U]$. The kinetic energy equals

$\mathbf{j}(\mathbf{r},t)\bullet\mathbf{E}(\mathbf{r},t)=\int d^3\mathbf{r}'\mathbf{E}(\mathbf{r},t)\bullet\frac{\partial}{\partial t}\chi(\mathbf{r},\mathbf{r}',t)\bullet\mathbf{E}(\mathbf{r}',t)=\int d^3\mathbf{r}'\mathbf{E}(\mathbf{r},t)\bullet\frac{\partial}{\partial t}\varepsilon(\mathbf{r},\mathbf{r}',t)\bullet\mathbf{E}(\mathbf{r}',t)$, which allows us to evaluate the energy transport velocity once the local fields and the optical response function of the media is known [8]. In the case of a general classical dispersive and absorbing dielectric medium, it has been shown that the group velocity gives an incorrect characterization of energy transport velocity as compared to the microscopic definition given here [8].

LOCAL-FIELD ELECTRODYNAMICS OF NANOSTRUCTURED MEDIA

The electromagnetic energy transport in dielectric media is determined by the interplay between the longitudinal and transverse field electrodynamics. This is particularly important for metallic nanostructures, where the excitation of the longitudinal plasmon-polariton mode dominants the optical response in the visible spectrum [5,7]. Since the local-field electrodynamics is qualitatively different for the longitudinal and transverse field, we split the microscopic Maxwell equation into sets describing transverse dynamics

$$\nabla\times\mathbf{B}(\mathbf{r};\omega)=\frac{-i\omega}{c^2}\mathbf{E}_T(\mathbf{r};\omega)+\mu_0\mathbf{j}_T(\mathbf{r};\omega),\nabla\times\mathbf{E}_T(\mathbf{r};\omega)=i\omega\mathbf{B}(\mathbf{r};\omega), \tag{5}$$

and longitudinal dynamics $\mathbf{j}_L(\mathbf{r};\omega)-i\varepsilon_0\omega\mathbf{E}_L(\mathbf{r};\omega)=0,\nabla\bullet\mathbf{E}_L(\mathbf{r};\omega)=\dfrac{\rho(\mathbf{r};\omega)}{\varepsilon_0}$ after Fourier

transforming to the frequency domain. Using the dyadic Green's function (also known as the propagator) technique [2,5], we express the transverse electrical field in terms of the transverse part of the external field and the current density as

$$\mathbf{E}_T(\mathbf{r};\omega)=\mathbf{E}_T^{ext}(\mathbf{r};\omega)-i\mu_0\omega\int_V[\mathbf{D}_0^T(\mathbf{r}-\mathbf{r}';\omega)+\mathbf{g}_T(\mathbf{r}-\mathbf{r}';\omega)]\bullet\mathbf{j}(\mathbf{r}';\omega)d^3\mathbf{r}'. \tag{6}$$

The longitudinal electrical field is $\mathbf{E}_L(\mathbf{r};\omega)=-i\mu_0\omega\int_V\mathbf{g}_L(\mathbf{r}-\mathbf{r}';\omega)\bullet\mathbf{j}(\mathbf{r}';\omega)d^3\mathbf{r}'$. Here $\mathbf{D}_0^T$ is

the transverse part of the well-known vacuum electromagnetic propagator describing the

retarded propagation of the radiated field $\mathbf{D}_0(\mathbf{r}-\mathbf{r}';\omega)=-[\mathbf{U}+(1/q_0^2)\nabla\nabla]\dfrac{e^{iq_0|\mathbf{r}-\mathbf{r}'|}}{4\pi|\mathbf{r}-\mathbf{r}'|}$, $(q_0=\omega/c)$

and $\mathbf{g}_T(\mathbf{r}-\mathbf{r}';\omega)=\dfrac{1}{3q_0^2}\delta_T(\mathbf{r}-\mathbf{r}'),\mathbf{g}_L(\mathbf{r}-\mathbf{r}';\omega)=\dfrac{1}{q_0^2}\delta_L(\mathbf{r}-\mathbf{r}')$ are the transverse and longitudinal

self-field electromagnetic propagator respectively [5,6]. Adding the two equations together, we obtain the total local field in terms of the full electromagnetic propagator

$$\mathbf{E}(\mathbf{r};\omega)=\mathbf{E}_T^{ext}(\mathbf{r};\omega)-i\mu_0\omega\int_V[\mathbf{D}_0^T(\mathbf{r}-\mathbf{r}';\omega)+\mathbf{g}_T(\mathbf{r}-\mathbf{r}';\omega)+\mathbf{g}_L(\mathbf{r}-\mathbf{r}';\omega)]\bullet\mathbf{j}(\mathbf{r}';\omega)d^3\mathbf{r}'. \tag{7}$$

Since $\mathbf{D}_0^T$ has both near-field (NF) and far-field (FF) part $\mathbf{D}_0^T(\mathbf{R};\omega)=\mathbf{D}_{FF}^T(\mathbf{R};\omega)+\mathbf{D}_{NF}^T(\mathbf{R};\omega)$,

$\mathbf{D}_{FF}^T(\mathbf{R};\omega)=\dfrac{e^{iq_0R}}{4\pi R}(\mathbf{U}-\mathbf{e}_R\mathbf{e}_R),\mathbf{D}_{NF}^T(\mathbf{R};\omega)=-\dfrac{q_0}{4\pi}[\dfrac{1}{(iq_0R)^3}+(\dfrac{1}{(iq_0R)^2}-\dfrac{1}{(iq_0R)^3})e^{iq_0R}](\mathbf{U}-3\mathbf{e}_R\mathbf{e}_R)$, the

local fields can be readily divided into the long-range (LR) and short-range (SR) parts

$$\mathbf{E}^{LR}(\mathbf{r};\omega)=\mathbf{E}_T^{ext}(\mathbf{r};\omega)-i\mu_0\omega\int_V\mathbf{D}_{FF}^T(\mathbf{r}-\mathbf{r}';\omega)\bullet\mathbf{j}(\mathbf{r}';\omega)d^3\mathbf{r}', \tag{8}$$

$$\mathbf{E}^{SR} = -i\mu_0\omega\int_V [\mathbf{D}_{NF}^T(\mathbf{r}-\mathbf{r}';\omega)+\mathbf{g}_T(\mathbf{r}-\mathbf{r}';\omega)+\mathbf{g}_L(\mathbf{r}-\mathbf{r}';\omega)]\bullet\mathbf{j}(\mathbf{r}';\omega)d^3\mathbf{r}'. \qquad (9)$$

COUPLED-DIPOLE EQUATION OF THE LOCAL FIELDS IN METALL NANOPARTICLE CHAINS

To obtain the local fields in the coupled light-matter system, we need to supplement the field equations with the constitutive equation $\mathbf{j}(\mathbf{r};\omega)=\int d^3\mathbf{r}'\sigma(\mathbf{r},\mathbf{r}';\omega)\bullet\mathbf{E}(\mathbf{r}';\omega)$. The nanostructured system of interest here is composed of linear array of closely-packed metal nanoparticles excited by a transverse electromagnetic field $E_T^{ext}(r;t)$, which may be either a monochromatic wave or a short optical pulse. In first-order many-body density-matrix perturbation theory [5,7], the optical properties of metallic nanostructures are dominated by the diamagnetic response $\sigma_{dia}(\mathbf{r},\mathbf{r}';\omega)=\dfrac{ie^2}{m\omega}N_0(\mathbf{r})\delta(\mathbf{r}-\mathbf{r}')\mathbf{U}=\sigma_{dia}(\mathbf{r};\omega)\delta(\mathbf{r}-\mathbf{r}')$, where $N_0(\mathbf{r})$ is the density of conduction electrons. The constitutive equation simplifies to $\mathbf{j}(\mathbf{r};\omega) = \sigma_{dia}(\mathbf{r};\omega)\bullet\mathbf{E}(\mathbf{r};\omega)$. The nanoparticles are electronically decoupled from each other, so the conductivity tensor is the sum of that of the individual nanoparticle $\sigma_{dia}(\mathbf{r};\omega) = \sum_i \sigma_{dia}^i(\mathbf{r};\omega)$. Since both the dimension of the nanoparticles and the inter-particle spacing are much smaller than the wavelength of the incident light, the local fields inside the nanoparticle chain are dominated by the induced near-field interaction between neighbor nanoparticles as well as more distant ones. Note that unlike the field associated with the incident light $\mathbf{E}_T^{ext}(\mathbf{r};\omega)$, the local field $\mathbf{E}(\mathbf{r};\omega)$ in general *varies rapidly even on an atomic scale*. A rigorous derivation of the coupled-dipole equation often used in near-field optics [3,4] requires careful separation of the far-field and near-field part of the local-field electrodynamics [5].

From Eq. (8), the radiated field existing far away from the nanoparticle chain
$$\mathbf{E}^{ext}(\mathbf{r};\omega)=\mathbf{E}_T^{ext}(\mathbf{r};\omega)-i\mu_0\omega\int_V \mathbf{D}_{FF}^T(\mathbf{r}-\mathbf{r}';\omega)\bullet\sum_i\mathbf{j}(\mathbf{r}';\omega)d^3\mathbf{r}'=\mathbf{E}_T^{ext}(\mathbf{r};\omega)-\mu_0\omega^2\sum_i\mathbf{D}_{FF}^T(\mathbf{r}-\mathbf{R}_i;\omega)\bullet\mathbf{p}_i(\omega), \quad (10)$$

is the incident field plus the radiated field from the point dipoles $\mathbf{p}_i(\omega)=\dfrac{i}{\omega}\int\mathbf{E}(\mathbf{r}';\omega)d^3\mathbf{r}'$ located at the center of mass $\mathbf{R}_i$ of the i-th nanoparticle, since the far-field part of the propagator $\mathbf{D}_{FF}^T(\mathbf{r}-\mathbf{r}';\omega)$ varies slowly across each nanoparticle. This part of the field corresponds to the radiation loss from the nanoparticle waveguide and should be minimized by proper design of the nanoparticle size/shape and waveguide geometry to achieve maximal destructive interference of the radiated field [4].

From Eq. (9), the local field existing inside the i-th nanoparticle can be divided into a "background" and self-field part $\mathbf{E}(\mathbf{r}_i;\omega)=\mathbf{E}^B(\mathbf{r}_i;\omega)+(3i\varepsilon_0\omega)^{-1}\mathbf{j}_T^i(\mathbf{r}_i;\omega)+(i\varepsilon_0\omega)^{-1}\mathbf{j}_L^i(\mathbf{r}_i;\omega)$, where the background field $\mathbf{E}^B(\mathbf{r}_i;\omega) = \mathbf{E}_T^{ext} +\sum_{j\neq i}[(3i\varepsilon_0\omega)^{-1}\mathbf{j}_T^j(\mathbf{r}_i;\omega)+(i\varepsilon_0\omega)^{-1}\mathbf{j}_L^j(\mathbf{r}_i;\omega)]$ is the sum of the external field and the longitudinal/transverse self-field stemming from the other nanoparticles in the chain. Unless the nanoparticles are very close to each other, the background field can be approximated by

$$\mathbf{E}^{B}(\mathbf{r}_{i};\omega)=\mathbf{E}_{T}^{ext}-\frac{2}{3i\varepsilon_{0}\omega}\sum_{j\neq i}\frac{(3\mathbf{e}_{\mathbf{r}_{i}\text{-}\mathbf{R}_{j}}\mathbf{e}_{\mathbf{r}_{i}\text{-}\mathbf{R}_{j}}-\mathbf{U})}{4\pi|\mathbf{r}_{i}-\mathbf{R}_{j}|^{3}}\int \mathbf{j}^{j}(\mathbf{r}_{j};\omega)d^{3}\mathbf{r}_{j}\,. \tag{11}$$

Note that the local field and the background field inside the i-th nanoparticle are related through $\mathbf{E}(\mathbf{r}_{i};\omega)=\int \mathbf{\Gamma}^{i}(\mathbf{r}_{i},\mathbf{r}_{i}';\omega)\mathbf{E}^{B}(\mathbf{r}_{i}';\omega)d^{3}\mathbf{r}_{i}'$, where $\mathbf{\Gamma}^{i}(\mathbf{r}_{i},\mathbf{r}_{i}';\omega)$ is the non-local field-field response function which can be obtained from the local-field calculation of the isolated i-th nanoparticle [5]. Since the background field varies slowly across each nanoparticle, an electrical dipole-dipole polarizability can be defined $\alpha_{j}(\omega)=\iint d^{3}\mathbf{r}_{j}d^{3}\mathbf{r}_{j}'\,\sigma_{j}(\mathbf{r}_{j};\omega)\mathbf{\Gamma}^{j}(\mathbf{r}_{j},\mathbf{r}_{j}';\omega)$ such that $\int \mathbf{j}^{j}(\mathbf{r}_{j};\omega)d^{3}\mathbf{r}_{j}=-i\omega\alpha_{j}(\omega)\bullet\mathbf{E}^{B}(\mathbf{R}_{j})$. Inserting the above equation into Eq. (11), we obtain the following coupled-dipole equation between the background fields at each nanoparticle [5]

$$\mathbf{E}^{B}(\mathbf{R}_{i};\omega)=\mathbf{E}_{T}^{ext}+\sum_{j\neq i}\mathbf{W}(\mathbf{R}_{i}-\mathbf{R}_{j};\omega)\mathbf{E}^{B}(\mathbf{R}_{j};\omega),\,\mathbf{W}(\mathbf{R}_{i}-\mathbf{R}_{j};\omega)=\frac{2}{3}\frac{(3\mathbf{e}_{\mathbf{R}_{i}\text{-}\mathbf{R}_{j}}\mathbf{e}_{\mathbf{R}_{i}\text{-}\mathbf{R}_{j}}-\mathbf{U})\,\alpha^{j}(\omega)}{4\pi|\mathbf{R}_{i}-\mathbf{R}_{j}|^{3}}\,. \tag{12}$$

Note that the background field describes the induced near-field coupling between different nanoparticles. The local field inside each nanoparticle is the background field plus its own self-field through the self-field electromagnetic propagator.

The above equations provide the rigorous basis for performing local field calculation and studying energy transport in metal nanoparticle waveguides, if the conduction electron density and current density can be obtained using, e.g., time-dependent density-function theory or random-phase approximation of the optical response of metal nanoparticles. Such calculations will be discussed elsewhere.

ACKNOWLEDGEMENT

REFERENCES

1. *Near-Field Optics*, edited by D.W. Pohl and D. Courjon (Kluwer Academic, Dordrecht, 1993).
2. C. Girard and A. Dereux, *Rep. Prog. Phys.* **59**, 657 (1996).
3. M. Quinten, A. Leitner, J.R. Krenn, and F.R. Aussenegg, *Opt. Lett.* **23**, 1331 (1998).
4. M.L. Brongersma, J.W. Hartman, and H.A. Atwater, *Phys. Rev. B* **62**, 16356 (2000); S.A. Maier *et al. Nature Mater.* **2**, 229 (2003).
5. O. Keller, *Phys. Rep.* **268**, 85 (1996); O. Keller, in *Progress in Optics,* Volume **XXXVII**, edited by E. Wolf (North-Holland, Amsterdam, 1997).
6. C. Cohen-Tannoudji, J. Dupont-Roc, and G. Grynberg, *Photons and Atoms* (Wiley, New York, 1989).
7. U. Kreibig and M. Vollmer, *Optical Properties of Metal Clusters* (Springer, Berlin, 1994); D. Pines and P. Nozieres, *The Theory of Quantum Liquids* (W.A. Benjamin, New York, 1966).
8. R. Loudon, *J. Phys. A* **3**, 233 (1970); D.F. Nelson, *Phys. Rev. Lett.* **76**, 4713 (1996); S. Glasgow, M. Ware, and J. Peatross, *Phys. Rev. E* **64**, 46610 (2001).

W5.17

Optical and Mechanical Properties of Photoassisted, Self-assembled Nanoparticle Films

G. A. Gaddy,[1†] G. A. Miner,[2] Diane M. Stoakley,[2] Edward P. Locke,[3‡] Rick L. Moore,[3] John Schultz,[3] Don Creyts,[3] and Michael Knotts[3]

[1]United States Army Research Laboratory, Sensors and Electron Devices Directorate, Adelphi, MD 20783
[2]NASA Langley Research Center, Advanced Materials and Processing Branch, 6 West Taylor Street, Mail Stop 227, Hampton, VA 23681, U.S.A.
[3]National Research Council Post Doctoral Fellow, NASA Langley Research Center, Advanced Materials and Processing Branch, 6 West Taylor Street, Mail Stop 227, Hampton, VA 23681, U.S.A.
[4]GeorgiaTech Research Institute, STL, 400 West 10th Street, NW Atlanta, GA 30332, U.S.A.
[†]Previously: National Research Council Post Doctoral Fellow, NASA Langley Research Center, Advanced Materials and Processing Branch, 6 West Taylor Street, Mail Stop 227, Hampton, VA 23681, U.S.A.
[‡]Current address: K & M Environmental, Inc., Virginia Beach, VA 23454, U.S.A.

ABSTRACT

This paper presents research funded under the Defense Advanced Research Projects Agency (DARPA) MetaMaterials program for design and development of nanoparticle based, mesoscale electromagnetic and optical materials. Specifically, we present results of formulation and near infrared measurement-model validation for photoassisted, self-assembled multilayer metallic nanoparticle films. The multilayer films may be used as optical filters and absorbers. We demonstrate that nanoparticles can be formed in advanced polymer films that exhibit new electromagnetic constitutive properties. Metal nanoparticle films are produced from a single homogeneous resin containing a soluble precursor. Films cast from doped resins are exposed to UV radiation followed by a controlled thermal cure. The combination of UV exposure and thermal curing creates a multiphase material composed of low volume fractions of dispersed metallic Pd clusters (10–20 nm in size) and high concentrations of Pd nanoparticles which form surface and embedded metallic layers in the films. The layer separation is a function of UV exposure. These materials show significant absorption in the optical and near IR region of the spectrum. Furthermore, these films exhibit mechanical properties similar to bi-metallic layers, specifically, the films display reversible bending with exposure to light and an accompanying rapid temperature increase. This paper presents formulation processes, optical-mechanical measurements and measurement model comparison.

INTRODUCTION

MetaMaterials are designer composite materials that exhibit properties not readily observed in nature. The primary goal of this effort was to develop and validate integrated atomic level to macro scale physics models, then to apply the validated models to engineer nano and meso scale materials with superior electromagnetic (EM) properties. For the nanoparticle films presented in

this paper, the physics-based model combined effective medium theory with transmission line analysis. This "meta-model" effectively describes composites with microstructures that exist over varying (orders of magnitude) length scales.

Materials development for model validation was based on advances in metallized polymer films, more specifically self-metallizing polyimide films. Self-metallizing high-performance polyimides have been investigated for aerospace applications for many years.[1,3] These polyimide-based systems were chosen because of previously demonstrated control of surface metal particle formation within thermally imidized films.[3] To gain more precise control of both the formation/size of metal particles and the placement of formed metal particles within the polyimide films, a process was developed which includes exposing the metal ion doped polyamic acid film to UV light prior to thermal imidization. This paper presents a model fitted to the optical to near IR spectrum of the multi-layered, nanocomposite resulting from the modified self-metallizing film process.

EXPERIMENTAL

3,3', 4,4'-Benzophenonetetracarboxilc dianhydride (BTDA) and 4,4'-oxydianiline (ODA) were obtained from Allco Chemical and Wakayama Seika Kogyo, respectively. $PdCl_2$, anhydrous N, N- dimethylacetamide (DMAc) and dimethyl sulfide were obtained from Aldrich. All chemicals were used as received without further purification. Polyamic acid resins (12-15 weight %) were prepared by reacting equimolar amounts of BTDA and ODA in DMAc. The resin was stirred under N_2 for 15-20 h and then stored at 10 °C under N_2. $Pd[S(CH3)_2]_2Cl_2$ was synthesized from $PdCl_2$ as described previously for the Pt analog of this compound.[4] Resins were doped at room temperature with $Pd[S(CH3)_2]_2Cl_2$ to produce polymer films containing 5 weight % Pd. The resins were sealed under N_2 and placed on an automatic shaker for 4 h, then stored at 10 °C. All films were cast on glass substrates at 330 μm with a 2" Gardco Microm Film Applicator. The freshly cast films were placed directly into a horizontally positioned Rayonet 200 photochemical reactor equipped with RPR-3500A lamps and exposed for varying amounts of time to 350 nm light with an average intensity (I_0) of 10^{17} hv s^{-1}. After photolysis, the films were cured using a programmable forced air oven (Blue M model DC-256 C) to remove DMAc solvent, induce imidization of the polyamic acid and further reduce Pd^{2+} ions. The oven was programmed to heat the samples in successive steps of 100, 200 and 300 °C for 1 h each, returning to ambient temperature over 2 h. Cured films had a thickness of 15-60 μm as determined with a TMI 49-60 micrometer.

Transmission electron microscopy (TEM) analysis of microtomed films was performed with a Zeiss EM 10CR microscope operating at 60 kV. Samples were illuminated at various intensities with a Fiber-Lite MI-150 high intensity illuminator. The illumination device was equipped with a 150-Watt type EKE halogen lamp and a 1/4″ Dolan-Jenner industrial-grade quartz light guide. Intensity measurements of the light exiting the guide were made using a New Focus model 2031 large area silicon photoreceiver with corrections for the varying color temperature of the bulb. The corrections were calculated based on a set of calibration measurements using narrow-banded optical filters. UV-Near IR spectra were collected using a Cary 500 UV/VIS/NIR spectrophotometer.

RESULTS/DISCUSSION

Non-irradiated Pd^{2+} doped thermally cured polyimide films (self-metallizing films) are composed of two distinct layers; a single metallized layer on the surface of the film and a Pd particle polymeric bulk layer. TEM images of a 15 hr irradiated Pd^{2+} doped thermally cured polyimide film are shown in Figure 1. The TEMs indicate that irradiated/thermally cured films are composed of four distinct layers. The layers formed in the irradiated Pd^{2+} doped thermally cured polyimide films include: (1) high density surface metallized layer, (2) a low density Pd particle polymeric layer (inter-layer), (3) an embedded high density metallized Pd layer and (4) a low density Pd particle polymeric layer (comprises bulk of film). These irradiated metallized PI films are multi-colored. The observed colors are a function of interlayer thickness (as determined by the distance between the metallic surface and embedded layers) and are postulated to be intensity dependent.[5] The mechanisms responsible for the photoinduced multilayer films are currently under investigation.

The multi-layered films exhibit optical-mechanical properties and have potential applications as MOMS devices (micro-optical-mechanical-system). Figure 2 shows a plot of the light intensity dependence of film deflection. The plot of the normalized radius of curvature verses power at 500 nm shows a linear relationship for the optically induced mechanical properties of the film. At relative light intensities < 5%, the radius of curvature of the films does not change. However, at relative light intensities > 5%, the radius of curvature varies linearly. The radii of curvature were determined from digital images taken at known impinging light intensities (example in inset of Figure 2).
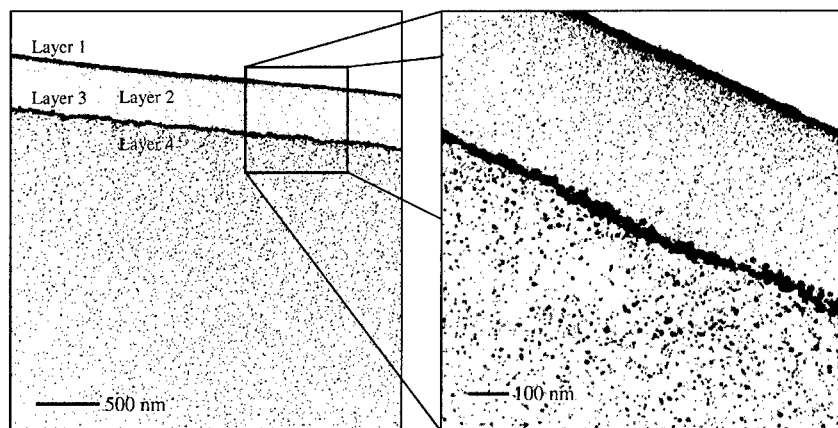
Figure 1. TEM images of 15 hr irradiated (350 nm) Pd^{2+} doped, thermally cured BTDA-ODA polyimide film.
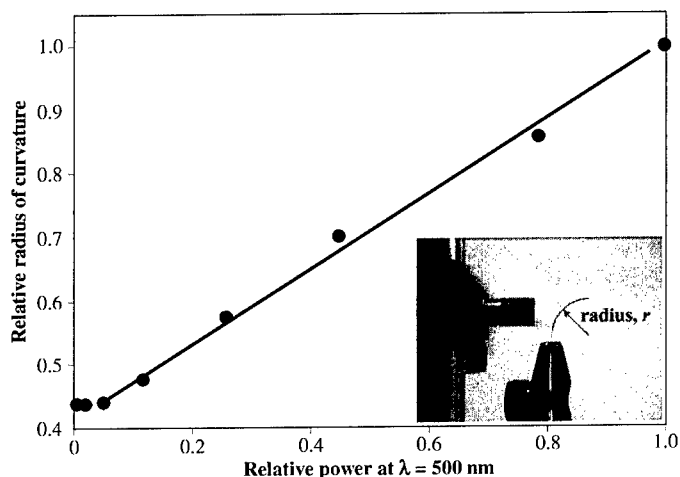
Figure 2. Relative radius of curvature of 15 hr Pd^{2+} doped, thermally cured polyimide film as a function of relative power at 500 nm from a white light source. Inset, digital image showing radius of film in caliper prior to illumination by the white light source located left of the film.

Figure 3(a) shows a comparison between the measured and modeled transmission spectra through the four layer film. The model calculation combines effective medium theory with transmission line (network analysis) theory to predict the electromagnetic performance of a four layer film of palladium embedded within a polymer matrix. The model was based on the usual Bruggeman effective medium theory for metal spheres in a dielectric host, equation 1:[6]

$$0 = v_i \frac{\varepsilon_i - \varepsilon}{\varepsilon_i + 2\varepsilon} + v_m \frac{\varepsilon_m - \varepsilon}{\varepsilon_m + 2\varepsilon} \tag{1}$$

where v_i and v_m are the relative volume fractions of inclusion and matrix, and ε_i, ε_m, and ε are the permittivities of the inclusion, matrix, and composite. This Bruggeman model was applied to each layer and the sum of the individual layers were computed via a cascade-matrix calculation.[7]

The model inputs included the thickness of each layer and the dielectric properties of the polymer and the palladium. The thickness of the layers was taken from TEM images, and the polymer and palladium properties were taken from handbooks.[8, 9] The average volume fraction of the entire film was known to be 0.56 vol% from the stoichiometry of the starting materials. Thus, 0.56 vol% was assumed as the volume fraction for the two thickest layers (layers 2 and 4 in Figure 1). The volume fraction of palladium in the thin layers (layers 1 and 3 in Figure 1) was used as a fitting parameter to achieve model-measurement agreement. The volume fractions of these thin layers were assumed to be approximately the same and were equal to 18 vol% for the
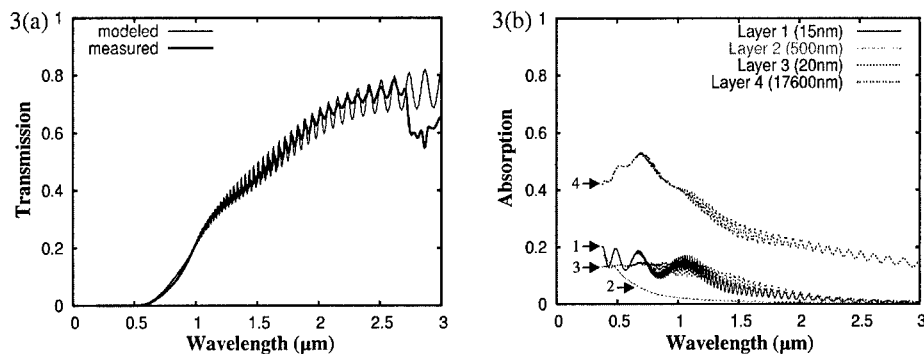
Figure 3. (a) Modeled and measured comparison of transmission spectra through multi-layered film in Figure 1. (b) Predicted contributions from layers 1-4 to the overall absorption spectrum of the multi-layered film in Figure 1.

fit of Figure 3(a). Note that the thin layers appear to be solid Pd in the TEM image (Figure 1), however, since the sample thickness is approximately 100 nm, the image projection is deceiving.

In addition to fitting the measured data, the model enables additional properties of the multi-layer films to be investigated. For instance, Figure 3(b) shows the absorption spectrum of the individual layers calculated from this model. This data shows that almost half of the total absorption occurs in the two thinnest layers (layers 1 and 3 in Figure 1), even though these two layers only make up 0.19% of the total film thickness.

CONCLUSIONS

In an effort to generate monodisperse Pd nanoparticles in polyimide films, a novel method for the formation of multiple Pd layers in polyimide films was developed. The method requires an irradiation pretreatment followed by a thermal process sufficient to reduce Pd^{2+} and induce imidization of the polyamic acid film. The four layer films resulting from this process are highly colored and display optical-mechanical properties. Through the combination of effective medium theory and transmission line theory, a model has been fitted to the experimental transmission spectra of the multilayer films. From this model, absorption spectra of each layer in the films have been calculated. The authors are currently determining the mechanisms responsible for the formation of the multi-layers, further characterizing the optical-mechanical properties of the films and abstracting film properties from the developed model.

ACKNOWLEDGMENTS

References

1. J. C. Carver, L. T. Taylor, T. A. Furtsch and A. K. St. Clair, *J. Amer. Chem. Soc.* **102**, 876 (1980)
2. M. L. Caplan, D. M. Stoakley and A. K. St Clair, *J. Appl. Poly. Sci.* **56**, 995 (1995).
3. R. E. Southward and D. M. Stoakley, *Prog. Org. Coatings* **41**, 99 (2001)
4. G. Kauffman and D. Cowan, *Inorgan. Syn.*, **6**, 211 (1960).
5. G. A. Gaddy, Edward P. Locke, G. Mills, G. A. Miner, Diane M. Stoakley, R. Broughton, T. Albrecht-Schmitt and M. E. Miller, submitted to *J. Phys. Chem. B*, November (2003).
6. D.E. Aspnes, *Am. J. Phys.* **50**, 704, (1982)
7. S. Ramo, J.R. Whinnery, T. Van Duzer, Fields and Waves in Communication Electronics, 2nd Ed, J. Wiley & Sons, (1984).
8. Polymer Handbook, 4th Ed., ed. J. Brandrup, E. H. Immergut and E. A. Grulke, John Wiley and Sons, Inc., (1999).
9. Handbook of Chemistry and Physics, 77th Ed., ed. David R. Lide, CRC Press, (1996).

AUTHOR INDEX

SUBJECT INDEX

anisotropic glass, 231
aperiodic lattice, 201
As_2Se_3, 193

biosensor, 27

cavity, 51
chalcogenide glass, 193
columnar thin films, 163
coupled photonic-crystal
    microcavities, 33
coupling, 109

discrete Fourier transform, 201

electrophoretic deposition process,
    151
electron beam lithography, 145
electrostatic phase imaging, 145

Fabry-Perot resonator, 3
ferroelectric, 139
Fibonacci, 39

glancing angle deposition, 163

hexagonal pillar arrays, 103
homogenization, 127

index of refraction, 127
infrared, 237
integrated optics, 121
interfacial energy, 193
ion beam, 69

Jahn-Teller effect, 57

lithium niobate, 145

mesoporous silicon, 33
metallic microcavity, 157
metamaterials, 255
micro
    cavity, 27, 225
    laser, 93
    photonic crystal, 151

microscopic electrodynamics, 249
microstructured optical fiber, 193
modeling, 169
multilayer, 39

nanolaser, 93
nanoparticle, 255
nanoscience, 209
nanostructures, 249
nanotechnology, 209
nonlinear optics, 33

on-chip, 63
optical
    communications systems, 181
    devices, 21
    switch, 121, 215
    waveguide, 121
ordinary and extraordinary wave,
    127

pendant drop, 193
Penrose quasicrystal pattern, 157
PES, 193
phase transition, 57
photoluminescence, 45
photonic(s), 15, 27
    bandgap, 3, 201
        fiber, 193
        waveguide, 63
    band structure, 157, 225
    crystal(s), 51, 57, 69, 75, 81,
        93, 103, 109, 133, 237
        couplers, 133
        fiber(s), 169, 181, 193
        tapers, 133
planar
    guided optics, 81
    photonic crystals, 115
plasmon, 231, 249
point defect, 51
polaritons, 139
poly(ether sulfone), 193
polymer film, 255
polystyrene, 151

265